Multifunctional Silicone Nanofilaments Composite Materials

Dissertation

zur

Erlangung der naturwissenschaftlichen Doktorwürde

(Dr. sc. nat.)

Vorgelegt der

Mathematisch-naturwissenschaftlich Fakultät

der

Universität Zürich

von

Xiaotian Zhang

aus

der V.R. China

Promotionskommission

Prof. Dr. Stefan Seeger (Vorsitz)

Prof. Dr. David Tilley

Prof. Dr. Karl-Heinz Ernst

Zürich, 2019

To the gentle readers

Contents

Contents III
Abstract V
Acknowledgements VII
Publications and Conferences IX
  Research Articles IX
  Contribution to Conferences X
1 Introduction 1
2 Background 3
  2.1 Wetting Phenomenon 3
    2.1.1 Wetting on homogeneous planar surface 3
    2.1.2 Wetting on rough and homogeneous surface 6
    2.1.3 Wetting on inhomogeneous surface 7
    2.1.4 Super-wetting and super-nonwetting 9
    2.1.5 Dynamic wetting 10
  2.2 Silicone in Material Science 13
    2.2.1 Polyorganosiloxane 13
    2.2.2 Precursors and Poly-condensation 14
    2.2.3 Silicone Nanostructures 17
  2.3 Polystyrene-SNFs Composite Material 23
    2.3.1 Polystyrene 23
    2.3.2 Oil-Water Separation 28
  2.4 SNFs Nano-Composite Materials and their Applications 33
    2.4.1 Supported TiO_2 Nanoparticles 33
    2.4.2 Multifunctional Gold Nanoparticles 37
    2.4.3 Hierarchical Structure 40
3 Material and Methods 43
  3.1 Chemicals and Materials 43
  3.2 The Silicone Nanofilament Coating 45
    3.2.1 Surface cleaning, activation and annealing 45
    3.2.2 Gas Phase Coating 46
    3.2.3 Liquid Phase Coating 48
    3.2.4 Surface Activation of Silicone Nanofilaments 49
  3.3 Functionalization on Silicone Nanofilaments 50
    3.3.1 Surface Initiated Polymerization of Polystyrene 50

- 3.3.2 Surface in situ growth of TiO_2 Nanoparticles ... 51
- 3.3.3 Surface deposition of Gold Nanoparticles ... 51

3.4 Hierarchical Structure Formation ... 53

3.5 Applications of Different Functional Composite Materials ... 55

- 3.5.1 Test of Catalytic Activity ... 55
- 3.5.2 Test of Oil Absorption ... 56
- 3.5.3 Test of Anti-Bacterial Ability ... 56
- 3.5.4 Test of Mechanical Durability ... 57
- 3.5.5 Test of Surface Enhanced Raman Spectroscopy ability ... 58

3.6 Analytic Methods ... 59

4 Results and Discussion ... 61

4.1 Morphology-Tuneable PS-SNFs Composite Material ... 61

- 4.1.1 The morphology control of PS@SNFs ... 61
- 4.1.2 The size control of bead-shaped PS@SNFs ... 66
- 4.1.3 Oil-water separation ... 70
- 4.1.4 Photocatalytic Reaction ... 75

4.2 Hierarchical Structured Self-Cleaning Composite Material ... 83

- 4.2.1. Preparation of the Functional LDPE Substrates ... 83
- 4.2.2 Self-cleaning Ability ... 89
- 4.2.3 Abrasion Tests ... 96
- 4.2.4 Anti-bacterial Tests ... 101

4.3 Multifunctional AuNPs-SNFs Composite Material ... 106

- 4.3.1 Characterization of Functional Substrate of AuNPs@SNFs ... 106
- *4.3.2 SERS of the functional substrate* ... 112
- 4.3.3 Catalytic ability of the functional substrate ... 117

4.4 Fabrication of Flexible and Robust SNFs-PE Composite Material ... 124

- 4.4.1 The Fabrication and Characterization of The Synthesized Material ... 125
- 4.4.2 The Mechanical Durability Tests ... 128
- 4.4.3 The Chemical Resistance Tests ... 134
- 4.4.4 The Self-Cleaning Effect ... 137

5 Summary and Outlook ... 141

6 References ... 145

Abbreviations ... 164

Curriculum Vitae ... 166

Abstract

Nanocomposite materials, including ultrathin films, one-dimensional wires, and nanoparticles, have remarkably different properties compared with that of the same composition in bulks. Each component provides and enhances the functionalities in a way the bulky materials cannot. The increased interest in this field is driven by the urgent need for the development of new composite materials that simultaneously exhibit multiple structures and functions.

The aim of the presented thesis is to explore the new combination of properties of nanomaterial systems, in which silicone nanofilaments play a key role as the main structural and functional material. Silicone nanofilaments can be seen as a carpet-like and quasi-porous superstructure, made of numerous one-dimensional filaments. The intrinsic superhydrophobicity, high surface-to-volume ratio due to nano-effect, facile fabrication, inexpensive precursors and the compatibility on various substrates determine silicone nanofilaments a promising system in nanotechnology and surface chemistry.

In the first part of the thesis, the new nanocomposite system of polystyrene-silicone nanofilaments is reported. The high surface area achieved by the SNFs is further enlarged by grafting with polystyrene. By changing the polymerization conditions and post-treatments, the morphology of grafted polystyrene can be easily tuned into three types. The grafted polystyrene enhanced the oil-water separation capacity compared with SNFs solely. The tunable morphology of the polystyrene endowed the system with improved photocatalytic activity when TiO_2 nanoparticles were in situ grown on the composite.

In the second part, an approach to fabricate a novel mechanical durable self-cleaning material was provided, as self-cleaning materials are energy- and labor-saving and environmentally friendly. A hierarchical structure approach combining micro- and nanoscale architectures is provided to protect the nanoscale surface roughness from mechanical contacts. Briefly, glass beads were embedded into a low-density polyethylene film. This composite was subsequently coated with silicone nanofilaments, which provide the nanoscale surface roughness for superhydropbobicity and work as the support for the photocatalyst TiO_2 nanoparticles. The self-cleaning effect was proved using wettability measurements for various liquids, degradation of organic contamination under UV irradiation, and antibacterial tests. The enhanced mechanical durability of the composite material was demonstrated by abrasion tests.

The following part introduces a new system of the combination of gold nanoparticles and silicone nanofilaments, which leads to a promising multifunctional nanocomposite with unique properties. Size-controllable AuNPs were obtained through a modified Turkevich method and deposited on SNFs substrates which grew according to a droplet-assisted growth and shaping (DAGS) mechanism. The novel nanocomposite material was demonstrated to have a remarkable sensitivity in SERS detection with an enhancement factor of ~10^9. In addition, the SERS reproducibility was proven by Raman mapping. Another functionality of catalysis was verified in the hydrogenation reaction of 4-nitrophenol. Further experiments confirmed the new nanocomposite material to have a considerable catalytic activity, stability, and low leaching.

In the final part, a simple, solvent-free and environmentally friendly approach to fabricate flexible and robust superhydrophobic composite films with durable self-cleaning functionality is presented. The mechanical durability is achieved by forming a hierarchical microscaled wrinkle structure on PE film by heating. Notably, the composite film exhibits mechanical robustness under cyclic abrasion, tape-peeling, flexing, intensive finger wiping and knife cutting, maintaining superhydrophobic after long-time exposure to a high humidity environment, and highly corrosive species. In addition, even after oil contamination, the composite film maintains its water repellency and self-cleaning functionality.

Overall, it is demonstrated that silicone nanofilaments can be used as a main functional and structural component in a nanocomposite system. They provide the intrinsic superhydrophobicity and high surface-to-volume ratio, which can be utilized in polymer grafting, hydrogenation, photodegradation, SERS detection and self-cleaning. The two approaches for the fabrication of hierarchical structure enable a wider range of application scenarios for future studies due to the enhanced mechanical durability.

Acknowledgements

First of all, I would like to thank Prof. Dr. Stefan Seeger sincerely for giving me the opportunity to conduct my PhD in his group and giving me all the support and freedom to explore diverse fields in nanoscience and surface chemistry.

I would also thank my committee members Prof. Dr. David Tilley and Prof. Karl-Heinz Ernst for their kind help.

I am deeply thankful to Dr. Margrith Meier for leading me into the silicone world and surface chemistry all the time, especially at the beginning of my PhD.

I am grateful to my senior colleagues Dr. Georg Artus, Dr. Zonglin Chu and Dr. Yuan Li for sharing their invaluable knowledge and expertise.

I would like to thank Dr. Shanqiu Liu sincerely for being an excellent teamwork and giving me insightful advises.

I am grateful to the whole Seeger team who have accompanied me during the last years and made the time fly: Dr. Georg Artus, Dr. Diana Serrano Garcia, Dr. Deb Patra, Dr. Zonglin Chu, Dr. Xiang Fei, Dr. Fangjian Lin, Dr. Yuan Li, Neha Singh, Steve Kappenthuler, Noah Naef, Alessandro De Crema, David Bottone, Rabab Azizi, Kangwei Chen, Yuen Yee Lau, Nathalia Münch, Behzad Sardari, Samet Varol. Big thanks to Dr. Sandro Olveira for him great organizing in many group activities. Special thanks to Naeem Saddiqi and Valentin Dubois for the great time we spent together in the lab and gym.

My sincere gratitude goes to Wei Cui, Jingguo Li, Madhusudhan Jarpla and Tian Liu for their kind support in different fields of technologies.

I would thank all my Chinese fellows for the wonderful time we spent together and the warm atmosphere they created while we are thousands of miles from home. Special thanks go to my flat-mate Wenchao Wan for his great cooking skills and scientific advises and Zenghui Wang for companying and supporting in the gym.

I would also thank the people from administration, IT support and workshop, especially Fabienne Stutz, Chantal Henningsen-Conus, Roland Zehnder, Mirko Hofer and Sascha Giger for their strong support and help.

My thanks also go to the staff in the Center of Microscopy and Image Analysis: Dr. Andres Käch, Dr. Moritz Kirschmann, Dr. Gery Barmettler and Johannes Riemann. Without them, I would not be able to finish my work. Sincerest Thanks belong to Dr. Andres Käch who introduced me with the microscopic technologies in the very beginning of my PhD.

The graduate school CMSZH is acknowledged for the financial support and the activities they organized.

Last, and most important, I am very grateful to my family, especially my parents, my girlfriend Alma, my best friend Kai for being there together with me unconditionally.

Publications and Conferences

Research Articles

[1] Chapter 4.1

Xiaotian Zhang; Stefan Seeger:

Morphology Tuneable and Multifunctional Polystyrene-Silicone Nano-Composite Materials

ChemNanoMat 2019, 5 (7), 964-971.

[2] Chapter 4.2

Xiaotian Zhang; Shanqiu Liu; Alma Salim; Stefan Seeger:

Hierarchical Structured Multifunctional Self-Cleaning Material with Durable superhydrophobicity and Photocatalytic Functionalities

Small 2019, 15 (34), 1901822.

[3] Chapter 4.4

Shanqiu Liu; **Xiaotian Zhang (co-first author)**; Stefan Seeger:

Solvent-free Fabrication of Flexible and Robust Superhydrophobic Composite Films with Hierarchical Micro-/Nanostructures and Durable Self-cleaning Functionality

ACS Applied Materials & Interfaces 2019 11 (47), 44691-44699

[4] Shanqiu Liu; Wenchao Wan; **Xiaotian Zhang**; Alessandro De Crema; Stefan Seeger:

All-organic Fluorine-free Superhydrophobic Bulk Material with Mechanochemical Robustness and Photocatalytic Functionality

Chemical Engineering Journal 2020 385, 123969

[5] Chapter 4.3

Xiaotian Zhang; Valentin Dubois; Shanqiu Liu; Stefan Seeger:

Multifunctional nanocomposite material with gold nanoparticles immobilized on silicone *nanofilaments in SERS detection and catalysis* (Manuscript under preparation)

[6] Valentin Dubois; Diana Serrano; **Xiaotian Zhang**; Stefan Seeger:

Structure Analysis of Amyloid Aggregates at Lipid Bilayers by Supercritical Angle Raman Microscopy

Analytical Chemistry **2020** 92 (7), 4963-4970

Contribution to Conferences

[1] Xiaotian Zhang, Stefan Seeger:

Mechanical durability enhanced self-cleaning composite material with superhydrophobic and photocatalytic ability

Poster presentation, 28th International Conference and Expo on Nanosciences and Nanotechnology, Barcelona, Spain, October 2018

[2] Xiaotian Zhang, Stefan Seeger:

Nanocomposite surface coating of Silicone Nanofilaments (SNF) with diverse-shaped Polystyrene and its application

Poster presentation, 34th Annual Meeting of the Swiss Working Group for Surface and Interface Science (SAOG), Fribourg, Switzerland, February 2018

1 Introduction

In the past decades, multifunctional composite materials (MFCM) attracted remarkable attention in both research and industry. MFCM, as the name states, perform a variety of functions by the combination of different parts of materials. Normally, there is one part, which provides structural functions such as strength, stiffness and stability. Meanwhile the other parts, usually are non-structural functional, provide specific functionalities, like energy storage, self-cleaning, sensing and detecting, actuation as well as a protecting function, etc.[1] In recent years, the demand for MFCM is increasing at a phenomenal speed due to their multiple functions and the broad range of applications. By combining one or several functional composites, the need of excess components is excluded, which brings the advantage that the total mass or volume of the system can be reduced and the overall efficiency can be improved.[2]

The categorization of the MFCM can be done in terms of function, which includes but is not limited to: (1) autonomy MFCM, which possess characteristics like self-healing or self-assembling. (2) Highly tailorable MFCM, which allow the tuning of the structure as well as the functions. (3) Sound/vibration damping MFCM, which lowers noise by the special composition and spatial structure. (4) Electrical/thermal isolating/conductive MFCM. (5) Radiation protecting/emission MFCM. (6) Energy storage MFCM. (7) Environmental MFCM, which includes remediation ability, recyclability, and biodegradability. (8) Chemical reaction functional MFCM such as catalysts and selective permeating stuff. (9) Information storage MFCM etc.[3]

Among numerous materials, one type of the most popular materials is the silicone materials because of their inherent hydrophobic property. Silicone nanofilaments (SNFs), as one of the silicone materials, were discovered by Seeger group in the early 2000s. They exhibit great potential in various applications due to the intrinsic superhydrophobicity and high surface-to-volume ratio. Besides, SNFs coating can be applied on many kinds of surfaces like glass, wood, textiles and polymers by spraying coating, gas phase or liquid phase growth. The fluorine-free and flexible chemical tunability further ensure SNFs as an excellent surface material in many fields.

The aim of this thesis is to explore new and practical functionalities for the nano-composite materials in which silicone nanofilaments (SNFs) stand in the center as the core substrate. For this purpose, certain functionalities were selected which are widely used in research and industry, including photocatalysis from metal oxides particles, Raman spectroscopy detection and hydrogenation-heterogeneous catalysis from noble metal particles, and oil-water separation and self-cleaning from superhydrophobic surfaces. Meanwhile, to solve the problem of mechanical durability and further enhance those functionalities, other approaches have been taken. In the first part (chapter 4.1), to better extend the high surface-to-volume ratio, polystyrene (PS) was composited on SNFs via free radical polymerization. The precursor vinyltrichlorosilane (VTCS) was used to form the specific SNFs as the vinyl groups work as the initiating sites for the surface growth polymerization of PS. The prepared substrate was tested in oil-water separation and photocatalysis to prove the enhanced properties. In chapter 4.2, a novel self-cleaning material was presented. The superhydrophobicity from the intrinsic property of SNFs, combing together with the photocatalytic activity from the deposited TiO_2 NPs in situ grown on SNFs, endowed the material with excellent self-cleaning functionality. To overcome the mechanical susceptibility, a two-scale hierarchical structure was introduced on the surface by embedding glass beads (75 µm) on polyethylene (PE) film. The third chapter (4.3) presents with a multifunctional AuNPs-SNFs composite material. Such a system enables heterogeneous hydrogenation catalysis while working as a SERS detector. In the last chapter (4.4), another hierarchical surface structure was obtained by utilizing the thermal property of PE film. The formed surface morphology protects the SNFs from the damages of the external forces.

2 Background

2.1 Wetting Phenomena

Wetting phenomena are everywhere in nature and industry. A solid surface, which is exposed to the environment, is inevitably covered by a layer of fluidic materials. During wetting, the solid surface is transferred from solid-gas interface to solid-liquid interface. The liquid can either tend to spread on the surface, which is called "wetting", or tend not to spread on the surface, which is called "non-wetting". However, the process of wetting remains complicated as it contains various physicochemical aspects. In this section, different wetting scenarios are discussed and basic concepts and principles of wetting are provided.

2.1.1 Wetting on homogeneous planar surface

A parameter, wettability, is used to determine the ability that a liquid can be extended on one solid surface. The wettability of a solid surface can be characterized in general by measuring the static contact angle (CA) of the interface. In 1805, Thomas Young derived the Young's equation which related the interfacial energies of a liquid drop on a surface and its macroscopic shape:[4]

$$\cos\theta = \frac{\gamma_{SV} - \gamma_{SL}}{\gamma_{LV}} \tag{2.1.1}$$

In which γ_{SV}, γ_{SL}, and γ_{LV} are the solid/vapor, solid/liquid and liquid/vapor interfacial energies, respectively. Θ is the angle that is measured by the liquid/vapor/solid contact line ("three-phase contact line"). The Young's equation is reached by balancing the surface tension forces, which are parallel to the substrate surface on the three-phase contact line (in Figure 2.1.1). In another word, at such an equilibrium, the interfacial surface energies are in balance at the three-phase contact line too.

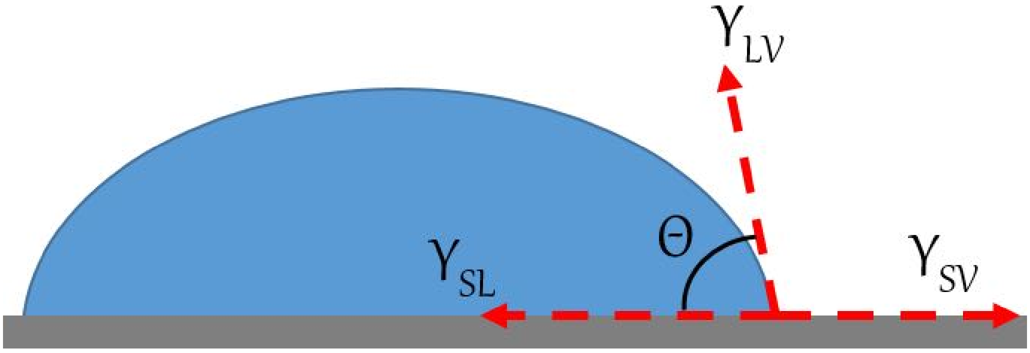

Figure 2.1.1 Balance of the surface tension forces at the three-phase contact line and the contact angle *Θ.*

In consideration of energy, the total surface energy of the system can be described as:[5]

$$S = E_{dry} - E_{wet} = \gamma_{SV} - (\gamma_{SL} + \gamma_{LV}) \tag{2.1.2}$$

In which, S is the spreading parameter, representing the difference between the energetic states of dry and wet surface. When S is positive, which means the energy of the dry surface is higher than that of the wet surface, a complete spreading happens. In this situation, $Y_{SV} \geq Y_{SL,} + Y_{LV}$. Hence, in reality, a high surface energy substrate, like glass, can be wetted by low surface energy liquid (e.g., toluene). On the other hand, when S is less than zero, the energy of the dry surface is lower than that of the wet surface. A droplet of liquid will form on the surface, which is also called partial wetting. In those cases, $Y_{SV} \leq Y_{SL,} + Y_{LV}$, where water droplet forms on a PDMS substrate.[6]

From equation 2.2.1, it is demonstrated that the CA is directly correlated to the interfacial energies that stem from the adhesion strengths between different phases. In general, measuring the CA is a simple and straightforward method to gain insight into the wetting behavior of a liquid on a solid surface. Thus, CA becomes a main characteristic for the analysis of the surface chemistry.

Up to the CA, a solid/liquid interface can be classified as wetting ($\Theta < 90°$) and non-wetting ($\Theta > 90°$).[7] In the case that water is the liquid on a planar surface, commonly four states can be defined in Figure 2.1.2: superhydrophilic (Θ < 5°), hydrophilic (5°<Θ < 90°), hydrophobic (Θ > 90°), and superhydrophobic (Θ > 150°).

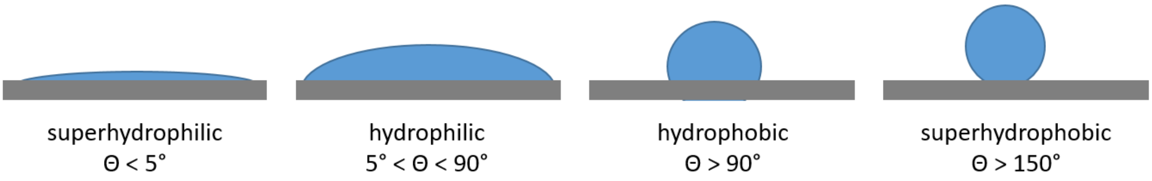

Figure 2.1.2 Four states of wetting for water droplets on a solid surface.

Similarly, when oil is the liquid on a solid surface, four different states are named as superoleophilic (Θ < 5°), oleophilic (5°< Θ < 90°), oleophobic (Θ > 90°), and superoleophobic (Θ > 150°).[8]

In most of the cases, the solid/liquid surface tension is affected by the kind of interactions that occur on the interface. Thus, the value of the individual surface tension is not the only determination, which influences the wetting behavior of a liquid on a solid surface. There are a few theories that divide surface energies into smaller components. Owens and Wendt once mentioned that the surface energies can be divided into a disperse part and a polar part:[9]

$$\gamma = \gamma^D + \gamma^P \tag{2.1.3}$$

The dispersion component contains all non-polar interactions, such as van der Waals force. The polar part includes dipole-dipole, dipole-induced dipole, hydrogen bonding and other site-specific interactions. In the case of a droplet on a solid surface, the solid/liquid surface tension can be expressed as:

$$\gamma_{SL} = \gamma_{SV} + \gamma_{LV} - 2(\gamma_{SV}^D \gamma_{LV}^D)^{\frac{1}{2}} - 2(\gamma_{SV}^P \gamma_{LV}^P)^{1/2} \tag{2.1.4}$$

By applying the equation 2.1.4 into Young's equation, it leads to:

$$\cos\theta = 2\frac{(\gamma_{SV}^D \gamma_{LV}^D)^{\frac{1}{2}}}{\gamma_{LV}} + 2\frac{(\gamma_{SV}^P \gamma_{LV}^P)^{\frac{1}{2}}}{\gamma_{LV}} - 1 \tag{2.1.5}$$

Equation 2.1.5 gives the information that the surface wetting behavior is mainly affected by the polar and disperse parts contributing to the interfacial energies.

The CA of the Young's equation is only valid for a smooth and homogeneous perfect surface. In fact, there are always some defects or inhomogeneity existing on all solid surfaces. These can be micro- or nano-scaled roughness. As a result, when describing the wetting phenomenon on a rough and inhomogeneous surface, it is indispensable to take further consideration into account.

2.1.2 Wetting on rough and homogeneous surfaces

On a surface with roughness, the simple Young's equation is not valid anymore since the surface tension equilibrium at the three-phase contact line will be changed by the surface roughness (in Figure 2.1.3).

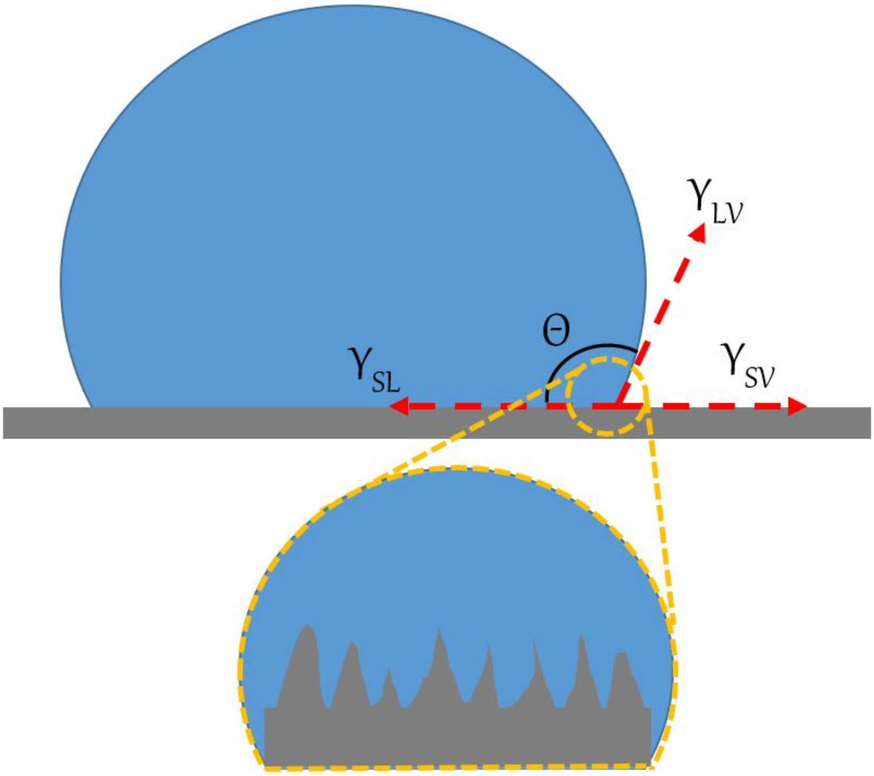

Figure 2.1.3 Balance of the surface tension forces at the three-phase contact line on a rough surface in a Wenzel wetting state.

Thus, the projection of the interfacial energies parallel to the rough surface is different compared with that of a smooth planar surface. Wenzel brought up a non-dimensional roughness factor r:[10]

$$\mathrm{r} = \frac{actual\ surface}{geometric\ surface} \qquad (2.1.6)$$

By introducing this factor, the solid surface tension projected parallel to the macroscopic interface has such a relation with the surface tension of the flat surface:

$$\gamma^* = \mathrm{r} \cdot \gamma \qquad (2.1.7)$$

Thus, the CA at the balance of the surface forces now is:

$$\cos\theta^* = \frac{\gamma^*{}_{SV} - \gamma^*{}_{SL}}{\gamma_{LV}} = \frac{r \cdot \gamma_{SV} - r \cdot \gamma_{SL}}{\gamma_{LV}} = r \cdot \frac{\gamma_{SV} - \gamma_{SL}}{\gamma_{LV}} \qquad (2.1.8)$$

Therefore, we have the so-called Wenzel equation:

$$\cos\theta^* = r \cdot \cos\theta \qquad (2.1.9)$$

The apparent CA θ^* obtained by measuring on a rough surface is related to the intrinsic CA θ which determined by the material properties.

From equation 2.1.9, the surface roughness can enhance the intrinsic wetting behavior of a surface. A wettable surface can be more wettable once it becomes rougher. Meanwhile, a non-wettable surface will reduce its wettability with the increasing of roughness.

The Wenzel equation provided an approach for the wetting behavior of a rough but homogeneous surface. For inhomogeneous surfaces, other methods are required and will be discussed in the coming section.

2.1.3 Wetting on inhomogeneous surface

Solid surfaces in reality are often inhomogeneous. They consist of different type of chemical composite or have impurity on the surface. To describe the wetting behavior on a heterogeneous surface, the Cassie-Baxter equation was introduced:[11]

$$\cos\theta^* = \sum_i f_i \cdot \cos\theta_i \tag{2.1.10}$$

$$1 = \sum_i f_i \tag{2.1.11}$$

in which f_i represents the area fraction on the surface of chemical component *i* that is wetted by the liquid and θ_i is the intrinsic CA on patch *i*. In a system, which contains two chemical compositions, the Cassie-Baxter equation can be described as:

$$\cos\theta^* = f_1\cos\theta_1 + (1 - f_1)\cos\theta_2 \tag{2.1.12}$$

The equation 2.1.10 builds a relation of the apparent CA observed macroscopically with the microscopic chemical composition of the solid surface. Particularly, the equation is used in the wetting situation where air is trapped inside of the grooves of a solid surface under the liquid (Figure 2.1.4).

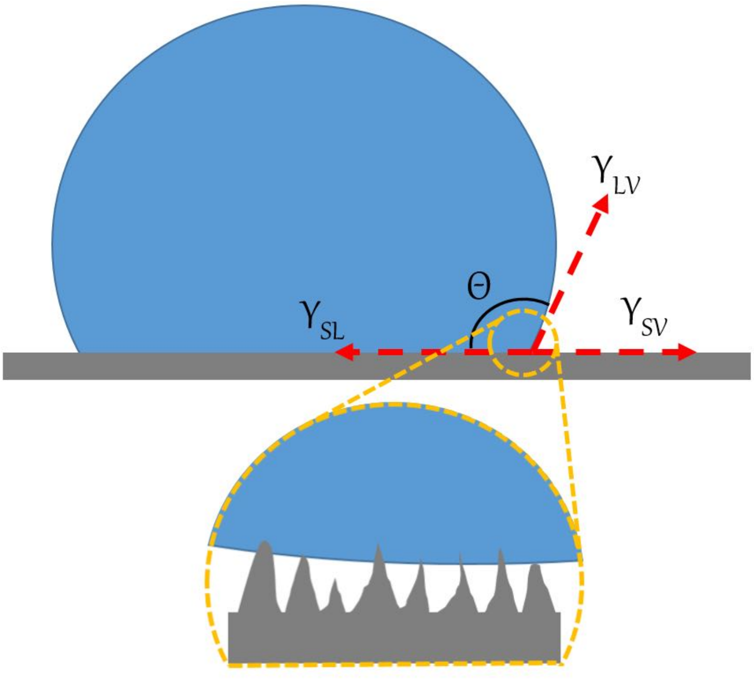

Figure 2.1.4 Balance of the surface tension forces at the three-phase contact line on a rough inhomogeneous surface with air trapped in grooves in a Cassie-Baxter state.

In a Cassie-Baxter state, on the contrast to the Wenzel model, the air trapped in the grooves keeps the liquid from permeating. Therefore, the droplet has a considerably low contact area in comparison with the droplet in Wenzel model. The transition between a Cassie-Baxter state and a Wenzel state was observed but the mechanism and accurate control are still a subject of active research.[12] A normal method to convert a Cassie-Baxter state to a Wenzel state is to apply pressure on the liquid droplet. Other approaches such as changing the temperature and evaporating the liquid were also reported.[12-14]

2.1.4 Super-wetting and super-nonwetting

Super-wetting state refers to situations where the liquid completely wets the solid surface and super-nonwetting state, instead, refers to a case in which the surface is totally not wettable at all by the liquid. In the former case, CA is approaching to zero and normally less than 5°. No exactly rigorous terminology was applied to define the super-wetting state, but it is commonly recognized that CA should be more than 150° in this situation.

The extreme values of the CAs are of great interest in both research and industry. For example, superhydrophilic coating on mirror exhibited antifogging properties;[15] superoleophilic nanofibers can be applied on membranes for oil-water separation;[16] superhydrophobic stainless steel was proved to have remarkable anti-icing property in aviation;[17] superoleophobic surfaces provide the feasibility of microdroplet manipulation technology for microreactors and labs-on-chips.[18, 19]

Among the abovementioned phenomena, the superhydrophobic state attracted the most interest as its broad applications in industry and science. To form a superhydrophobic surface, the roughness is a prerequisite to exhibit a CA larger than 150°. Theoretically, a smooth surface made of the material with the lowest surface tension material (fluorinated materials) can only ensure a water CA no larger than 120°.[20] By involving roughness on a low-surface tension surface, the superhydrophobicity can be achieved with CA up to even 180°.[21]

As mentioned in the last section, there is a significant difference between Wenzel and Cassie-Baxter states, even though in both cases, the same CA was measured in the superhydrophobic range. In the Cassie-Baxter state, the liquid only partially sits on the solid surface and the contact area of the droplet is really small in comparison, which leads to a low liquid adhesion behavior. High adhesion causes the droplet sticks on the surface steadily without rolling off in Wenzel state. On the other hand, once a small tilt of the surface occurs, the droplet can roll off easily in Cassie-Baxter state.

As the CA value in both states can be larger than 150°, while the non-wetting behaviors are fundamentally different. Additional information about the dynamic wetting behavior is necessary to further distinguish the wetting states. Here we introduce the sliding angle and CA hysteresis in the next section.

2.1.5 Dynamic wetting

Sliding angle (SA) and CA hysteresis measurements are common methods to determine the dynamic wetting state of a superhydrophobic surface (CA > 150°). A water droplet starts to roll off the surface once a certain angle α reaches by slowly tilting the horizontal surface where the droplet is placed. This angle α is defined as SA. During the inclination of the surface until the droplet starts to roll off, the CA measured at the forefront of the droplet constantly increases and CA at the back of the droplet decreases continuously. The gravity causes the deformation of the droplet from a symmetric shape during tilting (in Figure 2.1.5). The former CA is called advancing CA and the later one is called receding CA. The SA depends on the retention force of the droplet to the surface, which correlated to the CA hysteresis. Thus, we have the equation:[22, 23]

$$\frac{m \cdot g}{w} \cdot \sin\alpha = \gamma_{LV} \cdot (\cos\theta_R - \cos\theta_A) \tag{2.1.13}$$

where m is the mass of the droplet, g is the acceleration of gravity, w is the width of the droplet, α is the SA and θ_A and θ_R represent the advancing and receding angles respectively.

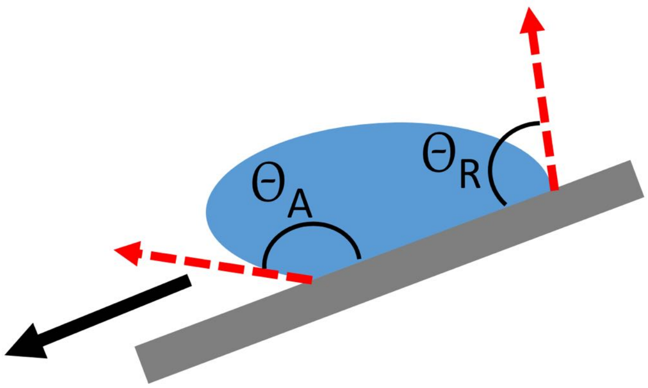

Figure 2.1.5 A droplet of water on a tilting surface.

A similar phenomenon can be observed if the volume of the droplet placed on the superhydrophobic surface is changing gradually. An increase of the volume leads to an increase of the CA value while a decrease of the droplet volume leads to a decrease of the CA value (Figure 2.1.6). These two CAs are also called advancing and receding CA, respectively.

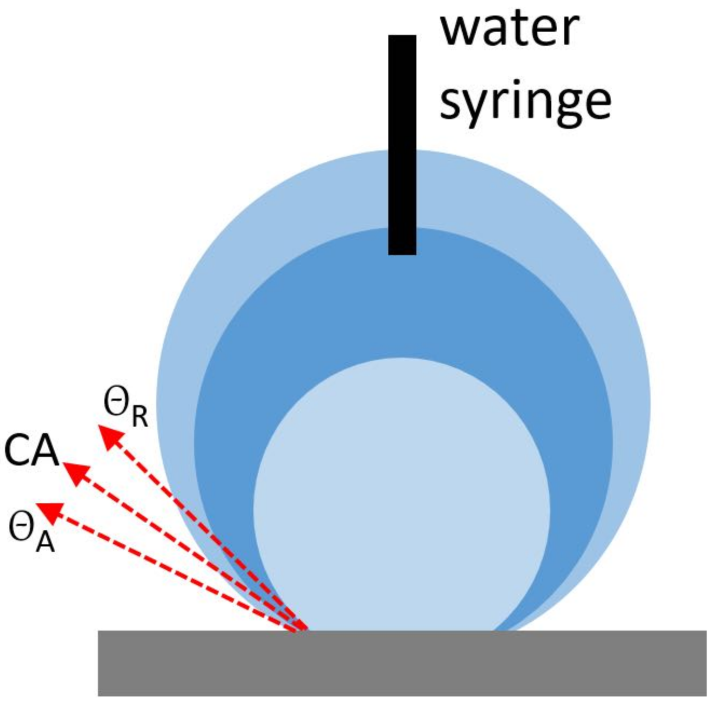

Figure 2.1.6 A droplet of water with the change of the volume on a horizontal surface.

Normally, on a smooth planar surface without defects or inhomogeneities, CA hysteresis is initially very low due to the low number of defects that can pin the liquid/solid contact line.

Theoretically, the advancing CA is the same value as receding CA (planar smooth surfaces with the change of liquid volume). However, in reality, almost all surfaces exhibit certain roughness or inhomogeneities, which represent the pinning points on the surface and lead to a distinguishable CA hysteresis.[24] With higher surface roughness, consequently the CA hysteresis increases. This relation holds as long as the wetting behavior belongs to Wenzel state.[25] Notably, the dynamic wetting behavior of Wenzel state is different from that of Cassie-Baxter state. The contact area between the solid surface and liquid drop is relatively lower in Cassie-Baxter state since the droplet sits only partially on the surface and air is trapped in the grooves. The majority of the area beneath the drop can be considered as a homogeneous liquid/air interface, which contains very few defects. Only the small area where the liquid contacts the solid asperities act as the defects as well as the pinning points. Thus, in the Cassie-Baxter state, even though with high surface roughness, the surface can be considered to have higher homogeneity and fewer defects than that in a Wenzel state. As a result, a low CA hysteresis was observed.[26-28]

What’s more, in 1964, Johnson and Dettre simulated the transition from Wenzel to Cassie-Baxter state on a hydrophobic surface by increasing the surface roughness ratio.[29] Initially a smooth surface had a CA hysteresis of almost 0°. With the increase of the roughness ratio r, the CA hysteresis became larger. At a certain point during the increasing of roughness ratio (approximately $r = 1.8$), the CA hysteresis had a sudden reduction, which indicated at this roughness ratio, the transition from Wenzel to Cassie-Baxter state occurred.

Moreover, Öner and McCarthy in 2000 discovered that on a surface of Cassie-Baxter state, the density, shape and size of the asperities influenced the dynamic wetting behavior.[30] By changing the shape from square to staggered rhombus, star or indented square, an increase of the receding CA was observed. After changing the dimension of square posts from 2 µm to 64 and 128 µm, the water droplets changed from easily sliding to pinning on the surface. According to the article, a 3-dimensional and random rough surface with nano-structured asperities should exhibit very low CA hysteresis and SA in superhydrophobic range. This leads to the synthesis of artificial surfaces, which have superhydrophobicity and self-cleaning properties in industry.

2.2 Silicone in Material Science

Silicone (or polysiloxane) materials are widely used in industry and daily life. For example, in automotive industry, silicone rubber, with a high strength, is used as the coatings and sealants for airbags; silicone combined with thermoplastics is used in car coating for better scratch-resistance; sheet silicone is applied in automotive engines and transmissions as gaskets. In human care field, silicone ingredients were adopted to enhance the hair sheen and in creme to keep moisture of the skin.[31-33] The broad range of applications of silicone materials is beneficial from their versatile intrinsic properties, such as thermal stability, low flammability, non-toxicity, biocompatibility, flexibility, resistance to chemicals and so on.[34] In this chapter, the history of silicone material and development, the precursor, the synthesis and finally the nano-structured silicone material are described.

2.2.1 Polyorganosiloxane

The word “silicone” was literally a combination of “silicon” and “ketone” coined by Kipping in 1901. The original word “silicketone” is no longer the correct term and siloxane (polysiloxane or polyorganosilane) is the correct according to the nomenclature of modern chemistry.[35, 36] The structure described of silicones actually contain Si-O-Si backbones or net, without oxygen double bond linked to Si atom.

As the electronegativity of silicon is 1.8 compared with that of oxygen 3.5, the Si-O bond in the backbone is strongly polar, which leads to a high bond strength of 447 kJ / mol in comparison with C-O bond of 358 kJ / mol.[37] That explains the thermal stability and chemical inertness of silicone materials. A good example for the thermal stability is polydimethylsiloxanes (PDMS) whose degradation temperature is above 300 C° in a nitrogen atmosphere.[38] The bond length of Si-O is about 1.63 Å, which is longer than the C-C bond of 154. Å.[39] Thus, the rotation of Si-O is easier. Notably, the Si-O-Si angle was reported to be above 140 °, usually around 147 °.[40] In comparison, the C-C-C was found to be ~110 ° as sp^3 carbons.[41] So the rotation energy for polysiloxanes is smaller than carbon polymers when they have the same side groups. This was confirmed that the rotation energy of CH_2-

CH_2 bond in polyethylene was 13.8 kJ / mol and that of Si-O bond was 3.3 kJ / mol. As a conclusion of the abovementioned information, polysiloxanes have a small energy configuration, causing polysiloxanes as more flexible polymers than polymers based on C-C backbone. When the residue groups on the Si-O-Si chain is nonpolar, they shield the Si-O bond and make the intermolecular force relatively weak. Thus, the low energy of rotation and low intermolecular force lead to a favored configuration where the hydrophobic groups face externally, which determines polysiloxanes low surface tension materials. The intrinsic low surface tension, high thermal stability and chemical inertness make polysiloxanes one of the most widely used polymers in human life.[42]

The classification of polysiloxanes is usually according to the molecular weight and degree of crosslinking. Silicone fluids, silicone elastomers and silicone resins are the main three categories.[43] Silicone fluids, with the polymerization degree from 0 - 10000, show different viscosity. The fluidic property, high compressibility and thermal stability make them widely used as lubricant, heat transfer media and refrigerant in many fields.[44] Silicone elastomers are also linear polymers as silicone fluids but contain cross-linkers in the structure. The rubber-like behavior, high stability at wide temperature range, and gas permeability make them a good material for contact lens, filtration membranes and footwear materials.[45] Silicone resins, in comparison, are polysiloxanes, which have a highly cross-linked structure. By showing the dual characteristics of organic resin and inorganic materials, silicone resins have been used as insulating materials, heat-resistant and anti-corrosion coatings and household products.[46]

To synthesize different types of silicone materials, the understanding of the building block, as called precursors, is of essential importance.

2.2.2 Precursors and Poly-condensation

Organo-substituted silanes are the building unit and starting material for the polymerization of polysiloxanes. The more common name used for silanes is precursor. Until the successful synthesis of silanes on a large scale, the industry of polysiloxanes became prosperous. After the first synthesis of silane reported by Kipping in the early 20th Century (Figure 2.2.1a), Müller and Rochow independently discovered the approach to synthesize methylchlorosilane on an industrial scale.[47]

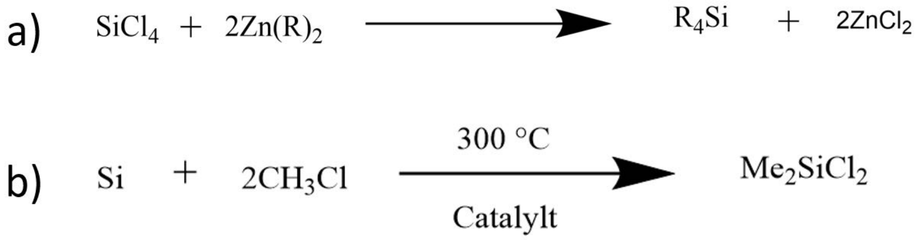

Figure 2.2.1 Synthesis of silanes

In one of the typical organic synthesis of silanes, the methyl chloride reacted with solid silicon metal, in the presence of copper catalysts and other promoters to produce a mixture of chlorosilanes as shown in Figure 2.2.1b.[47] The products are normally a mixture of silanes with different numbers of organic residues and hydrolysable groups. The selectivity towards certain silanes can be controlled by using a designed mixture of metallic catalysts.[48] The separation and purification of the mixture of products are done through distillation followed by crystallization.[49]

The precursors for silicone polymerization, silanes, are of the general chemical formula $R_nSiX_{(4-n)}$, where the R represents organic residues and X hydrolysable groups, such as alkoxy, amine or halogen. Depending on the organic residue and hydrolysable groups, the silanes show different reactivity and solvent solubility. The hydrolysis reaction of dimethyldichlorosilane occurs quickly after the presence of water to form silanols (Figure 2.2.2).

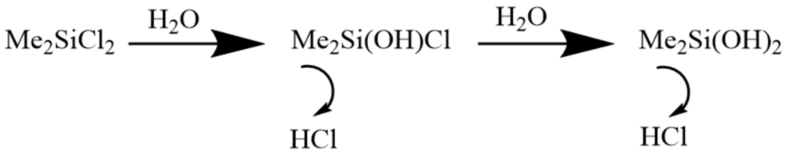

Figure 2.2.2 Hydrolysis of dialkyldichlorosilane to dialkysilandiol

After the hydrolysis, the condensation happens to form the polysiloxanes (Figure 2.2.3a). The intermolecular condensation usually is catalyzed by either acid or base.[50] The initial poly-condensation leads to short linear chains (n = 10-40) or small cyclic structure (m = 3-6) in the case of using dimethyldichlorosilane as a precursor (Figure 2.2.3b). Further condensation catalyzed by acids or bases leads to a larger linear structure of higher molecular weight.

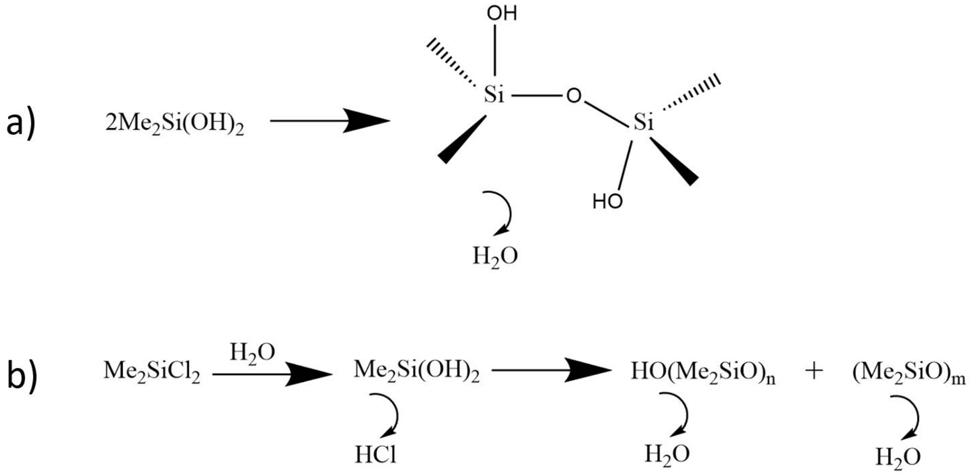

Figure 2.2.3 Intermolecular condensation of siladiols to form linear or cyclic polysiloxanes

The number of hydrolysable groups in silanes determines the number of bridge oxygen atoms, which connect to two silicon atoms. So, the silanes are classified into four types: mono- (M), di- (D), tri- (T) and quadro- (Q) functional, with the formulas of the corresponding polysiloxanes of $R_3SiO_{1/2}$, $R_2SiO_{2/2}$, $RSiO_{3/2}$ and $SiO_{4/2}$, respectively. Mono-functional silanes, such as triethylchlorosilane, are used as a terminator for poly-condensation to control the molecular weight and chain length. Di-functional silanes, as mentioned earlier, are essential to form linear or cyclic polysiloxanes. Tri- and tetra-functional silanes have the ability to crosslink so that network structure can be obtained by adding them. With the diversity of the silanes types, polysiloxanes with different molecular weight, crosslinking degree and structure can be synthesized, containing a large variety of properties and functionalities.

Another prominent function for silanes is the surface silylation. When hydroxyl groups on the surface exposed to silanes, the condensation reaction occurs and several types of products will be formed, including monolayer or long-chain polymers (Figure 2.2.4).[51, 52] The silylation makes silanes widely used in surface modification.

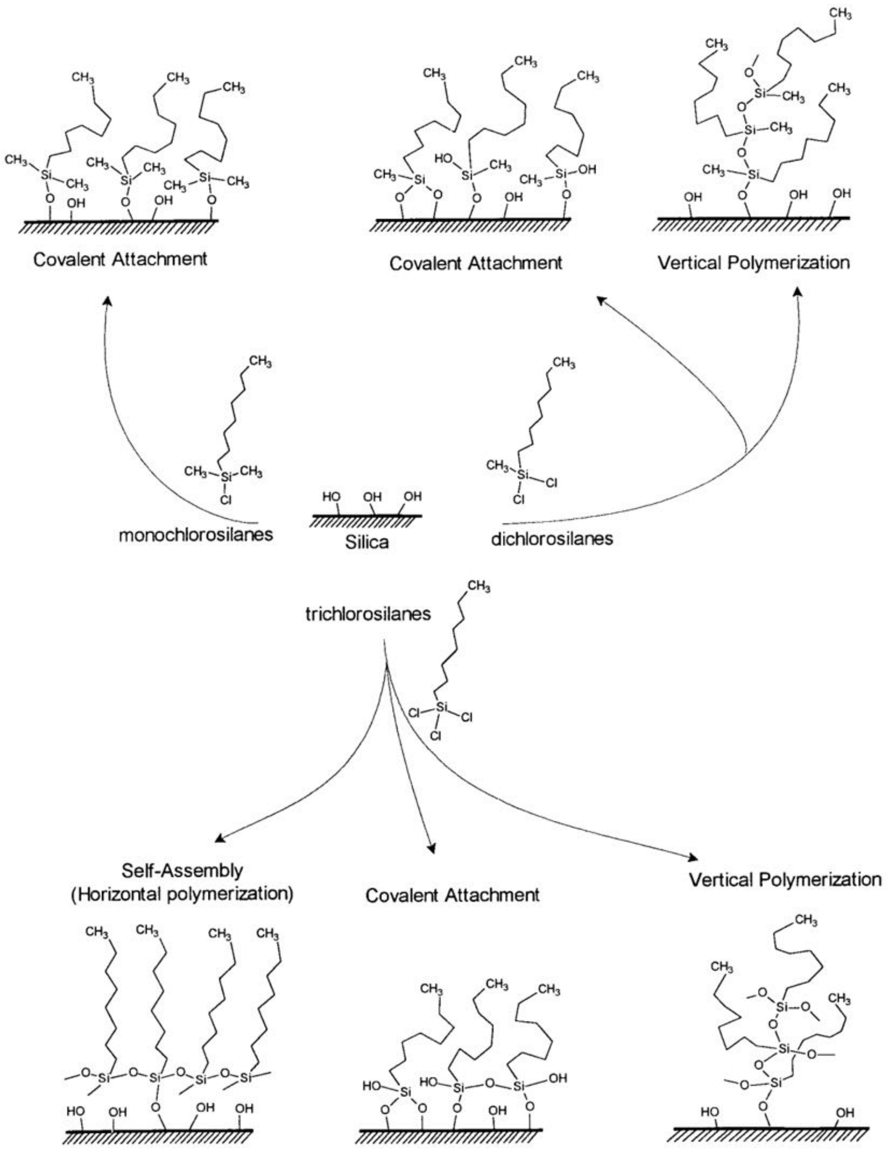

Figure 2.2.4 Surface silylation on a silica surface, adapted with permission from [51].

2.2.3 Silicone Nanostructures

Polysilsesquioxanes

Polysilsesquioxanes are an important subgroup of silanes. The prefix “sesqui” in Latin means one and a half, referring here the ratio of oxygen and silicon in each building unit in a polysiloxane structure. With an empirical unit formula $RSiO_{3/2}$, polysilsesquioxanes are synthesized via the polycondensation of tri-functional silanes. A variety of network structures, from random disordered to extended ladder- or cage-shape, are possibly to form during the condensation of tri-functional silanes as shown in Figure 2.2.5.

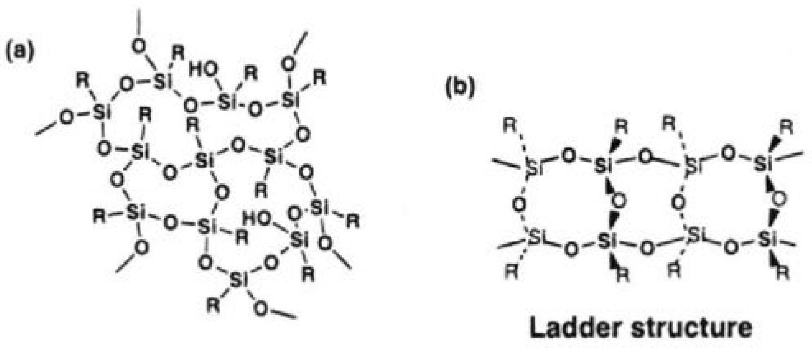

Ladder structure

Random structure

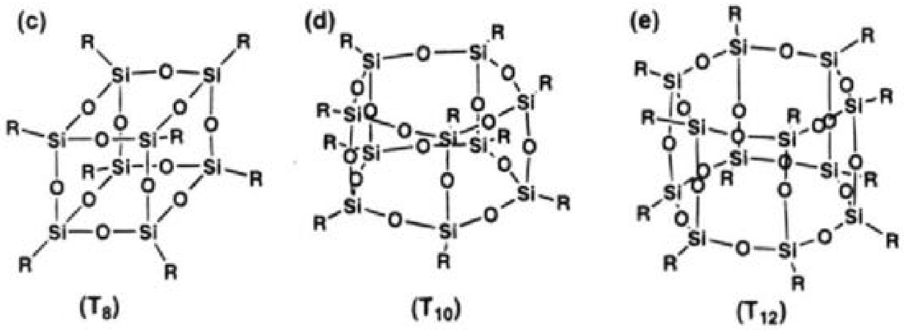

Cage structures

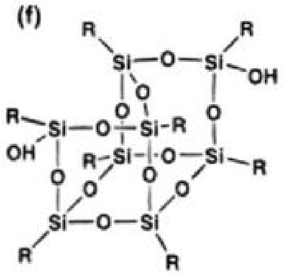

Partial cage structure

Figure 2.2.5 The various type of structures of silsesquioxanes (Adapted with permission from [32]).

The microscopic view of polysilsesquioxanes is very diverse. Most of the structures, such as rods, volcanoes, starts, fibers, chalices, helices and tubes can be obtained by altering the reaction condition, surface treatment and precursor types (see in Figure 2.2.6).[53, 54]

Notably, the development of porous or quasi-porous 3D polysilsesquioxanes has promoted a large body of researches and industrial applications in catalysis, oil-water separation, ionic exchange, self-cleaning fields.[55] Silicone nanofilaments (SNFs), as one of the polysilsesquioxanes discovered by Seeger group more than a decade ago, attracted great interest as its potential use in a wide range of fields.[56]

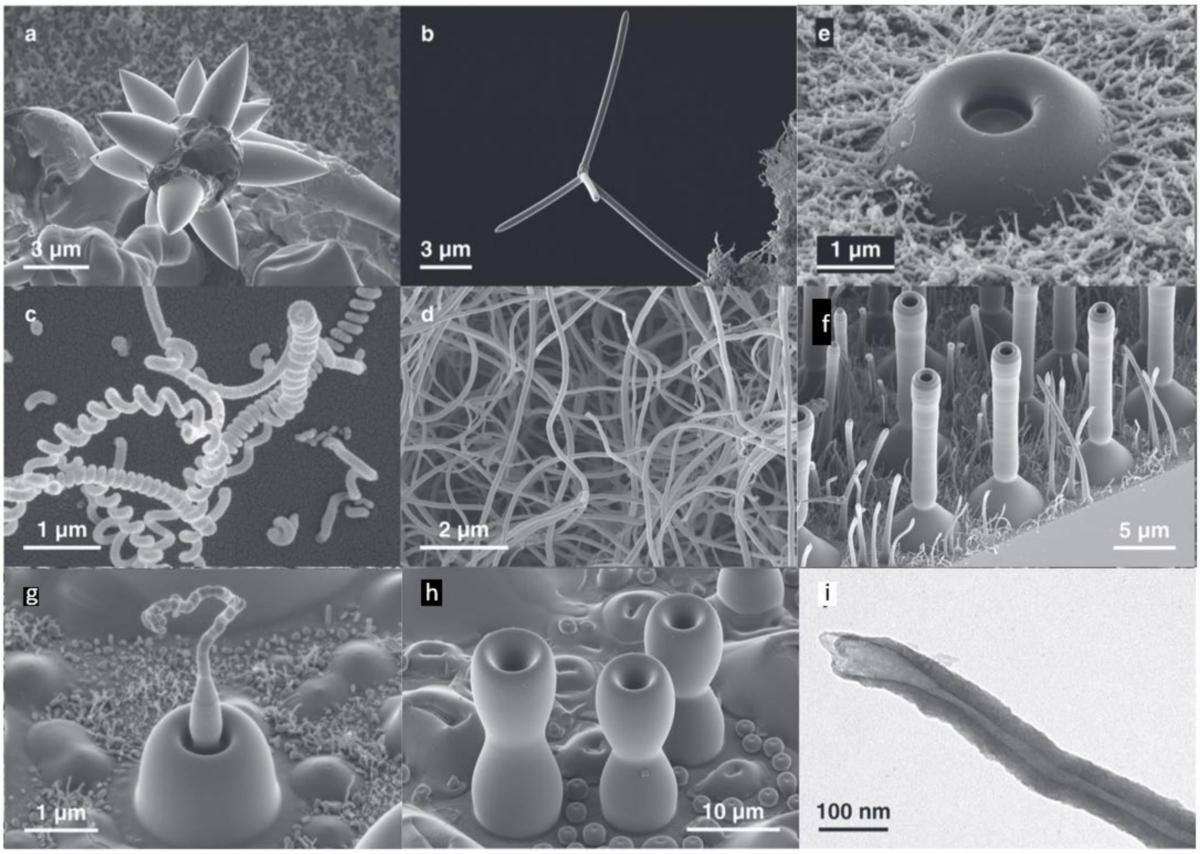

Figure 2.2.6 Structures of polysilsesquioxanes: (a,b) stars, (c) helices, (d) filaments, (e) volcano, (f) rods on volcanoes, (g) filament on volcano, (h) chalice, (i) tube. (Adapted with permission from [57].)

Synthesis of SNFs

The synthesis of SNFs is template free and can be achieved through chemical vapor deposition (CVD) or in liquid phase by using a solvent like toluene.[58] The liquid phase growth of SNFs involves organic solvent as the reaction media. Thus, the gas phase growth is much favored, due to less organic waste and less energy consumption in comparison. The non-porous, carpet-like structure was made of many 1D silicone filaments with a length of several micrometers and a diameter from 20 – 100 nm. Typical precursors that have been employed for the SNFs formation include methyltrichlorosilane (MTCS), methyltrimethoxysilane

(MTMS), ethyltrichlorosilane (ETCS), vinyltrichlorosilane (VTCS) and so on. We noticed that the hydrolysable group chloro- is more active than alkoxy-. Thus, the structure is decided by the formation condition and the precursor employed. Silanes with large organic groups cannot assemble into the 1D nanofilaments because of the steric hindrance. However, the addition of a certain amount of tetra-functional silanes as a spacer can help the nanostructure formation even if precursors with a long alkyl chain were used.[59]

SNFs have been proved to be able to grow on various substrates, from glass, silicone, wood, cotton, polyethylene, polyvinylchloride to titanium and other metals as long as the presence of water on the substrates.[60-62] Surface hydroxylation, therefore, ensures almost the growth of SNFs on any surface. A usual way for surface hydroxylation is to use Piranha solution (98% H_2SO_4/H_2O_2 = 7:3, v/v) but it is not suitable for some soft polymer substrate as its high oxidation and acidity lead to overoxidized products.[63] Other methods such as UV photo-oxidation and confined photocatalytic oxidation need the involvement of either UV-irradiation or catalysts.[64, 65] In our projects, we constantly used the low-pressure oxygen plasma treatment to generate the surface hydroxyl groups on various substrates. The approach is feasible and flexible as the power and time of the plasma generator can be tuned accord to different susceptibilities of different materials.[63, 66]

Formation mechanism

Recently, research work from our group fundamentally explained the mechanism of the formation of SNFs, which contributed to the silicone and surface chemistry. The mechanism of the template-free one-dimensional silicone nanostructure is named as droplet assisted growth and shaping (DAGS).[57] As the name says, small water droplets appear and gather on the hydrophilic surface of the substrate because of the relative humidity (gas phase) or saturation concentration (liquid phase). The water droplets serve as the reaction chamber for the hydrolysis and condensation of silanes, where there are water, silane, silanols, HCl and polysilsesquioxanes. The HCl, as a byproduct, also works as the catalyst to accelerate the poly-condensation. It dissociates in water and the released proton is the actual catalyst. Reaction inside the droplet chamber continues as long as the conditions permit the supply. The growth of the SNFs stops once the droplet displaces or consumed during the reaction. Other nanorod and -filament synthesis strategies in the field of metal and related structures, such as vapor-liquid-solid (VLS), solution-liquid-solid (SLS) and supercritical fluid-liquid-solid (SFLS) methods have similarities with DAGS.[67-69]

Superhydrophobicity

The most remarkable characteristic of SNF-coated surfaces is their non-wettability as long as the precursors used possess alkyl residue, which shows very low surface free energy. Low surface energy materials are hydrophobic and exhibit a static water CA greater than 90°. Together with the surface roughness as we introduced in the earlier chapter, the surface can have superhydrophobicity according to the Cassie-Baxter wetting theory.[70]. With the carpet formed by many tangled 1D silicone filaments, SNFs show an extreme non-wettability.[71] Other morphologies as we listed in Figure 2.2.6 all exhibited superhydrophobicity except the microvolcano type, whose CA is about 130°.[54]

Applications

Similar to other silicone materials, SNFs show good biocompatibility, environmental, chemical and thermal stability.[72] With the very intriguing superhydrophobicity, SNFs have a broad scope of applications. SNFs, for example, serve as an excellent medium for oil-water separation and selective protein enrichment due to the water-repellency and oil-affinity.[73, 74]

Besides, the high surface area generated by the SNFs network can be used for an enhanced immobilization of different functional groups, molecules, or particles.[60] Several researches have been done to demonstrate that substrates coated with SNFs layer enable a higher loading amount of catalysts originating from the nanostructured morphology compared with the pristine substrates.[62] Thus, an improved catalytic activity of the composite material can be achieved. In another work, the loaded photocatalysts can improve the resistance of surperhydrophobic surfaces against oily/biological by degrading the surface dirt or contaminants.[75] Therefore, the combination of SNFs and photocatalysts leads to a very practical application as self-cleaning materials.

Moreover, the feasibility of further surface modification makes it possible to easily switch SNFs from superhydrophobic to superhydrophilic by oxygen plasma activation as well as other functionalization with amino, carboxyl and thiol groups, which largely broaden the utility in surface chemistry.[76]

2.3 Polystyrene in Composite Materials

In this chapter, we will discuss polystyrene-based composite materials. The history of PS, its monomer and the synthetic mechanism will be introduced. General information about oil/water separation, as one of the most important applications for PS-SNFs composite, will be provided.

2.3.1 Polystyrene

General Information

Polystyrene (PS) is a well-developed, broadly used, light-weight, thermoplastic with many good properties, such as dimensional stability, chemical inertness, feasible fabrication, and low cost.[77] It has been frequently used in households, electronics, disposable cutlery, medical device, packing industry and so on.[78, 79]

The first PS was discovered in 19th century by accident. Simon from Berlin got the monomer he named as styrol (later it is called styrene) after distilled an oily substance. And it turned to be thickened as a jelly.[80] Years later, German chemist Staudinger demonstrated that heating styrol caused a chain reaction to form macromolecules, which in the end led to the current name polystyrene.[81]

From a perspective of chemistry, PS is a long chain hydrocarbon with a formula of $(C_8H_8)_n$ (Figure 2.3.1). The backbone of PS is of hydrocarbon, so the intramolecular strength is high. On the contrary, the intermolecular forces are relatively weaker, as most of them are van der Waals attractions between polymer chains. Though the cumulative attractive force among chains can be large due to thousands of atoms, the chains can slide past each other and have a high degree of conformation when PS is heated. This property enables PS to be softened and molded by high temperature.

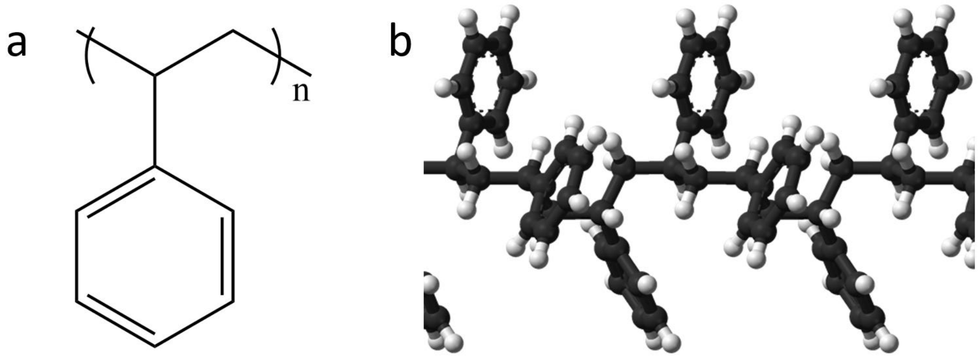

Figure 2.3.1 Polystyrene formula (a) and ball-stick model (b)

Polystyrene Composite

PS based nanocomposites have been largely studied due to their remarkable mechanical, thermal and chemical durability. Therefore, considerable progress has been made to modify and improve the properties by mixing or compositing PS with carbon black, carbon nanotubes, clay, silicon dioxide and graphite.[82-84]

PS/metal composites are of great importance in research and industry. The inorganic constituents are conventionally not expensive in polymer materials. Thus, they have been extensively used as additives to alter the thermal and mechanical properties. Zhuo has made the monodispersed PS-silver composite particles with PS as core and silver as shell. By tuning the surface roughness of the particles and thickness of the silver shell, the composite became a good building block for photonic metallo-dielectric crystals.[85] By blending $LnCl_3$ and acetoacetylethyl methacrylate, PS-derivative products of composite spheres were prepared by Abdelrahman. Spherical particles composed of different metals at various concentrations were assembled. Hydrolysed Polyvinylpyrrolidone (PVP) was added as stabilizer for the particle synthesis, with –COOH groups on the surface of particles. An alternative seeded emulsion approach was used to graft poly (methacrylic acid) chain at the exterior of the particles. The as-prepared particles ensure the superficial bioconjugation of neutravidin. Therefore, the particles are favourable contenders to obtain multiplexed bioassay (Figure 2.3.2).[86]

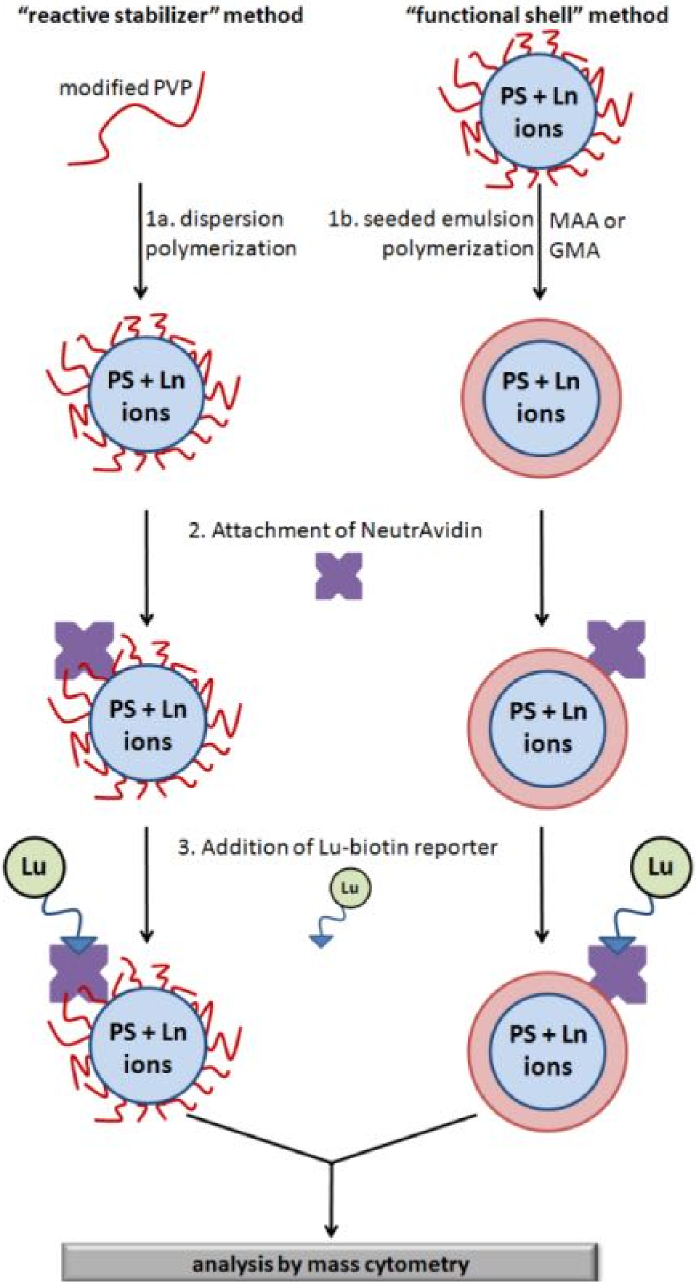

Figure 2.3.2 The bioconjugation conditions used to attach NeutrAvidin to the surface of the PS-Ln composite particles. (Adapted with permission from [86].)

PS/Carbon composites are another important category. Kumar manufactured a composite of syndiotactic PS/carbon nanofiber (CNF) by using melt processing and molding compression. Blending of liquid crystalline polymer (LCP) was also used to tune the properties. The obtained composite resulted in improved electrical and thermal properties.[87] Aly analysed the influence of incorporating various carbon nanocomponents (CNC) on the mechanical properties of PS composite. With an increase of CNC ratio, the hardness increased and the friction coefficient decreased.[88] Through a casting method, PS/carbon nanotubes (CNT) composites were prepared by Rabee and Hashim.[89] The electrical conductivity, dielectric loss, dielectric constant can all be altered by varying the ratio of components of the composite. Some others have reported PS/graphite (or graphite oxide GO) composites. By mixing the component in solution, Yang prepared the PS/GO composite, whose glass transfer temperature was increased due to the incorporation of GO. Besides, the thermal stability and storage modulus were also improved. Because of the heterogeneous nucleation induced by GO sheets, the PS/GO foam demonstrated to have smaller cell size and higher cell density compared with PS foam.[90]

On the contrary to PS/metal or PS/carbon composites, there were fewer researches about the PS/silicone composites. It was reported that SiO_2/PS nanocomposite particles of a core/shell structure have been synthesized.[91] An investigation of the effect of silicone rubber on the properties of blends of syndiotactic PS and silicone rubber has been performed by Bose *et al*.[92] Silicone matrix composites containing PS-formed particles have been used to incorporate NiMnGa particles.[93] However, no studies have examined the composite material comprising of SNFs and PS, which motivated us to launch the project published in 2019[62].

Free Radical Polymerization

PS is formed by polymerization of the monomer styrene via a chain-growth mechanism. In usual cases, a high molecular weight can be obtained quickly and the monomer concentration drops steadily in opposite to step-growth polymerization. Each time the reaction active atom attaches to one monomer and increases the chain length by one monomer at a time.

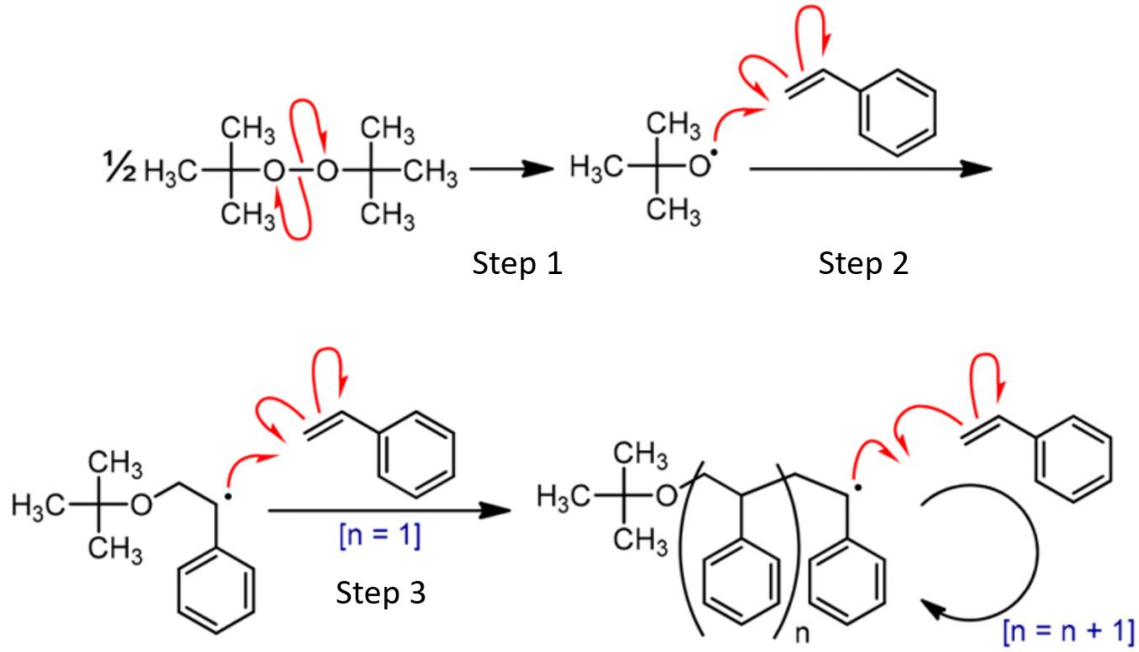

Figure 2.3.3 Polymerization Mechanism by using di-tert-butyl peroxide (DTBP) as initiator (Adapted with permission from [94]. Copyright 2019 American Chemical Society).

There are four different types to initiate the chain growth polymerization: free radical, cationic, anionic and coordination. Among them, free radical polymerization (FRP) is the most common and economical approach in PS synthesis, as the reaction mixture does not require high purity reactants and rigorous condition control[95]. The major types of initiators used in PS FRP synthesis include azo compounds (R-N=N-R’), organic peroxides (R-O-O-R’), inorganic peroxides and halogens. The homolytic cleavage occurs through thermal decomposition or photolysis.[96] AIBN is a typical azo compound, which releases two radicals and nitrogen upon heating or irradiation per molecule (Figure 2.3.3a). Similarly, organic peroxides go through a decomposition once heated, generating two radicals per initiator molecule (Figure 2.3.3b). Halogens undergo the hemolytic cracking easily by irradiation with UV light (Figure 2.3.3c). However, they are used seldom as initiators but more for halogenation of alkanes.

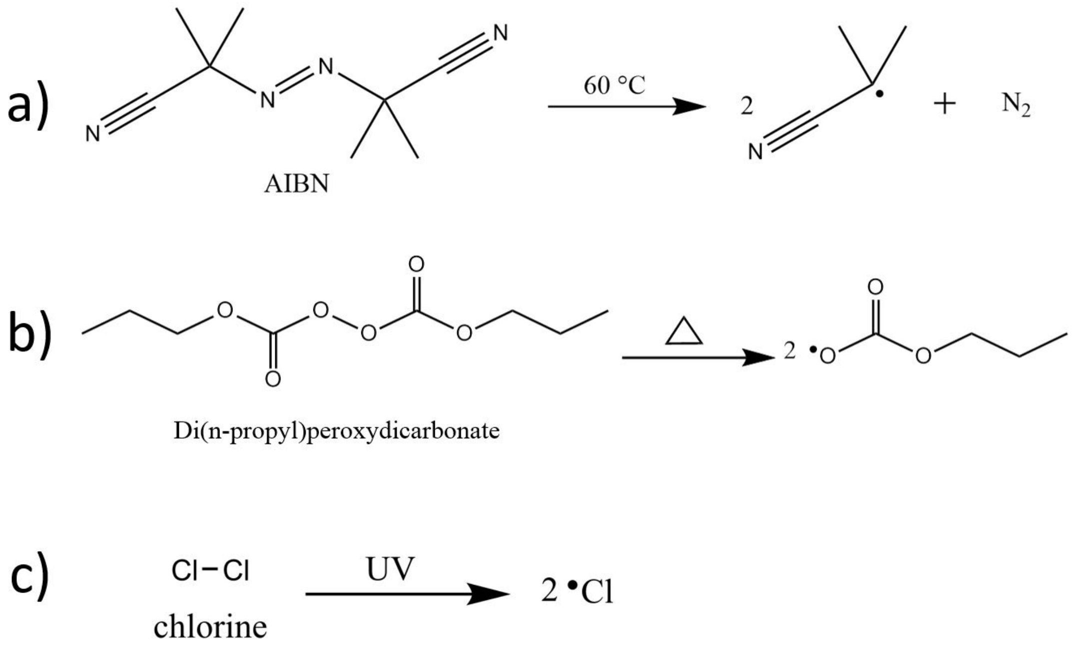

Figure 2.3.3 Types of initiators and their radical generation: (a) azo compound AIBN, (b) peroxide compound Dipropyl peroxydicarbonate, (c) chlorine.

After initiation, the polymer goes through the propagation and increase its chain length. A termination happens inevitably since the high activity of radicals.

2.3.2 Oil-Water Separation

General Background

Purification of industrial or life generated wastewater is of essential importance to keep the human society sustainable as well as a critical challenge worldwide, as the increasing growth of industrial production and pollution caused by various factors.[97] Besides the countless types of pollutants, there is also accidental oil leakage or spill in soil and water, which causes a serious threat to both ecosystem and human health.[98]

Facing such many effluents, the treatment is on urgent necessity. *In situ* burning, dispersant treatment, physical adsorption or biodegradation are the commonly used approaches.[97] Mechanical devices from industry have been developed, including oil skimmers or booms, to purify and oil/water mixture. In the emergency of ocean oil leakage, normal foams or sponges are commonly used to absorb oil and generally are burned or buried on the ground.[99, 100]

However, these methods are criticized for their associated high expense, second-time pollution, low capacity and selectivity, a degree of toxicity, high demand of energy input, and time-consuming procedures.[101]

To solve the various issues and find alternatives for the current normal treatments, scientists and companies are devoting a lot of energy to the development of novel oil-water separation materials as well as new technologies.[102] The materials and technologies should fulfill the quality of cost-effective, environmentally friendly, reusable and effective to treat a large volume of mixtures. Based on recent reports, a huge increase in publications describing oil/water separation has been noticed (in Figure 2.3.4a). The relevant materials mentioned are summarized in Figure 2.3.4b.

In the following sections, we will introduce the recent progress in developing novel oil/water separation technologies based on filtration and adsorption methods by using a variety of new materials.

Materials and Methods for Oil-Water Separation

Functional meshes and membranes with super-wettability or super-nonwettability attracted numerous researchers' interest as an approach for oil/water separation due to their simplicity, low cost and other advantages. Meshes are capable to separate a bigger volume of oil/water mixtures in a given time with a high flux than membranes. This property originates from the larger pore diameter of meshes. However, membranes with smaller pore size can separate emulsions of oil/water mixture. Meanwhile meshes are only able to filtrate out droplets which are bigger than their pore sizes.[101] Many materials have been used for the fabrication of meshes/membranes. Inorganic materials, such as copper oxides (CuO or $Cu(OH)_2$) were used for the surface functionalization on meshes, resulting in a highly hydrophilic surface and working as a water-selective mesh.[103] Silica particles are also widely used to create nanostructures on metal meshes, increasing the surface roughness.[104] Organic materials, for example, polypropylene (PP) membranes with polyethyleneimine (PEI), were converted from hydrophobic to hydrophilic for better water removal.[105] Thick layers of cross-linked polyacrylamide (PAM) hydrogels can be utilized to alter meshes surface, turning into superoleophobic underwater for separating a range of oils such as diesel and gasoline.[106]

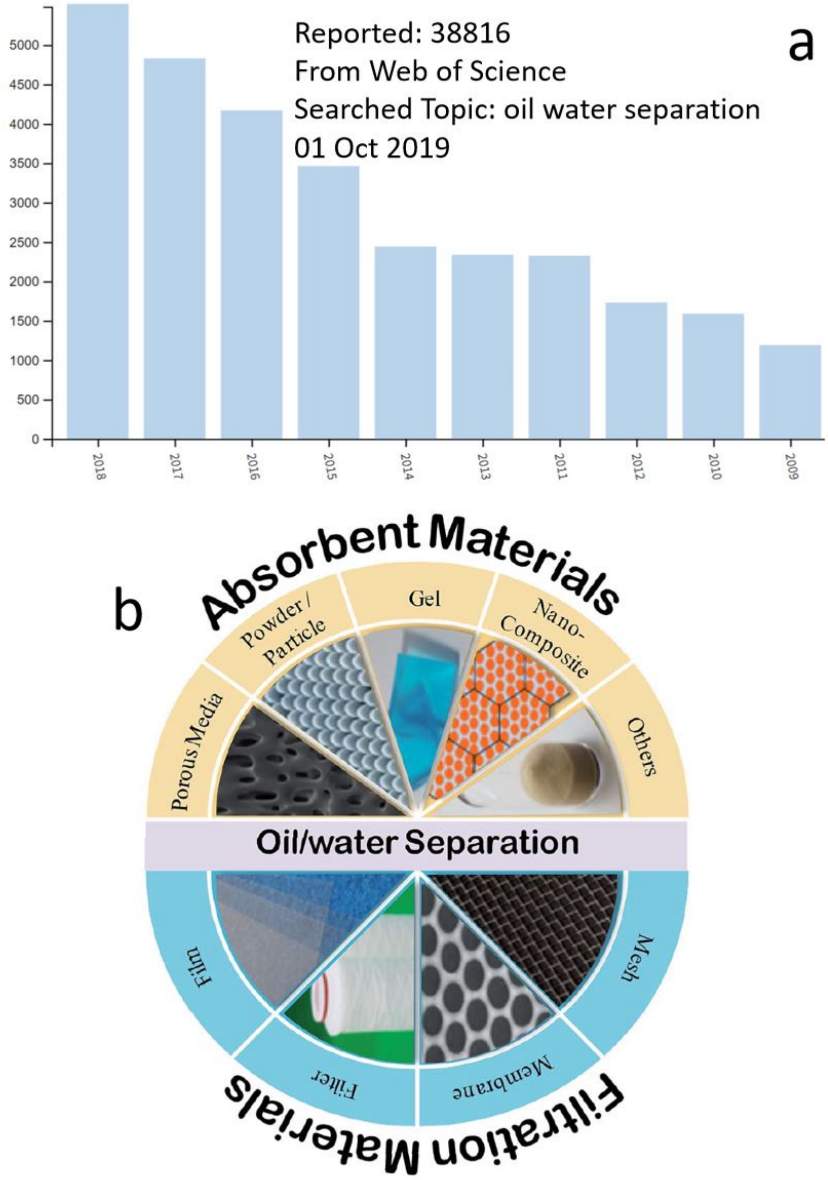

Figure 2.3.4 (a) Search result statistic from Web of Science by topic “oil water separation”. (b) Material types used in oil/water separation (Adapted with permission from [101]).

Fabrics and nanofibers are also a big category of materials for oil/water separation, as these substrates are low cost, light weighted, flexible and corrosion resistant. Zhou *et al*. incorporated polyaniline and fluorinated alkylsilane to cotton fabric, which exhibited a CA of

156° with superoleophilicity, having a separation efficiency as high as 97.8 %.[107] Controllable in situ growth of nano-crystals on textile is an alternative to turn surface. Wang *et al*. made a robust superhydrophobic fabrics via growing metal oxides and metallic nano-crystals.[108] The modified surface showed multiscale roughness with special wettability for oil/water separation.

The addition of nanoparticles (NPs) to other materials is a common and effective method to achieve additional surface roughness. Dip coating is frequently used to assemble NPs on surface. Ge *et al*. submerged PU sponge in a dispersion of SiO_2 NPs and polyfluorowax, resulting in a sponge with increased robustness against compression and a high absorbance capacity for various oils and solvents.[109] Cao *et al*. introduced dopamine polymer to PU sponges and further functionalized them with 1*H*,1*H*,2*H*,2*H*-perfluorodecanethiol to achieve superhydrophobicity. They exhibited great resistance to high temperature solvents and corrosive liquids.[110]

Natural products-based materials are of increasing importance in industrial applications since they are abundant, inexpensive, and environmentally friendly. Yong et al. provided a simple, green, low cost, and highly effective method for oil/water separation by using sands taken from Tengger Desert. The underwater superoleophobicity endows the sands with excellent water absorbance capacity.[111] Zhang's group discovered the shrimp shells repel crude oil so that they coated meshes with chitosan, a derivative from the chitin of shrimp shells. The superhydrophilicity of the functionalized mesh exhibited selective water removing ability.[112]

SNFs in oil/water separation

Some work has been done to utilize the superhydrophobicity of SNFs for oil/water separation.

Zhang *et al*. prepared a superhydrophobic and superoleophilic PE textile by adapting SNFs on the textile via a CVD approach.[113] Even the microfibers that were deeply imbedded inside textile could be coated well with SNFs. The prepared sample can only be wetted by liquids with low surface tension. He made the coated textile as a membrane for oil/water separation as well as a bag for selectively oil collection from water. The efficiency and reusability demonstrated the functionalized textile a promising material.

Chu *et al*. functionalized porous glass filter plates (diameter of 40 mm and thickness of 5 mm, pore size 10-250 µm) with SNFs. Trifunctional silane was used as the precursor. The as-prepared substrate can be used to separate water-in-oil emulsions. Notably, all the emulsified water droplets can be removed even the sizes of the droplets are smaller than the pore size of the substrate. The possible explanation is that the oil/water separation is based on coalescence separation, which intercepted the emulsified droplets by coalescence of droplets in the numerous tortuous micro-channels, instead of size-sieving filtration.[114]

These examples proved SNFs a promising material in the oil/water separation. Together with the oleophilic material PS, the composition of PS/SNFs would show an excellent oil/water separation efficiency and capability. That leads to our published work, which will be presented in the later chapter.

2.4 SNFs Nano-Composite Materials and their Applications

Nanoparticles (NPs) are defined as objects that range in size from 1 – 100 nm, which differ from the bulk material in size. They have been used for centuries due to their unique properties and structures without fully understanding the fundamental mechanism.[115] In recent decades, with the increasing interest in nanotechnology, more unique physical properties and mechanisms have been discovered along with a wide variety of novel NPs. Their applications cover the fields such as life science, energy, electronics, and environmental science to name a few.[116]

The classification of NPs can be organized into four categories: (1) inorganic-based NPs, which include metal and metal oxide NPs; (2) organic-based NPs, which contain polymers, liposomes and micelles NPs; (3) Carbon-based NPs, such as carbon black, graphene and fullerenes; (4) composite-based NPs that are multiphase NPs with more complicated structures.[117]

In this section, we will introduce two types of NPs, which are tightly related to our projects: TiO_2 NPs and AuNPs.

2.4.1 Supported TiO_2 Nanoparticles

General Background

With the fast development of human society, the standard of living significantly improved but many environmental problems come long at the same time. The pollutants from the industry are increasing tremendously, together with the appearing of chemicals synthesized every year from various fields. Among all of them, water shortage is one of the most urgent and serious issues human society is facing now. The factors cause the water problem include global warming which causes abnormal climate change, uncontrolled groundwater exploitation, a rapid increase of wastewater from industry and daily life and so on.[118] Particularly, the wastewater is the hardest challenge for human society due to the diversification of pollution sources, the non-degradability, and the severity of wide ranges of pollutants.[119]

In recent decades, different methods to purify water system and solve the contamination have been developed. Physical coagulation and precipitation is a way that precipitates the suspended solids by adding coagulants and separates the suspended solids from water.[120] However, the use of chemicals causes further environmental problems. Oxidation treatment breaks down organic compounds by strong oxidative agents as they generate OH radicals. But the sludge produced during the process or the excessive expense for secondary treatment limits the broader use of it.[121] Other novel water treatment technologies that can process the wastewater quickly, efficiently and in a large volume are needed.

Technology that utilizes the catalytic activity of semiconductive metal oxides has attracted many researchers and companies. The semiconducting materials can be used for photocatalytic purification of water. Semiconductor contains a valence band (VB) occupies with stable electrons and a conduction band (CB) which is empty but with higher energy. The electrons can transit through the band gap of the semiconductor after irradiated with photo-energy, which exceeds the band gap. Thus, an electron-hole pair is induced. The electrons and empty holes can go through propagation to the surface of the material where the oxidative and reductive reactions are promoted. In a water solution, the oxidative and reductive reactions generate radicals which can degrade organic compounds.[118]

Among the numerous semiconductive materials, titanium dioxide TiO_2 that is photocatalytic, is the most popular candidate. The reasons are: (1) TiO_2 only need the input of photo-energy without extra addition of chemicals; (2) The processing cost is low if solar energy is used as the energy source. (3) Another fact is that TiO_2 is abundant in mineral reserve.

Nanocomposites with TiO_2 NPs

There are three natural polymorphs of TiO_2: rutile, anatase and brookite. Rutile is the most thermodynamically stable bulk phase, while anatase is very common and stable as nanomaterials. Brookite is considered to have a higher photocatalytic activity than anatase.[122]

TiO_2 NPs have advantages over the conventional bulk materials. Their phase, size and morphology can be widely tuned and tailored for specific target applications. Thus, TiO_2 NPs provide the convenience and feasibility for engineering various photo-electrochemical devices.[123] Their high surface-to-volume ratio stays in the center of all advantages. As most of the photocatalytic reactions occur by the surface adsorption of chemical on the surface of TiO_2 NPs, a high surface-to-volume ratio endows a high density of reactive centers, leading to a higher efficiency of desired degradation reactions.

The synthesis methods of TiO_2 NPs can be listed as sol-gel, hydrothermal, sonochemical, and miscellaneous methods. Sol-gel is considered one of the most versatile ways to fabricate ceramic materials. Bessekhouad *et al*. reported that the titanium precursors were hydrolyzed by an acid catalytic step followed with condensation, resulting in loosely packed particles.[124]Hydrothermal approach is commonly used as well. Chae *et al*. synthesized TiO_2 NPs by reacting titanium isopropoxide (TTIP) in an acidic ethanol-water solution.[125]

As mentioned before, TiO_2 NPs are widely used in photocatalytic and photovoltaic applications. Since Fujishima *et al*. described the mechanism of photocatalysis on the surface of TiO_2 and its application in water purification, many researches have been followed and developed.[126] Harifi et al. prepared iron-doped Ag/TiO_2 nanocomposite by wet impregnation process for photocatalytic application, which achieved an enhanced photocatalytic performance by doping.[127] Wang *et al*. reported to obtain a novel metal hydroxide/TiO_2 NPs with stronger photocatalytic activity by a wet precipitation route at low temperature.[128]

Immobilization of the NPs provides a safer approach to minimize the potential environmental and health hazards, in comparison with mobile NPs. Ghanem et al. prepared a hyperbranched PET/TiO_2 NPs composite, which was proved to have extensively higher photocatalytic performance.[129] Xiao et al. achieved a polyamide/aramid fabric with deposited TiO_2 /Al_2O_3 nanolayer, resulting in a composite substrate with high UV resistance.[130] Arain et al. demonstrated the antimicrobial efficiency of cotton fabric with AgCl-TiO_2 colloid.[131]

The immobilization of NPs is accompanied by one drawback, which is the reduced amount of catalyst, the limited surface area and the less catalytic active sites. Thus, it generates the necessity of having a nanostructure support for the catalysts that can increase the surface area with catalytic activity. We applied the SNFs and SNFs composites as the catalyst support in our reported projects.[62, 132]

Photocatalyst in Self-Cleaning

Self-cleaning materials inspired by nature, such as lotus leaf,[133] the legs of the water strider,[134] and the wings of cicada, [135] have attracted much attention due to their broad range of potential applications and various advantages like labour-saving, environmental friendly, long duration in dirty condition.[136, 137] Many companies have attempted to commercialize the technology into applicable materials in multifunctional products used frequently in daily life.[138]

In the perspective of surface wettability, self-cleaning surfaces can be categorized into two main types, superhydrophilic and superhydrophobic. The cleaning mechanisms on these two types of surfaces are different in terms of the wetting behaviour of water. Superhydrophilic surfaces, where the water CA is usually less than 5°, can be wetted and cleaned by the spreading of water across the surface or a stream of water, like rainfall.[126] In contrast, on superhydrophobic surfaces, water cannot wet the surface but forms spherical droplets rolling over the surface, carrying away contamination particles.[14, 139, 140] This phenomenon is named as the “lotus effect”,[141] whose origin stems from the surface energy and the roughness of the corresponding surface.[142-144] There are more advantages in choosing superhydrophobicity over superhydrophilictiy as self-cleaning materials. Superhydrophobic surfaces can more effectively reduce the bacterial and contamination adhesion,[145] and they are also water-proof and anti-mist, which lead to a longer life span for as a product.[146]

To achieve a superhydrophobic surface with a water CA greater than 150°, low surface energy materials are indispensable, as well as a high roughness of micro- or nano-structured surface architecture. Thus, hydrophobic polymers, alkyl silanes, or semi-fluorinated silanes are candidates for the creation of superhydrophobic surfaces.[147, 148] Methods for constructing nano- or microstructure surfaces are important for realizing superhydrophobic surfaces. However, surface superhydrophobicity could be damaged by the oily contamination from organic compounds or bacterial biofilm.[149] As a result, a functionality which can maintain the surface superhydrophobicity is of pivotal importance to keep the durability of self-cleaning materials. One of the most widely adopted and effective ways to achieve that is by compositing photocatalysts.

For instance, Yamashita *et al*. developed a co-deposition technique to generate a surface consisting of TiO_2 and polytetrafluoroethylene (PTFE) and the material is both superhydrophobic and photocatalytic.[150] Wang *et al*. fabricated a UV-stable superhydrophobic coating from the dispersions of polydimethylsiloxane (PDMS) and TiO2 NPs, which can be easily applied to a wide range of substrates by spray coating.[151] Lee *et al*. mixed PDMS-coated silica NPs with N-doped TiO_2 to distribute on glass substrate, resulting in a superhydrophobic film with photocatalytic activity under UV and visible light. Numerous researches have been done to create a self-cleaning surface with superhydrophobicity and photocatalytic activity. We are motivated to provide a durable and practical composite material in our project.[132]

2.4.2 Multifunctional Gold Nanoparticles

General Background

Nanoparticles of noble metals such as gold, silver, palladium and platinum have attracted extensive attention due to their special optical,[152] electronic, [153, 154] and thermal properties;[155] the biocompatibility in medicine and diagnostics;[156, 157] and the facile synthesis.[158] Their unusual properties bring promising applications in the fields of catalysis,[159] optical and medical device,[160] drug delivery,[161] and environmental sensing.[162] Among all the noble metal nanoparticles, gold nanoparticles (AuNPs) are the most widely investigated one and have advantages over other nanoparticles.[163] There are three main reasons for the success and popularity of AuNPs: first of all, the high chemical and physical stability; secondly, the feasibility of functionalization with biological and organic molecules; thirdly, the multitude of optical properties induced by surface plasmons.[164-166] Thus, AuNPs possess a broad range of applications: due to their chemical inertness and biocompatibility, AuNPs have been used for medical purposes in cell imaging and photo-thermal therapy.[167] Owing to the special size and affinity, AuNPs were also applied in drug, gene and protein delivery.[168] The unique surface plasmon resonance effect resulting from collective oscillation enables AuNPs to detect molecules on the particle surface.[169] The nanoscale effect provides AuNPs with a catalytic activity at ambient temperature or less.[170]

AuNPs for Surface Enhanced Raman Spectroscopy

Among all the various utilities, surface-enhanced Raman scattering (SERS) detection and catalysis are the most widely used applications in both research and industry.[171, 172] SERS is considered as one of the most powerful and promising analytic techniques in detecting chemical and biological analytes due to its high selectivity, sensitivity, quick response and convenient portability.[173, 174] There are two widely accepted factors contributing to the SERS signal amplification phenomenon: (1) chemical enhancement, where the analytes are assumed to bond directly on the nanoparticles and a change in polarizability of the molecule leads to the enhancement of SERS intensity up to 10^3.[175] (2) electromagnetic enhancement, which is resulted from the amplification of the electromagnetic field of the particles and analytes by surface plasmon resonance and reaches a magnitude of 10^7-10^{10}.[176] Therefore, the electromagnetic enhancement is considered to play a more important role in SERS applications. A larger size of nanoparticles and rougher nanostructures are believed to contribute to the electromagnetic enhancement.[177]

AuNPs for Heterogeneous Catalysis

Unlike the bulky gold or even micrometric scale, once reaching the nano-metric scale, AuNPs exhibited a great catalytic activity at mild conditions.[178] Haruta group discovered in 1980s that Au composited with oxide can be used to oxidize CO at a temperature below 0 C°;[179] Hutchings et al. found that gold catalysed the hydrochlorination of ethane;[180] The selective hydrogenation for unsaturated hydrocarbon was proved by Bond.[181] Since a considerable number of researchers proved AuNPs as a very promising candidate in different types of catalysis, more investigations for a better fundamental understanding of the nanoscopic behaviour of AuNPs are needed to apply them in multiple industrial applications. Though many mechanisms for the catalytic activity of AuNPs were established, it is commonly recognized that the catalytic activity depends primarily on the particle size, which determines the surface-to-volume ratio. In the past three decades, scientists discovered that a remarkable catalytic activity can be achieved when the size falls into the regime of 3-50 nm.[182] Some literature pointed out an obvious size dependence in reactivity with size below 10 nm.[183] And the best gold-based catalysts are found in the range of 3-7 nm.[184]

Supported AuNPs

A fine control of the particle's physical properties, such particle size, size distribution and anti-aggregation will lead to improved performances in both of the abovementioned applications. Compared with homogeneous catalysis, heterogeneous catalysis, where nanoparticles deposited on a support material can obtain a highly dispersed form without the trend of aggregation. Thus, it allows for more effective and economical usage of noble metal catalysts.[185] In addition, a good support material facilitates metal recovery and provides a greater resistance to catalyst leaching, which is crucial for producing compounds with a high purity in biomedicine and pharmacy.[186] For SERS substrates, unlike the nanoparticles in suspension, the immobilization of nanoparticles on a solid support material provides a means to bring nanoparticles into closer proximity with each other in order to achieve a higher density of "hotspots" with better detective activity.[187] As a result, an ideal support material for the immobilization of the nanoparticles is essential for further enhance the catalytic and detecting abilities. Silicone nanofilaments (SNFs), which were first invented by Seeger group in the early 2000s, are considered as an ideal support material in various fields due to their specific advantages.[56] The 3D carpet formation of SNFs can be achieved via a droplet-assisted growth and shaping (DAGS) method. The obtained nano-roughness of SNFs layer ensures the superhydrophobicity with a water contact angle above 165 °. Meanwhile the enlarged surface area due to surface roughness, the feasibility of modifying the surface properties and the chemical/thermal stabilities enable SNFs to be applied in various fields, including self-cleaning, protein enrichment, photocatalysis and oil/water separation.[62, 74, 76]

The motivation to fully exploit the multifunctionality of AuNPs with an ideal support material that ensures the long durability of the functional substrate leads to our project and the prepared manuscript.

In this project, we present a simple and facile approach for the preparation of the AuNPs-SNFs composite functional material. The controlling of the AuNPs size (6.7, 9.5, 18.1 nm) was achieved by adjusting the amount of reductant trisodium citrate in the reaction, which leads to a tuneable performance in further applications. Surface modifications, including hydroxylation and thiolation, were applied on SNFs layer to enable the deposition of AuNPs on SNFs. The prepared substrate (Figure 1a) was demonstrated to have a remarkable SERS activity together with good reproducibility. Also, the hydrogenation of 4-nitrophenol experiment proved its catalytic activity and recyclability.

2.4.3 Hierarchical Structure

General Background

Superhydrophobic surfaces have attracted great interest in both research and industry due to their great potential in various applications, such as self-cleaning,[188] waterproofing,[189] anti-icing,[190] anti-corrosion,[191] anti-bacterial,[192] drug release/delivery,[193] water-oil separation,[194] and transport of fluids.[195] Motivated by these attractive diverse functionalities, numerous techniques have been developed to fabricate superhydrophobic surfaces. The methods include spray coating,[196] chemical vapor deposition,[72] lithography,[197] chemical etching,[198] electro-spinning, self-assembly, etc. The general strategy to form water repellent surfaces includes two parts: (1) using materials with low surface tension; (2) introducing the surface roughness.[142] The highest water CA a planar surface can reach is less than 120°.[20] Thus, the creation of surface roughness, which is micro-/nanostructured, is indispensable.

However, the fragility of nano-dimensional protrusions for generating the surface roughness according to the Wenzel or Cassie-Baxter models remains a challenge for creating a mechanical durable superhydrophobic surface.[70] A weak mechanical force, such as finger wipe or pressing on superhydrophobic surfaces, leads to the destruction of the micro/nanoscaled surface structures which is essential to sustain the non-wetting property, resulting in a reduction of their non-wettability and the adhesion of water/contaminants on the surface. This mechanical susceptibility, due to the fragileness of the micro-/nanostructures, severely limits the widespread usage of superhydrophobic surfaces in practical applications.

Methods to achieve

To overcome this issue, fabrication of mechanically durable surfaces featuring non-wetting property has recently been explored extensively.

A commonly used strategy is to create superhydrophobic surfaces based on substrates that are intrinsically mechanical durable, like elastomers or metals. For example, Zhong *et al*. reported the fabrication of superhydrophobic polydimethylsiloxane films using a duplication process based on a Femtosecond Laser Ablated Template.[199] Tan *et al*. prepared the micro–nanostructure on the brass surface via micro-etching technique, followed by surface modification with stearic acid to tune the surface into superhydrophobic.[200] Wang and the group fabricated a superhydrophobic steel surface by using hydrogen peroxide and acids to etch and achieved a hierarchically structured surface on the steel, followed with a surface modification treatment.[201] Although the superhydrophobic surfaces provided in these researches exhibited good mechanical durability, these strategies are limited in applications by the relatively high cost and the complexity of the production.

As an alternative, spray coating of hydrophobic particles (e.g., fluorinated nanoparticles) together with adhesives has been commonly used to prepare mechanical robust superhydrophobic surfaces because of its relatively uncomplicated process. Tiwari *et al*. provided a multi-fluorination strategy to prepare robust superhydrophobic surface by spray coating the mixture of fluorinated epoxy resin and polytetrafluoroethylene nanoparticles dispersed in acetone.[202] In the work, the authors demonstrated that the obtained superhydrophobic coating exhibited good mechanical durability and water-permeating resistance. Parkin *et al*. reported that spray coating perfluoro-silane modified TiO_2 NPs on adhesive tapes resulted in a superhydrophobic surface which exhibited good mechanical stability.[203] However, other concerns arise as the fluorinated substances and organic solvents involved in these methods are not environmentally friendly and involve safety issues. Additionally, the superhydrophobic surfaces generated by these spraying methods usually show chemical instability when exposed to organic solvents. As such, fabrication of mechanochemically robust superhydrophobic surface via a simple eco-friendly way is of pivotal importance to broaden the applications.

Hierarchical roughness, which contains two or more length scales, is another approach to increase the stability of the superhydrophobic surface structure.[204-206] The basic concept involves robust microscale structures, providing spatial protection for relative fragile nanoscale protrusions (*e.g.*, SNFs) from mechanical contacts, leading to the enhanced durability of the whole surface roughness and its non-wettability. Hybrid porous micro/nanocomposites, textile fibers, and wood substrates were all used to protect SNFs composites.[114, 207] The advantages of the hierarchical structure include the low cost, convenience to fabricate, tuneable surface roughness and enhanced mechanical durability, all of which motivated us for the two published projects.

3 Material and Methods

3.1 Chemicals and Materials

Name	Specification	Supplier
(3-Mercaptopropyl)trimethoxysilane	95 %	Sigma-Aldrich
2,2′-azobis (2-methylpropionamidine) dihydrochloride	≥ 99 %	Sigma-Aldrich
4-Nitrophenol	≥ 99 %	Sigma-Aldrich
Acetone	≥ 99.8 %	Merck
ACS grade ampicillin sodium salt		Carl-Roth AG
BL21 *Escherichia Coli* strain		Life Technologies
Calcium chloride dihydrate	≥ 99 %	Sigma-Aldrich
Chloroform	≥ 99.5 %	Sigma-Aldrich
Citric acid		Sigma-Aldrich
Deconex 11 Universal		Borer Chemie
Dimethylformamide	≥ 99.8 %	Sigma-Aldrich
Dodecane	99 %	Acros Organics
Ethanol absolute	99.98%	VWR Chemicals
Ethylbenzene	99.8 %	Acros Organics
Ethyltrichlorosilane	≥ 97 %	Merck
Glass beads, diameter 75µm	acid-washed	Sigma-Aldrich
Gold(III) chloride hydrate	99.50%	Sigma-Aldrich
Heptane	extra pure	Acros Organics
Hydrochloric acid	37%	Sigma-Aldrich
ITO coated glass 703192	8-12 Ω m^{-2}	Sigma-Aldrich
LB broth		Carl-Roth AG
Low-density polyethylene film		Sigma-Aldrich
Magnesium sulfate	≥ 98 %	Sigma-Aldrich
Manganese(II) nitrate tetrahydrate	≥ 97 %	Sigma-Aldrich
Methyl orange	95%	Sigma-Aldrich
Methylene blue	99.80%	Sigma-Aldrich
Methyltrichlorosilane	98 %	ABCR

Microscope glass slides		Menzel Gläser
Octane	98%	Sigma-Aldrich
Oil red O	≥ 75 %	Sigma-Aldrich
Paraffin	≥ 98 %	Sigma-Aldrich
pGEX-4T-1 vector		GE Healthcare
p-Xylene	99 %	Acros Organics
Rhodamine 6G	95%	Sigma-Aldrich
Silver nitrate	≥ 99 %	Sigma-Aldrich
Sodium bicarbonate	≥ 99.7 %	Sigma-Aldrich
Sodium borohydride	≥ 98 %	Sigma-Aldrich
Sodium chloride	≥ 99.5 %	Sigma-Aldrich
Sodium citrate dehydrate	≥ 99 %	Sigma-Aldrich
sodium hydroxide	≥ 97 %	Sigma-Aldrich
Sodium sulfate	≥ 99 %	Sigma-Aldrich
Styrene	≥ 99 %	Sigma-Aldrich
sulfuric acid	99.80%	Sigma-Aldrich
Tetrahydrofuran	≥ 99.5 %	Sigma-Aldrich
Titanium(IV) fluoride	99%	Sigma-Aldrich
Toluene anhydrous		Fisher Scintific
Trisodium citrate	> 99.5 %	Fluka
Vinyltrichlorosilane	97%	Sigma-Aldrich

All silane precursors were stored and handled under nitrogen atmosphere to avoid undesirable hydrolysis.

Water

Ultrapure water (18.2 MΩ cm) was prepared by a Simplicity water purification system (Millipore, USA). Double distilled water was made by an automated laboratory distillation unit GFL 2302 (Gesellschaft für Labortechnik, Germany).

3.2 The Silicone Nanofilaments Coating

In this section, three different coating methods to obtain silicone nanostructures on the surface of various substrates are described. The gas and liquid phase coating was developed and optimized by an earlier research in our group.[58] Between two of them, the gas phase was further applied to most of the experiments and applications as it consumes the least organic solvent, requires the least energy, and therefore is the most environmentally friendly method in comparison.

3.2.1 Surface cleaning, activation and annealing

Surface cleaning and activation

All these three methods share common processing steps, which are substrate cleaning, activation and annealing. Surface activation and cleaning are the pre-steps before silicone nanostructure coating. However, it plays an important role in achieving a homogeneous and smooth surface. In return, the resulted well-coated substrates will exhibit stable and homogeneous physical properties for further applications.

Standard substrates such as microscope glass slides or fluorine-doped tin oxide (FTO) were placed in a glass staining jar. 10 % (v/v) aqueous solution of Deconex 11 Universal (Borer Chemie, Switzerland) was added into the staining jar as cleaning detergent. After ultrasonication in an “Elmasonic P H60” (Elma Gmbh & Co. KG, Germany) at 50 C° for 20 min, the samples were removed out and rinsed with 70 % (v/v) ethanol for several times and followed by copious amounts of deionized water. Deconex 11 is a mildly alkaline water solution (pH = 11), in which the effective ingredient is a kind of surfactant. The cleaning steps mentioned above effectively removed the organic and inorganic contaminations on the surface as well as improved the hydrophilicity of glass slides. Samples were handled with a clean plastic tweezer and a stream of nitrogen was applied to blow the surface to dry. Good care should be taken so that no streaks or fingerprints would be left on the slides which cause an inhomogeneity of the coating. The cleaned slides were stored and carried in a plastic slide container.

For special samples like polyester foam or low-density polyethylene (LDPE) film, a specific surface activation step was indispensable, since the richness of hydroxyl groups on the surface was not as much as glass slides. After the same cleaning procedure, samples were put into an oxygen plasma generator chamber (Diener Electronics GmbH &Co. KG, Germany) for 10 min at 100 Watt. The samples were carefully taken out of the chamber and store for further use.

Annealing

When the coating procedure finished, annealing would be applied on the substrates if the hydrophobicity needed to be improved. High temperature facilitates the silanol condensation reaction which results in a higher water repellency. Annealing was then performed in an oven (Heraeus, Switzerland) under ambient air at 200 °C for 1-2 h. Afterwards, the samples were rinsed with deionized water to remove possible dust and combustion residues.

3.2.2 Gas Phase Coating

The method was invented and developed as a standard method for SNFs coating by Seeger group.[208] For different substrates, slight adjustments were needed, including the change of coating time, precursor amount and so on.

The experimental setup was illustrated in Figure 3.1. It contains three parts: desiccator, hygrometer and gas mixer. The substrates were placed inside of the desiccator (Schott volume = 6.5 L, Duran, Germany), which serves as a sealed reaction chamber. In the centralized position of the desiccator, there was a stage made by a watch glass that was placed on a 10-cm high glass stand in the reaction chamber. The desiccator was connected by a soft silicone hose to the gas mixer, which is joint by two nitrogen lines. One line supplies dry nitrogen from the laboratory nitrogen valve. The other line provides wet nitrogen which passes a gas washing bottle filled with water. There are two flow-meters (Wisag, Switzerland) for each of these two lines, by which the ratio of dry and wet nitrogen can be adjusted to control the humidity in the desiccator. The hygrometer (E+E Elektronik, Germany), which monitors the relative humidity, was mounted to a water thermostat Julabo F34 (Julabo, Germany) where the two lines of nitrogen were directed together and the temperature in the chamber was controlled. A water circulation system was connected to the thermostat to ensure a stable temperature controlling.

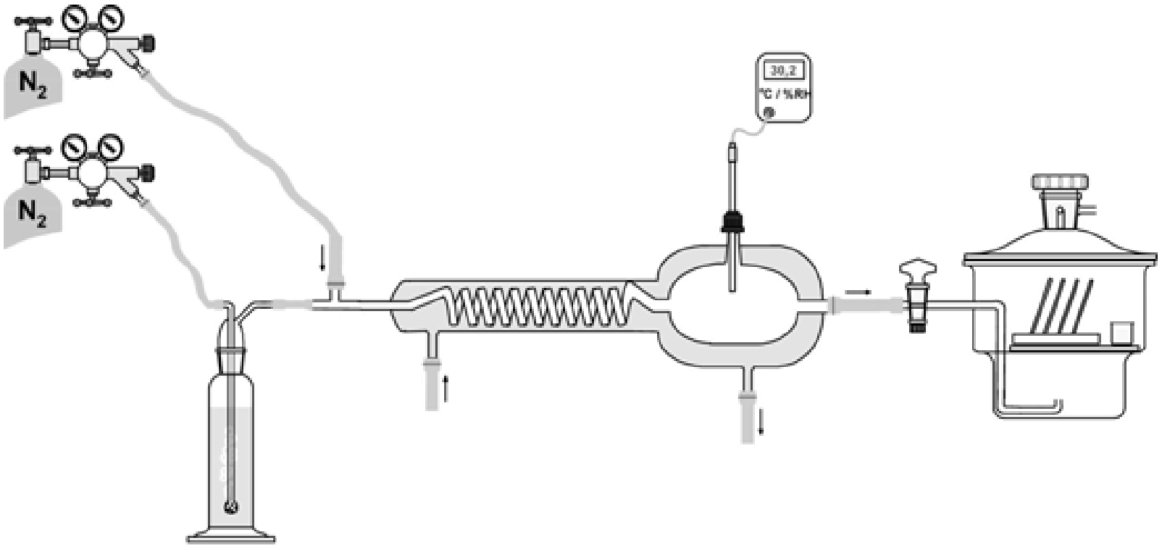

Figure 3.1 The experiment setup for gas phase coating of SNFs. (Adapted from [209] with permission)

Glass slides were placed inside of the desiccator upright on a customized Teflon holder. Other samples, like LDPE films, were put upright and around the central stage in a symmetric way to ensure the accessibility of precursors to both sides.

In a typical gas phase coating procedure, the following protocol was pursued:

1. Mount the prepared clean and activated sample in the desiccator and seal it.
2. Set the needed relative humidity by adjusting the ratio of the two flowmeters for dry and wet nitrogen. Wait until the number read from the hygrometer is stable for at least 10 min. The relative humidity is up to the desired structure and thickness. For a homogeneous SNFs coating, 40 % could be ideal.
3. Flush the desiccator for at least 1 h.
4. Switch off the inlet and outlet of the desiccator at the same time and wait for 10 min to make sure no turbulence inside of the chamber.

5. Inject the silane precursor via the septum on the top of the outlet controller and target on the central stage. The amount of silane differs from 0.2 µL to 1 mL according to the amount of substrates.
6. The reaction time depends on the desired structure and thickness of the SNFs layer. Usually, 4 h at 23 °C is sufficient enough to achieve a homogenous coating layer.
7. Before opening the desiccator, rinse it with dry nitrogen for 10 min for removing all gaseous residues.
8. Take out the samples and rinse with deionized water. If necessary, apply annealing for the samples.

3.2.3 Liquid Phase Coating

The reaction vessel was custom-built by the workshop of the department of Chemistry, University of Zurich. The cylindrical reaction vessel is made of Teflon which is of high chemical stability. The vessel contains a lid, which can seal it completely without leakage. In the middle of the lid, there places a septum, through which the needle inlet and outlet can be mounted to control and monitor the relative humidity of the reaction environment. Also, the reaction was initiated by the injection of precursor through the septum.

Prepared glass slides were mounted on a customized Teflon holder made by the same workshop. The holder was put inside of the vessel, after a magnetic stirrer was placed on the bottom of it. Normally, 100 mL of dry toluene was filled in the vessel. The reaction vessel was then sealed tightly. The vessel was under stirring at 500 rpm for 10 min to reach an equilibrium of water content. The water content was then measured by a coulometric Karl-Fischer Titrator DL32/C20 (Mettler Toledo, Switzerland). Sample of 0.5 mL was taken out to measure the water content each time. The adjustment of the water content is the same as the adjustment of relative humidity in the gas phase coating. Once reaching the desired water content (normally 150 ppm ± 5), the solvent was again equilibrated for another 10 min to confirm the stability of the water content. Subsequently, the precursor was injected into the vessel. Commonly 100 µL of methyltrichlorosilane was needed for two glass slides. The reaction was continuing for 4h usually to achieve an applicable layer of coating. After the reaction, the samples were taken out and rinsed in the order of toluene, ethanol and deionized water for several times.

3.2.4 Surface Activation of Silicone Nanofilaments

SNFs layer on substrates will make the surface superhydrophobic and chemically inert. In some applications, we need the surface re-activation to make it possible for further surface modification on SNFs. For example, if there is a step of deposition of metal particles on SNFs in aqueous solution, the hydrophobic surface will lead to the form of precipitation in the solution instead of on SNFs. Thus, in order to make the SNFs coated surface hydrophilic, the coated samples should be put in the oxygen plasma generator chamber (Diener Electronics GmbH &Co. KG, Germany) again for 10 min at 100 Watt. The oxygen plasma treatment created hydroxyl groups on the surface again, which enable SNFs for further applications or directly as the nucleation points for deposition precipitation.

3.3 Functionalization on Silicone Nanofilaments

The prerequisite of the functionalization of SNFs is based on the surface activation. As SNFs coating is chemically inert, thermally stable and superhydrophobic, in most of the cases, hydroxylation on the SNFs layer is indispensable. The detailed steps were provided in 3.2.4. The generated hydroxyl groups work as reaction sites for further functionalization.

3.3.1 Surface Initiated Polymerization of Polystyrene

Growth of SNFs by using vinyltrichlorosilane as precursor

In this section, however, the pre-surface- treatment of hydroxylation is not necessary. Instead, the surface modification was achieved through a grafting of polymerization of styrene by radical polymerization. The precursor used to form the SNFs coating is vinyltrichlorosilane so that the SNFs have C=C bonds all along the filaments for later polymerization. Either liquid or gas phase coating can be chosen to the growth of SNFs made of vinyltrichlorosilane.

Surface grafting of polystyrene onto SNFs by radical polymerization

The surface grafting of polystyrene (PS) on SNFs was developed by our research in 2019.[62] SNFs coated glass slides were immersed into 100 mL water/ethanol solution with a ratio of 3:7 (v/v) for reaction. Before the reaction started, the solution was deoxygenated by bubbling with nitrogen gas at room temperature with a flow rate of 1.5 L/min for 1 hour. A certain amount of 2,2′-azobis (2-methylpropionamidine) dihydrochloride (AIBA) was added once the temperature reached 75 °C and staying for 10 min. Then 1.0 mL (10.6 mmol) styrene was added into the solution. After 2-hour polymerization under nitrogen atmosphere, PS was successfully grafted on SNFs. The substrate was named as PS@SNFs. The PS was synthesized and covalently bonded on SNFs. The PS@SNFs slides were rinsed with different solvents for morphology control. If necessary, slide was annealed at 100 °C for another 2 hours to evaporate monomer and solvent.

The morphology control of PS@SNFs

The morphology control of PS@SNFs was targeted on two types: the grafted PS nanostructure shaping and the grafted PS bead size controlling. The former one was achieved by using different solvents for the post treatment of the glass slides immediately after being taken out of the polymerization solution. Three combinations of solvents were used for post-treatment: in order to form bead-shaped PS, ethanol/water was used; for leaf-shaped PS, acetone/ethanol was used; for well-wrapped PS, acetone was solely used. Nitrogen stream for drying was always used after rinsing irrespective of solvent combination. The controlling of PS bead size was obtained by changing the amount of AIBA used in reaction. Three different amounts of initiator AIBA were used in each experiment to ensure three different sizes of the PS beads.

3.3.2 Surface in situ growth of TiO_2 Nanoparticles

The method of growth of TiO_2 Nanoparticles (NP) was adapted from the previously reported protocols.[210, 211] It was later optimized in our work.[62] The substrates on which the TiO_2 NP grew were treated with oxygen plasma for 5 min at 100 W in a low pressure plasma generator (Femto, Diener Electronic, Germany). The substrates were then cut into pieces of 50 mm × 26 mm. After rinsing with deionized water and drying with nitrogen stream, one piece of the substrates was submerged in 100 mL mixture of ethanol/deionized water (v/v at 4:1). 50 mg (0.4 mmol) of TiF4 was added after reaching 60 °C. Reaction continued for one hour. Sample was taken out and rinsed with deionized water to remove solvent and the left hydrochloric acid, further dried at 80 °C for 2 hours. TiO_2 deposited substrate was then made.

Calcination was carried out if necessary. Substrates were put in oven for a few hours and heated up to 200 °C.

3.3.3 Surface deposition of Gold Nanoparticles

Surface sulfurization on SNFs

In order to deposit gold nanoparticles (AuNPs) on substrates, the SNFs first need to be functionalized with (3-Mercaptopropyl)trimethoxysilane (MPTMS). The slides coated with SNFs, were hydroxylated by oxygen plasma treatment with a 100 W power for 10 min in a low pressure plasma generator (Femto, Diener Electronic, Germany). The activated slides were then immersed into a teflon vial filled with 100 mL toluene which contained 150 ppm water. 1 mL MPTMS (5.3 mmol) was injected into the vial. The reaction went for 24 hours at room temperature at a stirring rate of 500 rpm. Afterwards slides were rinsed with ethanol and ultrapure water and dried with nitrogen stream.

Synthesis of AuNPs

A modified Turkevich method[212, 213] was applied to synthesize Gold nanoparticles (AuNPs). Before reaction, 1 wt % $HAuCl_4$, 1 wt % trisodium citrate, and 0.1 wt % $AgNO_3$ were prepared in aqueous solution and the three solutions were stored at 4 °C. One solution was prepared by mixing 170 µL $AgNO_3$ and 2 mL $HAuCl_4$, followed by adding different amounts of trisodium citrate aqueous solution (0.5 mL, 2 mL or 8 mL) to correspondingly synthesize AuNPs with average sizes of 18.1 nm, 9.5 nm and 6.7 nm. The mixed solution was further diluted to a total volume of 10 mL with ultrapure water. After 140 mL ultrapure water was heated to boiling, the prepared mixed solution was then injected into the container. The colour of the system turned from light gold to earthy red in a few minutes. Different sizes of AuNPs were synthesized after one-hour reaction, according to the volume of trisodium citrate aqueous solution. It is important to note that all glassware and stirrers must be washed by aqua regia and rinsed with ultrapure water for copious times.

Assembly of functional substrates

The prepared slides were immersed in 50 mL as-prepared solutions with various sizes of AuNPs. After 6 hour at 80 °C, the AuNPs were well deposited on SNFs. Subsequently, the slides were taken out and rinsed with deionized water thoroughly several times and dried with nitrogen stream to obtain the final functional substrates.

3.4 Hierarchical Structure Formation

3.4.1 Drop-Cast Glass Beads on LDPE film

Hierarchical structure was used to improve the mechanical durability of the functional substrates. The formation of the hierarchical structure contains the following steps:

Drop casting glass bead on LDPE substrate

A certain amount of 75 µm-diameter GBs was put into 100 mL pure ethanol and under high agitation to form a dispersion. The dispersion was treated with 20-min ultrasonication at 40°C and was kept under magnetic stirring at a speed of 1000 rpm to prevent precipitation. Three milliliters of the dispersion was taken out and cast dropwise on a cleaned low-density polyethylene (LDPE) film within an area of 50 cm^2. After evaporating the ethanol, the substrate was moved in an oven at 165°C for 10 min and taken out to cool down at room temperature. The GBs were partially embedded into the LDPE matrix, and microscale architecture of the GB@LDPE was therefore formed.

SNFs coating and functionalization

The SNFs layer was created normally through a gas phase coating on the GB@LDPE by using the same procedure described in 3.2.2. Further functionalization, such as TiO_2 NPs deposition, was similar to what has been described in the previous section.

Hydrophobic modification

Surface modification is aimed at changing the surface properties of the functionalized substrates. The hydrophobic modification was conduct according to the same abovementioned method for SNFs coating in gas phase. while a part of the reaction condition was changed with a lower relative humidity of 35%. Only 100-µL ethyltrichlorosilane (ETCS) was injected and the reaction time lasted for 20 min.

3.4.2 Thermal Annealed Polyethylene Film

In order to prepare the micro/nanostructured hierarchical surface, the polyethylene (PE) film was first activated by O_2 plasma in a plasma chamber (Diener Electronics, Nagold Germany) at 100-watt power for 10 min under the O_2 flow rate of 25 mL/min. Subsequently, the activated film was coated with SNFs in a gas phase by using the previously introduced method. The obtained SNFs coated film (SNF-PE) was then thermally annealed at 180 °C for 10 min to create the hierarchical surface topography.

3.5 Applications of Different Functional Composite Materials

3.5.1 Test of Catalytic Activity

Photocatalytic Degradation of Methylene Blue by TiO_2 NPs Substrates

Methylene blue (MB) degradation was chosen for photocatalytic measurement. Substrates composited TiO_2 NPs were immersed into a quartz beaker which was thermostated at 25°C by a water circulation system. 50 mL MB solution (0.67 ppm MB in methanol: water at 1:1 or in pure water solution) was filled in the quartz beaker. An oxygen flow (30 mL/min) was bubbled into the solution to maintain the oxygen concentration during the whole photocatalytic reaction. A photocatalytic reactor RPR-200 model (SNE Ultraviolet Co, USA) was mounted with eight light bulbs (SNE Ultraviolet Co, USA) around the beaker with emission wavelength at 350 nm. Samples (0.3 mL) were taken at defined time intervals, and absorbance was measured immediately by a Perkin-Elmer Lambda 650S UV/vis spectrometer.

Hydrogenation of 4-Nitrophenol by AuNPs Substrates

The catalytic reaction was conducted by hydrogenation of 4-nitrophenol to 4-aminophenol. The procedure was adapted from an early literature.[214] All experiments were performed at 25 C°. A quartz cuvette was used for the reaction. Drops of sodium hydroxide was added into 15 mL of 4-nitrophenol solution (1.2 mM) for basification (to pH = 10). Large excess amount of sodium borohydride was added to the reaction system (208:1 in mole). The excess use of $NaBH_4$ assumed that the reaction rate was determined only by the concentration of 4-nitrophenol. A piece of 1 cm × 5 cm of AuNPs-SNFs functional substrate was immersed into the solution to initiate the hydrogenation reaction. UV-vis spectrometer (Perkin-Elmer Lambda 650S) was used to monitor the hydrogenation rate with an acquired interval of 30s over a wavelength range of 200-600 nm.

3.5.2 Test of Oil Absorption

A polyester sponge of 2 cm × 2cm × 0.5 cm was treated with oxygen plasma for 10 min at 100 W in the plasma generator and coated with PS@SNFs by using the abovementioned methods. Oxygen plasma treatment was conducted one more time to activate the coated surface with hydroxyl groups, a second thin layer of SNF was coated as the previously mentioned SNFs coating step to obtain the superhydrophobic and oleophilic properties for water/oil separation. In order to measure the maximum oil absorption capacity, the prepared sponge was dipped into paraffin oil, chloroform and octane correspondingly for 2 seconds, removed out subsequently for another 2 seconds and weighed immediately before the evaporation of the solvents. The oil absorption capacity (α) was calculated at room temperature:

$$\alpha = (M_1 - M_0)/M_0 * 100$$

where M_1 is the weight of the sponge saturated with oil after dipping, M_0 is the weight of the original dry sponge.

3.5.3 Test of Anti-Bacterial Ability

To confirm the anti-bacterial effect of the materials, we used the BL21 *E. coli* strain transformed with the pGEX-4T-1 vector (GE Healthcare), which carries the ampicillin resistance gene. LB (Luria-Bertani) liquid medium supplemented with 100 µg/mL of ampicillin was inoculated with a glycerol stock of bacterial cells, which were cultivated overnight in an orbital shaker at 37°C with 230 rpm. By then, the Cell density reached 1.58×10^9 cells/mL based on the optical density at 600 nm (OD_{600}). The cell density needed to be adjusted with same fresh LB to 1.36×10^8 cells/mL ($OD_{600} = 0.17$). The substrates were immersed into 10 mL *E. coli* solution and incubated under darkness or 350 nm UV irradiation for 90 min (intensity was 6.32 mW/cm^{-2}) at room temperature. Next, bacterial growth was followed by measuring the optical density at 600 nm (OD_{600}) over the next 210 min at 37°C, which facilitated to achieve a fast propagation. For the counting of colony forming units (CFUs), the original suspension with bacteria was diluted by 1000 times, out of which 5 µL was taken and cast on agar plates for overnight growth (12 h) at 37°C.

3.5.4 Test of Mechanical Durability

Abrasion test

Quantitative measurement was operated by an abrasion tester AB5000 (TQC, Germany) on the desired substrate. ASTM standard D4213 for testing abrasion or scrub resistance of coatings and paints was adapted to assess the abrasion resistance of the as-prepared substrates. A sponge abrasion head was cover with a nitrile glove, with a load of 200 g on the substrate. The sponge abrasion head moved back and forth on the tested substrate for certain times. During each time of the movement, the effective rubbing distance was 6.5 cm. After the abrasion test, the properties of the tested substrate, such as contact angle and catalytic activity, were determined in other experiments. The water contact angle and sliding angle change normally were plotted as a function of the abrasion cycle.

For measuring the loading amount of metal nanoparticles (AuNPs or TiO_2 NPs), substrate was put into a highly concentrated sulfuric acid solution (30% in volume) and heated to 110°C for 30 min to dissolve the metal NPs. The solution was then diluted into 10 times for measurement. The standard calibration of concentration vs. absorbance curve was conducted by using a standard solution and measure in a UV-Vis Cary 60 spectrophotometer (Agilent, USA). The amount loss of metal NPs scratched off during the abrasion test was measured by the spectrophotometer at the characteristic wavelength of the metal by absorbance.

Mechanical performance Tests

The flexural measurements were operated with an Instron 3345 universal testing device (Instron USA). A three-point bending setup was adopted. The support span was set to be 30 mm. The typical sample dimensions were 60 mm × 10 mm × 1.3 mm. The applied testing rate was 1 mm/min. For average values of the maximum stress and strain, at least three specimens were measured.

Tape-peeling test

An adhesive tape (3M, Scotch® Magic™ Tape 810) with adhesion force of 250 N/m to steel (ASTM D-3330) was used for the tape-peeling test. The tape was placed and pressed with a load of 900 g on the prepared film to achieve a uniform contact between the tape and the film. Then the tape was slowly peeling away from the surface. The contact angles and sliding angles of the tested substrates were collected as a function of tape-peeling cycles.

3.5.5 Test of Surface Enhanced Raman Spectroscopy ability

The measurement of Surface-Enhance Raman Scattering (SERS) was conducted in a customized measuring cell. The cell was cleaned with a three-step procedure under ultrasonication. Each washing lasted about 15 min in the following solutions: Deconex Cip7 (1% in water), ethanol and deionized water. The measuring cell was then coated with a Plastik 70 spray (Kontaktchemie, CRC Industries) and dried for 1 hour to homogenize surface and prevent corrosion. The functionalized substrate was glued on the measuring cells with Loctite 3311 (Henkel Corporation).

Afterwards, 8 µL of rhodamine 6G (R6G) aqueous solution with different concentrations (from 10^{-10} to 10^{-4} M) was dropped into the measuring cells which have a contact area of 0.8 cm^2 on the functional substrates, dried in darkness for further SERS measurements.

All the Raman spectroscopic measurements were accomplished by using a special custom-built microscopy setup developed in our group. The excitation beam was generated by a power-tuneable diode laser at 633 nm (Toptica, Germany). The power of the excitation beam was set between 10 and 70 mW to maximize the amount of scattered photons. Scattered light was injected through fiber couplers into a 200 µm core multimode fiber used for Raman measurements. The fiber output was connected to a spectrometer equipped with a low-noise CCD camera cooled to -70°C. LabSpec (Horiba, Irvine, CA, USA) software was used for the data processing. The general configuration for the Raman detector was an opening slit of 50 µm, a grating of 300 grooves/mm and accumulation of five-time scans. The acquisition time was between 1 and 10 sec. To confirm the reproducibility of the SERS substrates, 5 sites on the measuring cell were randomly selected to collect spectra. All measurements were performed at room temperature. Raman mapping was conducted by inVia Qontor (Renishaw, UK) confocal Raman microscope.

3.6 Analytical Methods

Contact and Sliding Angle Measurements

Water contact angle and sliding angle measurements were performed on the respective surfaces with a Drop Shape Analyzer (DSA100) (Kruss, Germany). Usually, a 10 µL droplet of ultrapure water was used. The software OCA (Dataphysics, Germany) was used for digital drop shape analysis according to Laplace Young fitting. At least five different positions were measured on each substrate surface. Each measurement was conducted within 1 min in order to prevent the shrinking of the droplet volume due to evaporation.

Scanning Electron Microscopy

Scanning electron microscopy (SEM) sample was cut into the desired size and glued on an aluminum stub with conductive carbon tape (Plano GmbH, Germany). A low-pressure sputter coating unit CCU-010 HV (Safematic GmbH, Switzerland) was set in vacuum and 10 nm platinum was sputtered on the samples to decrease the charging.

SEM analysis was done on a Zeiss Supra 50 VP (Zeiss, Germany) at 10 kV acceleration voltage and 3- 6 mm working distance, using the mixed detector of inlens and SE2 (1:1).

Transmission Electron Microscopy

Transmission electron microscopy (TEM) and energy dispersive X-ray (EDX) analysis were performed on a Tecnai G2 Spirit (FEI, Netherland) at 120 Kv with an Oxyford EDX system. Samples for TEM were scratched off from substrates into an absolute ethanol solution, and ultrasonicated for 20 min at 40 °C. The solution was then dropped onto the formvar/carbon film coating with copper grid (200 mesh, Plano GmbH, Germany) and dried under infrared light for at least 2 hours before use.

Thermogravimetric Analysis

Thermogravimetric analysis (TGA) was conducted using a Jupiter STA 449 F3 TGA (Netzsch, Germany). For each measurement, 10-15 mg samples were needed. The atmosphere was a combination of a gas flow of 50 mL argon and 10 mL nitrogen. Heating was controlled at a rate of 10 °C min^{-1} from 25°C to the desired temperature.

UV-Vis Spectrophotometer

The metal NPs were dissolved in concentrated acid. Samples were taken out and diluted from 10 – 100 times upon the original concentration. Trace element analysis was realized by the concentration measurement in a UV-Vis Cary 60 Spectrophotometer (Agilent, USA) at the desired wavelength. Calibration of a standard linear concentration to absorbance curve was predetermined by using a standard solution.

X-ray diffraction

For the X-ray diffraction (XRD) analysis of the AuNPs, the AuNPs solution was dropped on a glass slide until dry. The measurement was carried out on a STADI P diffractometer (STOE, Germany) in transmission mode (flat sample holders, Ge monochromator and Mo K_α radiation) equipped with a position sensitive detector.

Dynamic light scattering

Dynamic light scattering (DLS) was conducted on DynaPro Titan (Wyatt Technology, USA). The synthesized AuNPs solution was centrifuged for 10 min and 20 µL of the supernatant fluid was taken out for each DLS analysis, using 10 acquisitions with 5-10 s acquisition time each, and a laser power between 20 and 100 %. The average hydrodynamic radius of each sample was achieved by curve fitting with the provided Dynamics software.

4 Results and Discussion

4.1 Morphology-Tuneable PS-SNFs Composite Material

Parts of this chapter have been already published in ChemNanoMat.[62] In the following sections, a novel nanocomposite material made from the combination of silicone nanofilaments and surface grafted polystyrene was exhibited. The novel structure was characterized by SEM and TEM. We made the breakthrough that the surface grafted polystyrene morphology can be feasibly tuned and controlled according to the post-treatment after polymerization. The newly invented nanocomposite has an extended surface area, which further enhanced the surface loading ability for catalysts and the oil absorption ability.

4.1.1 The morphology control of PS@SNFs

Herein, vinyltrichlorosilane was used as precursor to form the SNFs in a gas phase coating. Different from the other SNFs made of traditional precursors used in the earlier researches in our group, SNFs made of vinyltrichlorosilane, with the C=C bonds on the side, can work as the grafting sites in a radical polymerization with initiators. (in Figure 4.1.1).

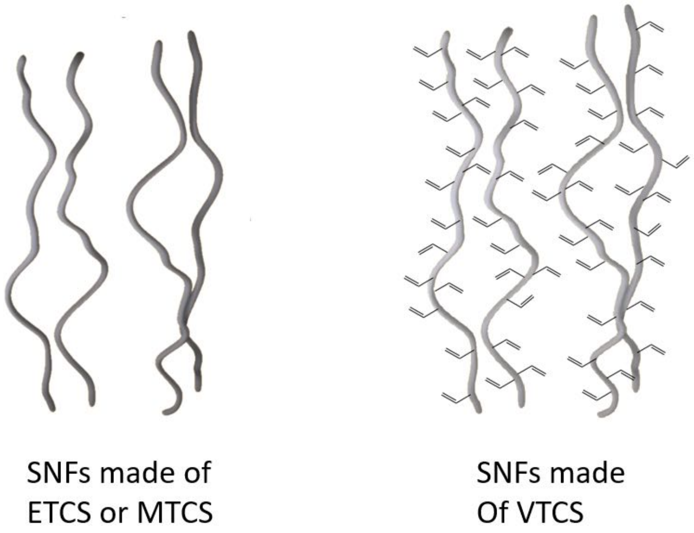

Figure 4.1.1 The schematic comparison of SNFs made of ETCS/MTCS and the SNFs made of VTCS.

The CC double bond from the vinyl groups remained unreacted during the formation of the SNFs. Thus, the C=C bonds had the potential to react with initiators which trigger the radical polymerization. The rate of the polymerization depends mainly on two factors: 1) the use of catalysts, and 2) the reaction temperature.[215] Other parameters such as solvent or stirring rate make difference, however, were not as important as the main factors. Structurally, polystyrene (PS) is a long hydrocarbon chain, with a phenyl group attached to every other carbon atom in the chain. As PS is a vinyl polymer, it is produced by free radical vinyl polymerization from the styrene monomer:

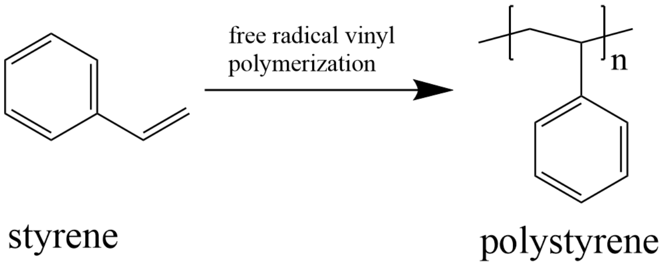

For a radical polymerization, radical initiators are indispensable, such as peroxide or some azo compounds. Some type of the initiators are listed below:[216]

(a) Thermal decomposition: the initiator is heated until the bond is cleaved homolytically, which resulted in two radicals.
(b) Photolysis: the initiator is cleaved with a bond homolytically under radiation and produces two radicals.
(c) Redox reaction: normally hydrogen peroxide or alkyl hydrogen peroxide are reduced by reductants and one radical is generated.

Among all of them, the thermal decomposed initiator was chosen for our experiments, as the surface polymerization on SNFs was preferred in a solution.

The reaction solvent was chosen to be the combination of water and ethanol as both of them were more environmentally friendly compared with organic solvent like toluene or chloroform. Besides, PS is poorly soluble in the water and well soluble in ethanol.[217] The combination use of both liquids allows the polymerization degree to a certain extent in the reaction system. Most of the initiators, from azo nitrile, azo ester to azo amide, are oil-soluble. A candidate initiator, which can be applied in water/ethanol solution, is essential to ensure the successful polymerization in the polar solution. Water-soluble initiator 2,2'-Azobis(2-methylpropionamidine) dihydrochloride (AIBA) was chosen as it exhibited good solubility in both water and ethanol.

Prior to polymerization, the successful synthesis of SNFs was obtained applying the DAGS mechanism developed by previous studies from our group.[56-58, 218] Gas phase coating was applied here for the growth of SNFs on glass slides. In Figure 4.1.1, the SEM images show a fibrous network of highly entangled filaments. Due to the high surface roughness and low surface tension, the coated slides exhibited great superhydrophobicity with a water contact angle of 165 ± 2° and sliding angle of 10 ± 3°.

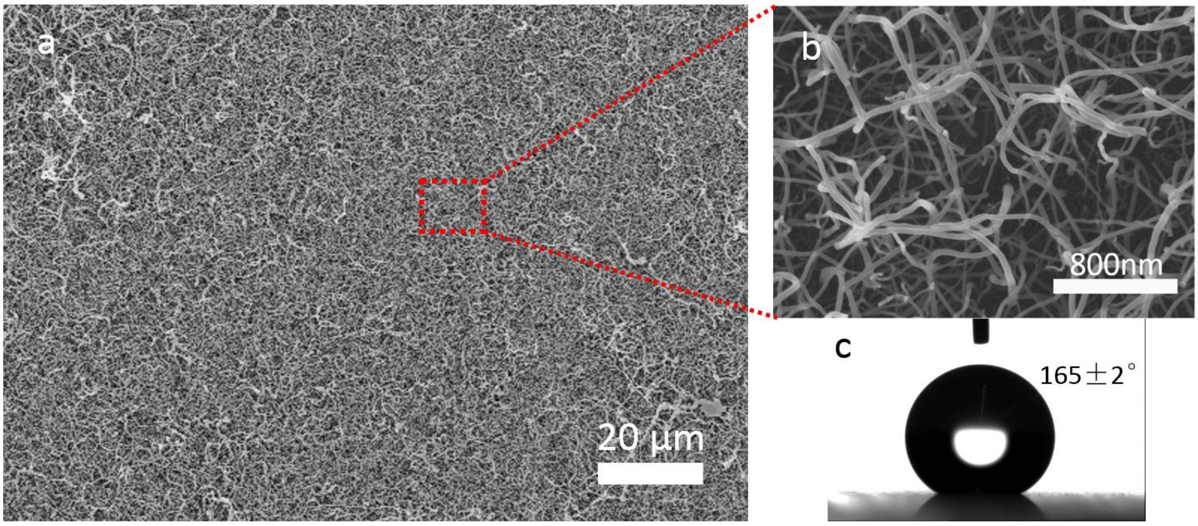

Figure 4.1.2 a-b) SEM images of superhydrophobic SNFs on glass slides; c) Contact angle measurement with a water droplet of 10 µL.

The polymerization of styrene was carried out in 100 mL water/ethanol solution (3:7 in volume). SNFs-coated glass slides were immersed into the solution. One-hour deoxygenation was accomplished by bubbling the solution with nitrogen gas flow of 1.5 L/min, because oxygen acts as a retarder to slow down the polymerization. Bubbling is good enough to remove the oxygen and ensure the performance of AIBA in initiation. Thus, no real need for freeze-pump-thaw degassing procedure by Schlenk line setup. Variable amounts of AIBA were added once the temperature reached 75 C° and stayed for 10 min, during which the activation of C=C bonds from SNFs was initiated by AIBA. A Fixed amount of monomer styrene was used in each experiment (1.0 mL, 10.6 mmol). The polymerization carried out for 2 hours under nitrogen atmosphere. The clear water/ethanol solution became opaque after a few minutes after the injection of styrene and in the end, milky-coloured dispersion was formed due to the insolubility of PS in water/ethanol. After polymerization, the SNF fibrous skeleton was grafted with PS and the substrate was named with PS@SNFs.

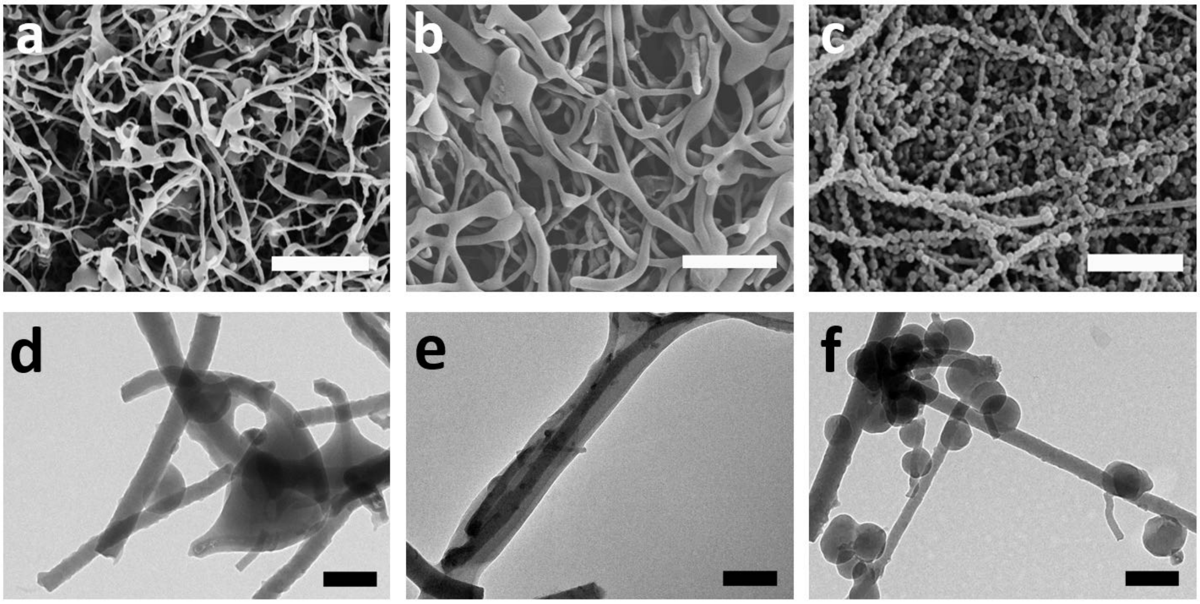

Figure 4.1.3 SEM (a-c) and TEM (e-h) images of the SNFs coating with (a,d) leaf-shaped PS, (b,e) with well-wrapped PS and (c,f) with bead-shaped PS. The white and black scale bars indicate 800 nm and 200 nm respectively.

The morphology control of PS@SNFs was obtained by changing the post treatments after the polymerization reaction. Slides were taken out of the reaction solution and rinsed with different combinations of solvents. To achieve bead-shaped PS, absolute ethanol was used for rinsing, followed by using deionized water and drying with nitrogen stream. The well-wrapped PS was treated by using only acetone and dried with a nitrogen flow. In order to get leaf-shaped PS, the slides were first rinsed by acetone, then by absolute ethanol and finally dried with nitrogen stream. The SEM and TEM images in Figure 4.1.3 show clearly the morphology of three different styles.

PS is not soluble in water, poorly soluble in ethanol and partially soluble in acetone (depending on its molecular weight).[219] However, due to the difference of polarity and solubility (see in Table 4.1.1), the radical polymerized PS exhibited various morphologies. The schematic illustration of the morphology tuneability of PS is displayed in Figure 4.1.4. Since the reaction solvent is ethanol/water mixture (7:3 v/v), the propagation reaction continued with certain limitations due to the low solubility in the mixture.[220] The differences among the three morphologies were the results of corresponding treatments after grafting.

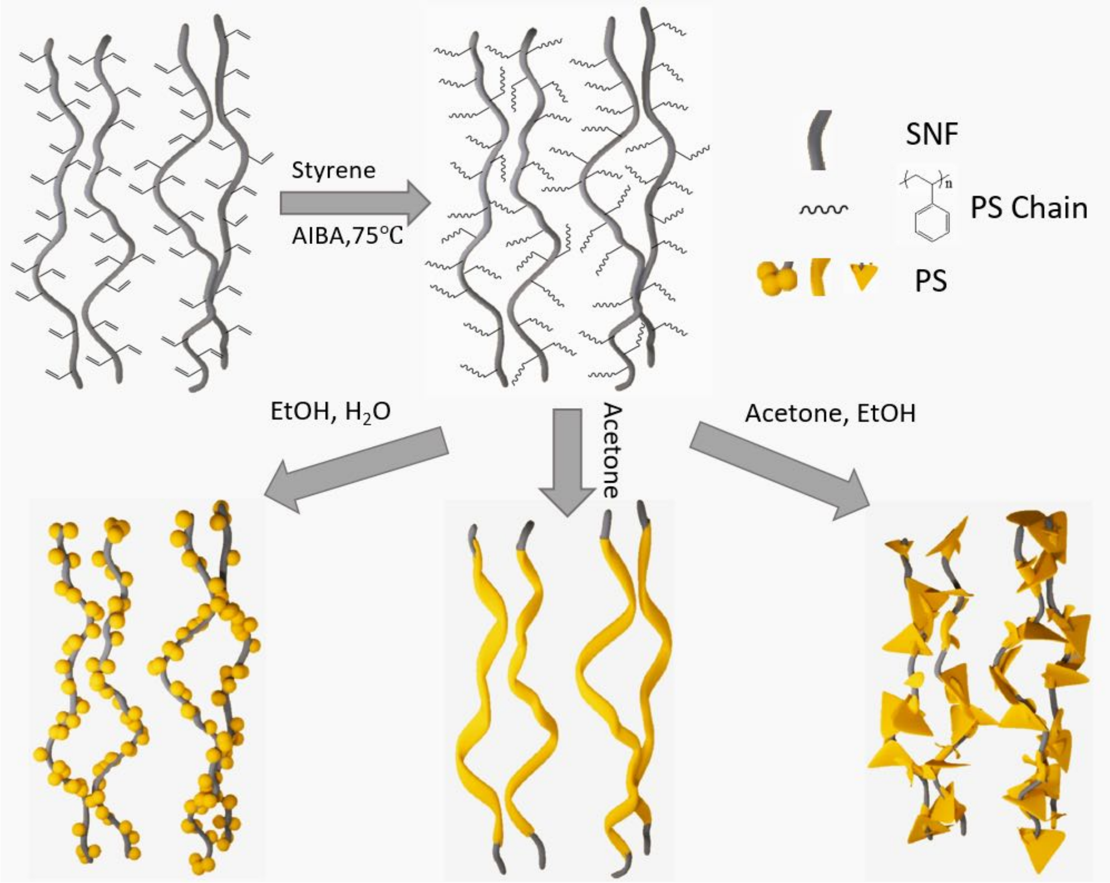

Figure 4.1.4. Schematic illustration of the post treatment procedures after PS was grafted on the surface of SNFs made of VTCS.

	Water	Ethanol	Acetone

Relative polarity	0.991	0.654	0.355

Table 4.1.1 Relative polarity of water, ethanol and acetone.

We hypothesize the phenomenon could be due to the solubility of PS chain in different solvents. The insolubility of long PS chains determined the polymerization once a certain chain length reached in diferent solvents. The grafted PS chain extended most in acetone, which has the lowest polarity among the three liquids we used. Thus, the PS chain has the largest solubility in acetone. With no further treatment but drying under nitrogen stream, the well-wrapped PS was formed which covers all around the SNFs along the length dimension. After using acetone, however, once PS was rinsed by ethanol, with a relatively higher polarity compared with acetone, less extension happened along the SNFs but with more extension in 2D dimension to form the leaf-shaped PS. In contrast, rinsed with ethanol at first, following with water, led to a maximum shrinking of the PS composite, and the PS chains tended to form spherical bead-shaped PS, which have the lowest surface energy in a polar solvent to stabilize the structure. The fundamental reason for the behaviour of grafted PS needs to be further investigated and studied in future research.

4.1.2 The size control of bead-shaped PS@SNFs

The size control of the bead-shaped PS@SNFs is a part of the tuneable morphology controlling of the novel nanocomposite material. PS bead size is controllable in general in the PS dispersion or emulsion. Yamamoto *et al*. controlled the size of the PS in soap-free emulsion by changing the concentration and valence of the used electrolytes, taking AIBN as initiator.[221] Im *et al*. produced highly monodisperse PS particles by modified dispersion in which aqueous alcohols, polyvinylpyrrolidone and ammonium persulfate were used as a medium, steric stabilizer and initiator, respectively.[222] Ober's group achieved the PS size control in a dispersion polymerization process and the resulted PS particles precipitated and stabilized by a steric barrier of dissolved polymer.[223] The particle size control experiments from which PS as a grafted layer on other particle cores or PS serves as the core for further grafting were reported in other literature.[224, 225] However, to our best knowledge, grafted PS bead on a macro-interface has not been reported yet.

Herein, we reported an innovative method for size control of interface-grown PS bead which was by changing the amount of the initiator AIBA. No extra stabilizer was needed. Figure 4.1.5 depicted the three different sizes of the obtained PS beads on SNFs by SEM (a-c) and TEM (d-f) images.

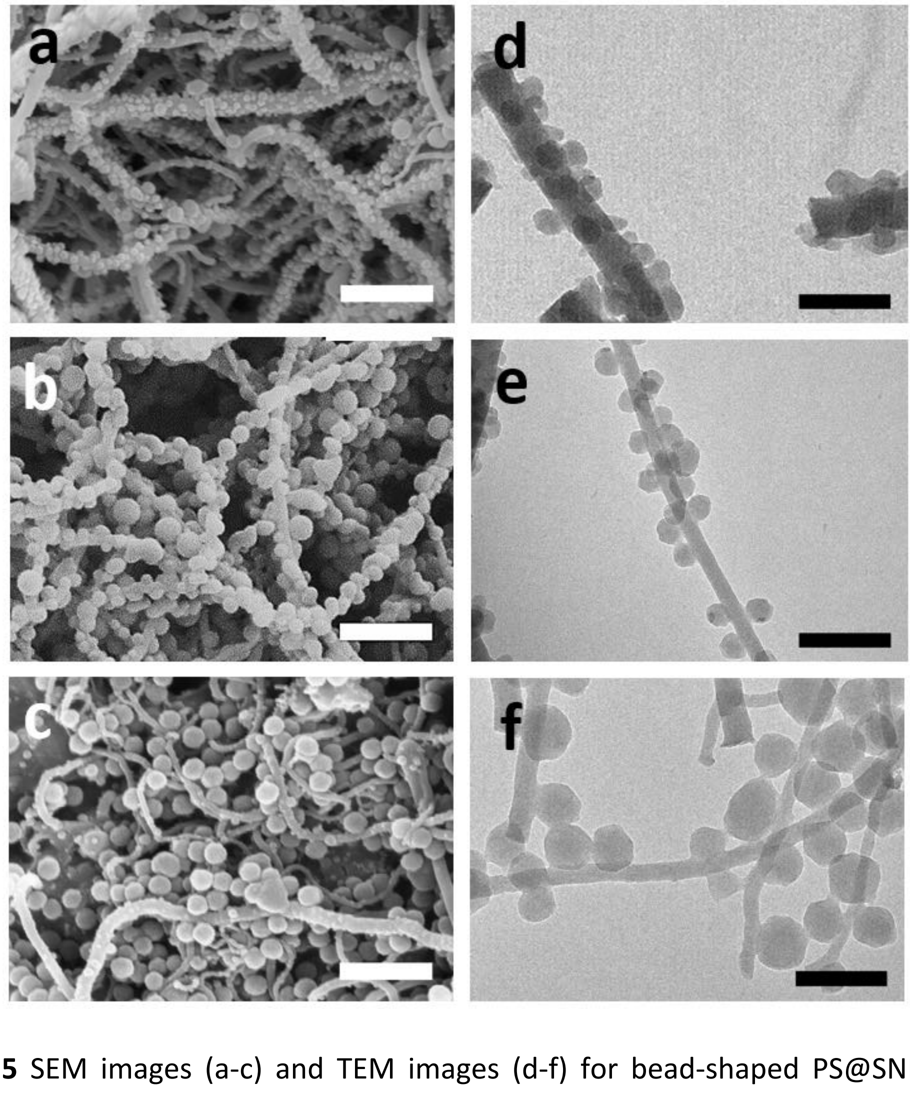

Figure 4.1.5 SEM images (a-c) and TEM images (d-f) for bead-shaped PS@SNFs with the average PS diameter 31.2 nm, 56.8 nm and 76.8 nm; the white and black scale bars indicate 800nm and 150nm respectively.

The surface grafting of PS on SNFs was followed with the method we introduced in 4.1.2. The water-soluble initiator AIBA was added into the reaction system after an hour of deoxygenation with bubbling nitrogen. The system was then heated and kept at 75 °C. The initiator AIBA was added 10 min before introducing the styrene monomer. In this order, the vinyl groups on SNFs from VTCS precursors firstly reacted with the initiator and were activated as initiation sites of the later polymerization. Followed with the injection of monomer styrene, the radical polymerization took place and could graft PS at a maximum number on the surface of SNFs. Comparing with adding AIBA and styrene together once it reached 75 °C, more polystyrene would be loaded on SNFs surface in the designed order. As adding together of AIBA and styrene results in more polymerization in the bulk solution and less on the initiation sites on SNFs. The corresponding post-treatment was applied to get the bead-shape PS.

The PS bead size was measured with the software ImageJ by using TEM images, counting no less than 300 beads in the available visual fields. The resulted relation between the initiator amount and the average PS diameter is presented in Figure 4.1.6.

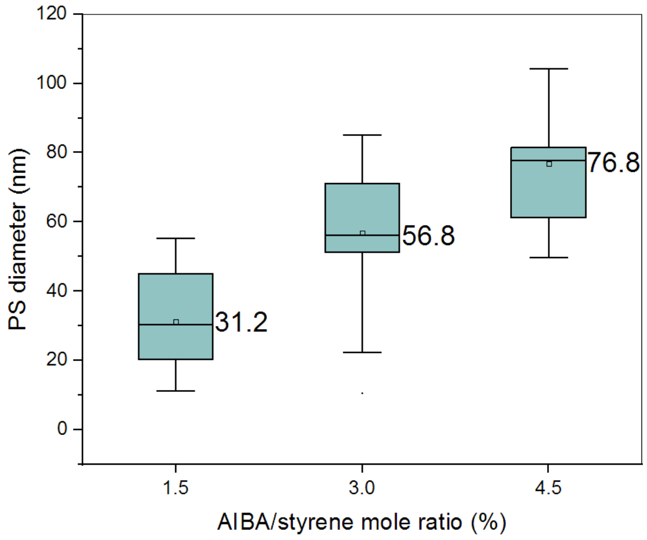

Figure 4.1.6 The relation between the PS bead diameter to the AIBA/styrene mole ratio

In all experiments, the amount of injected styrene was fixed. With the increase of the amount of initiator AIBA, the average diameter of PS bead decreased. The AIBA concentration applied was 0.15 mmol, 0.3 mmol to 0.45 mmol, which resulted to the AIBA/styrene molar ratios of

0.015, 0.03 and 0.045, respectively. The average coating weight of SNFs on the slides was weighted to be about 3.5 mg per slide, which turned to have 0.043 mmol of vinyl groups per slides. In comparison, the AIBA amount was in excess to the vinyl groups in all the cases. Most vinyl groups on SNFs could be activated by a thermal cracking once the temperature reached 75 °C. Adding even more initiator, the polymerization would take place preferentially in the solution instead of on the surface of SNFs, since the initiation sites on SNFs tended to be saturated, which led to a reduced loading amount of grafted polystyrene and higher amount of free PS in solution and resulted in smaller bead size after the post-treatment.

To confirm our hypothesis, the loading amounts of polystyrene were measured by the TGA experiment, shown in Figure 4.1.7. With the smallest average diameter, the weight loss of PS is about 35.62%, which represented by the curve from 310 °C to 460 °C. On the other hand, with the increasing of the diameter of PS beads, from 310 °C to 460°C more weight loss of PS was observed. It was 69.71% weight loss for PS beads with an average diameter of 56.8 nm and 78.50% for the ones with 76.8 nm diameter in the temperature range of 310 °C to 460 °C. That verified the relation of the loading amount of composited PS on SNFs to the PS bead diameter.

The realizing of controllable loading amount and shape of PS on SNFs could lead to an accurate control on other properties of the PS-SNFs composite material. It is well known that the specific surface area is determined(?) by the morphology of the nano-composite materials and the loading capability of catalysts is determined by the specific surface area. The composite material we fabricated here could have potential use in surface catalysis. Due to the good affinities to organic solvents from PS, the tuneable amount of PS will lead to other tuneable properties, such as oil absorption capacity and oil water separation efficiency.

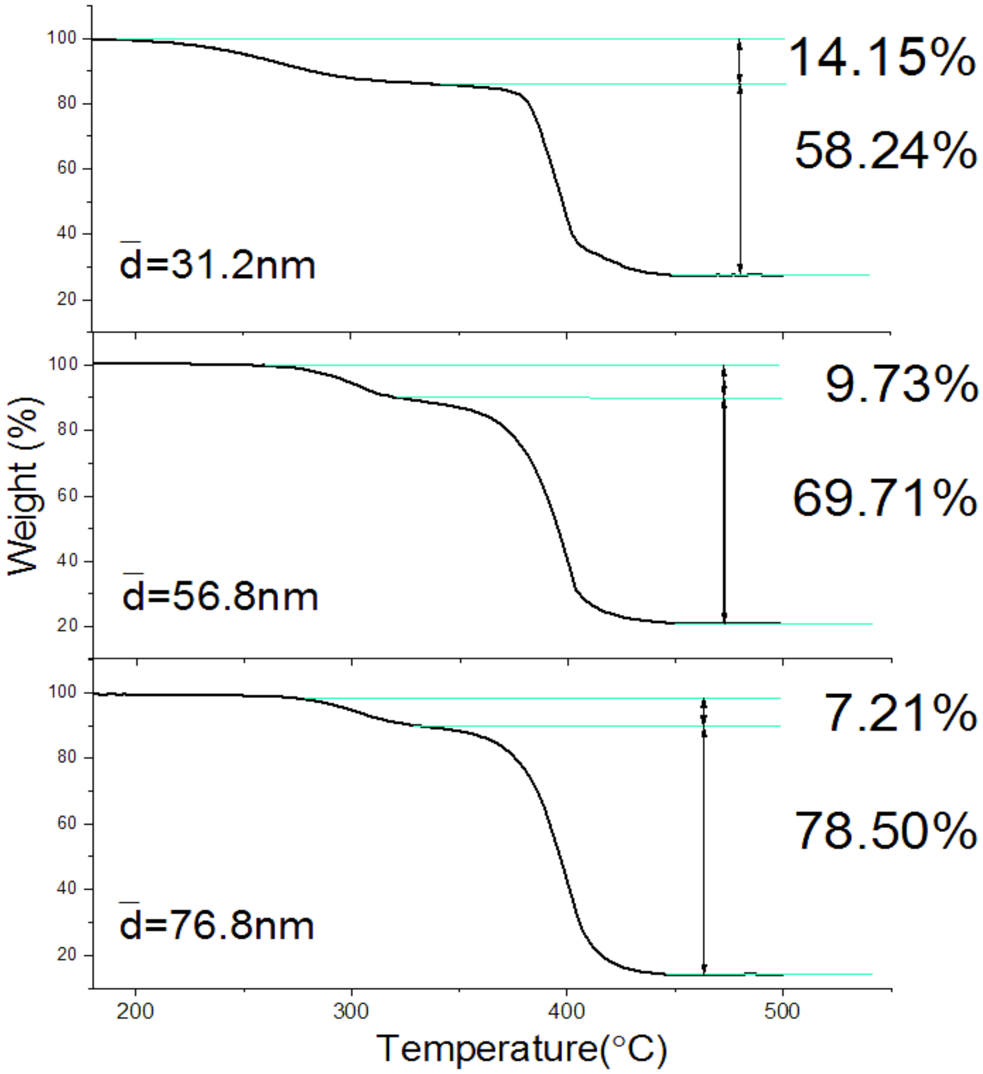

Figure 4.1.7 TGA analysis for the PS@SNFs with three sizes of grafted PS-bead size.

4.1.3 Oil-water separation

SNFs have already been proved as an excellent ingredient for oil-water separation.[73, 114] In this section, we investigated the new composite materials' properties for this application. Porous materials with superhydrophobicity and superoleophilicity are usually very good materials for the oil/water separation. The use of well-designed water-repellent materials is a reasonable approach for oil-spill remediation and oil separation by selective absorption, which leads to a simple operation and the possibility of reusing the materials for multiple times.[97] Natural fibrous sorbents such as wool, cellulose, cotton, hay, feather, and straw and natural mineral ones such as perlite, clay, peat moss, and vermiculite.[226, 227] However, there are shortages from the natural sorbents. For example, the substantial and fast fatigue, low absorption capacity, and poor recycling ability limit a broader usage in actual applications. Therefore, synthetic sorbents including rubber sponges, polyurethane (PU), nonwoven polypropylene mats and silicon aerogels were invented with a higher porosity to increase the capacity and stronger texture to elongate the durability.[102, 228, 229]

For executing an oil-water separation experiment, a polyester sponge was used as an oil-absorbing substrate. The sponge was treated with an oxygen plasma for the surface activation. The previously mentioned method of gas phase coating was adopted to coat the sponge with SNFs, followed by grafting PS onto SNFs as we did on glass slides (Figure 4.1.8). In order to have the oil/water separating ability, the functionalized sponge needed to be modified into hydrophobic. A further oxygen plasma activation was applied to hydroxylate the surface again in order to be hydrophilic enough to catch the humidity in the reaction chamber. A trace amount of VTCS was injected into the chamber. After 20-min reaction, the prepared sponge was converted into superhydrophobic again.

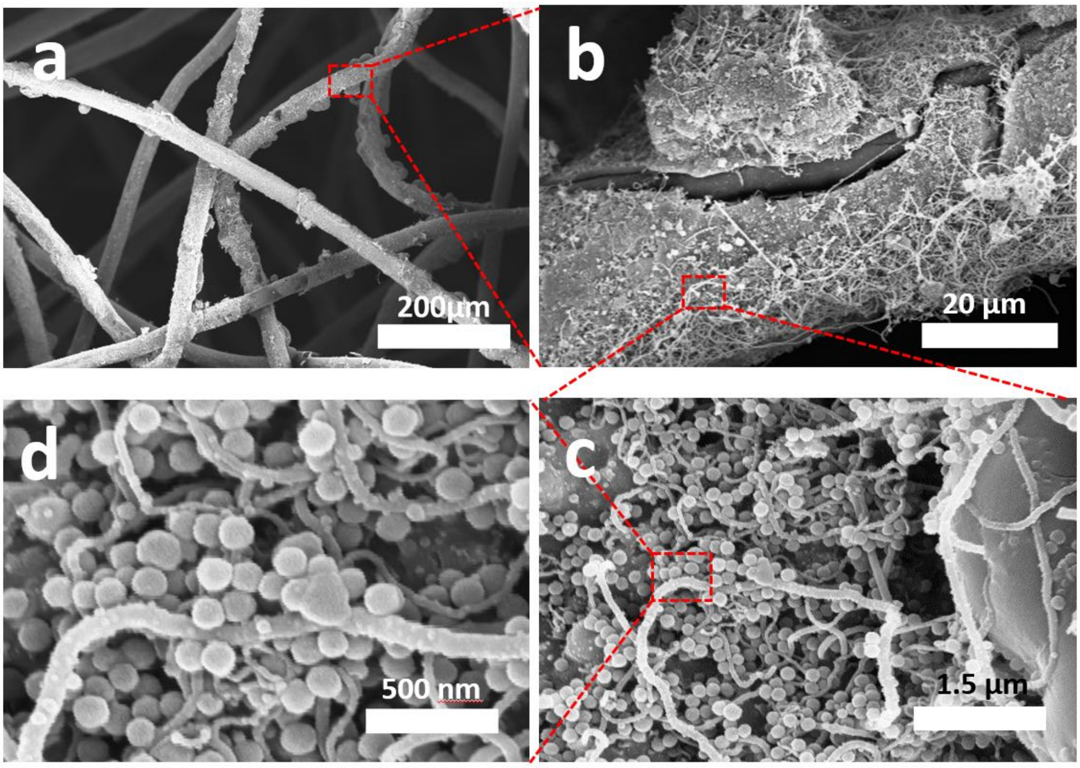

Figure 4.1.8. SEM Images of bead-shaped PS@SNFs coated sponge with different scale bars

The water contact angle was about 165 ° (in Figure 4.1.9a), though the sliding angle was hard to obtain due to the uneven surface of sponge. In Figure 4.1.9b, a layer of air was trapped between the sponge surface and the water,[230] which is called “plastron” layer due to the Cassie–Baxter wetting phenomenon from superhydrophobic surface.[142] After reaching the chloroform phase, the sponge absorbed chloroform (dyed with oil red) and was immediately fully loaded, indicating the superoleophilicity (Figure 4.1.9c).

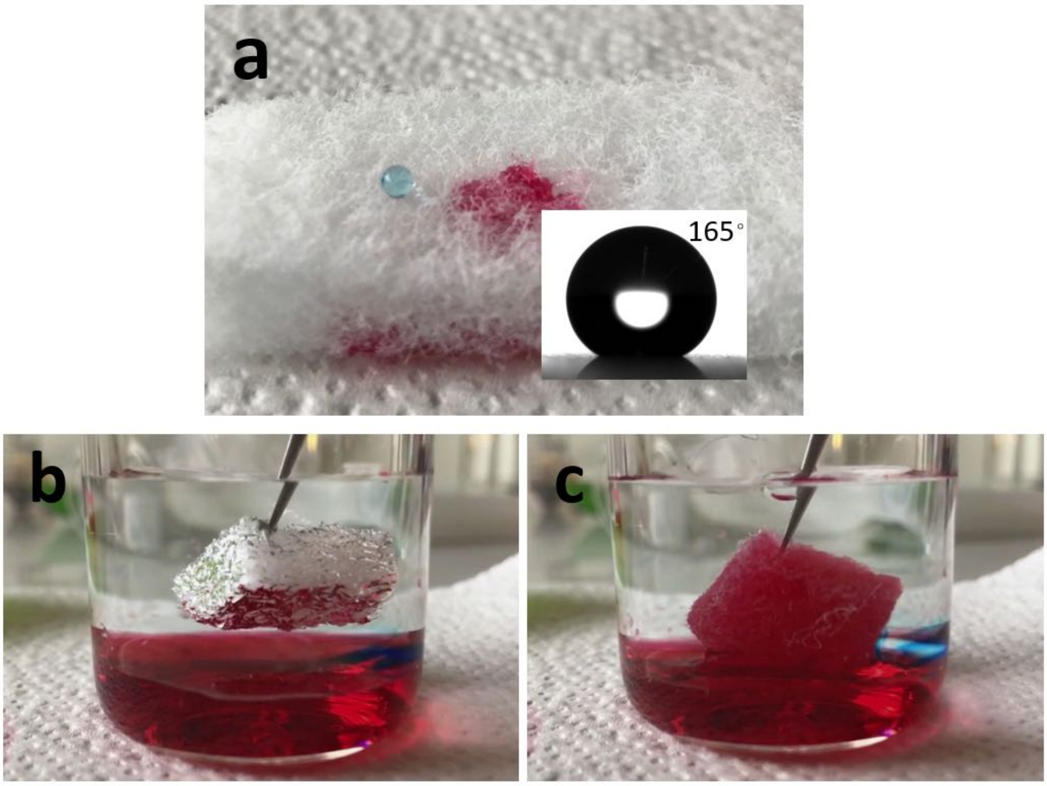

Figure 4.1.9. a) Image of water droplet (dyed with MB) on a PS@SNFs coated sponge with a contact angle of 165° and chloroform (dyed with Oil Red O) absorbed by the sponge; b,c) Oil-water separation experiment before b) and after c) absorbing chloroform (red layer);

The oil absorption capacity was the criterion for evaluating oil-water separation ability. To measure the oil absorption capacity, the functionalized sponge was weighed before using. Chloroform, octane and paraffin oil were chosen for the measurements, which are common organic solvents or oil in industry and research. The sponge was immersed totally into the oil or solvent for 2 seconds, taken out for another 2 second and weighed quickly before an apparent evaporation of solvents happened. The oil absorption capacity (α) was determined as:

$$\alpha = (M_1-M_0)/M_0 * 100$$

where M_1 is the weight of the sponge saturated with oil after immersing, M_0 is the dry weight of the sponge before using.

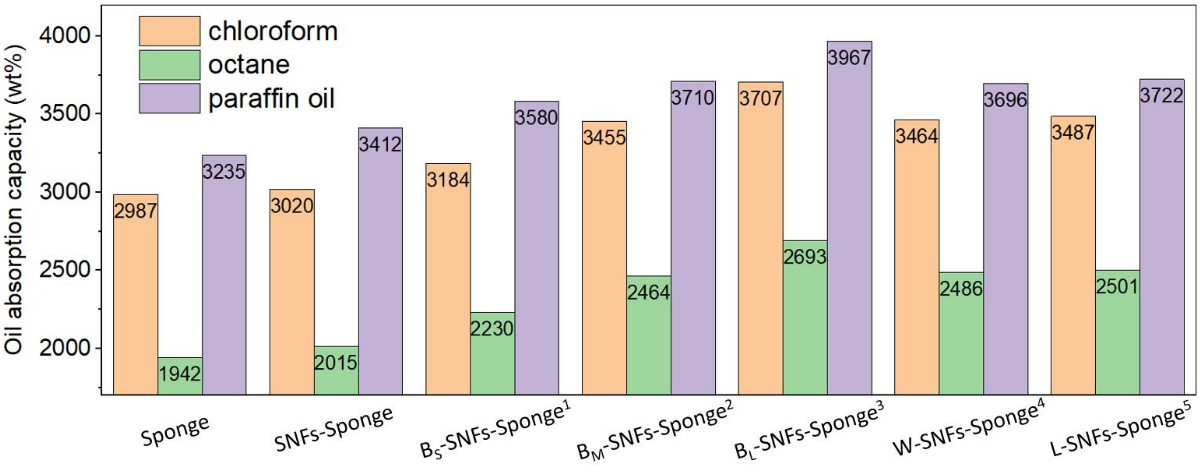

Figure 4.1.10. Oil absorption capacity for different substrates. Note$^{1, 2, 3, 4, 5}$: B_S, B_M and B_L represent bead-shape PS with average diameters of 31.2 nm, 56.8 nm and 76.8 nm from small, medium to large respectively; W represents well-wrapped PS; L represents leaf-shaped PS.

From Figure 4.1.10 and Table 4.1.2, the oil absorption capacity was correlated to the loading amount of PS on SNFs, which was fundamentally decided by the amount of AIBA used for polymerization. The sponge without any modification absorbed the least weight of oil. With a coating layer of SNFs on the sponge fibres, the oil absorption capacity was improved due to the superoleophilicity and the increased surface area by SNFs. The higher oleophilicity increased the affinity of substrate to the oil molecule. Thus, among the porous structure of the sponge, more oil was contained.

The B_M- SNFs-Sponge, the W- SNFs-Sponge and the L-SNFs-Sponge showed similar oil absorption capacity when the same amount of AIBA was used to graft the PS on SNFs. By changing the amount of AIBA to a higher concentration, the B_S-SNFs-Sponge exhibited the lowest oil absorption capacity. In contrast, the B_L-SNFs-Sponge showed the highest oil absorption capacity. That above-mentioned phenomenon demonstrated that the loading amount of PS on SNFs is essential to determine the oil absorption capacity instead of the morphology. As different morphologies were formed by post-treatment after the polymerization completed, the loading amount of PS on SNFs only related to AIBA/styrene ratio in the polymerization procedure. By using more initiator, the polymerization happened in bulk was accelerated due to more available free radicals formed in the bulk when reaching the pyrolysis temperature of AIBA. The polymerization reaction in the bulk hence consumed more monomers, which led to a lower loading amount of PS on SNFs, comparing to the situation where less AIBA was added. In other words, the amount of initiator affected the degree of polymerization, which in return influenced the loading amount of PS on SNFs. In Figure 4.1.7, the TGA result showed the same conclusion as observed in the oil absorption capacity. With an AIBA/styrene ratio of 0.045, 35.62% of the total weight was PS (mass loss from temperature 310 °C to 460 °C). 69.71% of the total weight was PS in the case that 0.03 of AIBA/styrene was used for the polymerization. The highest loading was obtained by applying an AIBA/styrene ratio of 0.015, which led to an almost 4：1 ratio of PS to SNFs in weight (78.5% mass loss due to PS). PS has a strong affinity to oil liquid owing to the hydrophobic and oleophilic properties,[231] which absorb oil and keep it in the space among the sponge fibres structure (see in Figure 4.1.8). As a conclusion, the oil absorption capacity was correlated to the loading amount of PS on substrate. With more PS loaded on SNFs, the modified sponge shows a better oil absorption capacity.

The tuneability of the oil absorption capacity of the PS-SNFs composite is a successful proof for the possible application in oil-water separation in industry or in emergency cases such as crude oil leakage accidents on the ocean. Besides, the feasibility of synthesis also makes the novel composite material a good candidate for an industrial scale of production.

Sample	AIBA/styrene mole ratio%
Sponge	No styrene
SNFs-Sponge	No styrene

B_S-SNFs-Sponge[a]	4.5
B_M-SNFs-Sponge[b]	3.0
B_L-SNFs-Sponge[c]	1.5
W-SNFs-Sponge[d]	3.0
L- SNFs-Sponge[d]	3.0

Table 4.1.2 Different substrate with AIBA/styrene mole ratio. Footnote[a, b, b, d, e]: B_S, B_M and B_L represent bead-shape PS with average diameters of 31.2 nm, 56.8 nm and 76.8 nm from small, medium to large respectively; W represents well-wrapped PS; L represents leaf-shaped PS.

4.1.4 Photocatalytic Reaction

Heterogeneous catalysis plays an important role in industry and research. It enables faster, large-scaled production and produces selective products.[232] In heterogeneous catalysis, the phase of the catalysts differs from the phase of reactants, which contrasts with the homogeneous catalysis. In the heterogeneous catalytic reaction, there are steps of surface diffusion, molecules adsorption, reaction, and desorption happening on the surface of catalysts.[233] The carrier or support for catalysts is essential in heterogeneous catalysis. With a good catalyst support, the active sites are highly dispersed, with the highest surface to volume ratio and carrying the least amount of active catalysts, which save the cost of catalyst.[234] Particles in nano-meter scale are suitable candidates as heterogeneous catalysts. SNFs have successfully used as carrier for catalysts and exhibited enhanced catalytic activities. SNFs are chemically inert and thermally stable. Thus, they have a good durability during catalytic reactions. Besides, considering the morphology and structure, SNFs act as a good dispersing carrier with an enlarged surface area. The Seeger group has fabricated SNFs supported nickel oxide catalyst, which proved to be a good strategy for oxygen evolution reaction. The designed catalyst had the advantages of binder-less as electrodes as well as facilitated the mass transport and release of products.[235] What's more, the immobilization of TiO_2 NPs on SNFs demonstrated that the combination had a promising photocatalytic activity and offered a prototype approach for other SNFs supported metal oxide catalysts.[236]

In this section, TiO_2 nanoparticles were used for water purification. We investigated the performance of the new PS@SNF composites as a support for this application. TiO_2 nanoparticles were well deposited on SNFs after 1-hour controlled hydrolysis of TiF_4 in the mixture of ethanol and water (4:1 v/v) at 60 °C. As shown in Figure 4.1.11a-d, the TEM images clearly exhibited the deposition of TiO_2 nanoparticles on (a) SNFs or (b-d) SNFs-PS composites. The average TiO_2 particle size was about 40-100 nm and they were deposited all over the surface. From the TEM image in Figure 4.1.11d, we observed that the leaf-shaped PS@SNFs substrates loaded with most TiO_2 nanoparticles on the PS leaves. The density of the deposited TiO_2 nanoparticles on TEM images was lower, compared with that from the SEM images in Figure 4.1.11e,f. The possible reason is that due to the harsh ultrasonication treatment required for TEM sample preparation, a certain amount of TiO_2 nanoparticles were vibrated off. The STEM-EDX in Figure 4.1.11g determined the composition of the formed PS-SNFs composite material. The extremely high Cu peak at 8.04 and 8.91 KeV from the spectrum are due to the copper grid sample holder; the high carbon signal is partially due to carbon atom on SNFs and PS but mainly to the polymer film on sampler holder. With the titanium signal at 4.5 KeV, the EDX analysis confirms the formation of TiO_2 nanoparticles on PS@SNFs.

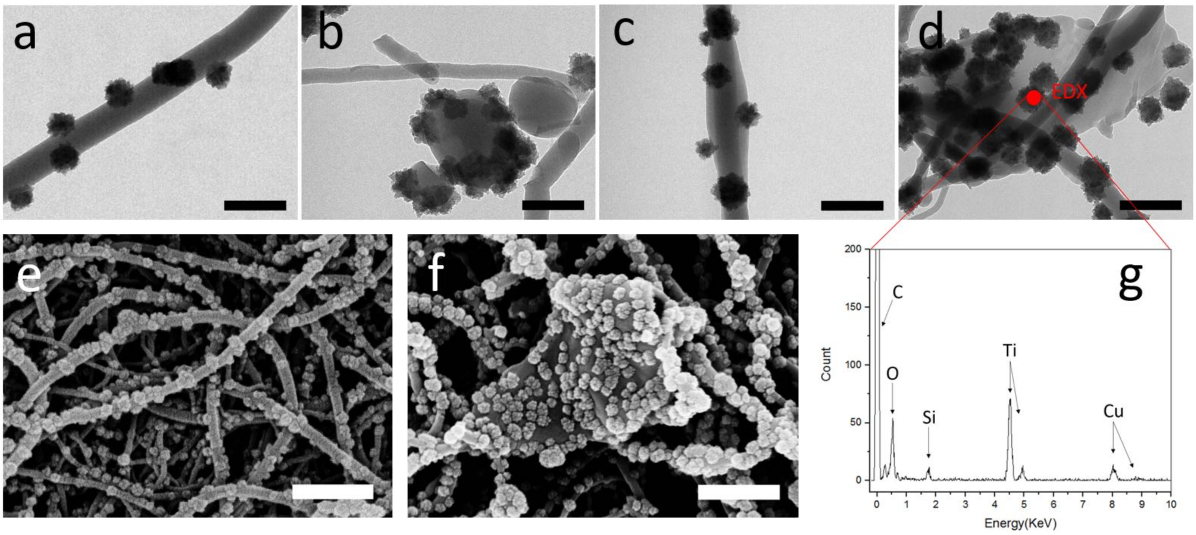

Figure 4.1.11. TEM images (a-d) of TiO_2 nanoparticles@SNFs: (a) without PS; (b) with bead-shaped PS; (c) with well-wrapped PS; (d) with leaf-shaped PS; SEM images (e,f) of TiO_2

nanoparticles@SNFs (e) without PS; (f) with leaf-shaped PS; (g) Representative STEM EDX spectrum of TiO_2 nanoparticle@leaf-shaped PS/SNFs composites (high peak of carbon and the Cu signals arise from the sample holder). The Black and white bars indicate 150nm and 800nm.

The photocatalytic performances of different composites were evaluated by monitoring the degradation of the organic standard test dye methylene blue (MB) under UV radiation at 350 nm. When the model compound MB dissolved in water, it formed a blue solution. It was necessary to eliminate the situation that the UV radiation at 350 nm degraded the MB in solution. Therefore, the absorbance spectrum of MB was collected in Figure 4.1.12. As we see, the UV-Vis spectrum of MB showed maximum absorption at 665 nm. The light source, which was used for emitting light at wavelength 350 nm, compared with the absorption spectrum of MB, shows very little overlap. Hence, we concluded that the direct energy absorption of MB from the light source could be excluded.

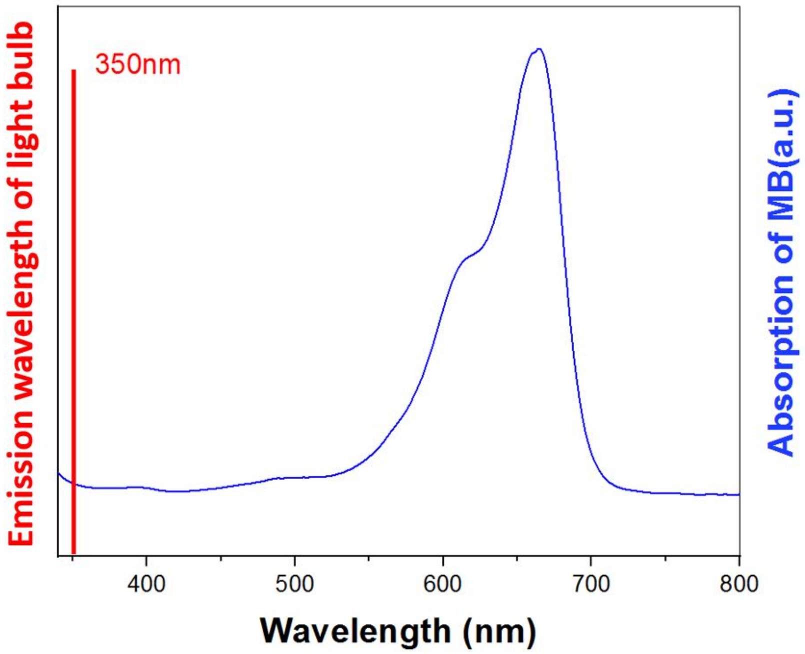

Figure 4.1.12. Emission wavelength of the light bulb (red) and absorption spectrum of MB (blue). Emission and absorption do not overlap which excludes an energy transfer from the light to MB.

Details about the sample preparation, experimental setup and procedure can be found in the experimental section. In Figure 4.1.13a, the changes of the absorption of the MB solution were exhibited in the presence of different composites, including the control sample. The self-degradation of MB without any photocatalytic substrate was not obvious. The absorption became 10.3% lower after 2 hours of illumination. To measure the influence of the loading and photocatalytic activity of TiO_2 on SNFs (TiO_2@SNFs), TiO_2 nanoparticles were deposited on a glass slide which was cleaned and treated with oxygen plasma with the same method to form a composite without the surface roughness of SNFs. The result showed a degradation of MB with a value of 25.6% after 2 hours. Compared with the performance of the substrate TiO_2@SNFs, it can be confirmed that with additional surface roughness owing to SNFs, the photocatalytic activity of TiO_2@SNFs composite is much better than that of the substrates without SNFs. The rooted reason is SNFs served as a support for catalyst and it provided with a higher specific surface area for loading more active sites. This has already been demonstrated by our group in an earlier work.[236] TiO_2@SNFs significantly lowered the MB degradation to 82.9%, which is more than 3 times more effective than the degradation of TiO_2@glass slide. Furthermore, our results also verified that the photocatalytic activity could be improved more when PS was grafted on SNFs as a composite support. The TiO_2@PS-bead@SNFs and TiO_2@PS-wrap@SNFs reached a performance of MB degradation of 93.3% and 95.7% after 2-hour illumination. The higher catalytic efficiency can be attributed to a larger loading amount of TiO_2 and more photoactive sites as a result of extra extended surface area created by PS. The TiO_2@PS-leaf@SNFs obtained the largest degradation with a value of 98.3%. Moreover, the degradation rate was highest with TiO_2@PS-leaf@SNFs as in the first hour the degradation was almost close to 98%, which was higher than any other substrates.

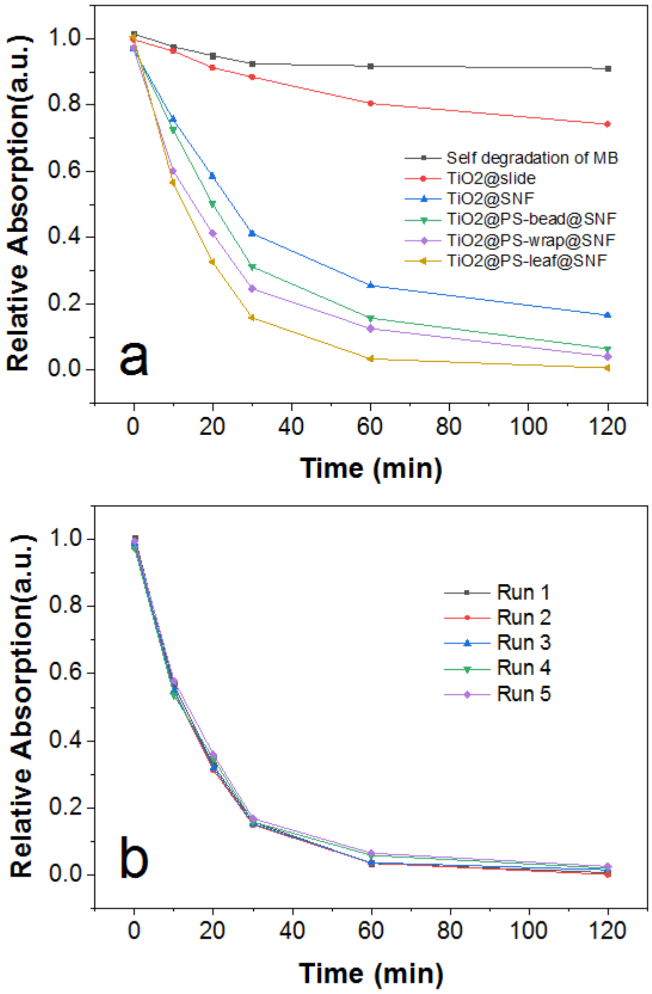

Figure 4.1.13. (a) Photodegradation of methylene blue (MB) in the presence of TiO_2@SNFs composites under UV irradiation at 350 nm (black = self-degradation of MB; red = TiO_2 on glass slide; blue = TiO_2 on SNFs; green = TiO_2@SNFs with bead-shaped PS composites; purple = TiO_2@SNFs with well-wrapped PS composites; yellow = TiO_2@SNFs with leaf-shaped PS composites. (b) Repeated recycling experiments for the photodegradation of MB under UV irradiation at 350 nm in the presence of TiO_2@SNFs with leaf-shaped PS composites.

We hypothesized that the morphologies of the three PS@SNFs substrates contribute differently to the specific surface areas. Unfortunately, the nitrogen adsorption (BET) experiment could not be conducted due to the very thin-film nature of SNFs. In our previous research, focused ion beam nanotomography was applied to certify that the SNFs coating multiplies the surface area of a flat substrate, such as glass slide, by a factor of ca. 13.[237] As a result, an alternative measurement of the loading amount of TiO_2 was employed by spectrophotometer to indirectly determine the specific surface area, according to a modified method.[238] The calibration of a standard line of absorbance to concentration was performed by using a standard titanium solution in a spectrophotometer, because TiO_2 are extremely robust and chemically stable in most of the acids, even in high concentration. Special treatment was needed to dissolve the titanium for measurement. Substrates were immersed into high concentration of sulfuric acid (50%) at 110 °C for 30 min to dissolve all TiO_2 NPs into titanium ion. The operation needed to be carefully conducted as the high temperature and high concentration of acid could be risky.

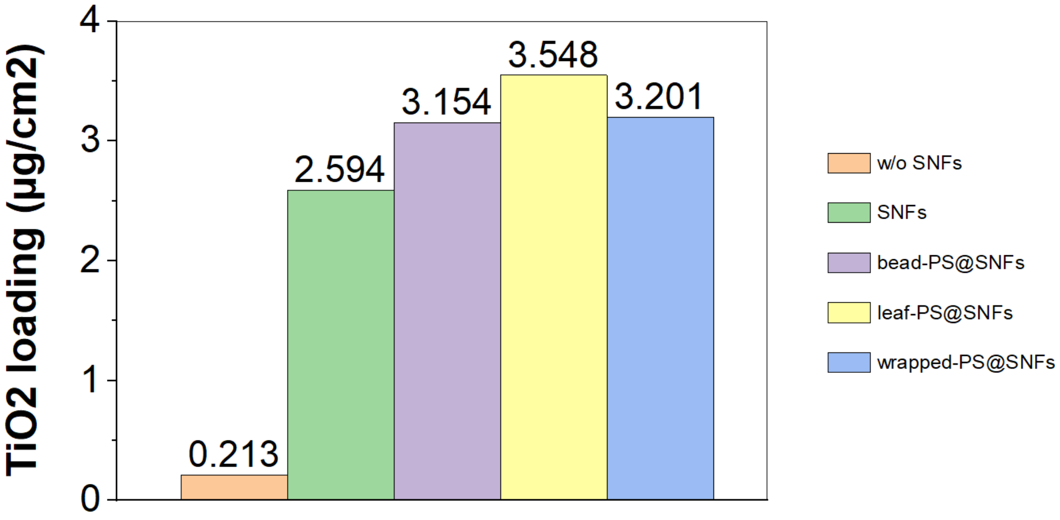

Figure 4.1.14 The loading amount (μg/cm^2) of TiO_2 on different substrates measured by spectrophotometer.

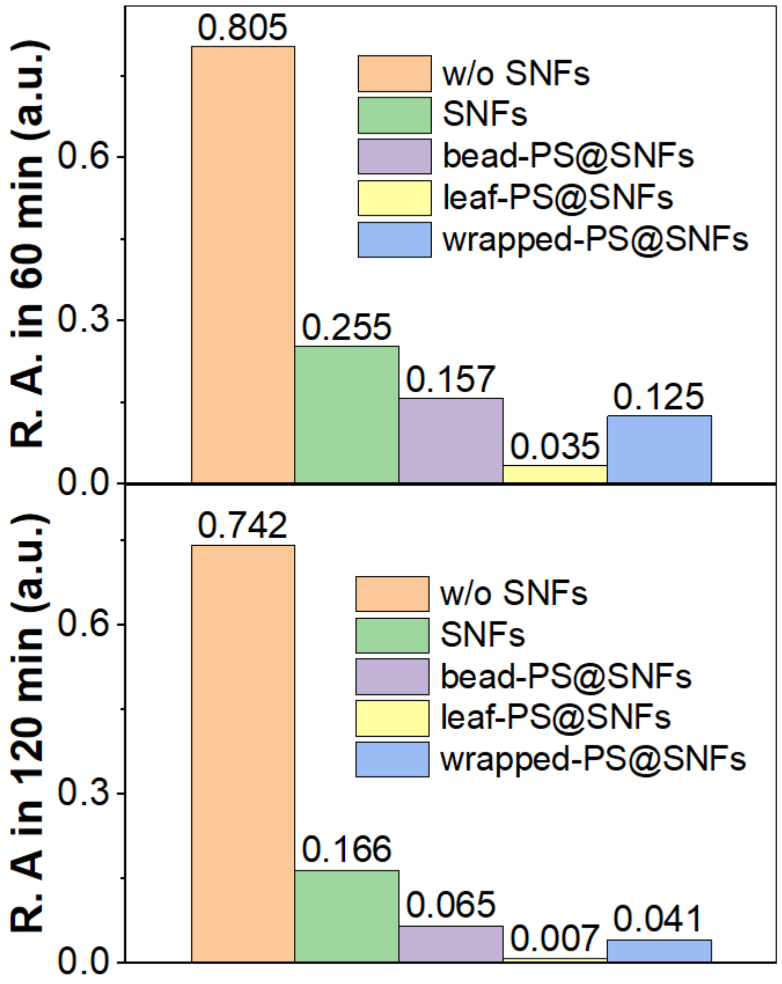

Figure 4.1.15. After 60 min (a), 120 min (b) of MB degradation, the relative absorption(R.A.) for different substrates.

The amount of titanium dissolved in acid solution was measured, with which the loading amount for all substrates was calculated and shown in Figure 4.1.14. The result corresponded with the photocatalytic performance measurement in Figure 4.1.15. Slides without SNFs had the least loading amount of TiO_2.only 0.213 µg/cm^2. In the case of SNFs without PS, there was less loading amount of TiO_2 compared with PS@SNFs. Thus, the compositing of PS on SNFs leade to the further extended surface area. Since the bead-shaped PS went through shrinking during the post treatment by polar solvent ethanol to lower the surface energy as we analyzed in previous section, its specific surface area is the smallest among the three SNFs-PS composites. For the wrapped-style PS, the low polarity of acetone made the PS extended fully along the filaments to form a cylinder layer wrapping around SNFs. However, with a certain thickness of the PS layer, the well-wrapped PS did not achieve the largest specific surface area. The leaf-shaped PS, in comparison with well-wrapped PS, had one more step of ethanol treatment. During that step, the grafted PS shrank along the silicone filaments and extended on the intersection of filaments to form PS leaves. It led to the highest specific surface area with the largest loading amount of TiO_2. This result fits the photocatalytic activity as shown in Figure 4.1.13a.

The recyclability of photocatalytic activity of the substrate TiO_2@PS-leaf@SNFs was proved by 5 times MB degradation as shown in Figure 4.1.12b.

The catalysis experiment conducted demonstrated the tuneability of the catalytic activity. With the tuneable morphology, the specific surface area could be controlled. This also inspired us to do further research to prove that this novel composite material can be used in other fields, such as protein absorption, surface detection and so on.

4.2 Hierarchical Structured Self-Cleaning Composite Material

Self-cleaning materials are becoming an integral part in daily life, as they are used in various applications, such as windows, solar panels, building walls and paintings. They were proved to have the advantages of labor-saving, longer life span for utility, and more environmentally friendly compared with consumable materials.[239] Usually the self-cleaning materials can be categorized into hydrophobic and hydrophilic according to their surface wettability.[137] The former one was inspired by natural phenomena, for example, lotus leaf, legs of water strider and wings of butterfly.[134, 141, 240] The water droplets slide and roll over the hydrophobic surfaces, taking away the dirt and contaminants. On the other hand, the hydrophilic surfaces, commonly made metal oxides, can be completely wetted. By the sheeting effect, the dirt or contaminants on such surfaces are removed by water. Moreover, another functionality of photocatalysis is often combined with hydrophilic surface. Because some of the metal oxides have an extra ability of decomposing the organic compounds on the surface.[241] For the hydrophobic surface, such functionality has to be integrated into the surface as a composite material.

4.2.1. Preparation of the Functional LDPE Substrates

For the preparation of the functional substrates, LDPE films were firstly rinsed with 70 % ethanol solution and dried under nitrogen flow before use. Glass beads were also cleaned in ethanol ultrasonification and dried in room temperature before use. A suspension of glass beads (GBs) in pure ethanol was treated with ultrasonication constantly and magnetic stirring was applied without stop to avoid sedimentation. The suspension was drop cast on the LDPE film within a limited area (50 cm^2) according to a protocol.[242] After evaporation of the ethanol on the surface, the substrate was heated in an oven at 165 °C for 10 min, followed by cooling to room temperature. At this temperature, LDPE film reached its glass transition temperature and gradually became viscous and rubbery. The glass beads started to embed into the resulted fluidic LDPE film. By controlling the time, the embedding depth of glass beads in LDPE was achieved.[243] Ten minutes inside of oven at 165 °C led to a defined depth. The micrometer-sized structures, which can protect the nano-meter SNFs, were obtained as shown in **Figure 4.2.1**.

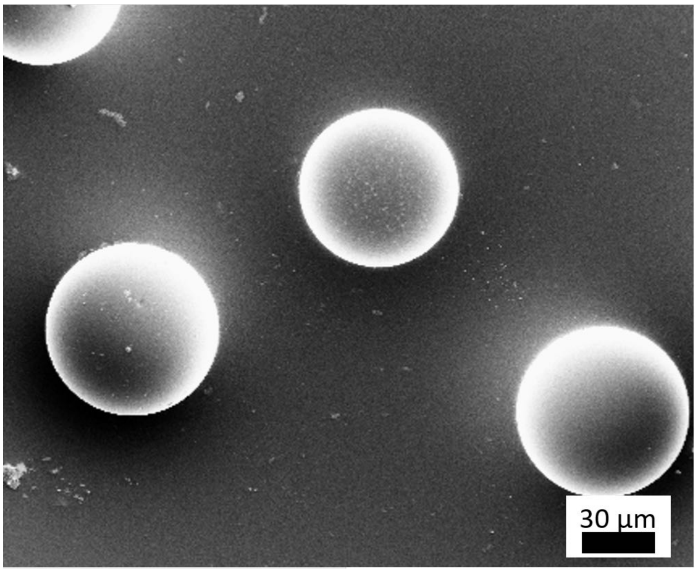

Figure 4.2.1 SEM images of the embedded glass beads on LDPE film.

The embedding depth of the GBs was calculated by the diameter of the hole after the GBs were scratched off with a strong force (see in Figure 4.2.2). The red arrow shows the direction of the scratching force and to where the GB was taken off. Therefore, among the lines, which are perpendicular to the arrow, the longest one was chosen to be the diameter of the hole. The depth was then easily calculated to be 20.82 µm.

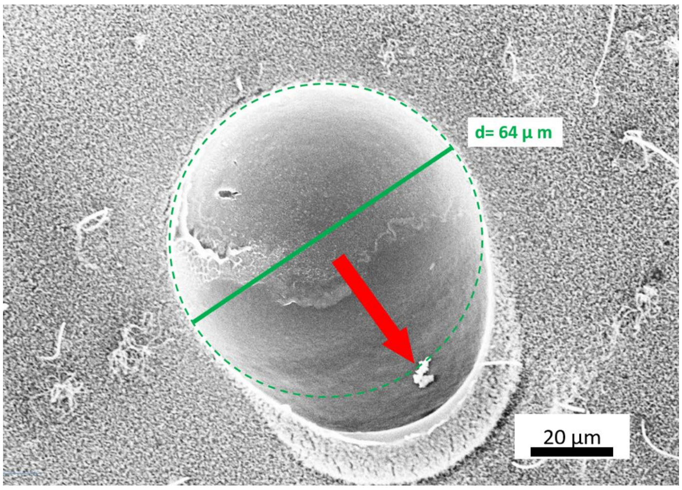

Figure 4.2.2 SEM image of the hole after the GBs were scratched off from LDPE by a strong external force. Depth of buried GBs was calculated according to this.

Direct growth of SNFs on LDPE substrates was described in our previous work.[58] In this project, we selected a trifunctional silane $CH_3CH_2SiCl_3$ as a precursor. The growth conditions were optimized by trials to provide a dense SNF coating with a high surface area, which is suitable for further utility as a catalyst support (Figure 4.2.3).

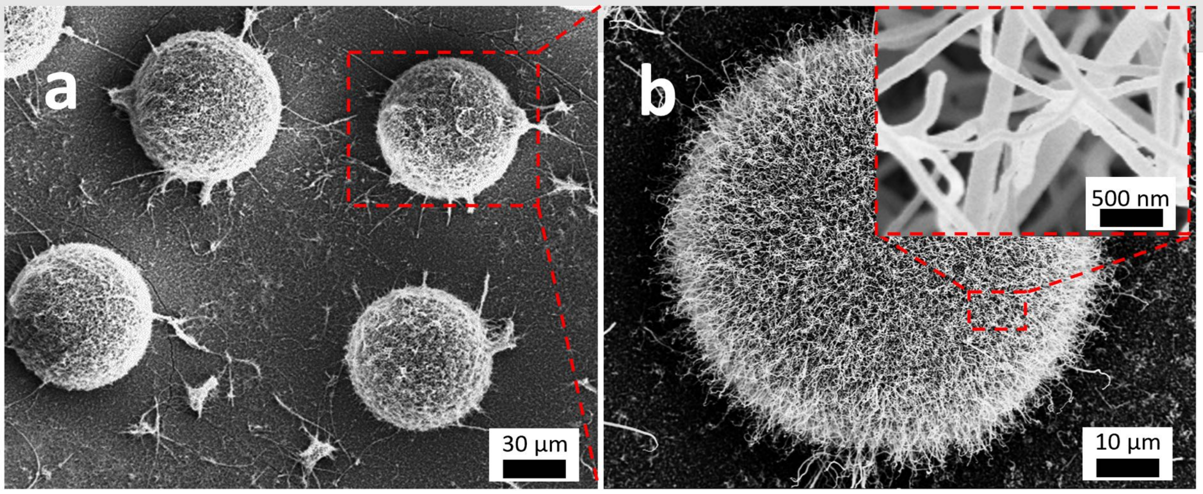

Figure 4.2.3 SEM images of GBs-LDPE matrix coated with SNFs with different scales.

The static water contact angle of the obtained SNFs-GB-LDPE composite material was measured to be 165 ± 2°, with a sliding angle of 8 ± 1°. Though the micro-meter structured GBs were fixed on the substrate surface, the superhydrophobicity was in line with the findings of our previous studies (SNFs coated on a flat glass slide).[218, 230] A side view of the SNFs-GB-LDPE substrates was also presented in Figure 4.2.4.

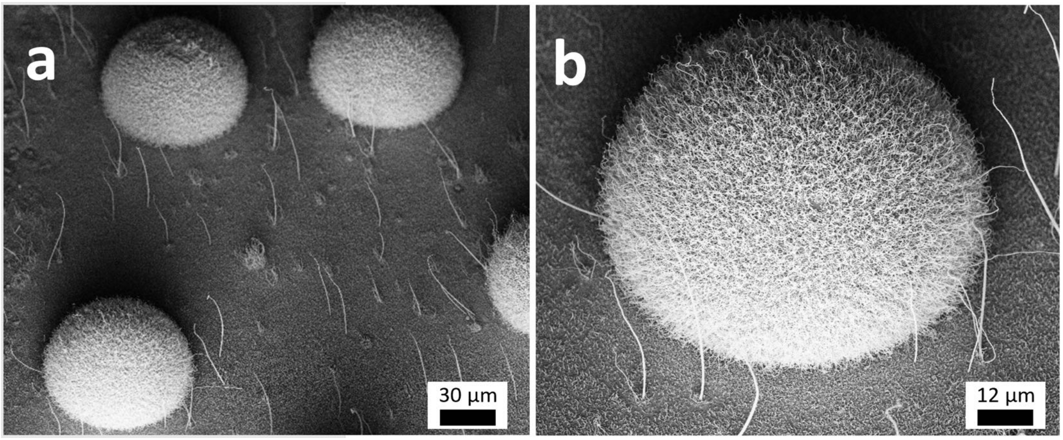

Figure 4.2.3 A side view of the SEM images of GBs-LDPE matrix coated with SNFs with an observation angle of 65°.

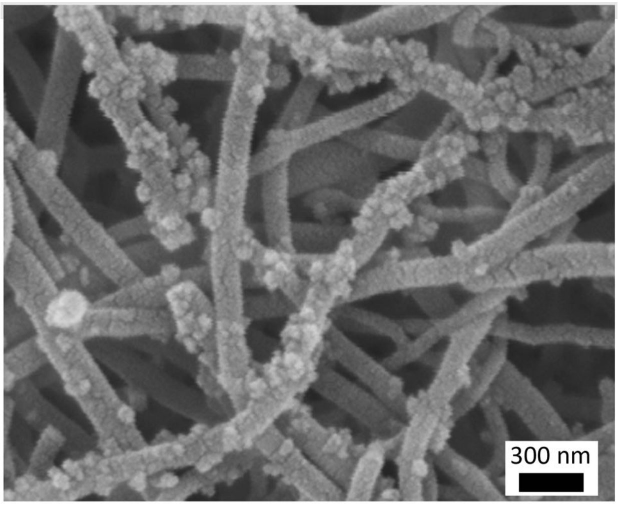

Figure 4.2.4 SEM image of the SNFs@GBs@LDPE with freshly deposited TiO_2 NPs.

Subsequently, the applied oxygen plasma in vacuum chamber turned the SNFs-coated surface completely hydrophilic with a contact angle of less than 10°, which indicated that the surface was hydroxylated. Therefore, the hydroxylated surface became a good deposition carrier for TiO_2 nanoparticles in the next procedure. The well-dispersed TiO_2 NPs deposition on SNFs was achieved through hydrothermal condensation of TiF_4 in ethanol/water (4:1 v/v) at an elevated temperature. The reaction conditions were optimized based on a previous study in our group.[236] After one-hour controlled hydrothermal reaction, TiO_2 NPs were deposited onto SNFs (Figure 4.2.4). The SEM images show a homogeneous distribution of TiO_2 NPs with an average particle size from 40–100 nm all over the surface of SNFs. The particle size was further confirmed by TEM image in Figure 4.2.5a. However, the observed density of TiO_2 NPs in TEM image was lower compared with the one from the SEM image, which was caused by the ultrasonication treatment during the TEM sample preparation.

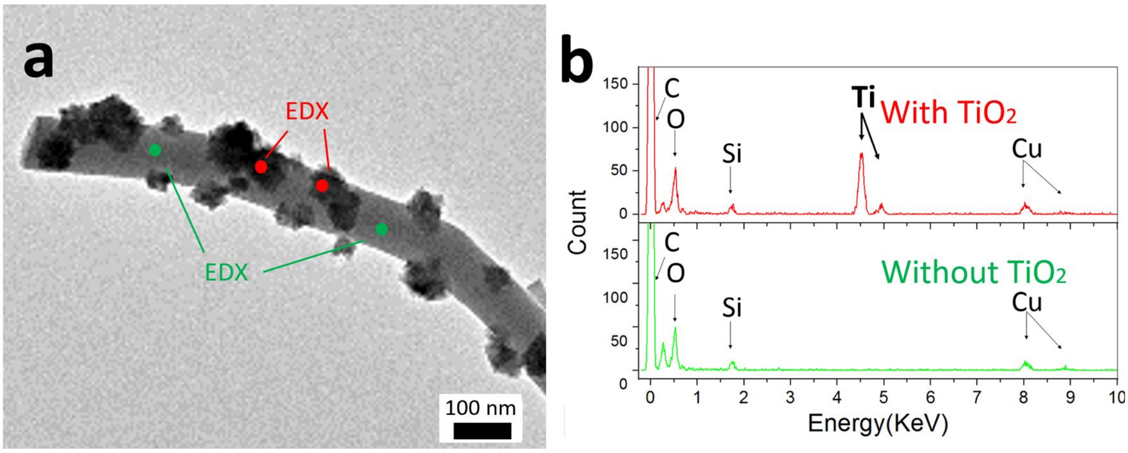

Figure 4.2.5 (a) TEM image of SNFs with deposited TiO_2 NPs and (b) EDX spectra corresponding to (a).

The chemical composition was determined by using energy dispersive X-ray analysis in STEM-EDX. The EDX spectra in Figure 4.2.5b shows that TiO_2 NPs were successfully immobilized on the SNFs. The silicon peak and part of the carbon and oxygen signals originated from SNFs. The majority of the high carbon peak and copper signal came from the formvar/carbon film-coated copper grid of the TEM sample holder. The titanium signal at 4.5 KeV and part of the oxygen signals arise from TiO_2 NPs.

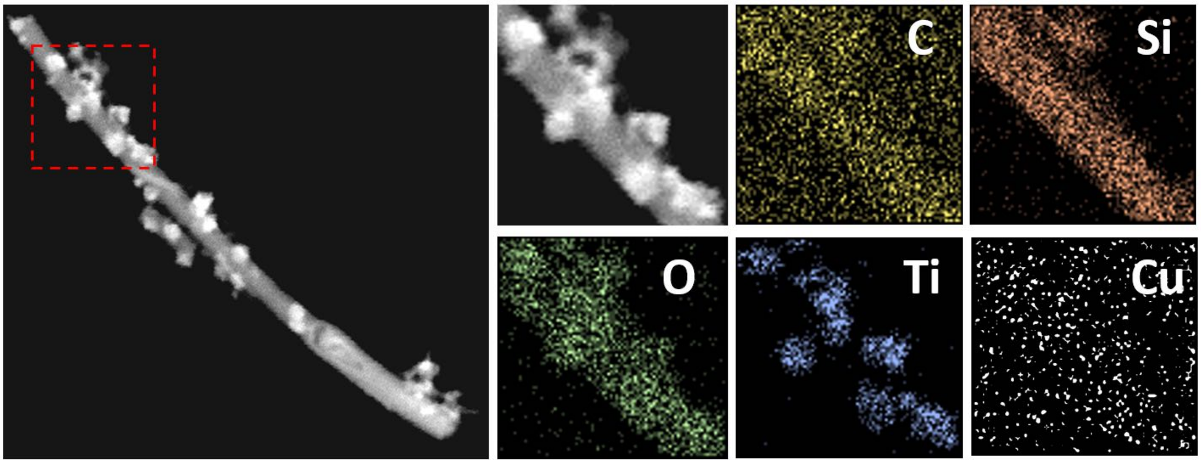

Figure 4.2.5 STEM EDX mapping of a single SNF coated with TiO_2 NPs according to elements.

Element analysis was also additionally performed by STEM EDX mapping of a single piece of TiO_2 NPs deposited SNF, as shown in Figure 4.2.6. We observed the copper signal from the mapping was full of the STEM vision, as the copper is the skeleton material of the sample holder. Carbon signal originated from the polymer film was detected in full vision as well. However, the filament shape was caught which indicated the existence of carbon atoms from SNFs. The silicone signal formed a perfect overlapping of the filament. The spotted titanium signal was a solid proof for the formation of TiO_2 NPs. Thus, the oxygen signal, which was along the filament and overlapped with titanium could be explained.

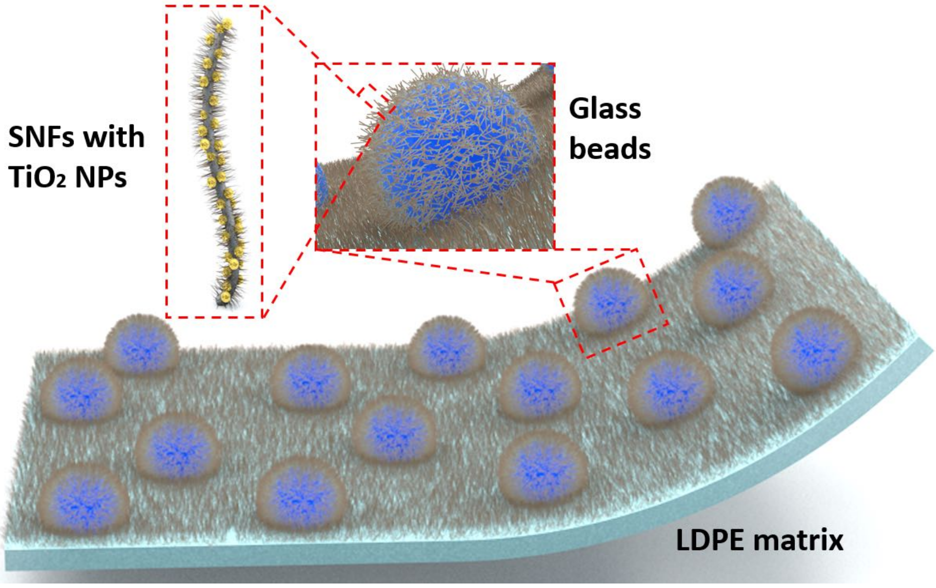

Figure 4.2.6 The schematic illustration of the completed functional substrate.

After the deposition of TiO_2 NPs the surface of the composite material remained hydrophilic. However, a superhydrophobic surface was preferred as we designed. As a result, a surface modification to tune the wettability on the surface was inevitable. Here a simple strategy was applied as we did for SNFs gas phase coating. The substrate was further hydrophobized with the same precursor (ethyltrichlorosilane). In this procedure, reaction conditions were slightly changed. The amount of precursor applied was 100 µL and the reaction time was shortened to 20 min. A low relative humidity of 30% was needed. Higher relative humidity was tried but it ended up with fully grown silicone layer, which inhibited the photocatalytic activity to some degree. After the hydrophobic modification, the functional substrate was switched from superhydrophilic to superhydrophobic, with a slightly higher contact angle (168 ± 1°) and similar sliding angle (8.5±1.5°). The unnoticeable improvement on contact angle was due to the higher surface roughness after two times of hydrophobic coating. Thus, a LDPE matrix with embedded GBs, coated with SNFs, and deposited TiO_2 NPs was achieved. The completed composite material was superhydrophobic and contained the functionality from TiO_2 NPs. Hereinafter the as-prepared superhydrophobic composite is referred to as TiO_2/SNFs-GBs-LDPE(illustrative graph in Figure 4.2.6).

4.2.2 Self-cleaning Ability

With this prepared novel composite material, the self-cleaning property is expected to occur by two principal mechanisms: the superhydrophobicity of the surface was used to allow mechanically removing of impurities by a water flow or drops due to the low adhesion and non-wettability of the surface; secondly, TiO_2 NPs are known to have photocatalytic activity and, therefore, catalyse the degradation of any attached organic contaminants under illumination.

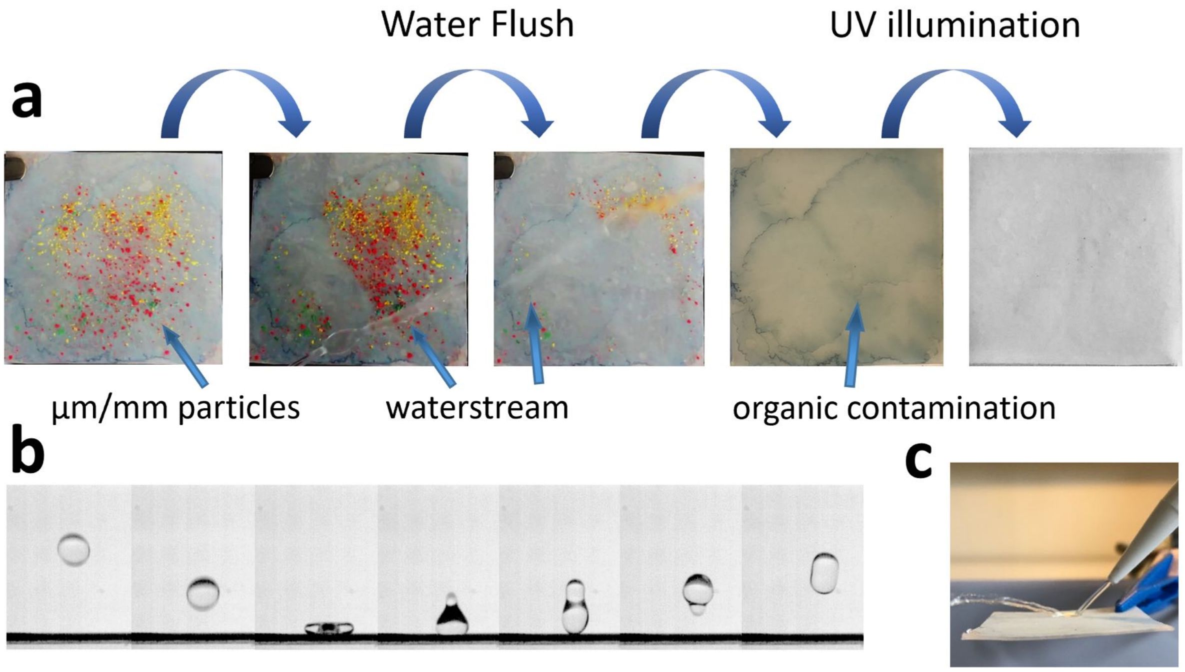

Figure 4.2.7 Self-cleaning properties of the functional substrate. (a) Image of the anti-fouling process. The substrate was contaminated by ground chalk particles and drop casted methylene blue ethanol solution. (b,c) Water repellence effect captured by b) high-speed camera and c) normal camera.

In Figure 4.2.7a, a substrate was contaminated with µm/mm-sized chalk particles and drop-cast methylene blue (MB) ethanol solution (MB in water solution could not wet the surface and no dyeing contamination happened). Flushing the surface with a flow of water led to the removal of the chalk particles (Videos are provided in the supporting information of our publication on *Small*). Rebounding of water was observed, proving the hydrophobicity of the substrate. We recorded the water repellency with a high-speed camera that clearly showed a rebound behaviour of a 10-µL water drop (Figure 4.2.7b) A normal camera was used to catch the water stream bouncing on the surface in Figure 4.2.7c and videos were provided on Wiley publisher as well. The remaining organic dye contamination could not be rinsed off. In such a scenario, the photocatalytic property was expected to function. The TiO_2 NPs decomposed the dye into small molecules, which were soluble in water under UV illumination. After rinsing again with water stream the original contamination became invisible on the surface of the functional substrate. The mechanism how TiO_2 NPs decompose the contaminants was well studied in many researches. The TiO_2 NPs, have a band gap from 3.0-3.2 eV, according to the crystal structures (anatase, brookite, or rutile), crystallinity, particles sizes, etc. Usually photo-irradiation (energy > 3.2 eV) leads to band gap excitation, resulting in electrons into conduction band (CB) and holes in valence band (VB). These photo-induced electrons and holes work as electron donors and acceptors on the photocatalyst surface, enabling the photocatalytic reaction. In our material surface, the photocatalysis causes the degradation of contaminants.[244]

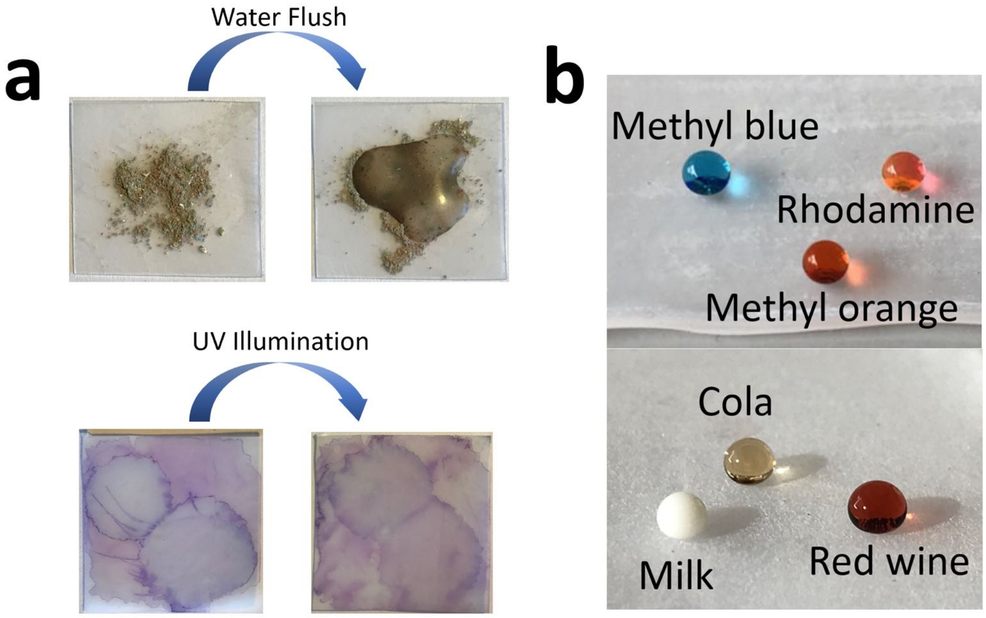

Figure 4.2.8 (a) Self-cleaning test on non-functionalized substrate for comparison. (b) The non-wettability of various liquids on the substrates.

The comparison experiment result was shown in Figure 4.2.8a. As observed, the water stream caused an accumulation of water on the surface, mixed with dirt. UV illumination was applied. However, it turned out no obvious removal of dye contamination.

Moreover, the surface of the functional substrate was free of sticking of the various liquids, such as aqueous solutions or other liquids like Cola, red wine or milk (Figure 4.2.8b).

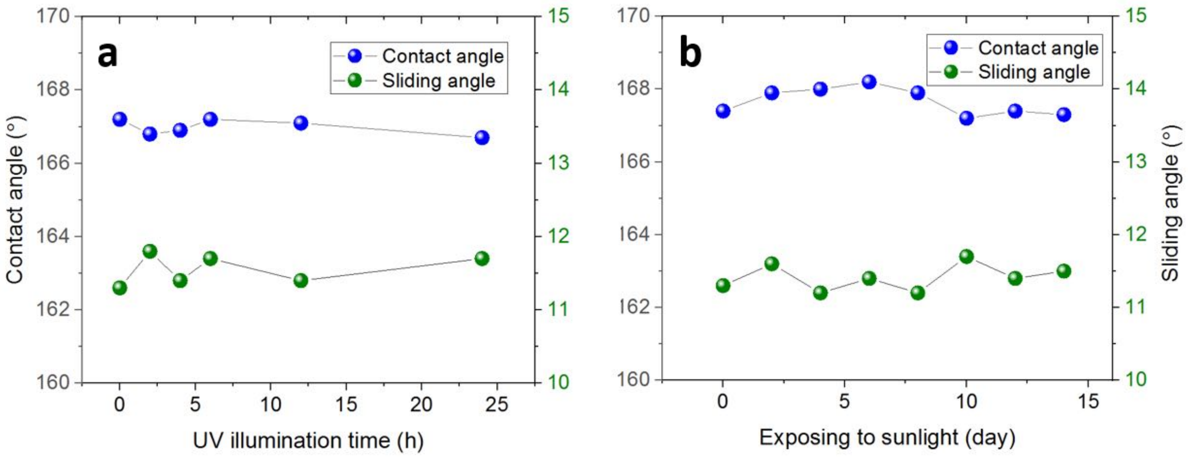

Figure 4.2.9 The stability of the functional substrate characterized by the change of the water contact angle and sliding angle after exposing to (a) UV illumination (350 nm, 4.5 ± 0.2

mW/cm^{-2}) for 24 hours; (b) daily sunlight in 2 weeks(season time: October 8th to 22th in Zurich, Switzerland).

The stability in life span is essential for the applications of self-cleaning material. To demonstrate the long-term stability, the water contact angle (CA) and sliding angle (SA) were measured as a function of time under continuous UV irradiation (350 nm, 6.32 mW/cm^{-2}). As shown in Figure 4.2.9a, the superhydrophobicity of the substrate did not change for 24 hours, with the CA remained above 166 ° and SA below 12°. When exposed to the real environment under daily sunshine (middle autumn in Switzerland), the CA and SA showed almost no change for 2 weeks (Figure 4.2.9b). The slight drop of the contact angle was probably the result of the attachment of dust from the atmosphere. Both experiments confirmed the durability of the superhydrophobicity of the material.

When the substrate was contaminated by oleic acid in ethanol solution (3:7 v/v), which was able to wet the superhydrophobic surface, the water contact angle dropped from 168° to 67°. Notably, after UV illumination at 350 nm (light intensity: 6.32 mW/cm^{-2}), the water contact angle turned back to the original value ~ 168°. This is ascribed to the deposited TiO_2 NPs as the photocatalyst in this composite material. Free radicals were generated during the electron transfer induced by UV illumination, which led to the degradation of oleic acid. The degradation products usually were smaller and water-soluble molecules could be rinsed away by water.[245, 246]

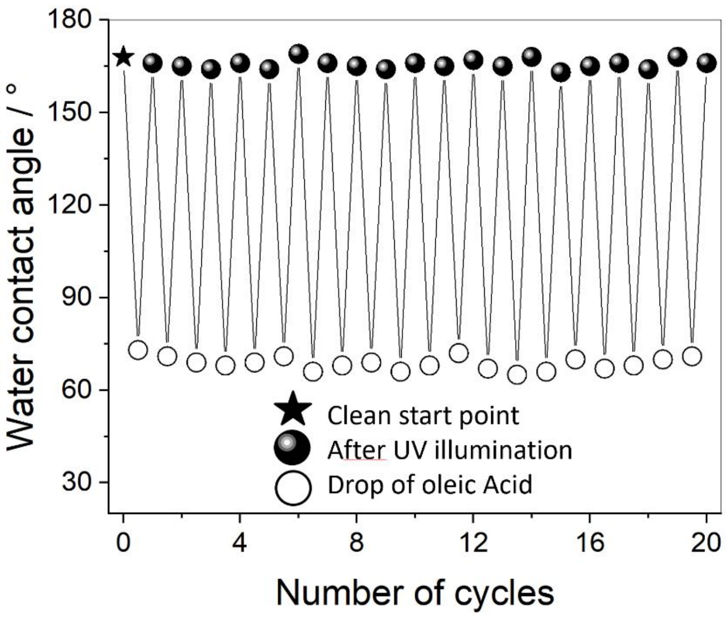

Figure 4.2.10 The recyclability of the substrate characterized by the contact angle after contaminated by oleic acid and UV illumination for 20 cycles.

After 20 cycles of cyclic oleic acid contamination and UV irradiation, the superhydrophobicity of the substrate remained stable (Figure 4.2.10) as well as morphology (Figure 4.2.11).

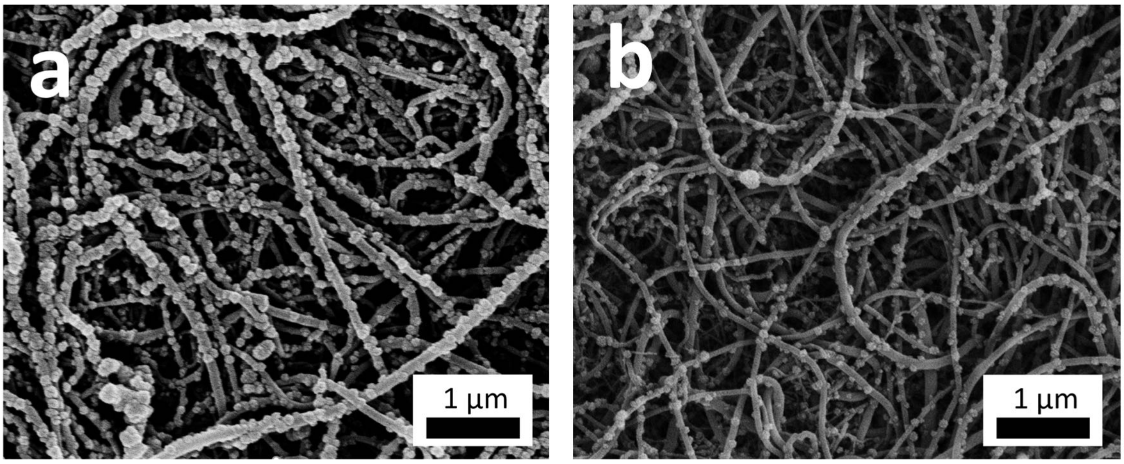

Figure 4.2.11 The morphology before (a) and after (b) 20-time of oleic acid contamination and UV irradiation repeat.

Surface adhesion of the TiO_2/SNFs-GBs-LDPE composite after cyclic UV irradiation was determined by the water sliding angle (SA). In Figure 4.2. After 20 cycles of UV irradiation, SA of the composite remained around 10.5°.

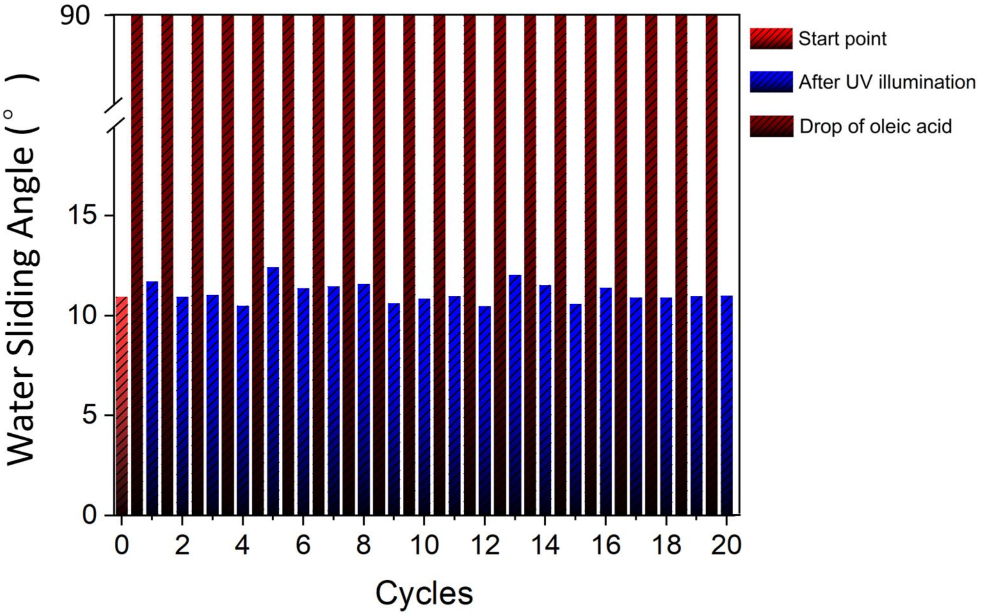

Figure 4.2.12 The sliding angle change during the 20 times of contamination-illumination cycles.

The photocatalytic property of the functional substrate was verified by the degradation test of methylene blue (MB) under UV irradiation at 350 nm (intensity: 6.32 mW/cm^{-2}) in a methanol/water solution (1:1 in volume in order to wet the material surface completely) with oxygen bubbling (30 mL/min) for 2 hours. A Perkin-Elmer Lambda 650S, UV-Vis spectrometer, was used to measure the absorbance ranging from 350 nm to 900 nm, in which the maximum absorbance peak was at 665 nm. The light source – eight light bulbs (SNE Ultraviolet Co, USA) with emission wavelength at 350 nm – showed very little overlap compared with the absorption spectrum of MB as we demonstrated in Chapter 4.1.

Figure 4.2.13a exhibited the absorption behaviour of MB during degradation in the presence of different substrates and the reference, respectively. There was only a small reduction of MB absorbance in the self-degradation (under UV illumination) without any substrates. After 2 h, the relative absorbance dropped by about 10.5%. To demonstrate the influence of SNFs on the loading amount of TiO_2 NPs and the consequent photocatalytic ability, a substrate GBs-LDPE without SNFs was treated with oxygen plasma, and subsequently, deposited with TiO_2 NPs according to the same hydrothermal reaction. The result showed that this substrate reached a reduction of relative absorbance of MB about 23.4% after two hours. The two substrates with TiO_2 NPs on SNFs, which were TiO_2/SNFs-LDPE (without the embedded GBs) and TiO_2/SNFs-GBs-LDPE, compared to these without the growth of SNFs, achieved a much higher photocatalytic activity resulting in a value of 88.9% and 89.3%, respectively. The observation confirmed that the exploiting of GBs on LDPE does not change the photocatalytic performance. It was concluded in our previous study that with additional surface roughness created by SNFs, the surface area was much higher than the one without SNFs. The multiplication factor of the additional surface area was ca.13.[237] Thus, this led to a relatively higher loading amount of TiO_2 NPs on the substrate surface, which significantly lowered the MB absorbance after UV irradiation.

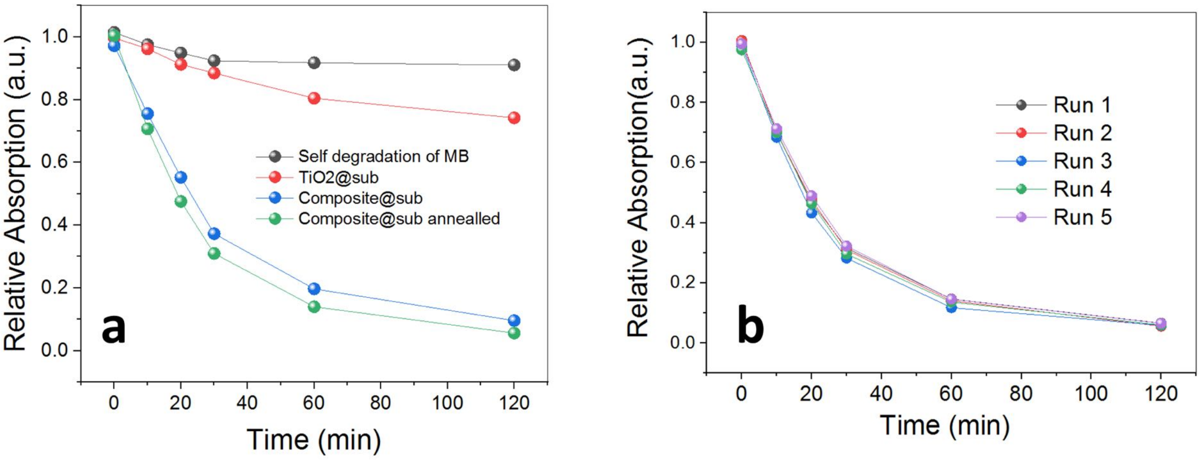

Figure 4.2.13 (a) The photodegradation of MB solution (1 ppm MB in 1:1 methanol-water mixture) in the presence of functional substrates with one side area of 6 cm^2 under UV irradiation at 350 nm (blank = degradation of MB without any substrate; red = degradation with TiO_2-GBs-LDPE; green = degradation with TiO_2/SNFs-LDPE; blue = degradation with TiO_2/SNFs-GBs-LDPE). (b) The recycling experiment of the degradation of MB with TiO_2/SNFs-GBs-LDPE substrate for five runs.

To further confirm the loading amount of TiO_2 NPs, the titanium content was measured by an absorbance spectrometry at a wavelength of 410 nm. Substrates were immersed into high concentration sulfuric acid at 110°C for 30 min in order to dissolve all TiO_2 NP. The solution was then diluted 10 times for measurement. The standard line of absorbance against concentration was calibrated with a commercial standard solution. The substrate without SNFs had a much less loading amount of TiO_2 NPs (about 0.183 mg/cm^2) relative to the functional substrates with SNFs of 1.85 mg/cm^2 for TiO_2/SNFs-GBs-LDPE and 1.87 mg/cm^2 for TiO_2/SNFs-LDPE due to the extended surface area provided by the SNFs.

It was certified that the functional substrate TiO_2/SNFs-GBs-LDPE exhibited a stable photocatalytic activity after 5 MB degradation experiments (Figure 4.2.13b).

4.2.3 Abrasion Tests

Practical applications of superhydrophobic materials are often limited due to the fragility of the nanoscale roughness, which is the drawback for most of the superhydrophobic materials. Often, a soft mechanical impact leads to a substantial decrease in the contact angle or even the total loss of the water-repellency property. However, the contact forces on material surface, such as scratching, pressing, or rubbing, are unavoidable in most of the applications. Mechanical resistance of the superhydrophobic materials remains one of the major challenges in this field and hinders a broader utility.

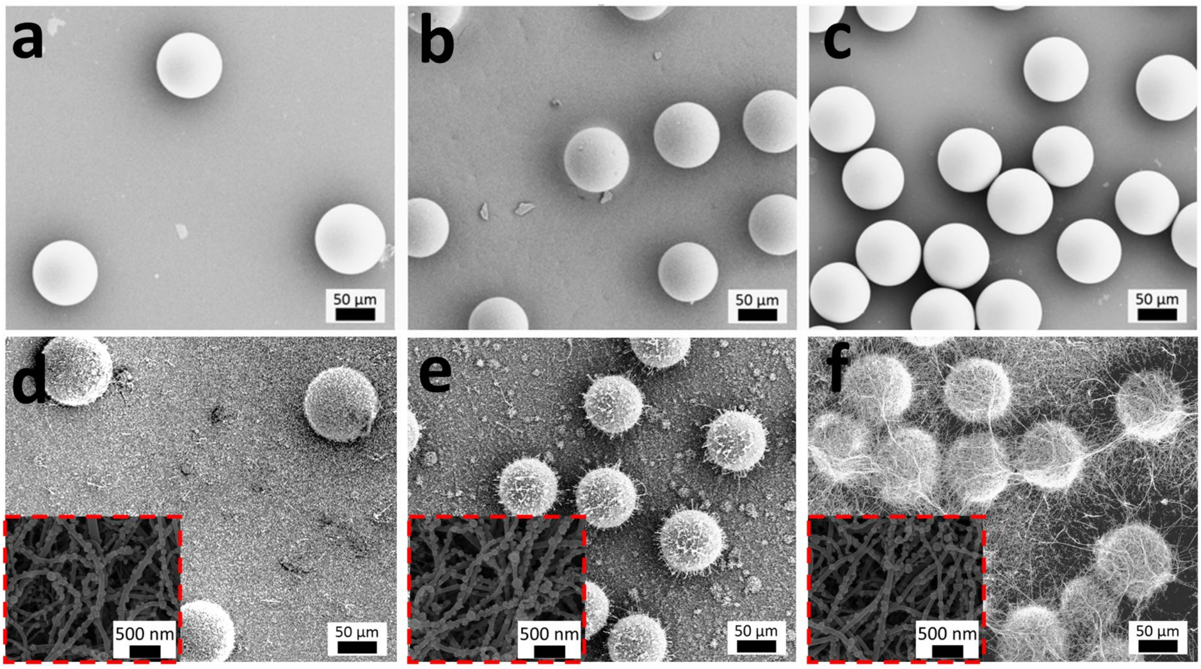

Figure 4.2.14 SEM images: (a-c) GBs drop cast LDPE templates with different density of 6.5, 32, 70 units of GBs/mm^2; (d-f) The Functional substrates with these three densities of GBs (LDPE templates further coated with SNFs, deposited with TiO_2 NPs and hydrophobic modification).

Therefore, we further investigated if the micro-meter superstructure does protect the nanoscale SNFs. The 75-µm glass beads (GBs) partially embedded into the LDPE matrix enabled such a superstructure, as the embedding depth was around 21 µm and more than half of the sphere of the GB was exposed. The drop-casting method was introduced earlier in this chapter. By changing the GBs concentration in the ethanol suspension, the density of the drop-cast GBs on LDPE was controlled. To evaluate an ideal density, we tried three different densities: 70, 32, 6.5 units of GBs/mm^2 (Figure 4.2.14a-c) to compare. The LDPE substrate was heated to 165°C to be above the glass transition temperature. As the LDPE film turned to be fluidic and viscous, GBs sank into the polymer matrix with a certain depth and were fixed in the matrix by cooling down to room temperature. Subsequently, the SNF-coating, TiO_2 NPs deposition, and hydrophobic treatment are executed as described earlier (Figure 4.2.14d-f).

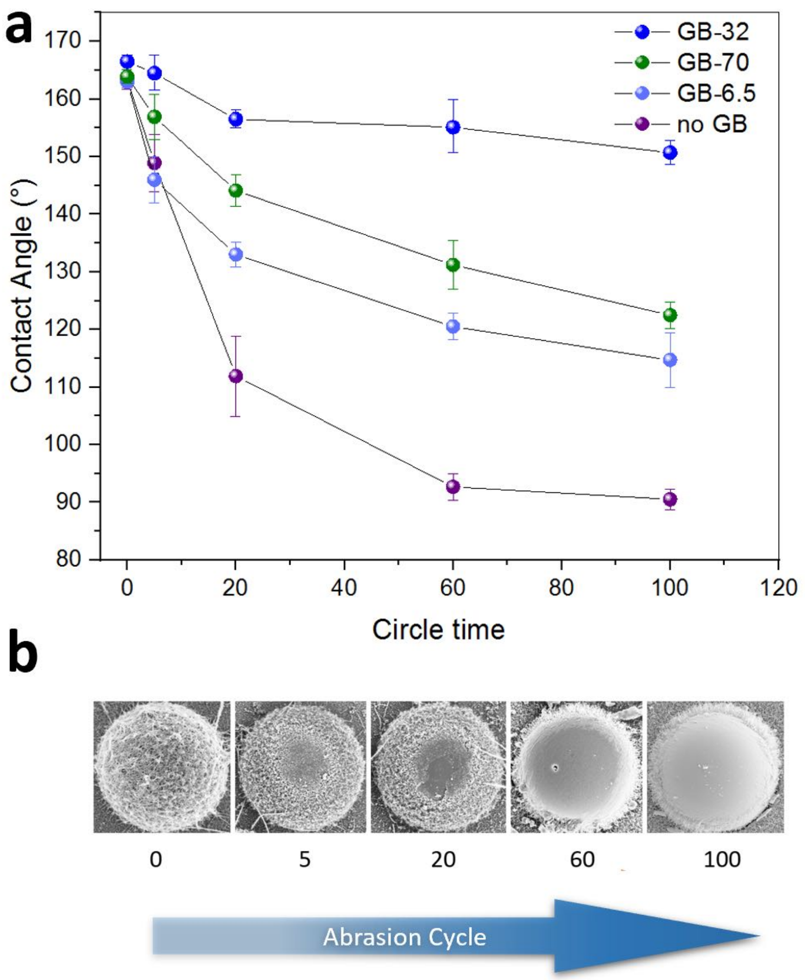

Figure 4.2.15 (a) Contact angle change trend of different functional substrates according to abrasion cycle time. (b) SEM images of GBs with incremental abrasion cycles.

The mechanical abrasion tests were conducted by using an AB5000 Washability Tester. A sponge abrasion head covered with a nitrile glove at a pressure of ca. 1.5 kPa was used in the abrasion test (the extra loaded weight was 200 g). The abrasion head moved back and forth along a straight track, pressing on the tested substrate with an effective rubbing distance of 6.5 cm for one direction movement. Subsequently, water contact angle of each tested substrate was measured as a function of the abrasion cycles. In Figure 4.2.15a, it is shown that the substrates with GB layer possessed a higher abrasion resistance. The water contact angle decreased by the abrasion cycles. The substrates without GBs showed a fast drop on non-wettability. After 100 cycles, it lost its superhydrophobicity completely with a CA dropped from 164° to 91° (though still hydrophobic due to the low surface tension of the silicone nano-layer), while the substrates with GBs exhibited a higher mechanical durability. The substrate GB-32 (with a middle density of GBs cast) was observed to own the best abrasion resistance, showing a CA of 154° even after 100 cycles. Thus, its superhydrophobicity was well maintained (CA > 150° by definition). Meanwhile, the GB-70 and GB-6.5 substrates had a decrease of CA of about 42° and 50°, respectively.

The GBs formed a "hill-like" microscale roughness, which fundamentally contributed to the enhanced mechanical durability of the functional substrates. Here, the fragile nanoscale SNFs were well protected by the GBs from contacting forces, like scratching, rubbing, and pushing. The SNFs among the GBs remained stable on the functional substrates after mechanical abrasion compared to the one without the protection from drop-cast GBs. A low density of embedded GBs on the surface (GB-6.5) leads to weaker hierarchical protection and results in a fast decrease on hydrophobicity, since a lot of SNFs were directly exposed to contact forces. On the other hand, the GB-70 and GB-32 substrates showed a much better abrasion resistance. At higher density, GBs could prevent the SNFs coated on the region among the GBs on LDPE surface and on the lower hemisphere of GBs from the damage of mechanical abrasion. However, GB-70, which has the highest embedded GB density, had a higher surface area from the GBs which were directly exposed to the abrasion forces. Stem from the larger exposure area and the intrinsic hydrophilicity of GBs surface, the CA of high-density cast substrate GB-70 decreased more than the middle-density cast one GB-32 at the same cycle number. In Figure 4.2.15b, the exposure area on the top of GBs was provided by SEM images according to the abrasion cycles.

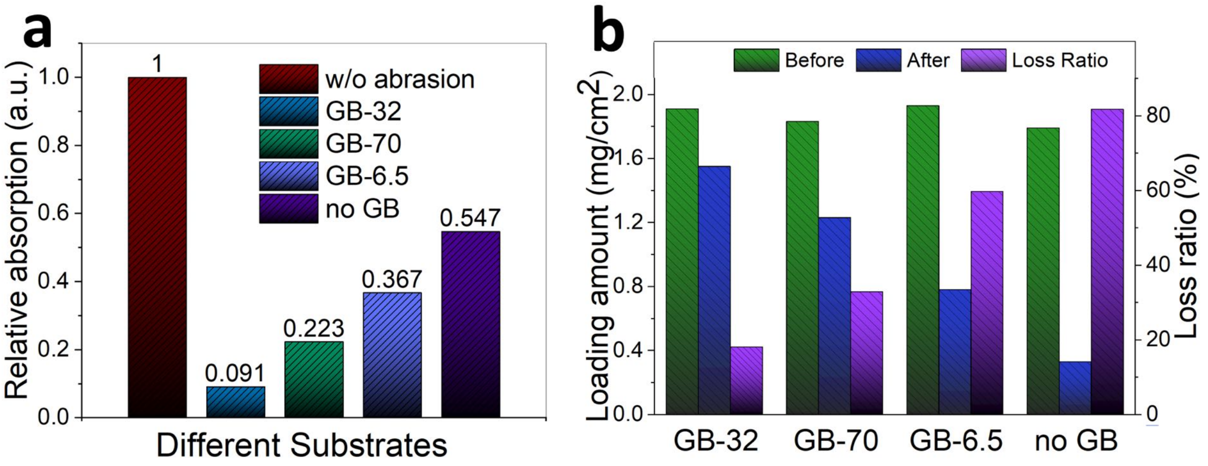

Figure 4.2.16 (a) The photocatalytic performance of two-hour MB degradation by different substrates after 100 cycles of abrasion. (a) The loading amount of TiO_2 NPs on different substrates before and after 100 cycles of abrasion and the loss ratio correspondingly.

Besides the non-wettability, the photocatalytic activity of the substrates was also determined after the abrasion test to further confirm the protection effectiveness of the hierarchical structure. The same photo-degradation of MB experiment was conducted again, and the relative absorbance was measured before and after the photocatalytic reaction (Figure 4.2.16a). In consistence with the CA change measurement, the substrate without GBs protection lost most of the photocatalytic activity among all substrates, followed by the substrate with low-density cast GBs. The substrates with a high and middle density of casted GBs exhibited similar photocatalytic activity due to the maintenance of the SNFs among the GBs for both substrates, regardless of the density of the GBs. The retained amounts of TiO_2 NPs on SNFs were determined according to the same method described in our previous research. Substrates were immersed into a high concentration of sulfuric acid (50%) at 110 °C for 30 min to dissolve all TiO_2 NPs into titanium ion. A calibrated standard line of absorbance to concentration was made by testing a standard titanium solution in a spectrophotometer. The remaining titanium was recorded for all substrates in Figure 4.2.16b. The result corresponded with the photocatalytic performance.

4.2.4 Anti-bacterial Tests

TiO_2 as an antibacterial material has attracted a lot of attention in the last decades due to its excellent photocatalytic activity.[247, 248] Researches have discovered the TiO_2 photocatalysts decrease the expression of the genes of bacteria that are involved in the synthesis of signal molecules.[249]

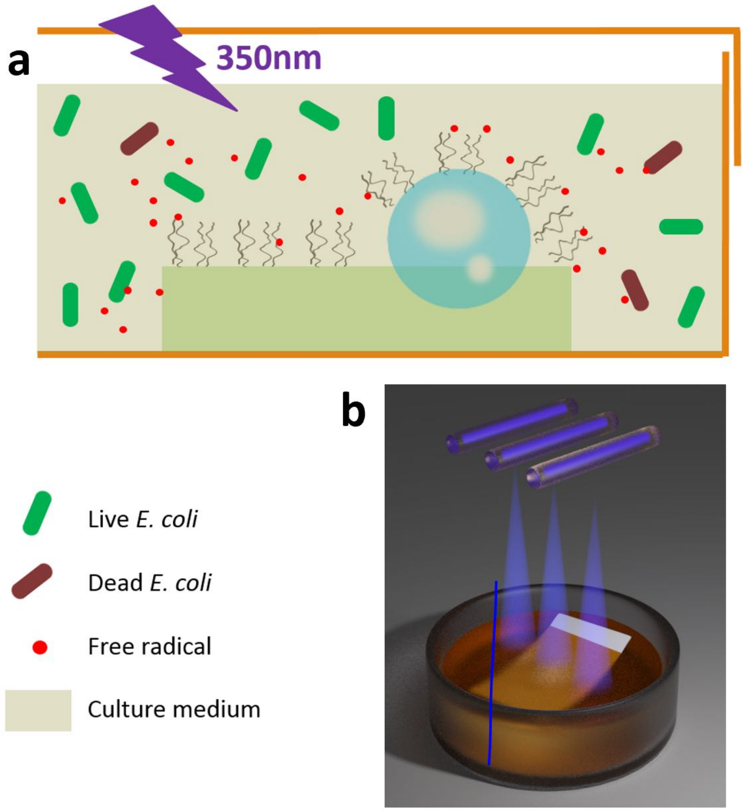

Figure 4.2.17 (a) Schematic illustration of the anti-bacterial experiment. (b) Illustrative graph of a tested sample exposed under UV illumination.

Therefore, antibacterial activity could be an additional advantage of the as-prepared functional material due to the induced TiO_2. In order to demonstrate and compare the anti-microbial ability, different substrates were used in the designed experiment. In this section, all LDPE films were functionalized with embedded GBs before differential treatment. LDPE with bare TiO_2 (TiO_2/GBs-LDPE), LDPE with TiO_2@SNFs coating (TiO_2/SNFs-GBs-LDPE), and LDPE as blank control (GBs-LDPE) were tested in *E. coli* bacterial solution. All vessels used in the tests were sterilized by autoclaving before use and stored in hygienic environment. The substrates were immersed into 10 mL *E. coli* solution and incubated under darkness or 350 nm UV illumination for 90 min (intensity: 6.32 mW/cm^{-2}) at room temperature. Figure 4.2.17a schematically illustrated the mechanism of how the functional substrates were expected to work as an anti-bacterial material. The sketch in Figure 4.2.17b shows how the sample was immersed in bacterial solution and exposed under UV illumination.

Next, we followed *E. coli* cell propagation at 37 °C during 210 min by measuring absorption at 600 nm (OD_{600}). Besides the OD_{600} tracking, five microliters of bacterial solution were taken out after the 90-min incubation and diluted with LB medium to 50 µL and spread on agar plates for overnight growth at 37°C.

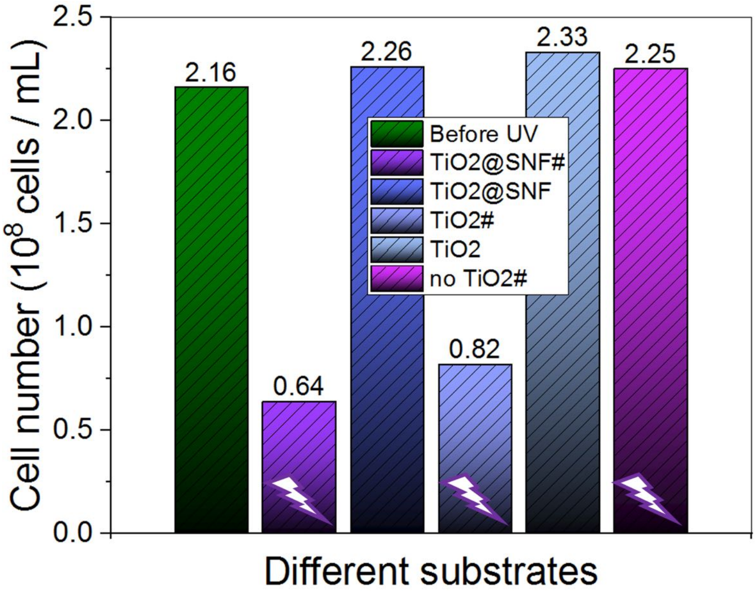

Figure 4.2.18 (a) Schematic illustration of the anti-bacterial experiment. (b) The cell concentration of the solutions with different substrates after 90 min under darkness or UV illumination at room temperature. Lightening sign represents the adoption of UV illumination for the substrates.

For the substrates containing TiO_2, after UV irradiation, they exhibited stronger antibacterial effect than those without TiO_2. The *E. coli* concentration decreased obviously after 90 min illumination (Figure 4.2.18). Due to more loaded TiO_2 NPs caused by the enlarged surface area of SNFs as we concluded from the last section, the substrate with TiO_2@SNFs showed the highest antibacterial activity (the concentration of *E. coli* after 90 min UV illumination was the lowest). The substrates containing TiO_2 without UV illumination or that without TiO_2 (control set) but under UV illumination showed no noticeable changes in bacterial inhibition. The propagation inhibition was collected and exhibited in Figure 4.2.19, which turned out to correspond with the results shown in Figure 4.2.18. Both experiments proved that substrates with TiO_2 under UV illumination possessed an inhibition effect on the propagation of *E. coli*.

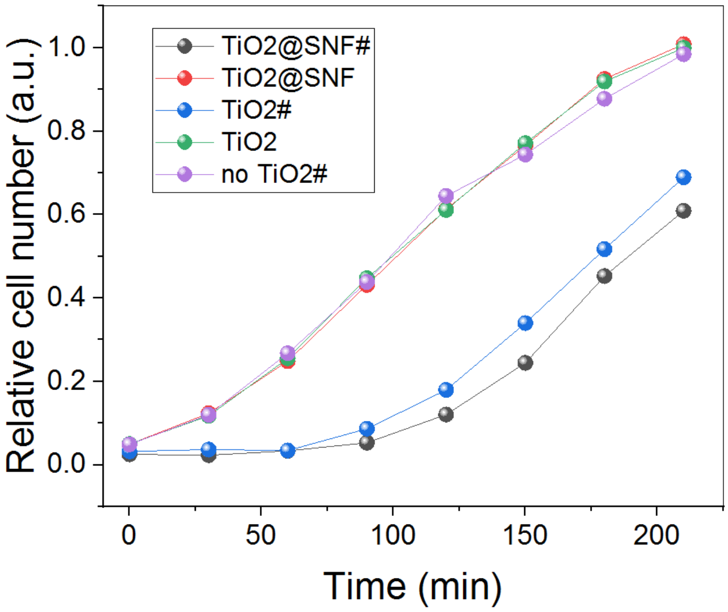

Figure 4.2.19 (a) Schematic illustration of the anti-bacterial experiment. (b) The cell concentration of solutions with different substrates after 90 min under darkness or UV illumination at room temperature. (c) The bacterial growth curve (OD_{600}) after 90 min of darkness or UV illumination.

Bacteria were not directly killed by the 350 nm UV radiation, which was prerequisite of the experiment. From literature, it was reported wavelengths between 250 and 300 nm were most effective at directly decomposing the cell structure of *E. coli*, which led to the inhibition of cell growth. The wavelength at 350 nm showed no direct damage to cell structure and propagation.[250] The mechanism for killing the bacteria is based on free radicals generated by photoactive TiO_2, damaging the cell membrane structure and causing the subsequent leakage of the inner content of *E. coli*. The same phenomenon was observed in other TiO_2 materials. Bekboelet et al. adopted anatase TiO_2 suspension under 300–400 nm irradiation to obtain the inactivation of *E. coli* due to the generated hydroxyl radicals.[251] Similarly, Ag/BiOI and C_{70}-TiO_2 composite were used as visible-light-driven photocatalysts, which could have a wider range of applications compared with only UV-driven catalysts. An apparent reduction of potassium ion (K^+) released from *E. coli* was observed by Fang et al. by using Ag/BiOI composite.[252] Ouyang et al. found that C_{70}-TiO_2 under visible light irradiation produced •OH radical from VB holes oxidization and O_2^-• from CB electron transfer, which resulted in an inhibited growth of *E. coli*.[253] It was further proved that the radicals generated by photocatalysts targeted mainly on lipids and proteins of *E. coli*.[254]

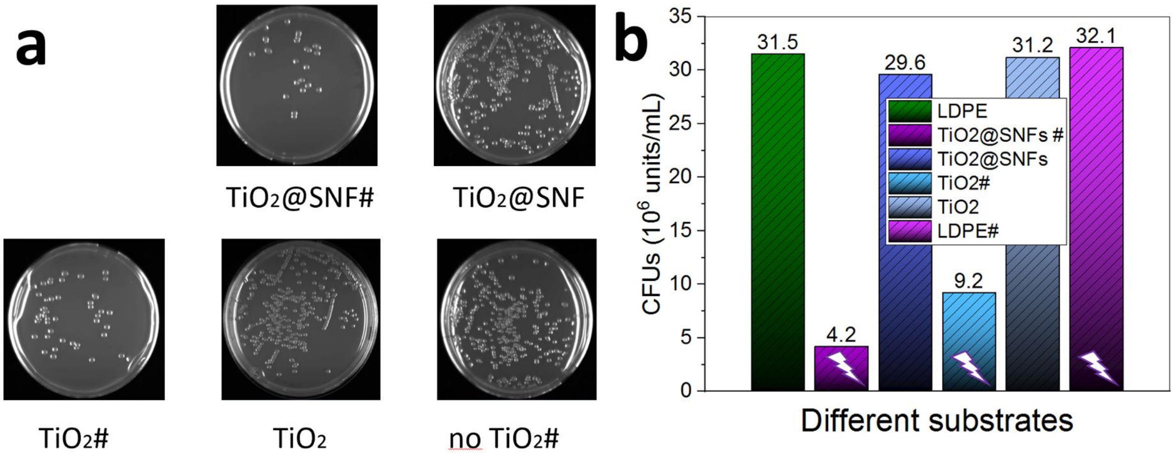

Figure 4.2.20 The colony forming units (CFUs) resulted from Incubation of E. coli in agar plates for 12 hours at 37 °C. The initial solutions were taken from the liquid media after 90 min under darkness or UV illumination cultivation with different substrates.

The test done on agar plates enabled us to get a better visual contrast. The colony forming units (CFUs) on agar plates were counted (Figure 4.2.20a). The bacteria suspensions were collected after the 90-min under UV or darkness, diluted by 1000 times, out of which 5 µL was brushed homogeneously on agar plates for overnight growth at 37°C. The CFUs were determined as shown in Figure 4.2.20b. The results from the CFU counting were consistent with the OD_{600} trend curves provided earlier.

Thus, the successful fabrication of the novel composite material proves its broad utilities as a self-cleaning material. The superhydrophobicity originating from the SNF coating prevents all kinds of aqueous contaminations due to the non-wettability. The composited TiO_2 NPs work as the photocatalyst under UV light to degrade any oily contaminants on the surface which cannot be removed by water rinse. The biggest problem for superhydrophobic surface, the mechanical durability, was well solved with the creative hierarchical structure, which consists of an LDPE film with embedded GBs.

For further development of the self-cleaning materials, other types of photocatalysts are recommended. The N-doped TiO_2 NPs could be a good candidate as they respond to visible light together with UV light, which can largely broaden the application range in life. New technologies, such as 3D printing, can assemble hierarchical structures much more easily, leading to a more economical production in the industry.

4.3 Multifunctional AuNPs-SNFs Composite Material

4.3.1 Characterization of Functional Substrate of AuNPs@SNFs

Microscope glass slides were chosen as the substrate because they match with the size of the experimental set-up (in Figure 4.3.1). Besides, in the later functionality of SERS detection, an adequate transparency was also required for substrates.

Figure 4.3.1 Schematic representation of the reaction chamber for the growth of SNFs.

In this project, ethyltrichlorosilane (ETCS) $CH_3CH_2SiCl_3$ was used as the precursor for the formation of SNFs. An earlier developed method from our group was applied for the growth of SNFs on slides.[255] The experiment conditions were optimized in order to obtain a homogeneous and dense SNFs coating layer since in the further steps SNFs work as a support for loading gold nanoparticles. In both applications of SERS detection and catalysis, a surface of homogeneous roughness is critical for objectively and accurately evaluate the performance. Non-homogenous surface usually lowers the average SERS intensity gathered from a certain region, leading to an inaccurate estimation of the surface attachment behaviour. The SEM images in Figure 4.3.2a,b and the EDX spectra (Figure 1e) show the homogeneous formation of the SNFs. The SEM images in Figure 4.3.2c,d and the EDX spectra (Figure 1e) show the homogeneous formation of the SNFs.

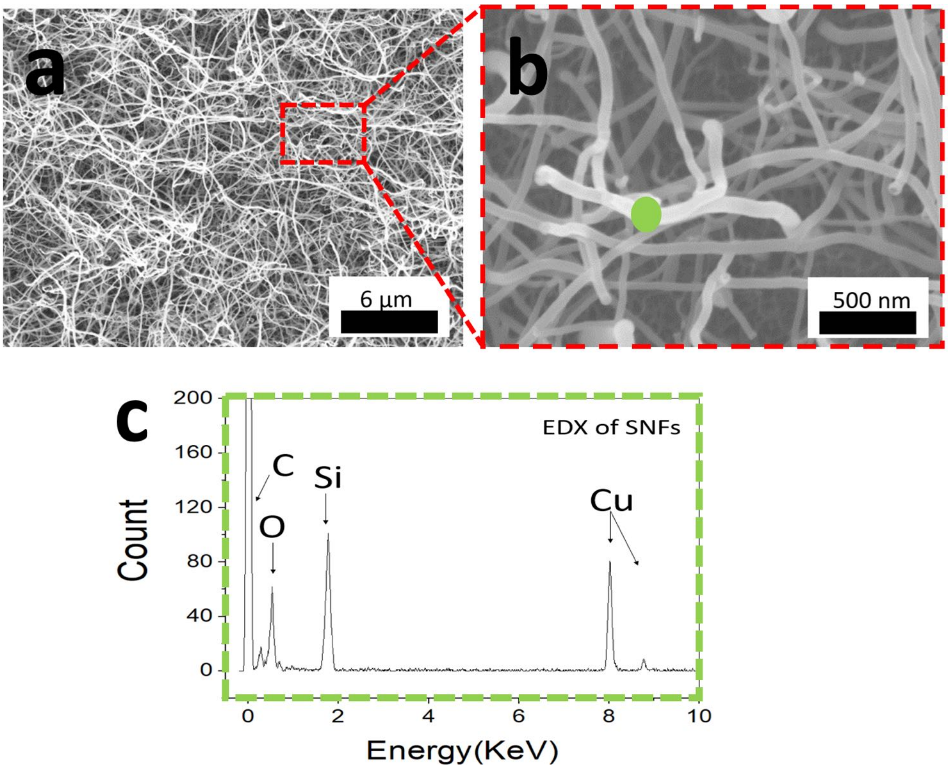

Figure 4.3.2 (a,b) SEM images of SNFs with different scales. (c) STEM EDX spectra of SNFs of the green spot in (b).

To facilitate the loading of AuNPs, the surface affinity of SNFs must be changed. The freshly coated SNFs layer was superhydrophobic, so that most of the deposition or surface nucleation behaviour occurs in aqueous solution could not happen on the interface of SNFs and water. A few steps of surface modifications were therefore indispensable. All the procedures for this purpose were summarized in Figure 4.3.3.

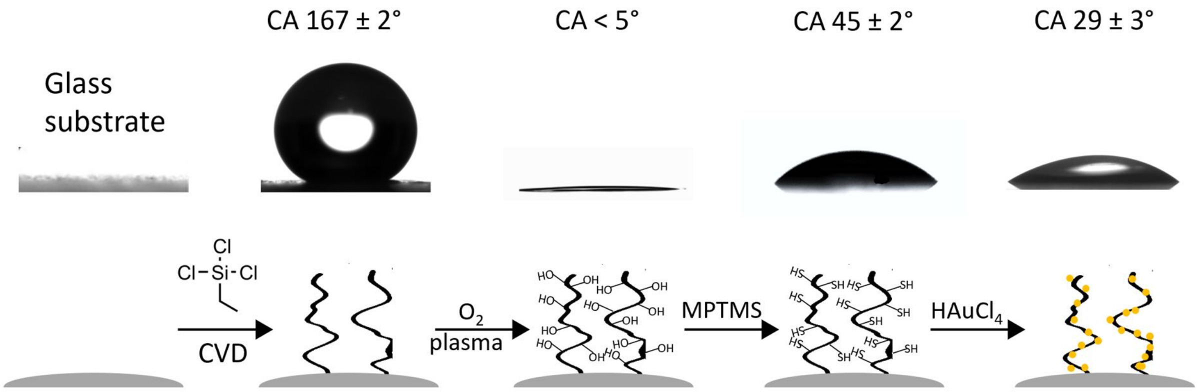

Figure 4.3.3 Schematic illustration of the steps for the surface modification of SNFs and deposition of AuNPs with the changes of the water contact angle values of each step.

In order to further functionalize the SNFs, oxygen plasma was applied to plant hydroxyl groups on the surface and switch it from superhydrophobic into superhydrophilic. A static water contact angle (CA) measurement exhibited the CA was reduced from 167° to less than 5°, which indicated the surface was hydroxylated. The generated hydroxyl groups enabled the original chemical inert surface with reactive sites. Thus, further chemical modification could be possible and feasible.

According to hard-soft acid-base concept, AuNPs have a strong affinity to sulfur.[256] Thiol groups were introduced to the surface of SNFs to immobilize AuNPs.[257-259] A linker molecule (3-Mercaptopropyl)trimethoxysilane (MPTMS) containing thiol group was reacted and anchored on the SNFs surface in toluene by reacting with the surface hydroxyl groups. The trifunctional molecules are chemically very active. Trace amount of water caused the replacement of chlorine group by O-Si-O bond, with hydrochloric acid as a side product. Thiol groups on the long chains remained unreacted and served for anchoring sites for AuNPs. After this thiolation, the modified surface was referred as SNFs-SH. The CA was observed to increase to 45 ± 2°, which indicates the loss of superhydrophilicity (<5°). As the hydroxyl groups on the surface reacted with MPTMS, the surface tension became lower, which decreased the wettability of the surface. We noticed that the observed CA of SNFs-SH was around 14° lower than the reported CA of a self-assembled layer of MPTMS on a flat surface.[260] Two factors could lead to this phenomenon: (1) the residue of OH groups, which haven't been reacted; and (2) the surface roughness generated by SNFs, which enhanced the hydrophilicity of MPTMS surface. The prepared substrates were store under inert gas atmosphere for further use as thiol groups are sensitive to the air.[261]

A modified Turkevich method was used to synthesize Gold Nanoparticles (AuNPs).[212, 262, 263] All glassware and stirrer were washed by aqua regia and rinsed completely with ultrapure water for copious times before use.

Prior to the reaction, 1 wt % $HAuCl_4$, 1 wt % trisodium citrate, and 0.1 wt % $AgNO_3$ water solutions were prepared and all of these three solutions were stored at 4 °C cold bath. After mixing 170 µL of $AgNO_3$ and 2 mL $HAuCl_4$ solutions, different amounts of trisodium citrate solution (0.5 mL, 2 mL, 8 mL) was added, which would lead to different size of AuNPs respectively. The mixture of three solutions was then diluted to 10 mL with ultrapure water. Together with another 140 mL boiling ultrapure water, the mixture was injected into reaction flask. $HAuCl_4$ was reduced to AuNPs with the presence of trisodium citrate and $AgNO_3$. Three sizes of AuNPs with average diameters of 6.7 nm, 9.5 nm and 18.1 nm were synthesized by controlling the relative volume of trisodium citrate.

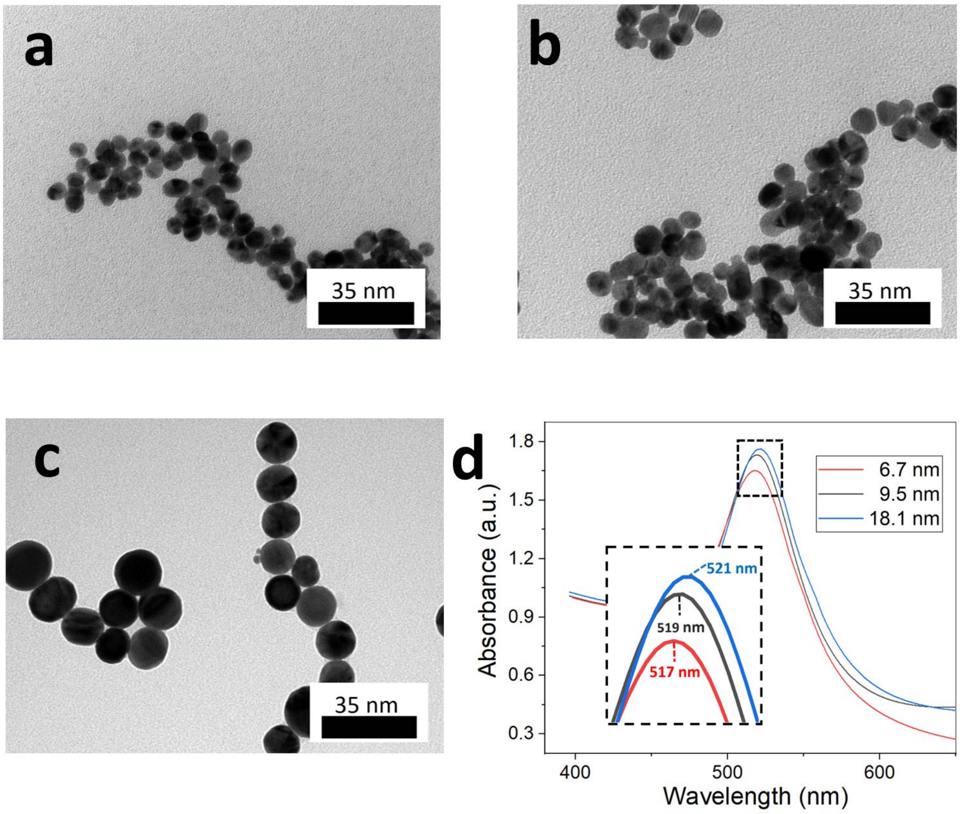

Figure 4.3.4 TEM images of synthesized AuNPs with the size of (a) 6.7 nm, (b) 9.5 nm, (c) 18.1 nm; (d) UV-Vis absorption spectra of the synthesized AuNPs;

Figure 4.3.4a-c presented the high-resolution TEM images of the AuNPs. The nanoparticle sized were measured by the software ImageJ by analyzing the TEM images, counting no less than 200 nanoparticles in the visual field. The diameter was also measured and confirmed with dynamic light scattering (DLS), which provided with relatively larger sizes respectively: 7.1 nm, 10.4 nm and 18.8 nm. DLS is an intensity based measurement and the hydrodynamic size of the particles was measured. Normally the hydrodynamic size includes a liquid layer which comes from the solvation. Besides, when aggregation happens to the targeted particles, the measurement leads to a relatively larger number. In comparison, the TEM image gave the image of a dry form of the particles by reflecting and receiving the electrons, which was more direct information[264]. Thus, the TEM results were taken as the right sizes of the AuNPs for record.

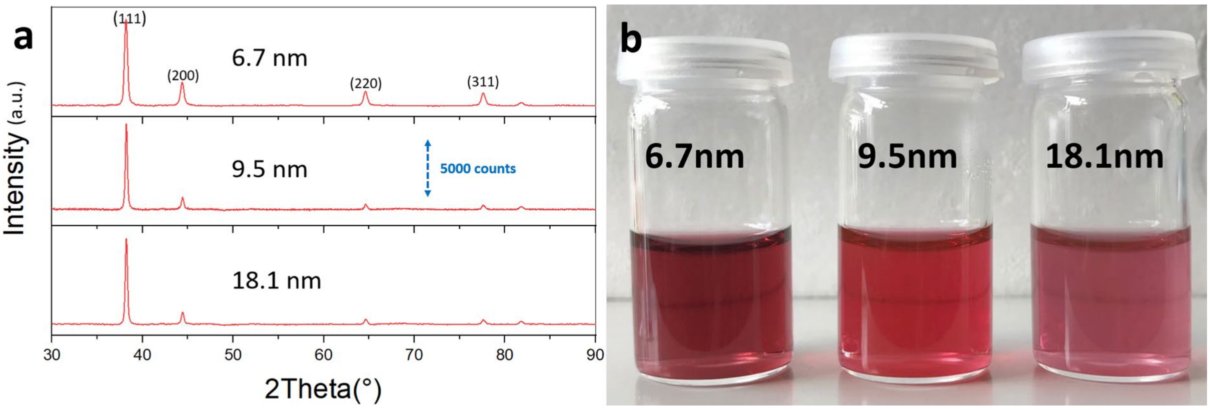

Figure 4.3.5 (a) XRD spectrum for different sizes of AuNPs. (b) Picture of the AuNPs solutions of different size.

Furthermore, in Figure 4.3.4d, we observed that the UV-Vis spectrum exhibited a slightly shift while increasing the particle size. With the AuNPs sizes increasing from 6.7 nm to 9.5 nm and 18.1 nm, the absorbance peak originally at wavelength of 517 nm was red-shifted to 519 and 521 nm. The increasing of the particle size led to the change on the surface plasmon resonance (SPL), which in the end caused the red-shift.[265, 266] From the X-ray diffraction result in Figure 4.3.5a, we observed that the peak width became smaller with the increasing of the particle size, which indicates a growth in the cell size of gold crystal according to Scherrer formula.[267]

A slight color difference though very unnoticeable, was observed as shown in Figure 4.3.5b: with the increasing of the particle size, the red color becomes slightly lighter, with longer wavelength being absorbed. The prepared AuNPs solutions were stored at room temperature for further use.

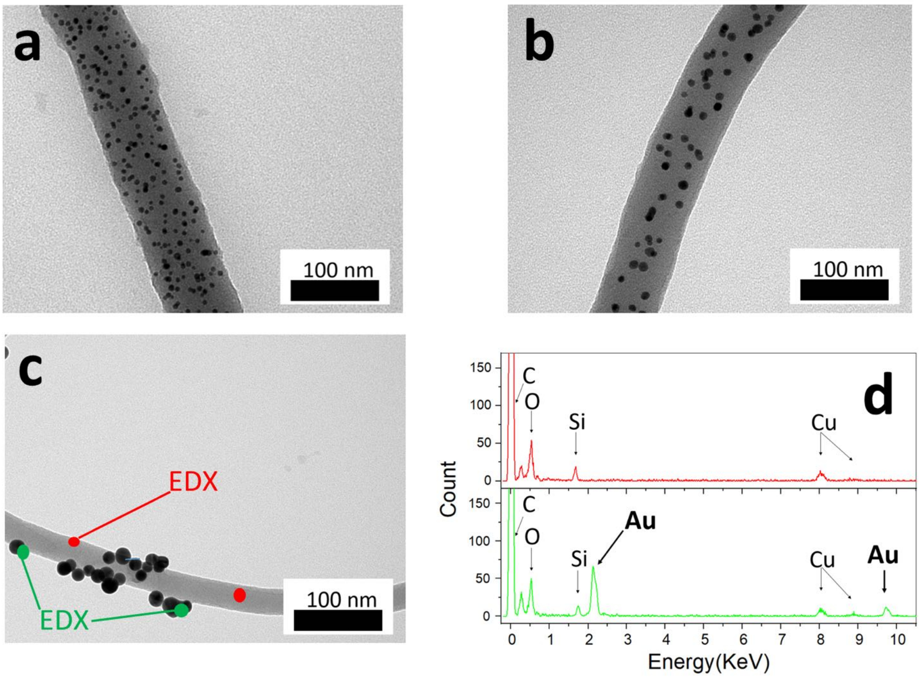

Figure 4.3.6 TEM images of the functional substrates with AuNPs size of (a) 6.7 nm, (b) 9.5 nm, (c) 18.1 nm; (d) EDX spectra correspondingly to (c).

The deposition method was used to assemble AuNPs on SNFs to achieve the functional substrate. The early prepared slides, SNFs-SH were immersed in the AuNPs solution. The temperature was kept at 80 °C and lasted for 6 hours. AuNPs were then successfully deposited on SNFs. The slides were taken out and rinsed with water. The functional substrates (AuNPs-SNFs) were referred as AuNP6-SNFs, AuNP9-SNFs and AuNP18-SNFs corresponding to the sizes of the deposited AuNPs of 6.7nm, 9.5 nm and 18.1 nm. In Figure 4.3.6a-c, the TEM images of these three functional substrates were exhibited. The comparison of EDX spectra of AuNP18-SNFs confirmed the existence of Au signal at 2.12 and 9.71 KeV.

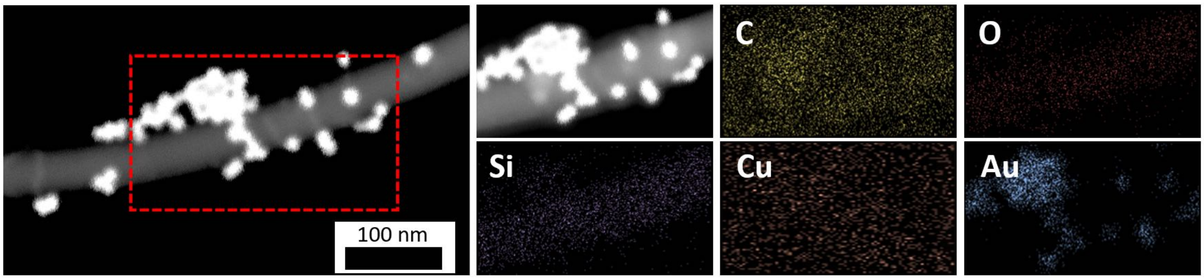

Figure 4.3.7 STEM EDX mapping of the prepared functional material with 18.1-nm-diameter AuNPs.

STEM EDX mapping in Figure 4.3.7 provided the evidence of the clear deposition of 18.1 nm AuNPs on SNFs (as AuNPs of 6.7 nm and 9.5 nm was a bit hard to be characterized on STEM EDX mapping). The functional substrates were successfully achieved and stored under inert atmosphere.

4.3.2 SERS of the functional substrate

Rhodamine 6G (R6G) was used in our experiment as the Raman probe to evaluate the SERS properties of different substrates. In this measurement, two things were mainly investigated: 1) the size effect of AuNPs and 2) the surface effect of SNFs.

To evaluate the surface effect of SNFs, three sizes of AuNPs were also deposited on glass slides, which have no SNFs coating layer as a comparison. The glass slides were treated with the same procedures of surface modification: oxygen plasma treatment at first and followed by sulfurization on the surface before the AuNPs deposition. After the assembling of AuNPs on the flat slides, the so-prepared slides were referred as AuNP6-G, AuNP9-G and AuNP18-G correspondingly, where “G” represents glass slide. Substrates AuNP6-G, AuNP9-G and AuNP18-G, together with substrates AuNP6-SNFs, AuNP9-SNFs and AuNP18-SNFs and blank glass slide were evaluated and compared in SERS detection.

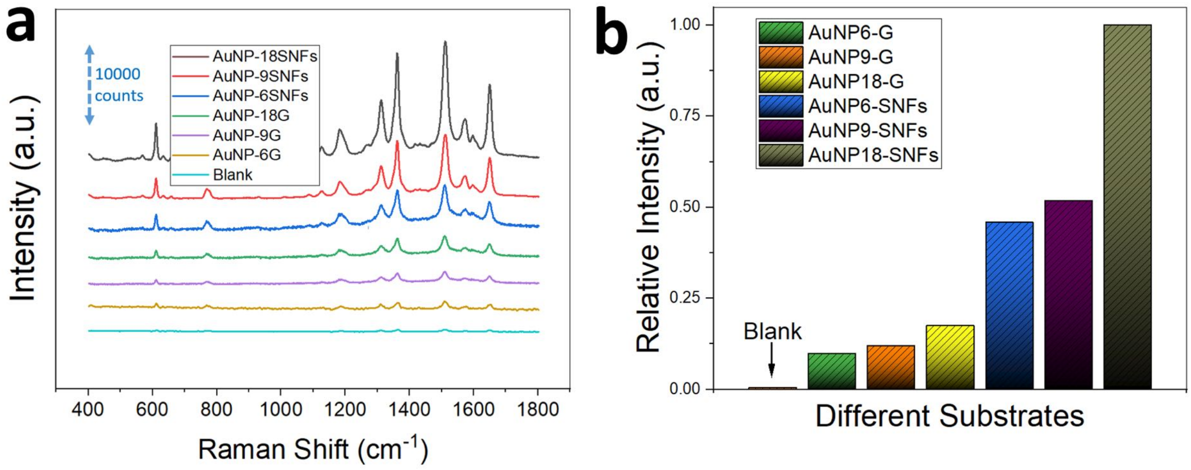

Figure 4.3.8 At a R6G concentration of 10^{-5} mol/L (a) SERS spectra and (b) the comparison of relative intensity at Raman shift 1510 cm^{-1} of different substrates

In Figure 4.3.8a all the SERS spectra by different substrates were recorded when the concentration of dropped R6G solution was 10^{-5} mol/L. It was proved that the blank shows no obvious Raman peaks at such a concentration. For the other substrates, all of which carried AuNPs, characteristic Raman spectra peaks of R6G were observed, though each of them shows different intensities. In the spectra, the peak at 613 cm^{-1} was the C-C-C ring in-plane bending, while the peak at 1360 cm^{-1} was caused by C-H in-plane bending. Another two peaks at 1510 cm^{-1} and 1652 cm^{-1} were all contributed by aromatic C-C stretching.[268] The highly enhanced Raman effect in comparison with the blank substrate, was due to the surface plasma coupling into SERS "hot-spots" created by the densely deposited AuNPs.[269] With the same size of AuNPs, the substrates with SNFs layer showed a higher enhancement for the Raman signal, which can be found in Figure 4.3.8b. The probable explanation was that with the 3-dimentional nano-structure, substrates containing SNFs layer have much more loading of AuNPs due to the nanoscale effect.[270, 271] In our earlier research, it was found that the nanoscale effect enhanced the surface area by a factor around 13 after the formation of SNFs.[237] That resulted in a higher amount of "hot-spots" which realised a considerably higher SERS enhancement. Besides, noble metal particles exhibit a great enhancement when the gap distance among them is less than 10 nm, according to the relation between inter-particle gap and SERS activity.[272] The SNFs coating layer on the glass slides formed a "grass carpet” morphology, where there were many intersections of the silicone filaments. Those intersections increased the possibility for nanoparticles to have shorter-distance gaps, which significantly enhance the Raman signal.

Furthermore, it was discovered that SERS signal enhancement increased together with an increasing of AuNPs size with the three sizes of the synthesized AuNPs in our experiments. It was certain that with a larger diameter of AuNPs, the surface area of a single particle becomes bigger. Hence, more probe molecules could be adsorbed on the surface of a single nanoparticle, which leads to a higher SERS intensity by physical adsorption.[273] Even though the AuNPs density on SNFs with the size of 18.1 nm was relatively lower compared with the ones with another two smaller diameters, it was noticed that the particles were more closely and densely packed, which resulted in more intensive hot-spots effect where the distance is less than 10 nm. Same results were observed and exhibited when the concentration of R6G solution was diluted to 10^{-6} mol/L in Figure 4.3.9. Therefore, we could conclude that among these prepared functional substrates, the SERS substrate with the highest enhancement effect was found to be the AuNP18-SNFs, showing a remarkably high sensitivity to the tested R6G probe.

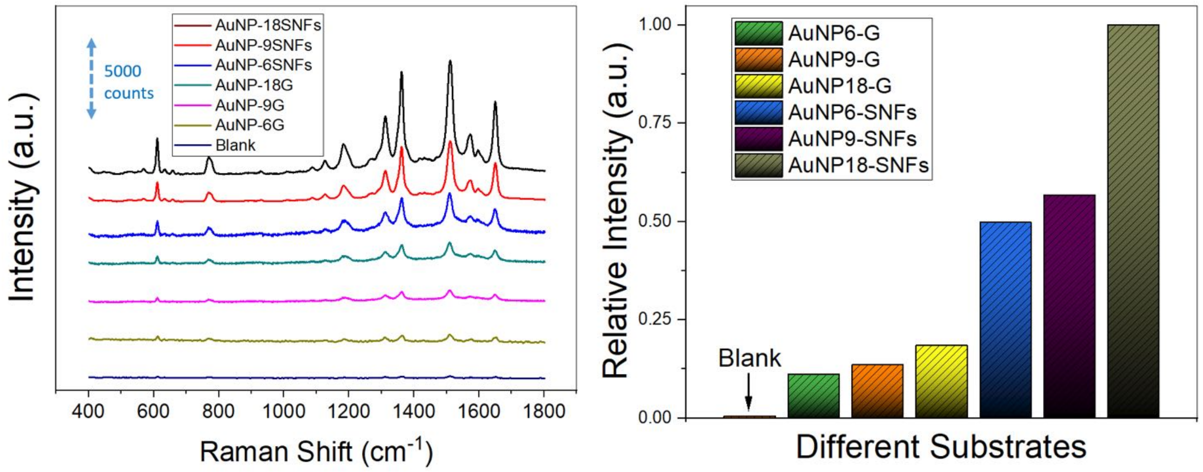

Figure 4.3.9 At a R6G concentration of 10^{-6} mol/L (a) SERS spectra and (b) the comparison of relative intensity at Raman shift 1510 cm^{-1} of different substrates

Limitation of detection (LOD) experiments were carried out to evaluate the enhancement ability of the AuNP18-SNFs substrate. The same probe R6G was used as the detection analyte. The intensity of the characteristic peak of R6G at 1510 cm^{-1} was chosen to plot as a function of concentration. The result was exhibited in Figure 4.3.10.

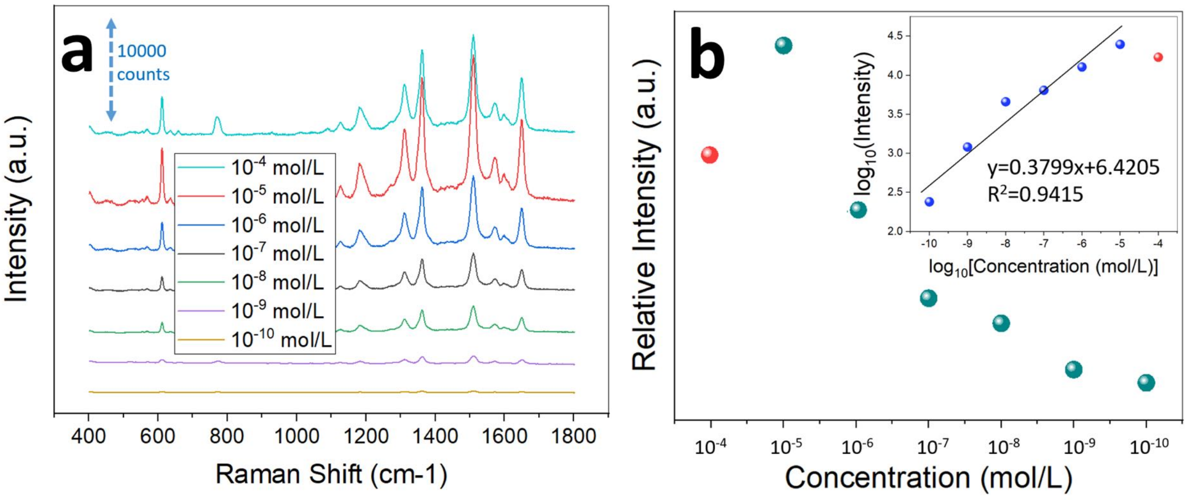

Figure 4.3.10 Limitation of detection (LOD) measurements of the substrate AuNP18-SNFs (a) SERS spectra at various concentrations of R6G and (b) Plotting a function of relative intensity at Raman shift 1510 cm^{-1} to concentration;

Notably, within the tested range of concentration, the SERS spectra with different concentrations of R6G show different SERS intensities. With progressively decreasing of the R6G concentration, the SERS intensity decreased. In Figure 4.3.10a, it was confirmed that the peak intensity for the sample with a concentration of 10^{-9} mol/L could still be clearly characterized. The peak intensity for the concentration 10^{-10} mol/L, however, was not distinguishable enough from the background noise. Therefore, we concluded that the LOD of R6G for substrate AuNP18-SNFs is 10^{-9} mol/L. There was an exceptional case noticed that the Raman intensity for the R6G concentration of 10^{-4} mol/L was lower than that of the R6G concentration of 10^{-5} mol/L. This phenomenon was also observed in other literature when the analyte solution was not diluted enough.[274] For a relatively high concentration of R6G, the R6G molecules could be condensed to aggregate and form a crystallized layer of R6G on the substrates (on the surface of AuNPs). When spotted by the laser beam, the crystallized layer may affect the Raman scattering negatively and hence hinder the SERS detection. The phenomenon is normally observed when the analyte solution is not diluted enough.

In addition to the LOD of the substrates, the surface enhancement factors (EF) of different substrates were also calculated via the given formula.[275]

$$EF = (I_{SERS}/I_{NR})\ (N_{SERS}/N_{NR})$$

Where I_{SERS} and I_{NR} are the intensities at specific peak (1510 cm^{-1}) in the SERS and normal Raman spectra. N_{SERS} and N_{NR} are the number of analyte molecules (R6G) adsorbed on the substrates to obtain the corresponding SERS spectra under illumination of the laser light and number of the solid analyte molecules in the laser illumination volume. The EF of AuNP18-SNFs reaches 9.56×10^6, which is sufficient enough for most of the academic and industrial uses.

The reproducibility of the functional substrates is an essential index to ensure the performance for potential applications. To measure the reproducibility of substrate AuNP18-SNFs, 10^{-5} mol/L R6G was selected as the probe. SERS spectra was acquired from 10 randomly selected positions. However, substrates AuNP6-SNFs and AuNP9-SNFs exhibited better reproducibility and uniformity than AuNP18-SNFs in the Raman mapping measurement (Figure 4.3.11), though they have a lower sensitivity. For the area where the intensity signal is higher than 80% of the highest intensity in the whole tested area, in substrates AuNP6-SNFs, AuNP9-SNFs and AuNP6-SNFs are correspondingly 82%, 87% and 74%. The reason is that from the TEM images (Figure 2e-g) the AuNPs on substrates AuNP6-SNFs and AuNP9-SNFs are more homogeneously distributed and less packing happened during their deposition.

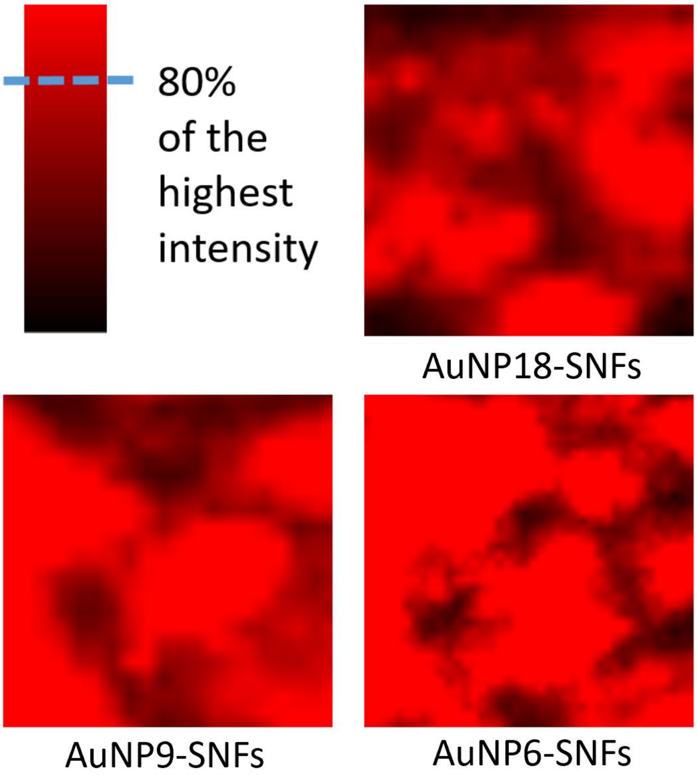

Figure 4.3.11 Raman mapping of different substrates at same concentration of analyte.

4.3.3 Catalytic ability of the functional substrate

The use of homogeneous catalysts is often accompanied with the problem of residual impurities of the catalysts in final products, which becomes a very serious problem when high purity of the products is required. Heterogeneous catalysts, on the other hand, could minimize the contamination from the residue of catalyst in products.[276] Thus, heterogeneous catalysis plays an important role in industrial production, especially in pharmaceutics, biology, and food industries.

The same functional substrate with AuNPs immobilized on SNFs worked as a heterogeneous catalyst substrate. The catalytic property of the functional substrate was determined and demonstrated by the hydrogenation reaction of 4-nitrophenol. This reaction was chosen due to the following reasons: (1) the reduction reaction is a model reaction; (2) the reaction proceeds at a mild condition, with room temperature and in aqueous solution; (3) the extent of the reaction can be monitored by UV/Vis spectroscopy conveniently and precisely; (4)besides, catalytic hydrogenation of organic compounds is of great interest in industry.

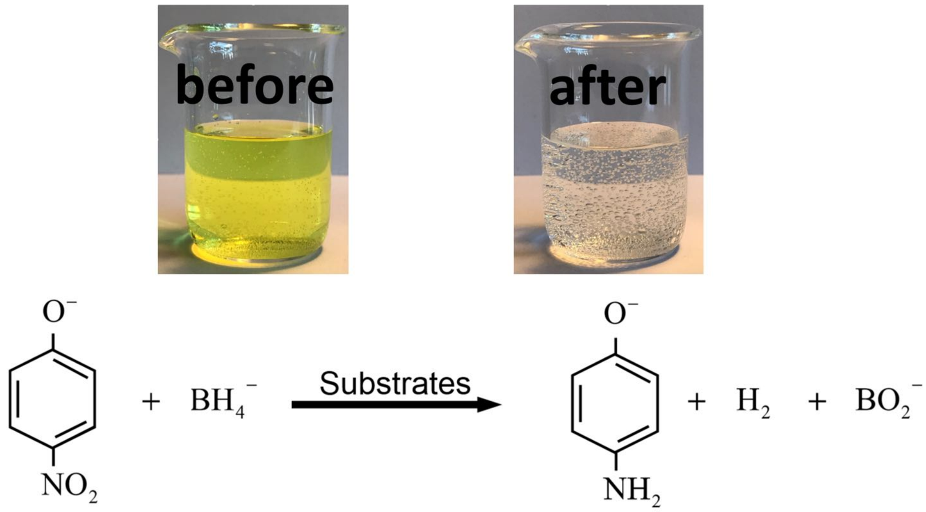

Figure 4.4.1 Reaction equation and the colour change before and after the reaction.

Figure 4.4.1 shows the hydrogenation conversion of 4-nitrophenol to 4-aminophenol. Sodium hydroxide was added into 4-nitrophenol solution for basification (to pH = 10). The colour changed from very light yellow to bright yellow. A large excess amount of sodium borohydride was added to the basified 4-nitrophenol solution (208:1 in mole) in order to make sure the supply of sodium borohydride sufficient and the reaction rate only determined by the concentration of 4-nitrophenol. The functional substrates were immersed in the prepared solution and the reaction started immediately. The reaction was followed by UV/Vis spectrum over time. The absorbance at 400 nm was measured as reaction proceeded, which is the representative peak for the reactant, 4-nitrophenol. Figure 4.4.2 exemplified the absorbance change over time for substrate AuNPs9-SNFs.

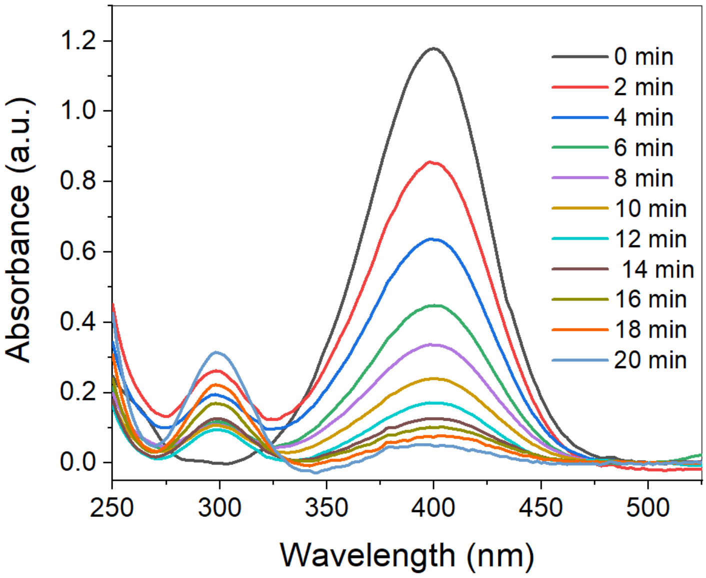

Figure 4.4.2 The exemplified absorbance change at wavelength of 400 nm with the substrate AuNPs9-SNFs.

In consistent with the generation of 4-aminophenol, a newly emerged peak at 317 nm appeared with the reaction time going on. Moreover, the solution turned from light yellow to transparent after the reaction is completed.

First of all, it was confirmed no reaction happened without the immersing of catalytic substrates. In addition, no reaction took place once the substrate was removed. Thus, the presence of our functional substrate was the prerequisite for the occurrence of the hydrogenation reaction. Besides, since removal of the substrate stopped the reaction immediately, it was indicated that the AuNPs, which worked as the effective catalyst, were boned tightly on the SNFs on slides without leaching. This was further confirmed in the later part. Figure 4.4.3 showed the relative absorbance change in the presence of different substrates.

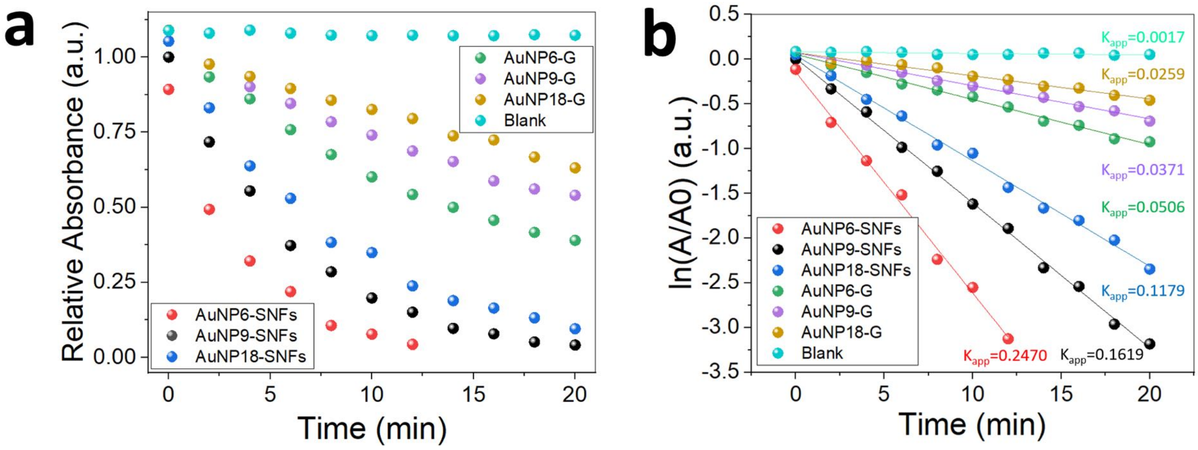

Figure 4.3.3 (a) Relative absorbance change over time for different substrates; (b) logarithmized result of (a)

The excess use of sodium borohydride made it possible to assume that the reaction rate was determined only by the concentration of reactant 4-nitrophenol during the whole measuring period. Figure 4.4.3a exhibited the different reaction rates of all substrates. There was no reduction of 4-nitrophenol determined when none-AuNPs-contained slide immersed into the solution. The kinetic barrier between BH_4^- and 4-nitrophenol anions is too high for the reduction reaction to happen at the set temperature when no catalysts involved.[277] Figure 4.3.3b indicated that the monitored kinetics followed well with the first order law, so that the apparent rate constants K_{app} could be calculated as the positive value of the slope of the logarithmic line.

It was proved that the substrates with SNFs coating layer exhibited a higher catalytic activity when the loaded AuNPs were of the same size. A similar phenomenon was observed in our previous study, which investigated the catalytic efficiency of TiO_2 NPs on SNFs.[62] The surface area of the substrates with SNFs was much higher than the substrates without SNFs, as additional surface roughness was created by the formation of SNFs layer. The additional surface areas according to calculation were multiplied by a factor of around 13.[237] Thus a higher amount of AuNPs on the substrates were loaded correspondingly, resulting in a higher efficiency for the hydrogenation reaction. In figure 4.3.4, the loading amounts of deposited AuNPs from different substrates were compared and it was confirmed by using spectrophotometer in a method our group developed in an earlier literature.[278] Substrates were immersed in aqua regia at room temperature for 30 min to dissolve all AuNPs into gold ions aqueous solution. A standard solution of gold ion was used for the calibration of standard relation of the absorbance to the concentration. The comparing result of the loaded AuNPs on substrates corresponded with the conclusion that with same size of AuNPs, substrates with SNFs layer obtained a better catalytic activity.

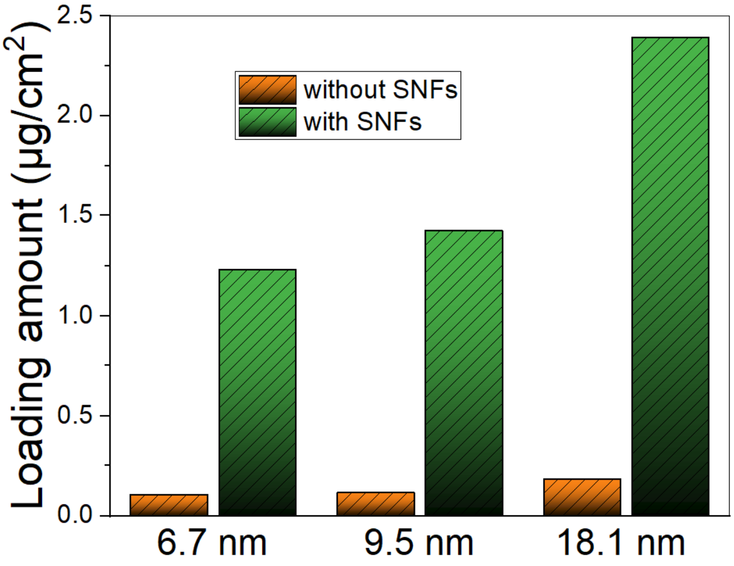

Figure 4.3.4 The loading amount of gold on different substrates.

Among all the functional substrates, which contained SNFs layer, such tendency was observed that the apparent rate constants grow steeper, with the size of the AuNPs decreasing. AuNP6-SNFs shows the highest catalytic efficiency, followed by AuNP9-SNFs and AuNP18-SNFs was the least active among all the three. The same tendency was noticed as well with the substrates, which had no SNFs layer. Same results were also reported in other literature.[279, 280] Compared with bulky gold that is not chemically active, AuNPs exhibited outstanding catalytic activity due to the nanoscale effect. The surface area of nanoparticles is inversely proportional to the particles size. The factors, which affect their catalytic activity, include particle size, shape, size distribution and surface characteristics. Besides, during heterogeneous catalysis, the properties of support material influence catalytic activity as well.[281] Herein, the particle size was analysed. Thus, the phenomenon observed in the experiment can be well explained. It needs to be noticed that exception exists when the AuNPs are extremely small in other literature. The catalytic activity is decreasing with the particle size getting smaller when the diameter is smaller than 5 nm. [282]

The stability and the recyclability of different substrates were also tested, as these properties are essential in industrial applications. AuNP9-SNFs and AuNP9-G were selected for the test. The result was presented in Figure 4f.

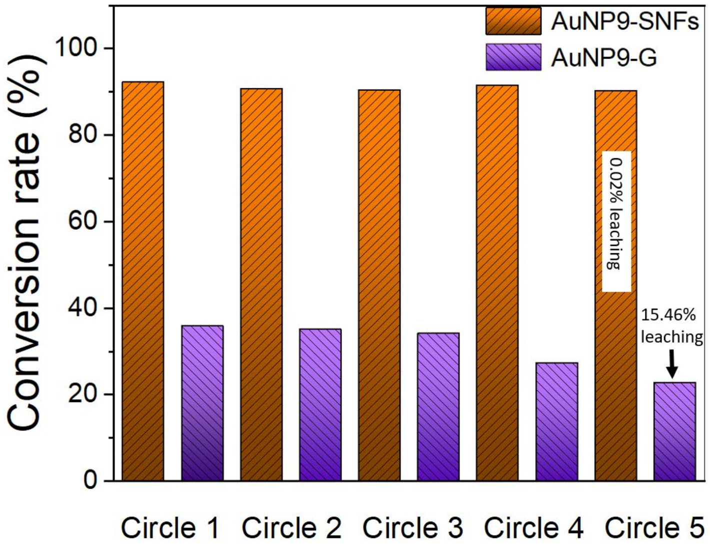

Figure 4.3.5 The recycling experiment of substrate AuNPs9-SNFs and the leaching measurement in the end.

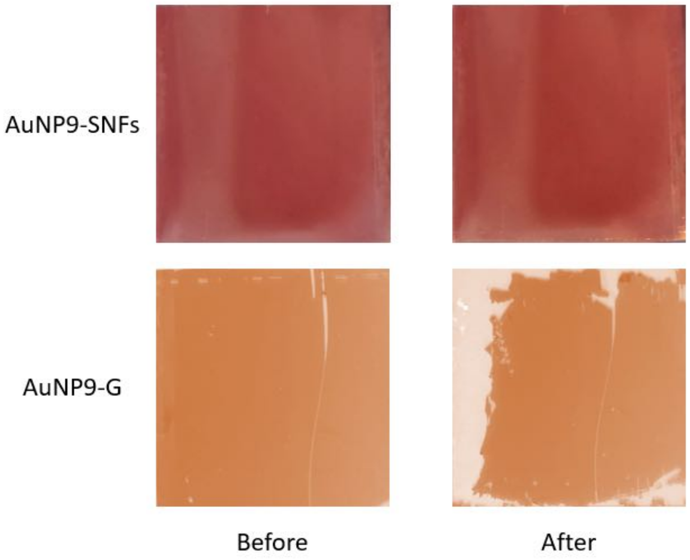

Figure 4.3.6 The comparison of the appearances of the substrates after 5-time cycle of hydrogenation reaction.

AuNP9-SNFs exhibited with a constantly stable performance in the five times of hydrogenation reactions. The conversion rate of AuNP6-G, however, after 3 reactions, began to drop. After five times recycle, apparent peel-off appeared on AuNP6-G (in Figure 4.3.6). It could be a possible explanation that without SNFs serving as a support, there were fewer thiol groups on the surface to anchor the AuNPs. During the reaction, the generated hydrogen “blew off” a part of the AuNPs. The extent of leaching of the catalytic substrates was measured by spectrophotometer. The result, presented in Figure 4f, was consistent with the catalytic performance in the recyclability measurements.

The novel composite functional substrate was successfully applied as a molecule detector with SERS technology. The compositing of AuNPs, which are widely used in various fields, makes it possible to be used in some other important fields, such as in drug delivery, thermal therapy, bio-imaging, etc. It also opens a door to other metal particles, like silver, platinum, or palladium since they are widely used as catalysts, bacteria inhibitors or drug delivers.[283]

4.4 Fabrication of Flexible and Robust SNFs-PE Composite Material

The lack of mechanical and chemical stabilities of superhydrophobic surfaces hinders their widespread usage in practical applications. To overcome these problems, fabrication of mechanochemically durable materials with non-wetting property has been extensively studied. A common method that adapted as a successful strategy is to create superhydrophobic surfaces based on the materials that are inherently mechanical durable, such as elastomers and metals.[199, 200] However, this strategy was limited by the complication and the high cost of the fabrication of such robust materials, even though the superhydrophobic surfaces exhibited good mechanical durability for maintaining non-wettability. Spray coating of fluorinated particles together with adhesive as an alternative solution has been tried as it is less complicated to implant. [202, 203] However, the involvement of fluorinated substances and organic solvents are not environmental friendly. In addition, the surfaces also face the problem that after exposure to organic solvents, the non-wettability could not be sustained. Thus, the fabrication of mechanochemical robust superhydrophobic surfaces through a feasible and eco-friendly method remains as a challenge.

In this chapter, a facile solvent-free method to manufacture a flexible superhydrophobic composite surface with a hierarchical structure to feature stable and robust water repellency was presented. Uniquely, the deploying of this new strategy avoids the usage of organic solvents, which contaminate the environment and increase the cost. The composite surface was generated coating SNFs on PE film, followed with thermal annealing at high temperature. The two-scale hierarchical structure of the surface was created after annealing. The mechanochemical durability was tested through a series of experiments and the composite surface shows great potential and advantages for a wide range of applications.

4.4.1 The Fabrication and Characterization of The Synthesized Material

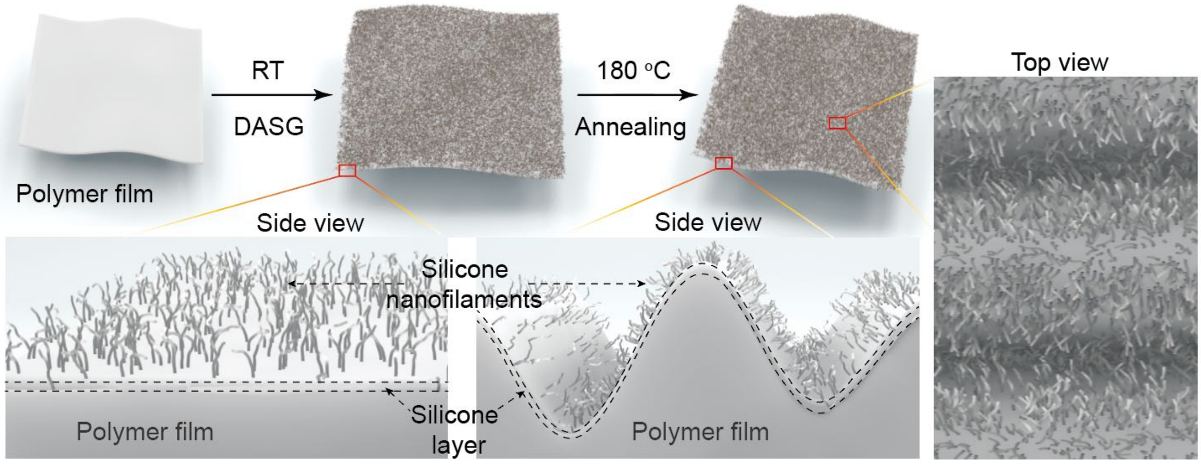

Figure 4.4.1 Schematic of the strategy for sample preparation. Scanning electron microscopy (SEM) images showing the micro/nanostructure of the sample

Figure 4.4.1 schematically exhibits the preparation of the superhydrophobic composite film with a hierarchically structured surface. Before the dense and homogeneous growth of silicon nanofilaments (SNFs) layer on both sides of the polyethylene (PE) film, the PE film was activated with an oxygen plasma on the surface to ensure the covering of hydroxyl groups. SNFs layer was formed at room temperature (RT) through the *droplet-assisted growth and shaping* (DAGS) method with ETCS as the precursor.[57] Subsequently, the obtained composite film was annealed at 180 °C for 10 min.

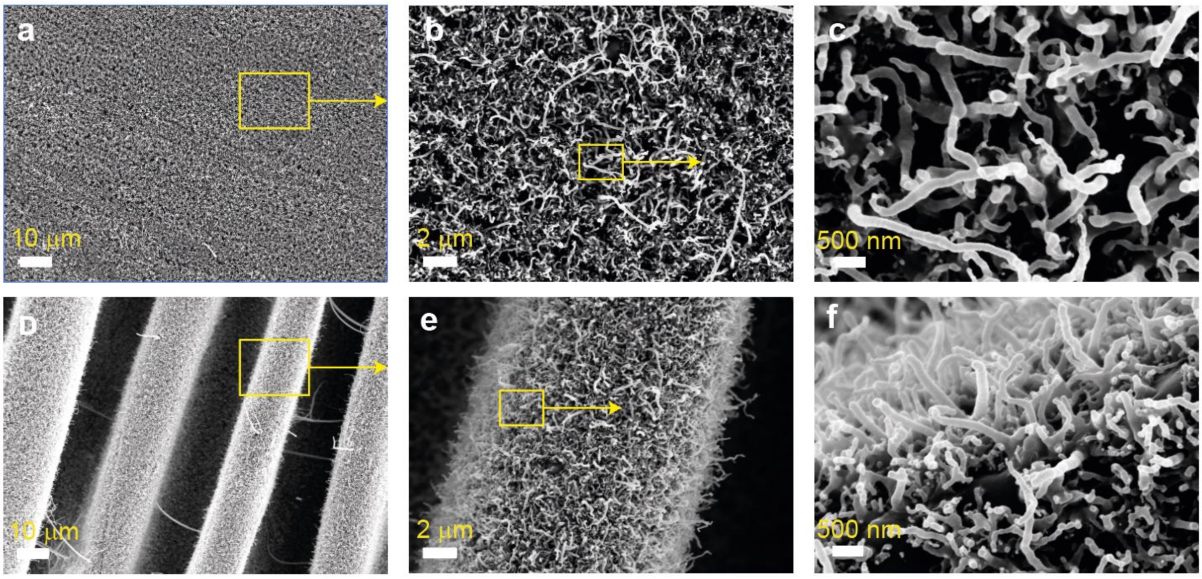

Figure 4.4.2 Scanning electron microscopy (SEM) images showing the micro/nanostructure of the sample (a-c) before annealing and (d-f) after annealing at different magnifications. The annealing temperature and time were 180 °C and 10 min, respectively.

Figure 4.4.2a-c show the scanning electron microscopy (SEM) images of the PE film after growing with SNFs layer, which was named as PE-SNF. A dense and homogeneous layer of SNFs on the film surface can be observed clearly. Strikingly, after thermal treatment at 180 °C for 10 min, the annealed composite film, which was called PE-SNF-A, features a hierarchical micro/nanometer structured surface, as shown in Figure 4.4.2d-f. For compression, the same thermal annealing procedure was performed for PE films without growing of SNFs. Whereas no micro-wrinkled structure was observed for the annealed PE films (see Figure 4.4.3).

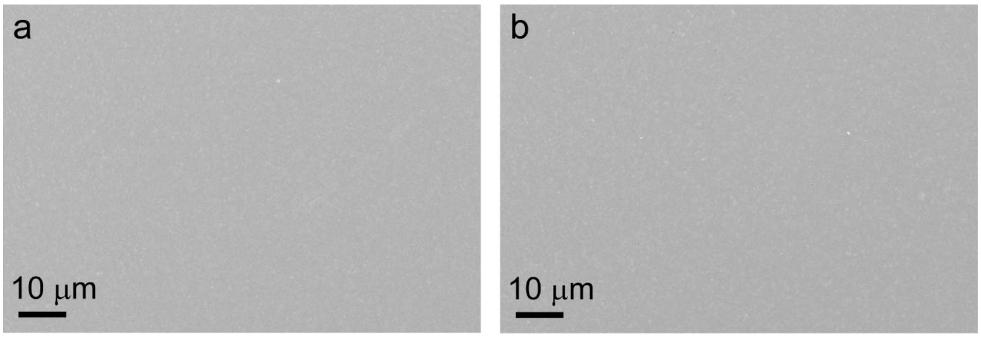

Figure 4.4.3 SEM images of LDPE films (a) before and (b) after annealing treatment.

Thus, we assumed that the appeared micro-meter wrinkles after annealing are ascribed to the different modulus and heat-shrink properties between the thermoplastic PE film and the rigid silicon layer from SNFs grown on the PE surface (see Figure 4.4.1).[284] [285] The presence of the silicon layer on PE film surface was confirmed by the Scanning electron microscopy (SEM) and Energy-dispersive X-ray spectroscopy (EDX) images of cross-sectioned PE-SNF-A films, as shown in Figure 4.4.4. A thin silicon layer between PE film and the SNF can be clearly observed (Figure 4.4.42c, f, i and l). The height of the micro-wrinkles and the thickness of the silicon layer were estimated to be ~19 µm and ~200 nm, respectively.

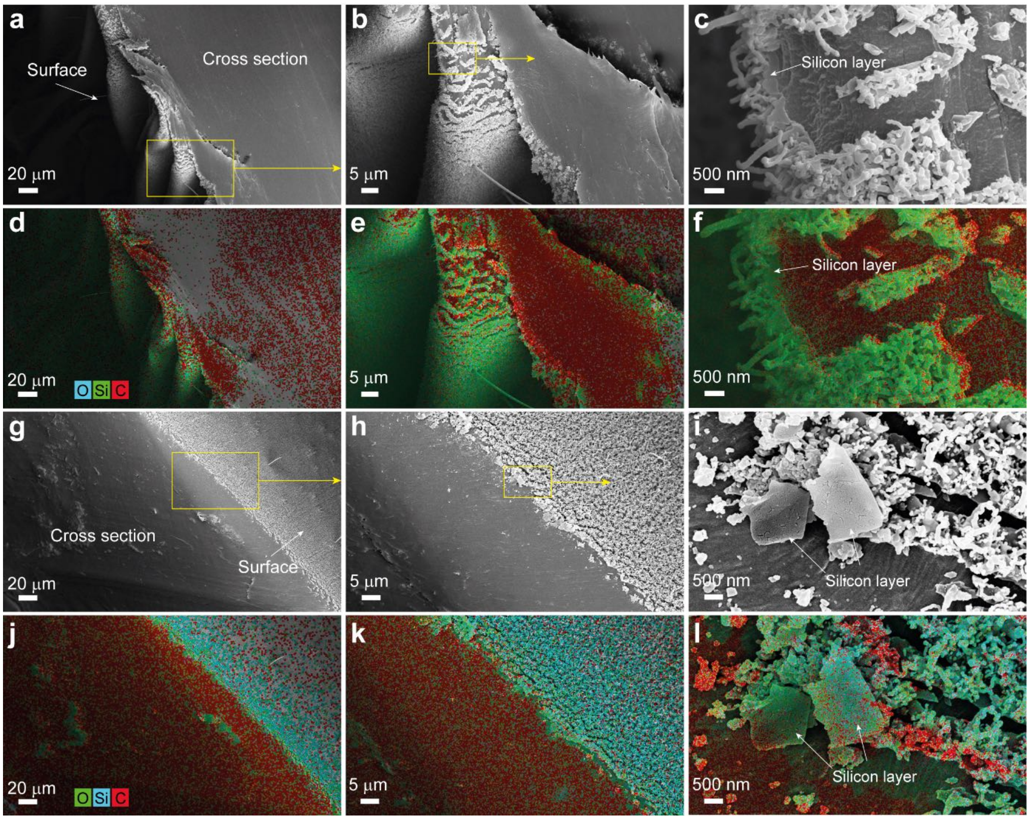

Figure 4.4.4 (a-c) SEM images of cross-sectioned PE-SNF-A film at different magnifications, and (d-f) the corresponding EDX mapping. (g-i) SEM images of cross-sectioned PE-SNF film at different magnifications and (j-l) their corresponding EDX mapping.

4.4.2 The Mechanical Durability Tests

Superhydrophobicity was one of the inherent properties of SNFs layer. The as-prepared PE-SNF film shows excellent water repellency as a result and, at the same time, good flexibility. As we can see in Figure 4.4.5a, the plastron effect was clearly observed when the sample was submerged into water, which indicates a trapped air layer between the water and the surface. The surface maintained non-wet after taking out from the water. In Figure 4.4.5b, a water flow can easily bounce off from the highly bent PE-SNF-A composite film surface without leaving any trace. This states the ultra-low adhesion between the film surface and water flow. The fundamental reason behind those phenomena was explained by the Cassie-Baxter model.[11]

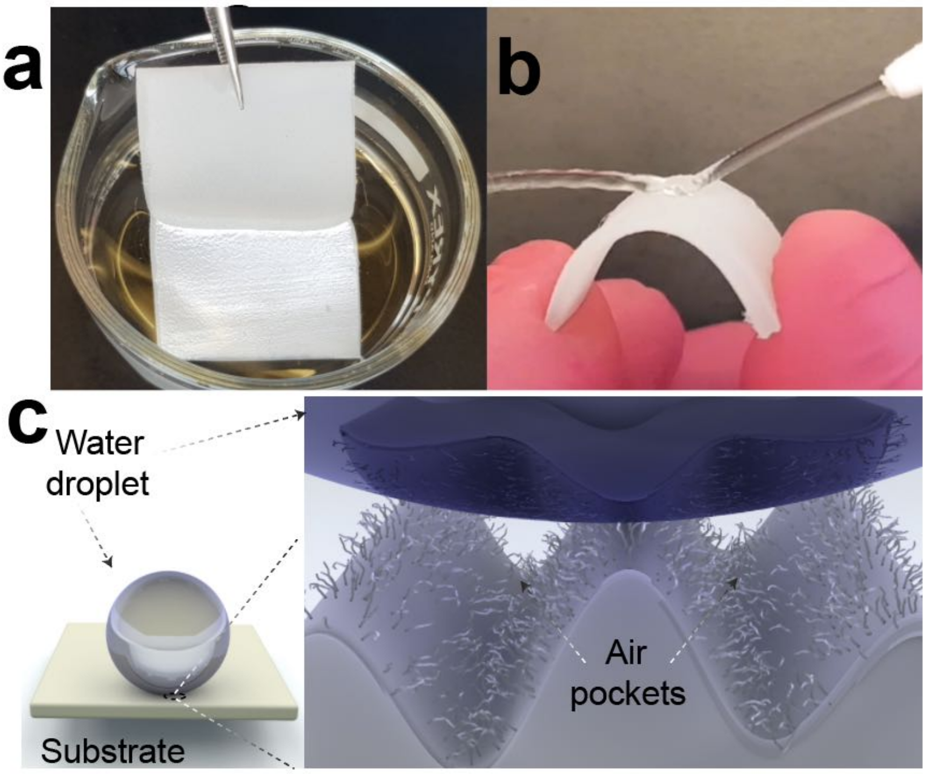

Figure 4.4.5 (a) The plastron effect. (b) A photo showing the water jet bounce off the highly bent PE-SNF-A film. (c) Cassie–Baxter wetting phenomenon in scheme.

To characterize the flexibility of the PE-SNF film, flexural measurement was conducted on the PE-SNF-A film to determine the bending property. The obtained flexural stress–strain curve is exhibited in Figure 3b. The average flexural strength and strain at maximum force were determined to be 8.1 MPa and 6.7%, respectively, both of which are relatively higher compared to that of the non-annealed PE-SNF films (6.1 MPa and 2.1%). We attribute the enhancement to the induced micro-wrinkled surface structure of the annealed film.

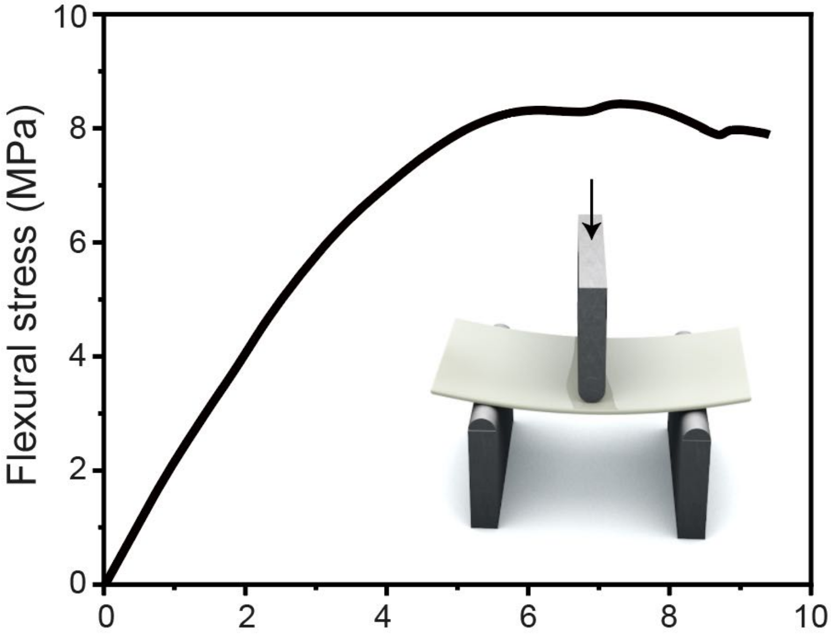

Figure 4.4.6 Flexural measurement result of the PE-SNF-A film.

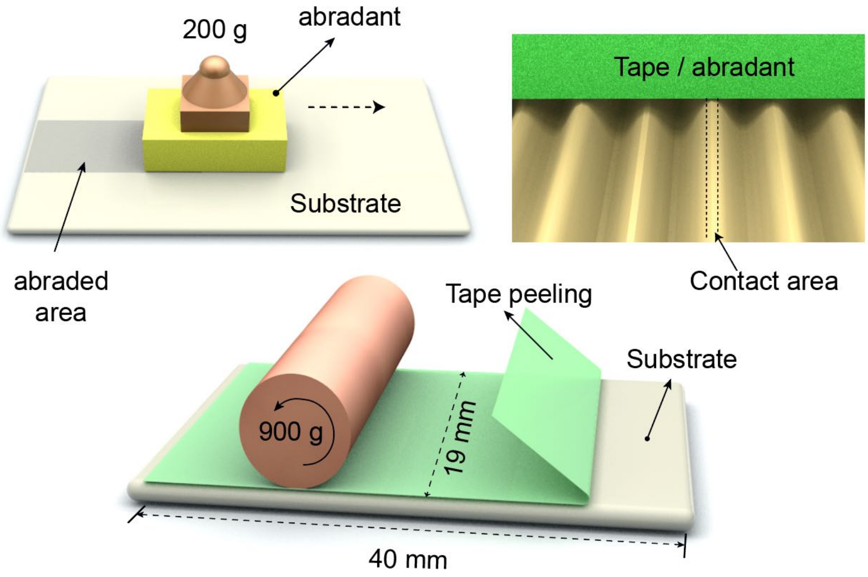

Figure 4.4.7 Schematic exhibition of the abrasion and tape-peeling tests.

Mechanical durability is of particular importance for the practical applications of superhydrophobic materials. In this project, two types of mechanical tests were performed for the as-prepared PE-SNF composite films: the abrasion and tape-peeling tests, both of which were presented in Figure 4.4.7 schematically.

In order to compare, water contact angle (Θ_{CA}), sliding angle, and (Θ_{SA}) as a function of abrasion and tape-peeling cycles for both annealed and unannealed PE-SNF films were measured and plotted. The obtained results are shown in Figure 4.4.8. Both of the annealed and unannealed PE-SNF films exhibited Θ_{CA} of around 171°, whereas the PE-SNF-A film exhibits a lower Θ_{SA} of around 3° compared to that of the PE-SNF film without annealing (Θ_{SA} of 5°). Notably, the PE-SNF-A film shows a significantly better resistance against tape peeling compared to the unannealed PE-SNF film (see Figure 4.4.8a,b). Even after 30 cycles of tape-peeling, the PE-SNF-A remained excellent superhydrophobicity, featuring the Θ_{CA} larger than 165° and Θ_{SA} of ~10°. In comparison, the unannealed PE-SNF film lost its superhydrophobicity after only one cycle of tape peeling. Its Θ_{CA} dropped below 140° and the Θ_{SA} became unmeasurable (above 90°). After 30 cycles of tape peeling, the Θ_{CA} was lowered to ~ 116° for PE-SNF film without annealing (see Figure 4.4.8c).

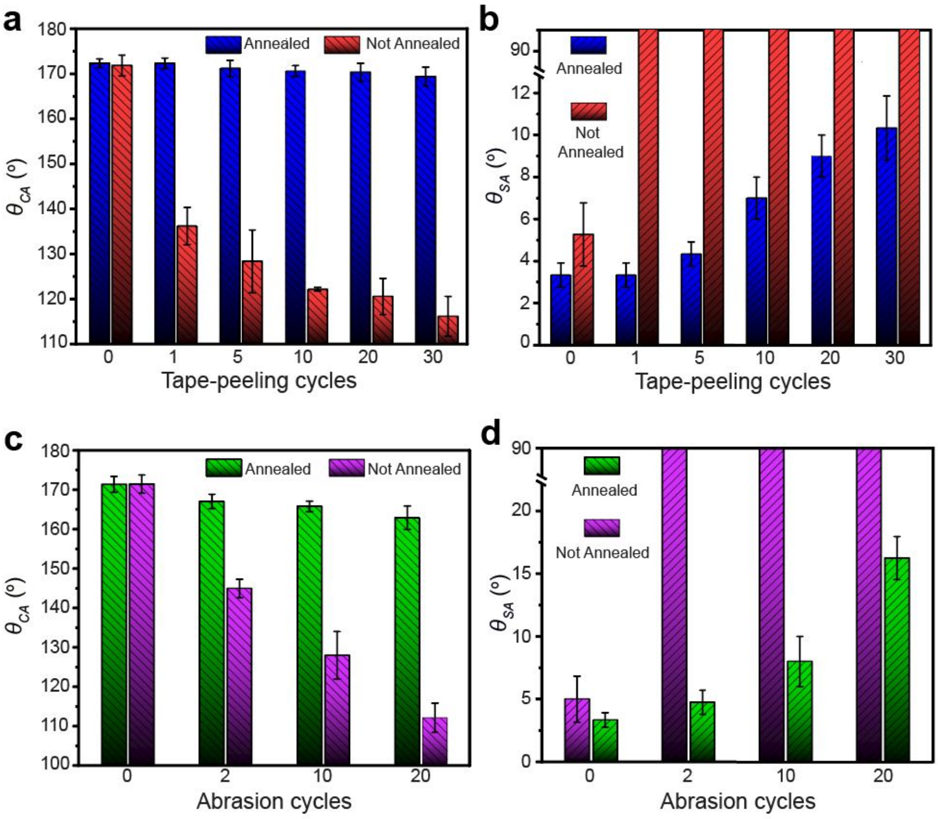

Figure 4.4.8 The effect of tape-peeling cycles on (a) Θ_{CA} and (b) Θ_{SA} of the composite PE-SNF films. The influence of abrasion cycles on (c) Θ_{CA} and (d) Θ_{SA} of the PE-SNF films.

As another mechanical robustness test ----the abrasion resistance of the substrates was conducted to compare. The unannealed PE-SNF film showed a higher abrasion susceptibility and lost its superhydrophobicity instantly after 2 cycles of abrasion. The similar results of SNFs coating losing superhydrophobicity were reported earlier.[286] [287] Apparently, after 2 cycles of abrasion, the Θ_{CA} was reduced to 145° and Θ_{SA} was increased to be above 90° for PE-SNF without annealing, which indicates the loss of superhydrophobicity. The mechanical susceptibility of the unannealed PE-SNF film is stemmed from the inherent fragility of SNFs, as the nano-scaled SNFs structure is easy to break.

On the other hand, the PE-SNF-A film maintained its superhydrophobicity even after 20 cycles of abrasion. The Θ_{CA} and Θ_{SA} remained around 162° and 16°, respectively, as provided in Figure 4.4.8c and d. The mechanical robustness of PE-SNF-A film was also evident from the rebounding of a water droplet on the tape-peeled or abraded surfaces (see in Figure 4.4.9). In addition, the PE-SNF-A film maintained its superhydrophobicity even after knife-cutting, finger-wiping and cyclic flexing (videos are available).

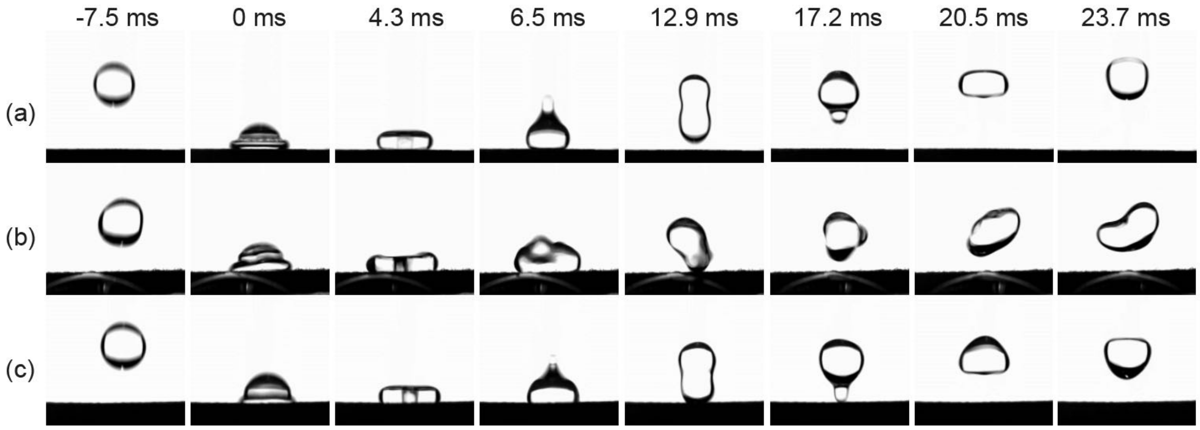

Figure 4.4.9 The Time resolved pictures showing the complete bounce of a 10 µL water droplet on the PE-SNF-A film (a) fresh without any test, (b) after 30 cycles of tape-peeling at 900 g load and (c) 20 cycles of abrasion at 200 g load.

The longer sustainability of the superhydrophobicity and better mechanical robustness for the PE-SNF film after annealing is due to the induced micro-wrinkled structure and the enhanced adhesion between silicon layer and the base layer of PE film. This is evidently supported by the SEM results, as exhibited in Figure 4.10.10.

After 30 cycles of tape peeling, the SNFs layer was totally removed and the silicon layer was partially peeled off from the unannealed PE-SNF film surface (in Figure 4.4.10a-b). A similar situation was observed for the PE-SNF film surface after 20 cycles of abrasion (in Figure 4.4.10e-f). This observation explains well the susceptibility of the superhydrophobicity by mechanical forces for the PE-SNF without annealing. In contrast to the unannealed PE-SNF, the SNFs were mostly retained on the PE-SNF-A after either 30 cycles of tape-peeing (Figure 4.4.10c-d) or 20 cycles of abrasion (Figure 4.4.10g-h). Only those “ridge” areas, which were exposed to the tape peeling or abrasive forces (Figure 4.4.10c-d, g-h and Figure 4.4.7) show signs of the scratched SNFs texture. Meanwhile the majority of the SNFs were protected by the micro-wrinkled structures. Strikingly, except the damaged SNFs structure, the hydrophobic silicone layer remained sticking to the ridge of the micro-wrinkles on PE film even after exposed to tape-peeling or adhesion (see Figure 4.4.10c-d and g-h). The retained hydrophobic silicone layer together with the micro-wrinkled roughness, as well as the protected SNFs between wrinkles maintains the superhydrophobicity of the PE-SNF-A film. This is the reason which explains the mechanical robustness of the superhydrophobic property of the PE-SNF film after annealing.

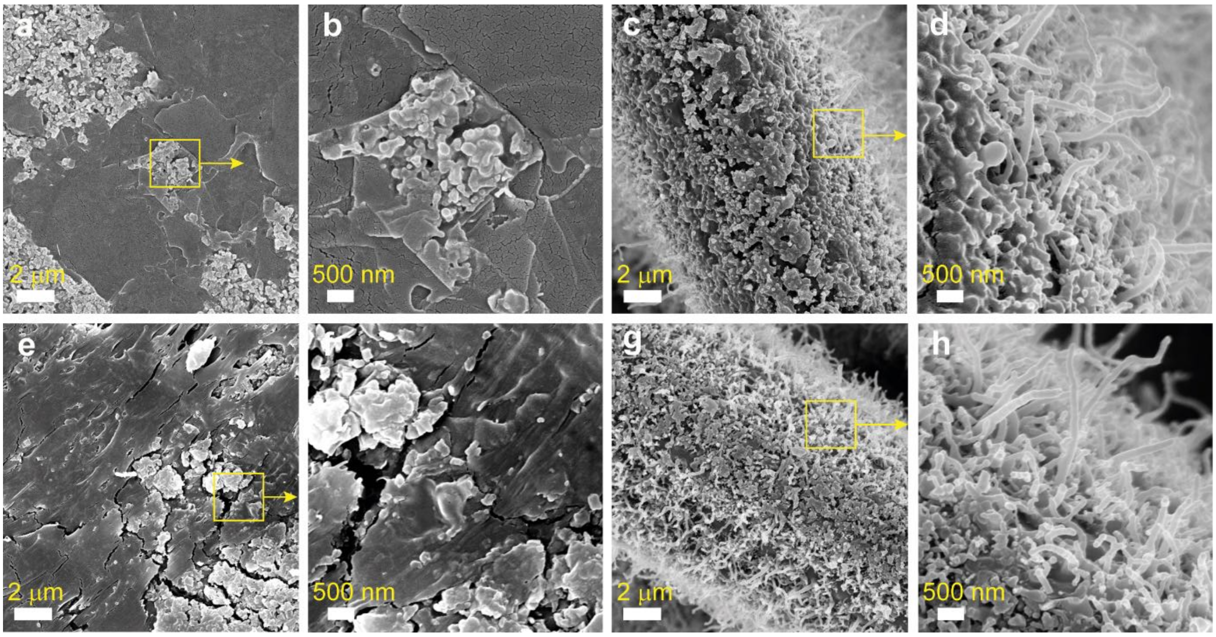

Figure 4.4.10 SEM images of the (a-b) unannealed PE-SNF and (c-d) PE-SNF-A film surfaces after 30 cycles of tape peeling at different magnifications. The (e-f) unannealed PE-SNF and (g-h) PE-SNF-A film surfaces after 20 cycles of abrasion.

To further investigate the stability of the superhydrophobicity for the obtained PE-SNF-A film, a water droplet of 10 μL was put on the film surface, as shown in Figure 4.4.11a. When the droplet gradually shrank because of the evaporation, it maintained perfect spherical shape and the Θ_{CA} was retained higher than 160° during the whole evaporation process (84 min in total). This proved that the as-prepared PE-SNF-A film is able to prevent even a very tiny sized water droplet from penetrating into itself, indicating an excellent and stable non-wettability. Moreover, in Figure 4.4.11b, we found that when exposed to an extremely high humidity condition (~90%) for a long period, the as-prepared PE-SNF-A film constantly exhibited Θ_{CA} and Θ_{SA} of ~170° and ~3°, respectively. After 16 days of exposure, there was no notable decrease of Θ_{CA} or increase of Θ_{SA} observed, suggesting a rather stable superhydrophobicity to the high humidity environment.

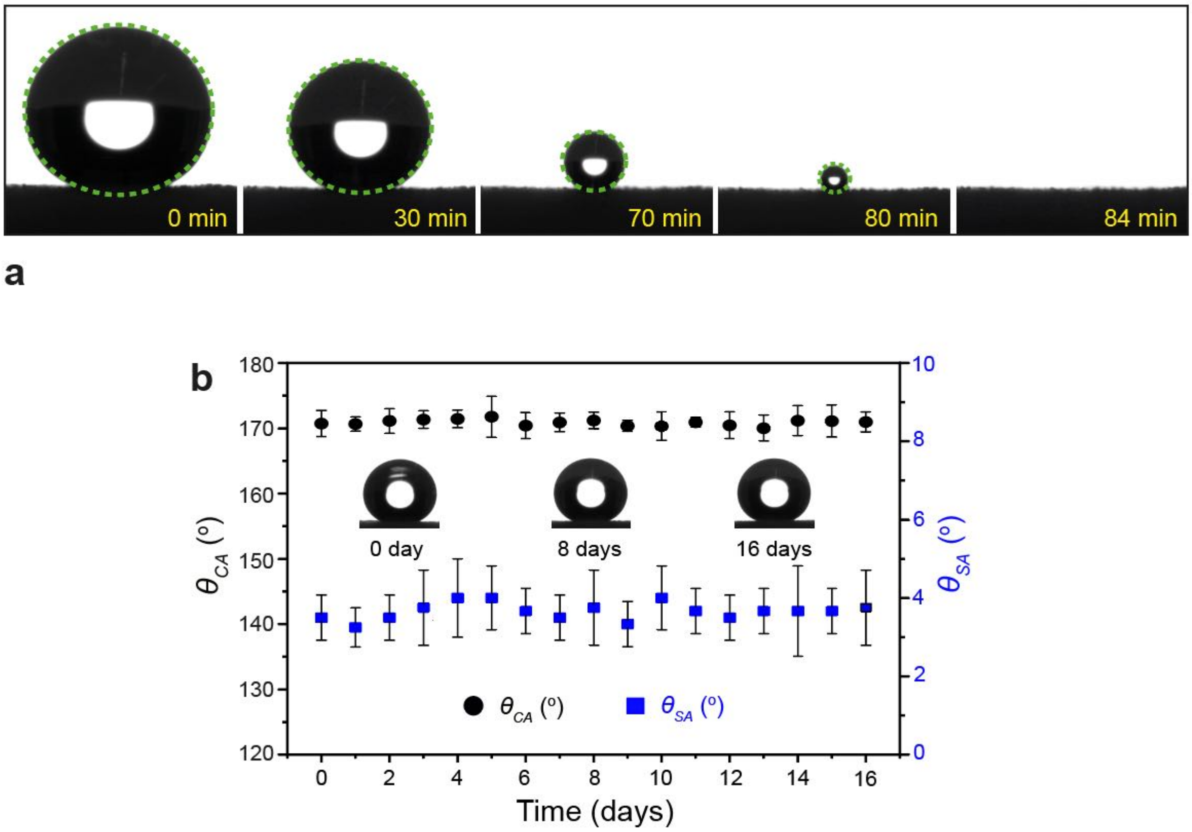

Figure 4.4.11 (a) A 10-µL droplet placed on the PE-SNF-A film gradually shrank over time due to the evaporation. The droplet maintained its perfect spherical shape with Θ_{CA} greater than 160° during the whole process. b) Θ_{CA} and Θ_{SA} of the as-prepared PE-SNF-A film as a function of time after being exposed to a ~90% humidity condition.

4.4.3 The Chemical Resistance Tests

To further assess the resistance of the superhydrophobicity to harsh chemical corrosions, several tests were conducted and reported.

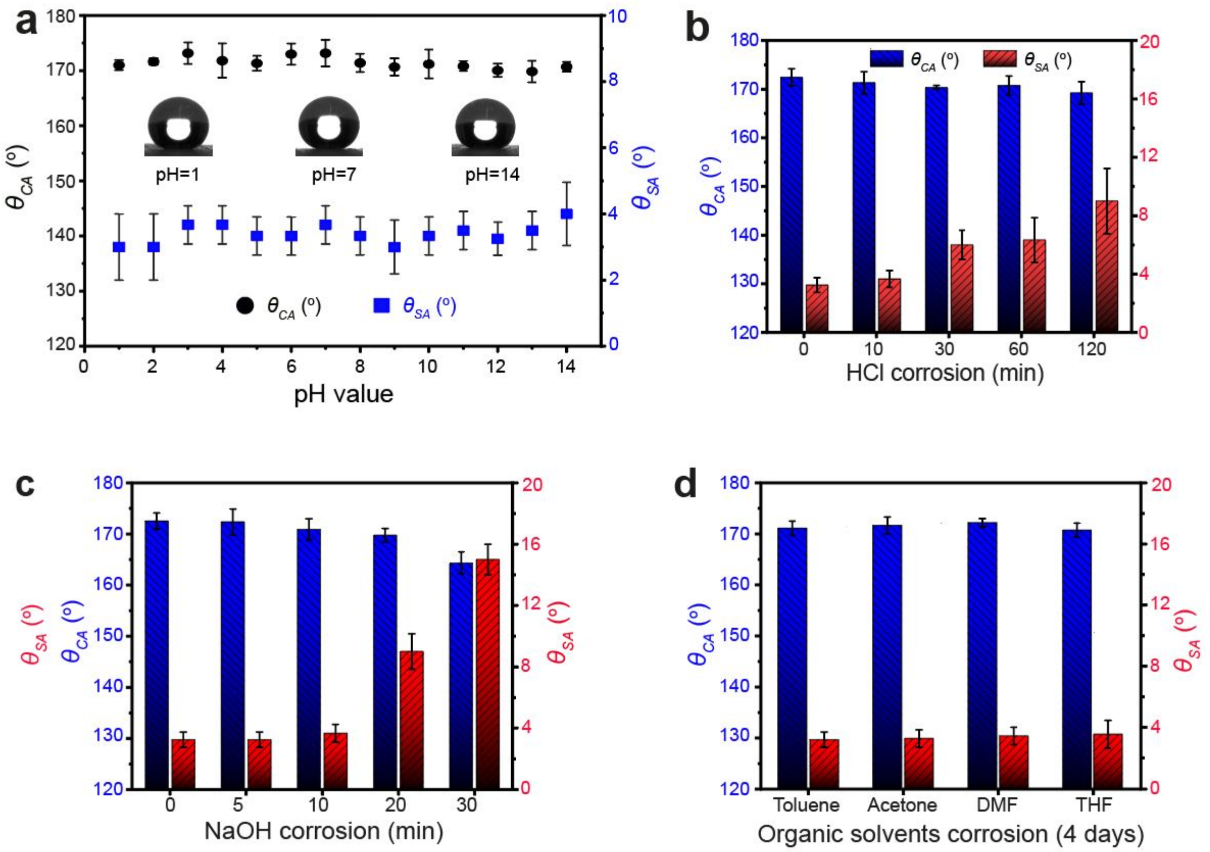

Figure 4.4.12 (a) Θ_{CA} and Θ_{SA} of the droplets of corrosive liquids with pH values vary from 1 to 14. Influence of (b) HCl and (c) NaOH solution on the water repellency of the PE-SNF-A film over time. (d) Θ_{CA} and Θ_{SA} of the PE-SNF-A film after 4 days corrosion in different organic solvents.

The obtained PE-SNF-A film presented with an excellent resistance with highly corrosive aqueous liquids, as shown in Figure 4.4.12a-c. In Figure 4.4.12a, all the corrosive liquid droplets varied from strong acid (pH 1) to strong base (pH 13), featuring all Θ_{CA} above 165° and Θ_{SA} below 5°.

The as-prepared PE-SNF-A films were also immersed in 0.1 M hydrochloric acid (HCl) and 0.1 M sodium hydroxide (NaOH) solutions. The water static Θ_{CA} and Θ_{SA} on the film as a function of corrosion time were collected and the results show the influence of corrosion time on Θ_{CA} and Θ_{SA} of the samples in HCl and NaOH solutions in Figure 4.4.12b and c, respectively. Strikingly, even with 2-hour HCl corrosion, the as-prepared film exhibited a stable superhydrophobicity, featuring Θ_{CA} and Θ_{SA} of ~ 169° and 9°, respectively (see in Figure 4.4.12b). In comparison, the Θ_{CA} and Θ_{SA} of the PE-SNF-A film also remained ~ 163° and ~ 15°

respectively, after 30 min corrosion in NaOH solution (in Figure 4.4.12c). Both cases suggested good survivability in strong acid and base solutions. Relatively higher resistance to acid solution was observed after comparison, which stems from the less activity of the silicone skeleton to hydrogen ions than to hydroxyl ions. SEM images of the PE-SNF-A surface show no observable damage after HCl and NaOH corrosion, which were presented in Figure 4.4.13a and b. Moreover, in contrast to the widely reported superhydrophobic surfaces prepared by spray coatings, the as-prepared PE-SNF-A film exhibited a rather stable superhydrophobicity to organic solvents, such as DMF, THF, toluene, etc.[202, 288] As shown in Figure 4.4.12d, the PE-SNF-A film maintained its excellent water repellency with a Θ_{CA} about 170° and Θ_{SA} about 3° after 4 days immersion in the above-mentioned organic solvents, and no obvious damage was observed from SEM images (in Figure 4.4.13c-f).

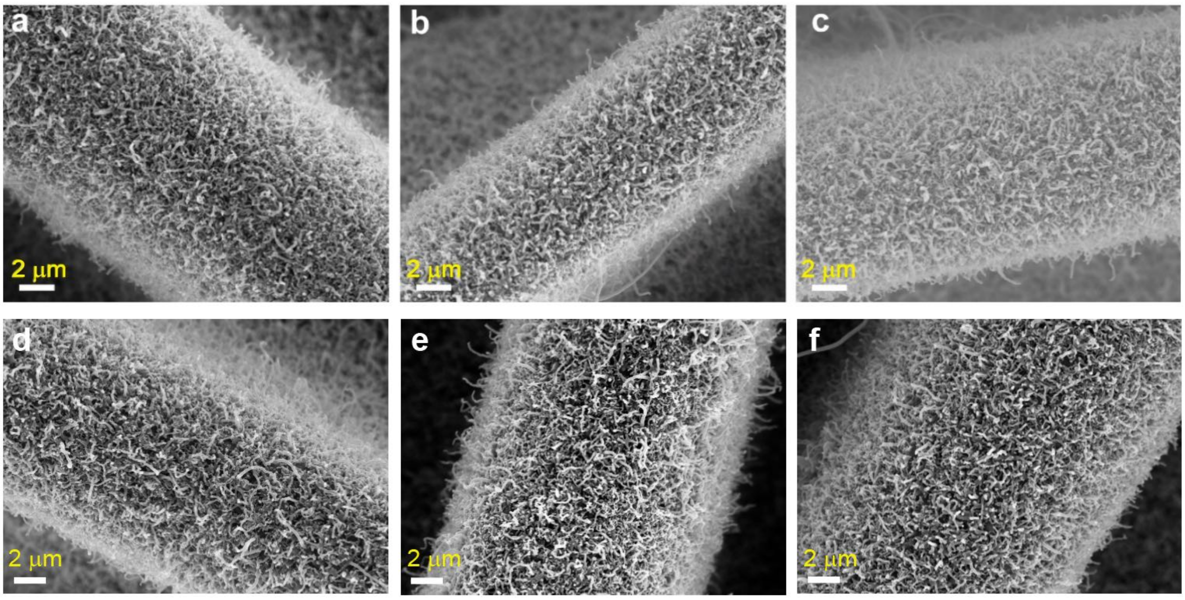

Figure 4.4.13 SEM images of the PE-SNF-A film surface after (a) 120-min corrosion in HCl, (b) 30-min corrosion in NaOH solution, and (c) 4 days corrosion in DMF. (d) tetrahydrofuran (THF), (e) acetone and (f) toluene.

Such stable superhydrophobicity and excellent resistance to chemical corrosions of the as-prepared PE-SNF-A film stem from the synergistic effect of the inherent chemical stability of the composite film and the micro/nano-hierarchical structured surface. The formed dual-scaled air pockets resulting from the trapped air within the micro/nanoscopic structure, prevented the water droplets and corrosive liquids from seeping through the film.

4.4.4 The Self-Cleaning Effect

Owing to its excellent superhydrophobicity, the PE-SNF-A film shows self-cleaning effect. The as-prepared PE-SNF-A film not only shows excellent water repellency, but also exhibits non-wettability to many other aqueous solutions such as soy sauce, coffee, wine, milk and cola (see in Figure 4.4.14).

Figure 4.4.14 Non-wettability behavior of PE-SNF-A film exposed to water, wine, cola, soy sauce, coffee and milk.

In Figure 4.4.15a and b, the self-cleaning effect of the film was demonstrated by using chalk powder as the mimic dirt. Micro/millimeter scaled powder particles were covered on the PE-SNF-A film. Water droplets were dropped on the surface and the dirt was picked up and taken away with the rolling down of the droplets. As a result, the surface became completely cleaned after removing all chalk powder by water droplets.

What’s more, the self-cleaning property of the as-prepared film functions as well after oil contamination when exposed to either air or oil. Figure 4.4.15c exhibited a water droplet forming a sphere and rolling off from the oil (hexadecane) immersed film surface instead of wetting or adhering on the surface. The phenomenon indicates that the film could maintain its self-cleaning functionality even after contaminated by organic solvent. In addition, the water droplets can still easily slip off from the contaminated surface after taking the sample out from the oil and exposing to air (Figure 4.4.15d and video is available online).

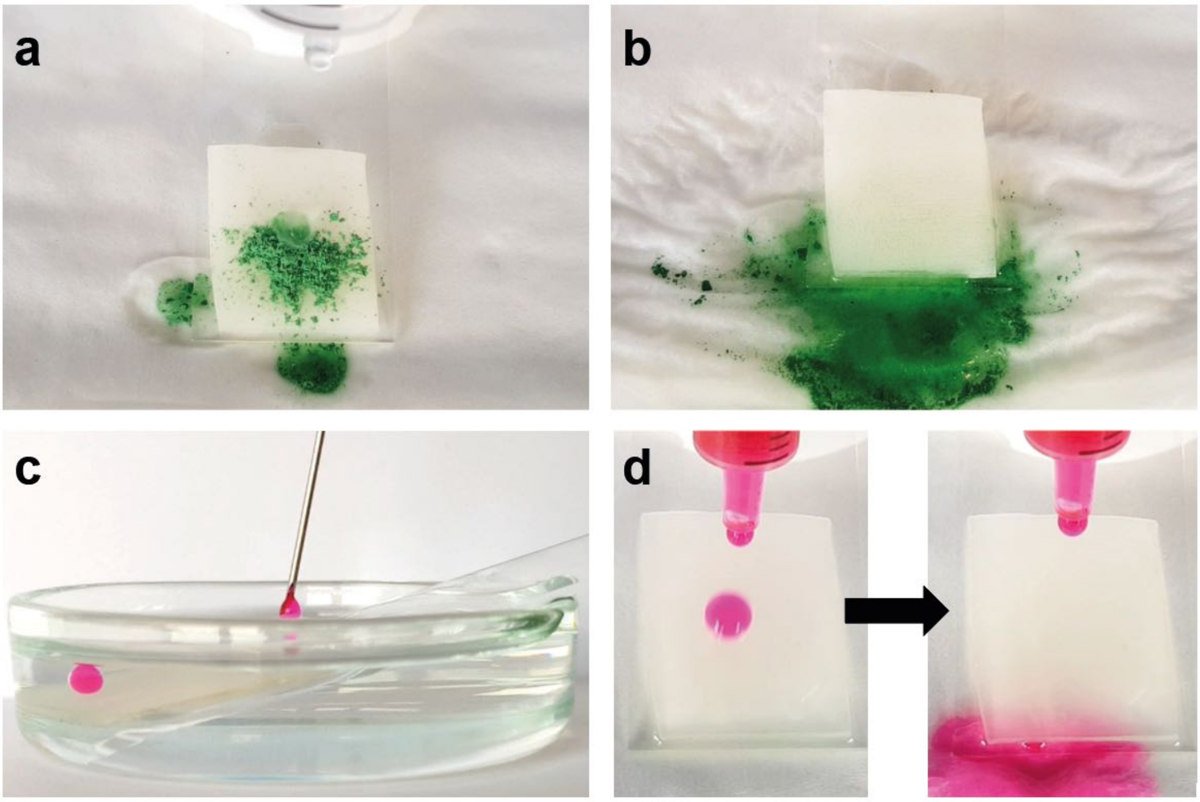

Figure 4.4.15 (a-b) Self-cleaning process on PE-SNF-A film surface when exposed to air. Chalk powder was used as the dirt to contaminate the surface. (c) Water droplet was slipping off from the film surface which was immersed under oil (hexadecane). (d) The proof that PE-SNF-A film surface retained its water repellency even after oil contamination.

Figure 6g-i shows a dirt-removal test on the PE-SNF-A film surface both in oil and air. The film was fully immersed into oil (hexadecane) followed by partly putting into the oil. The dirt (chalk powder) was also placed partly in oil and air onto the film surface, which was subsequently cleared by water (video available).

When the film was immersed in oil, the oil can gradually penetrate through its surface, and the water droplets were supported by both the micro/nanoscale structured surface and oil.[203] This results in similar water repellency and self-cleaning performance in oil to that in air.[289] In the air, after oil immersion, the hierarchical surface texture of the film can lock the oil contamination as a lubricating fluid leading to a slippery state,[290] as shown in Figure 6j. The dirt can be taken away from the film surface by the sliding over water drops. Hence, the oil contaminated film maintains its water repellency and self-cleaning functionality when exposed to either air or oil.

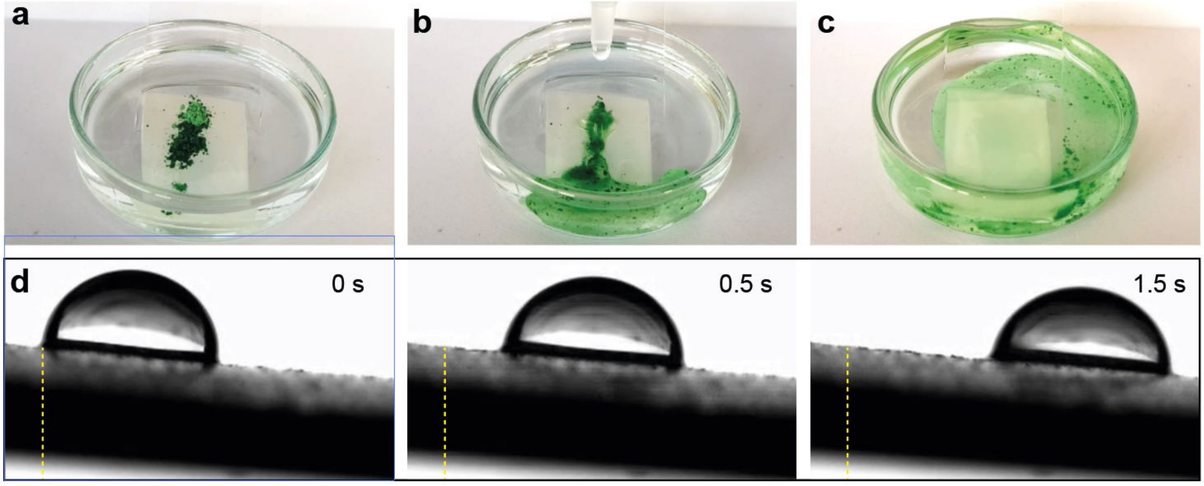

Figure 4.4.16. (a-c) Self-cleaning test at solid-oil-vapor interface. The dirt was partly put in oil and air (a), subsequently, the dirty was removed by water drops passing over the oil contaminated film surface (b) and became cleaned in (c). (d) Time resolved images showing a water droplet (10 µL) slipping off from the oil contaminated PE-SNF-A film surface.

Figure 4.4.16a-c shows a dirt-removal test on the PE-SNF-A film surface, which was half in the air and half in oil. The film was first fully immersed into oil (hexadecane) and then half of it was taken out of the oil. The dirt (chalk powder) was placed partly in the half exposed to the air and the other half which was still submerged under oil. As observed, a series of water droplets were dropped from the top of the film. Subsequently, the contaminated surface was cleared by water droplets (videos are available).

When the film was immersed in oil, the oil can gradually penetrate through its surface, and the water droplets were supported by both the micro/nanoscale structured surface and the oil, which formed a slippery slope.[291] This results in the similar water repellency and self-cleaning performance in oil to that in the air.[289] In the air, after oil immersion, the hierarchical surface structure of the film, or the space among SNFs can lock the oil contamination as a lubricating fluid leading to a slippery state, as shown in Figure 4.4.16d.[290] The dirt can be taken away from the film surface with the sliding water droplets. Hence, the oil contaminated film could still maintain its water repellency and self-cleaning functionality when exposed to either air or oil.

The project further continued the work of creating a robust self-cleaning surface. Instead of embedding GBs in LDPE film, the hierarchical structure was induced by annealing of the PE film and causing an intrinsic structure reformation. The reformation avoids problems like the loss of GBs on LDPE film in the last projects. Meanwhile, less materials and fewer steps are required in the procedure. Thus, the idea facilitates a more feasible approach in the case a large scale production is needed.

5 Summary and Outlook

Multifunctional nanocomposite materials are supposed to exhibit a variety of functions simultaneously apart from the primary functions. The need of excess components in forming a bulky material is eliminated by compositing one or more functional properties of subsystem in the total structure. As a result, the total system can benefit from the reduction of volume and mass as well as the improved efficiency. The design of multifunctional nanocomposite materials is still a challenge due to their complex structures. The fabrication process needs to ensure the addition of the desired functionalities and meanwhile preserve the primary properties. Thus, finding a facile, inexpensive, compatible system is of essential importance, which leads to our projects and this work.

Silicone nanofilaments fulfill the abovementioned requirement since the discovery in early 2000s due to the inexpensive precursors, facile and diverse synthesis methods, compatibility on various substrates and their intrinsic properties such as high surface-to-volume ratio and superhydrophobicity.

The first project focuses on forming a new composite structure, which combines the relatively stiff SNFs and soft and amorphous polystyrene (PS). We grafted SNFs with PS through a free radical polymerization of styrene in a water / ethanol mixture. The key to have surface grafted PS on SNFs includes two points: (1) the using of vinyltricholosilane as the precursor; (2) the right step for adding initiator and precursor. The SNFs formed by VTCS have vinyl bonds around the one-dimensional filament structure, which work as the initiating site of the surface grown PS. By adding a proper amount of AIBA before as initiator before the injection of precursor, the vinyl groups on SNFs were all activated, which leads to a higher amount of grafted PS on SNFs instead of polymerization in the bulk solution. The synthesized novel composite material has a tunable morphology. The methods to control the morphology of PS were proved to be easily operated and effective. Bead-shaped, leaf-shaped and well-wrapped PS structures were successfully achieved by using different combinations of solvents for post treatments.

The newly created composite material can be flexibly applied on various substrates. In the oil absorption capacity test, we applied the new composite material on a PE foam. Due to the oleophilicity of PS, the new material was more efficient in oil-water separation. For chloroform, octane and paraffin absorption, with the compositing of PS, new material exhibited correspondingly 22.75%, 33.65% and 16.21% more absorption capacity compared with the one without grafted PS. The oil absorption capacity mainly depends on the loading amount of PS. By changing the amount of initiator, different loading amounts of PS were controllably grafted on SNFs surface. Moreover, the composite material was introduced to act as a support material for depositing TiO_2 nanoparticles, which synthesized in situ through hydrolysis of TiF_4. The tuneable PS was proved to further extend the surface area by the morphology controlling after polymerization, resulting in a higher loading amount of TiO_2 NPs (from 2.59 to 3.55 μg/cm^2) and a correspondingly higher photocatalytic activity in a two-hour MB degradation under UV light (from 82.9% to 98.3%). The new catalytic composite was also verified to have stable performance after recyclability test. We believe that with the tuneable PS-SNFs structure, the novel composite will have various applications in heterogeneous catalysis, oil-water separation and other fields.

In the second part of the work, we have successfully synthesized a novel multifunctional composite material with superhydrophobicity, photocatalytic activity, and enhanced mechanical durability. This novel composite material can be categorized as one of the self-cleaning materials, which are of high popularity and interest due to their broad application scenarios in industry and daily life. The superhydrophobicity has been obtained by the convenient DAGS process: the reaction of a silane precursor ETCS, resulting in an SNFs coating layer with nanoscale roughness. The SNFs layer exhibited a water CA of 168°, non-wettability to various liquids, stability under UV irradiation and the self-cleaning effect with solid particles on its surface. TiO_2 NPs were deposited on SNFs, which work as a photocatalyst for the degradation of various organic compounds. It was proven that the photocatalytic property was stable by a repeated decomposition of oleic acid and a long-term experiment under daily UV exposure. To protect SNFs from different mechanical forces, GBs (75 μm) were embedded into an LDPE matrix to form a micro/nanoscale hierarchical structure. The abrasion tests showed a good retainability of superhydrophobicity and photocatalytic activity on the substrates with the hierarchical structure. The GBs density of 32 beads/mm^2 exhibited the highest enhancement of the robustness. We believe that with the improved mechanical resistance and the intrinsic multifunctionalities, the novel composite material reported will have a broad range of various applications in both industries and daily life in the future.

In the next part, for the first time, a system of noble metal NPs and SNFs was reported to be assembled, which can be used for SERS detection. We presented a simple and facile method to fabricate the AuNPs-SNFs composite functional material. The controlling of AuNPs size was achieved through a modified Turkevich method. Surface modifications facilitate the surface assembling of AuNPs on SNFs. The novel composite substrate exhibited great potential in SERS detection and heterogeneous catalysis. With an enhancement factor of ~10^9 and the good surface homogeneousness, the nanocomposite material was demonstrated to have outstanding SERS sensitivity and good reproducibility. AuNP18-SNFs shows the highest sensitivity among all tested substrates. At the same time, the functional substrates were verified with an improved heterogeneous catalytic activity compared with normal AuNPs substrates in the hydrogenation reaction. AuNP6-SNFs was proved to be the best catalytic substrates due to the fine dispersion of catalytic active sites and nanoscale effect. Remarkable resistance to catalyst leaching was observed for all AuNPs-SNFs substrates. We found that SNFs act as an ideal support material in both of the applications. With the demonstrated properties in our experiments, the novel AuNPs-SNFs substrate will have a big potential in commercial applications in the future.

In the last project, we sought for an easy and solvent-free method to fabricate flexible superhydrophobic PE film-SNFs composite with multiscale hierarchical structure. The creation of the two-scale hierarchical structure can be accomplished easily by heating the SNFs coated PE film to the melting point with a quick cooling down at room temperature. The obtained film exhibits a stable superhydrophobicity with a water CA of around 170° and SA below 4° due to its micro/nanoscale hierarchical surface roughness and low surface tension. Furthermore, the film was proved to remain its water repellency under a variety of harsh mechanical and chemical environments such as, tape-peeling, abrasion, knife-cutting, finger-wiping, flexing, and corrosions from strong acid/base solutions and various organic solvents. In addition, even after oil contamination, the composite film maintains its water repellency and self-cleaning functionalities when exposed to either air or oil. The robust water repellency of the flexible composite film potentially endows its practical applications in various industrial scenario as well as in daily life.

All in all, the results from all the presented work successfully demonstrated that SNFs, as a core structural component, can be utilized in the synthesis of various multifunctional composite materials. The unique carpet-like topography endows the surface roughness in nanoscale when SNFs are applied as a coating layer on different kinds of substrates. Together with the low surface tension of the residue group from the silane precursor, SNFs exhibited tremendous superhydrophobicity as the main property. Thus, SNFs can be applied as the self-cleaning material, since most of the self-cleaning materials adapt the superhydrophobic property instead of hydrophilicity. The type of NPs, which can be composited on SNFs, can be multiple. Noble metal NPs such as AuNPs and metal oxide NPs like TiO_2NPs can be deposited either through a surface deposition assembling or in situ precipitation. By exploiting the functionalities of the NPs, the SNFs composite materials can be much more broadly used in different application scenarios, which can be but not limited to sensing, detection, catalysis, stimulus responding, light-emission and so on. The approach, which can further extend the existing high surface-to-volume ratio of SNFs was also verified to be facile and feasible. Through the flexible morphology controllability of PS, the primary properties, like oil-absorption capacity and catalytic activity, were enhanced. In order to achieve widely practical applications, the efforts to increase the mechanical durability were also paid back. Two approaches by either embedding objectives or changing the morphology lead to the formation of hierarchical structures. Arising from the results, we can predict the bright future that SNFs play a more important role in industry and research.

6 References

1. Narayana, K. J.; Gupta Burela, R., *Materials Today: Proceedings* **2018,** *5* (2, Part 1), 5580-5590. DOI https://doi.org/10.1016/j.matpr.2017.12.149.

2. Sairajan, K. K.; Aglietti, G. S.; Mani, K. M., *Acta Astronautica* **2016,** *120*, 30-42. DOI 10.1016/j.actaastro.2015.11.024.

3. Ferreira, A. D. B. L.; Nóvoa, P. R. O.; Marques, A. T., *Composite Structures* **2016,** *151*, 3-35. DOI https://doi.org/10.1016/j.compstruct.2016.01.028.

4. Young, T., *Philosophical Transactions of the Royal Society of London* **1805,** *95*, 65-87. DOI 10.1098/rstl.1805.0005.

5. Bonn, D.; Eggers, J.; Indekeu, J.; Meunier, J.; Rolley, E., *Reviews of Modern Physics* **2009,** *81* (2), 739-805. DOI 10.1103/RevModPhys.81.739.

6. de Gennes, P. G., *Reviews of Modern Physics* **1985,** *57* (3), 827-863. DOI 10.1103/RevModPhys.57.827.

7. Rimmer, A.; Parlange, J. Y.; Steenhuis, T. S.; Darnault, C.; Condit, W., *Transport in Porous Media* **1996,** *25* (2), 205-215. DOI 10.1007/BF00135856.

8. Darmanin, T.; Guittard, F., *Materials Today* **2015,** *18* (5), 273-285. DOI https://doi.org/10.1016/j.mattod.2015.01.001.

9. Owens, D. K.; Wendt, R. C., *J Appl Polym Sci* **1969,** *13* (8), 1741-1747. DOI 10.1002/app.1969.070130815.

10. Wenzel, R. N., *Industrial & Engineering Chemistry* **1936,** *28* (8), 988-994. DOI 10.1021/ie50320a024.

11. Cassie, A. B. D.; Baxter, S., *T Faraday Soc* **1944,** *40* (0), 546-551. DOI 10.1039/TF9444000546.

12. Giacomello, A.; Meloni, S.; Chinappi, M.; Casciola, C. M., *Langmuir* **2012,** *28* (29), 10764-10772. DOI 10.1021/la3018453.

13. Vrancken, R. J.; Kusumaatmaja, H.; Hermans, K.; Prenen, A. M.; Pierre-Louis, O.; Bastiaansen, C. W. M.; Broer, D. J., *Langmuir* **2010,** *26* (5), 3335-3341. DOI 10.1021/la903091s.

14. Lafuma, A.; Quéré, D., *Nature Materials* **2003,** *2*, 457. DOI 10.1038/nmat924.

15. Wong, W. S. Y.; Nasiri, N.; Rodriguez, A. L.; Nisbet, D. R.; Tricoli, A., *J Mater Chem A* **2014,** *2* (37), 15575-15581. DOI 10.1039/C4TA03278K.

16. Li, H. M.; Zhang, Q. G.; Guo, N. N.; Zhu, A. M.; Liu, Q. L., *Chem. Eng. J.* **2015,** *264*, 329-335. DOI 10.1016/j.cej.2014.11.118.

17. Boinovich, L. B.; Emelyanenko, A. M.; Ivanov, V. K.; Pashinin, A. S., *Acs Appl Mater Inter* **2013,** *5* (7), 2549-2554. DOI 10.1021/am3031272.
18. Wu, D.; Wu, S.-Z.; Chen, Q.-D.; Zhang, Y.-L.; Yao, J.; Yao, X.; Niu, L.-G.; Wang, J.-N.; Jiang, L.; Sun, H.-B., *Adv Mater* **2011,** *23* (4), 545-549. DOI 10.1002/adma.201001688.
19. Zhao, S.; Xia, H.; Wu, D.; Lv, C.; Chen, Q.-D.; Ariga, K.; Liu, L.-Q.; Sun, H.-B., *Soft Matter* **2013,** *9* (16), 4236-4240. DOI 10.1039/C3SM27871A.
20. Nishino, T.; Meguro, M.; Nakamae, K.; Matsushita, M.; Ueda, Y., *Langmuir* **1999,** *15* (13), 4321-4323. DOI 10.1021/la981727s.
21. Vakarelski, I. U.; Patankar, N. A.; Marston, J. O.; Chan, D. Y. C.; Thoroddsen, S. T., *Nature* **2012,** *489* (7415), 274-277. DOI 10.1038/nature11418.
22. Furmidge, C. G. L., *Journal of Colloid Science* **1962,** *17* (4), 309-324. DOI https://doi.org/10.1016/0095-8522(62)90011-9.
23. Crawford, R.; Koopal, L. K.; Ralston, J., *Colloids and Surfaces* **1987,** *27* (4), 57-64. DOI https://doi.org/10.1016/0166-6622(87)80133-6.
24. Johnson, R. E.; Dettre, R. H., *The Journal of Physical Chemistry* **1964,** *68* (7), 1744-1750. DOI 10.1021/j100789a012.
25. Patankar, N. A., *Langmuir* **2010,** *26* (10), 7498-7503. DOI 10.1021/la904286k.
26. Feng, X. J.; Jiang, L., *Adv Mater* **2006,** *18* (23), 3063-3078. DOI 10.1002/adma.200501961.
27. He, B.; Lee, J.; Patankar, N. A., *Colloids and Surfaces A: Physicochemical and Engineering Aspects* **2004,** *248* (1), 101-104. DOI https://doi.org/10.1016/j.colsurfa.2004.09.006.
28. Gould, R. F., Contact Angle, Wettability, and Adhesion, Copyright, Advances in Chemistry Series. In *Contact Angle, Wettability, and Adhesion*, Robert, F. G., Ed. AMERICAN CHEMICAL SOCIETY: 1964; Vol. 43, pp i-iii.
29. Dettre, R. H.; Johnson, R. E., Contact Angle Hysteresis. In *Contact Angle, Wettability, and Adhesion*, AMERICAN CHEMICAL SOCIETY: 1964; Vol. 43, pp 136-144.
30. Öner, D.; McCarthy, T. J., *Langmuir* **2000,** *16* (20), 7777-7782. DOI 10.1021/la000598o.
31. Wake, W. C., *British Polymer Journal* **1988,** *20* (5), 452-452. DOI 10.1002/pi.4980200518.

32. Baney, R. H.; Itoh, M.; Sakakibara, A.; Suzuki, T., *Chem. Rev.* **1995,** *95* (5), 1409-1430. DOI 10.1021/cr00037a012.

33. Silicones, U., **2015**.

34. Chandra, G.; Maxim, L. D.; Sawano, T., The Silicone Industry and its Environmental Impact. In *Organosilicon Materials*, Chandra, G., Ed. Springer Berlin Heidelberg: Berlin, Heidelberg, 1997; pp 295-319.

35. Kipping, F. S.; Lloyd, L. L., *Journal of the Chemical Society, Transactions* **1901,** *79* (0), 449-459. DOI 10.1039/CT9017900449.

36. James E. Mark, H. R. A., Robert West, *Inorganic Polymers*. Oxford University Express: UK, **2005**.

37. Owen, M. J., *Industrial & Engineering Chemistry Product Research and Development* **1980,** *19* (1), 97-103. DOI 10.1021/i360073a023.

38. Zhou, W.; Yang, H.; Guo, X.; Lu, J., *Polymer Degradation and Stability* **2006,** *91* (7), 1471-1475. DOI https://doi.org/10.1016/j.polymdegradstab.2005.10.005.

39. Dietrich, H., *Angewandte Chemie* **1961,** *73* (14), 511-512. DOI 10.1002/ange.19610731425.

40. Dove, M. T.; Keen, D. A.; Hannon, A. C.; Swainson, I. P., *Physics and Chemistry of Minerals* **1997,** *24* (4), 311-317. DOI 10.1007/s002690050043.

41. Mcmurry, J. E., *Organic Chemistry* Cengage Learning: USA, **1992**.

42. Colas, A. Silicones: Preparation, Properties and Performance. (accessed 29-Sep).

43. Mazurek, M. H., 3.12 - Silicones. In *Comprehensive Organometallic Chemistry III*, Mingos, D. M. P.; Crabtree, R. H., Eds. Elsevier: Oxford, 2007; pp 651-697.

44. Murphy, J., CHAPTER 17 - Modifying Processing Characteristics: Lubricants, Mould Release Agents, Anti-slip and Anti-blocking. In *Additives for Plastics Handbook (Second Edition)*, Murphy, J., Ed. Elsevier Science: Amsterdam, 2001; pp 205-218.

45. Fearon, F. W. G. In *History of Silicone Elastomers*, High Performance Polymers: Their Origin and Development, Dordrecht, 1986//; Seymour, R. B.; Kirshenbaum, G. S., Eds. Springer Netherlands: Dordrecht, **1986**; pp 381-388.

46. Narisawa, M., *Materials* **2010,** *3* (6), 3518-3536. DOI 10.3390/ma3063518.

47. Reitmeier, L. R. P. J. R., Silicon Compounds, Organic. In *Ullmann's Encyclopedia of Industrial Chemistry*, 2000.

48. Jeon, M.; Han, J.; Park, J., *Acs Catal* **2012,** *2* (8), 1539-1549. DOI 10.1021/cs300296x.

49. Vorotyntsev, V. M.; Drozdov, P. N.; Vorotyntsev, I. V.; Manokhina, S. N.; Knysh, S. S., *Petroleum Chemistry* **2013,** *53* (8), 627-631. DOI 10.1134/S0965544113080161.

50. Lickiss, P. D., *Advances in Inorganic Chemistry* **1995,** *42*, 147-262. DOI https://doi.org/10.1016/S0898-8838(08)60053-7.

51. Fadeev, A. Y.; McCarthy, T. J., *Langmuir* **2000,** *16* (18), 7268-7274. DOI 10.1021/la000471z.

52. Fadeev, A. Y.; McCarthy, T. J., *Langmuir* **1999,** *15* (11), 3759-3766. DOI 10.1021/la981486o.

53. Artus, G. R. J.; Olveira, S.; Patra, D.; Seeger, S., *Macromol Rapid Comm* **2017,** *38* (4), 1-9. DOI 10.1002/marc.201600558.

54. Stojanovic, A.; Olveira, S.; Fischer, M.; Seeger, S., *Chem Mater* **2013,** *25* (14), 2787-2792. DOI 10.1021/cm400851k.

55. Mizoshita, N.; Tani, T.; Inagaki, S., *Chem Soc Rev* **2011,** *40* (2), 789-800. DOI 10.1039/C0CS00010H.

56. Artus, G.; Zimmermann, J.; Seeger, S.; Jung, S. Superhydrophobic Coating, EP 1644450. **2003**.

57. Artus, G. R. J.; Olveira, S.; Patra, D.; Seeger, S., Directed In Situ Shaping of Complex Nano- and Microstructures during Chemical Synthesis. In *Macromolecular Rapid Communications*, **2017**; Vol. 38.

58. Artus, G. R. J.; Jung, S.; Zimmermann, J.; Gautschi, H. P.; Marquardt, K.; Seeger, S., *Advanced Materials* **2006,** *18* (20), 2758-+.

59. Zhang, J.; Wang, A.; Seeger, S., *Polym Chem-Uk* **2014,** *5* (4), 1132-1139. DOI 10.1039/C3PY01293J.

60. Meier, M.; Suppiger, A.; Eberl, L.; Seeger, S., *Small* **2017,** *13* (4).

61. Chu, Z.; Seeger, S., *Adv Mater* **2015,** *27* (47), 7775-7781. DOI 10.1002/adma.201503502.

62. Zhang, X.; Seeger, S., *ChemNanoMat* **2019,** *5* (7), 964-971. DOI 10.1002/cnma.201900161.

63. Yang, P.; Yang, W., *Acs Appl Mater Inter* **2014,** *6* (6), 3759-3770. DOI 10.1021/am405857m.

64. Su, L.; Li, J.; Li, J.; Chu, Q.; Li, B.; Liu, Y., *Advances in Polymer Technology* **2019,** *2019*, 8. DOI 10.1155/2019/7831619.

65. Crabtree, R. H., *Journal of the Chemical Society, Dalton Transactions* **2001,** (17), 2437-2450. DOI 10.1039/B103147N.

66. Ferguson, G. S.; Chaudhury, M. K.; Biebuyck, H. A.; Whitesides, G. M., *Macromolecules* **1993,** *26* (22), 5870-5875. DOI 10.1021/ma00074a007.

67. Wagner, R. S.; Ellis, W. C., *Applied Physics Letters* **1964,** *4* (5), 89-90. DOI 10.1063/1.1753975.

68. Redwing, J. M.; Miao, X.; Li, X., 9 - Vapor-Liquid-Solid Growth of Semiconductor Nanowires. In *Handbook of Crystal Growth (Second Edition)*, Kuech, T. F., Ed. North-Holland: Boston, 2015; pp 399-439.

69. Wang, F.; Dong, A.; Sun, J.; Tang, R.; Yu, H.; Buhro, W. E., *Inorganic Chemistry* **2006,** *45* (19), 7511-7521. DOI 10.1021/ic060498r.

70. Cassie, A. B. D.; Baxter, S., *Transactions of the Faraday Society* **1944,** *40*, 0546-0550.

71. Zimmermann, J. Z., CH), Seeger, Stefan (Zumikon, CH), Artus, Georg (Birmensdorf, CH), Jung, Stefan (Kilchberg, CH) Superhydrophobic Coating. **2007**.

72. Zhang, J. P.; Seeger, S., *Angew Chem Int Edit* **2011,** *50* (29), 6652-6656.

73. Chu, Z.; Feng, Y.; Seeger, S., *Angew Chem Int Edit* **2015,** *54* (8), 2328-2338. DOI 10.1002/anie.201405785.

74. Zimmermann, J.; Rabe, M.; Verdes, D.; Seeger, S., *Langmuir* **2008,** *24* (3), 1053-1057.

75. M Cox, D., *High Surface Area Materials*. **1999**.

76. Zimmermann, J.; Rabe, M.; Artus, G. R. J.; Seeger, S., *Soft Matter* **2008,** *4* (3), 450-452.

77. Nasir, A.; Kausar, A., *Polym-Plast Technol* **2015,** *54* (17), 1819-1849.

78. Ming, W.; Jones, F. N.; Fu, S. K., *Macromolecular Chemistry and Physics* **1998,** *199* (6), 1075-1079.

79. Kaseem, M.; Hamad, K.; Ko, Y. G., *Eur Polym J* **2016,** *79*, 36-62.

80. Liebig, J., *Annalen der Chemie* **1832**, v.

81. Ringsdorf, H., *Angewandte Chemie International Edition* **2004,** *43* (9), 1064-1076. DOI 10.1002/anie.200330071.

82. Seo, M. K.; Park, S. J., *Chem Phys Lett* **2004,** *395* (1-3), 44-48.

---

83. Subramaniam, K.; Das, A.; Steinhauser, D.; Kluppel, M.; Heinrich, G., *Eur Polym J* **2011,** *47* (12), 2234-2243.
84. Boonmahitthisud, A.; Chuayjuljit, S., *Polym-Plast Technol* **2012,** *51* (3), 311-316.
85. CHEN Zhuo, Z. P., ZHANG Jian-Hui, WANG Zhen-Lin, ZHANG Wei-Yi, MIN Nai-Ben, *Chin. Phys. Lett.* **2003,** (8), 1369-1371%V 20.
86. Abdelrahman, A. I.; Thickett, S. C.; Liang, Y.; Ornatsky, O.; Baranov, V.; Winnik, M. A., *Macromolecules* **2011,** *44* (12), 4801-4813. DOI 10.1021/ma200582q.
87. Kumar, S.; Rath, T.; Mahaling, R. N.; Das, C. K., *Composites Part A: Applied Science and Manufacturing* **2007,** *38* (5), 1304-1317. DOI https://doi.org/10.1016/j.compositesa.2006.11.006.
88. A. Aly, M. M. a. A. O., *World Journal of Nano Science and Engineering* **2012,** *2* (2), 103-109. DOI doi: 10.4236/wjnse.2012.22013.
89. Rabee, B.; Hashim, A., *European Journal of Scientific Research* **2011,** *60*.
90. Yang, J.; Wu, M.; Chen, F.; Fei, Z.; Zhong, M., *Journal of Supercritical Fluids - J SUPERCRIT FLUID* **2011,** *56*, 201-207. DOI 10.1016/j.supflu.2010.12.014.
91. Zhang, S.-W.; Zhou, S.-X.; Weng, Y.-M.; Wu, L.-M., *Langmuir* **2005,** *21* (6), 2124-2128. DOI 10.1021/la047652b.
92. Bose, S.; Mukherjee, M.; Das, C. K., *Polym-Plast Technol* **2009,** *48* (2), 158-163. DOI 10.1080/03602550802577346.
93. Watanabe, Y.; Okuno, M.; Shimizu, Y.; Kanetaka, H.; Inamura, T.; Hosoda, H., *Advanced Materials Research* **2012,** *409*, 645-650. DOI 10.4028/www.scientific.net/AMR.409.645.
94. Wackerly, J. W.; Dunne, J. F., *Journal of Chemical Education* **2017,** *94* (11), 1790-1793. DOI 10.1021/acs.jchemed.6b00814.
95. Rudin, A.; Choi, P., Chapter 8 - Free-Radical Polymerization. In *The Elements of Polymer Science & Engineering (Third Edition)*, Rudin, A.; Choi, P., Eds. Academic Press: Boston, 2013; pp 341-389.
96. Engelhardt, H.; Holding, S., *Chromatographia* **2008,** *68* (11), 1079-1080. DOI 10.1365/s10337-008-0891-0.
97. Halake, K.; Bae, S.; Lee, J.; Cho, Y.; Jo, H.; Heo, J.; Park, K.; Kim, H.; Ju, H.; Kim, Y.; Hasani, A.; Pham, T. D.; Choi, J.; Hong, S.; Choi, S.; Lee, J., *Macromol Res* **2019,** *27* (2), 109-114. DOI 10.1007/s13233-019-7083-7.

98. Wang, B.; Wan, Y.; Zheng, G.; Hu, J., *Environmental Science & Technology* **2016,** *50* (6), 2956-2963. DOI 10.1021/acs.est.5b05755.

99. Nguyen, D. D.; Tai, N.-H.; Lee, S.-B.; Kuo, W.-S., *Energy & Environmental Science* **2012,** *5* (7), 7908-7912. DOI 10.1039/C2EE21848H.

100. Calcagnile, P.; Fragouli, D.; Bayer, I. S.; Anyfantis, G. C.; Martiradonna, L.; Cozzoli, P. D.; Cingolani, R.; Athanassiou, A., *ACS Nano* **2012,** *6* (6), 5413-5419. DOI 10.1021/nn3012948.

101. Gupta, R. K.; Dunderdale, G. J.; England, M. W.; Hozumi, A., *J Mater Chem A* **2017,** *5* (31), 16025-16058. DOI 10.1039/C7TA02070H.

102. Kang, Z.; Wang, S.; Fan, L.; Xiao, Z.; Wang, R.; Sun, D., *Mater Lett* **2017,** *189*, 82-85. DOI https://doi.org/10.1016/j.matlet.2016.11.088.

103. Zhang, F.; Zhang, W. B.; Shi, Z.; Wang, D.; Jin, J.; Jiang, L., *Adv Mater* **2013,** *25* (30), 4192-4198. DOI 10.1002/adma.201301480.

104. Li, B.; Liu, X.; Zhang, X.; Chai, W., *Eur Polym J* **2015,** *73*, 374-379. DOI https://doi.org/10.1016/j.eurpolymj.2015.10.031.

105. Raza, A.; Ding, B.; Zainab, G.; El-Newehy, M.; Al-Deyab, S. S.; Yu, J., *J Mater Chem A* **2014,** *2* (26), 10137-10145. DOI 10.1039/C4TA00806E.

106. Xue, Z.; Wang, S.; Lin, L.; Chen, L.; Liu, M.; Feng, L.; Jiang, L., *Adv Mater* **2011,** *23* (37), 4270-4273. DOI 10.1002/adma.201102616.

107. Zhou, X.; Zhang, Z.; Xu, X.; Guo, F.; Zhu, X.; Men, X.; Ge, B., *Acs Appl Mater Inter* **2013,** *5* (15), 7208-7214. DOI 10.1021/am4015346.

108. Wang, B.; Li, J.; Wang, G.; Liang, W.; Zhang, Y.; Shi, L.; Guo, Z.; Liu, W., *Acs Appl Mater Inter* **2013,** *5* (5), 1827-1839. DOI 10.1021/am303176a.

109. Ge, B.; Men, X.; Zhu, X.; Zhang, Z., *Journal of Materials Science* **2015,** *50* (6), 2365-2369. DOI 10.1007/s10853-014-8756-4.

110. Cao, N.; Yang, B.; Barras, A.; Szunerits, S.; Boukherroub, R., *Chem. Eng. J.* **2017,** *307*, 319-325. DOI https://doi.org/10.1016/j.cej.2016.08.105.

111. Yong, J.; Chen, F.; Yang, Q.; Bian, H.; Du, G.; Shan, C.; Huo, J.; Fang, Y.; Hou, X., *Adv Mater Interfaces* **2016,** *3* (7), 1500650. DOI 10.1002/admi.201500650.

112. Zhang, S.; Lu, F.; Tao, L.; Liu, N.; Gao, C.; Feng, L.; Wei, Y., *Acs Appl Mater Inter* **2013,** *5* (22), 11971-11976. DOI 10.1021/am403203q.

113. Zhang, J.; Seeger, S., *Adv Funct Mater* **2011,** *21* (24), 4699-4704. DOI 10.1002/adfm.201101090.

114. Chu, Z. L.; Seeger, S., *Adv Mater* **2015,** *27* (47), 7775-7781.

115. Kao, J.; Thorkelsson, K.; Bai, P.; Rancatore, B. J.; Xu, T., *Chem Soc Rev* **2013,** *42* (7), 2654-2678. DOI 10.1039/C2CS35375J.

116. Choi, C. L.; Alivisatos, A. P., *Annual Review of Physical Chemistry* **2010,** *61* (1), 369-389. DOI 10.1146/annurev.physchem.012809.103311.

117. Jeevanandam, J.; Barhoum, A.; Chan, Y. S.; Dufresne, A.; Danquah, M. K., *Beilstein J Nanotech* **2018,** *9*, 1050-1074. DOI 10.3762/bjnano.9.98.

118. Lee, S.-Y.; Park, S.-J., *J Ind Eng Chem* **2013,** *19* (6), 1761-1769. DOI https://doi.org/10.1016/j.jiec.2013.07.012.

119. Heikkinen, M.; Poutiainen, H.; Liukkonen, M.; Heikkinen, T.; Hiltunen, Y., *Mathematics and Computers in Simulation* **2011,** *82* (3), 450-459. DOI https://doi.org/10.1016/j.matcom.2010.10.021.

120. Hanay, Ö.; Hasar, H., *J Hazard Mater* **2011,** *189* (1), 572-576. DOI https://doi.org/10.1016/j.jhazmat.2011.02.073.

121. Ayodele, O. B.; Hameed, B. H., *J Ind Eng Chem* **2013,** *19* (3), 966-974. DOI https://doi.org/10.1016/j.jiec.2012.11.018.

122. Zhao, H.; Liu, L.; Andino, J. M.; Li, Y., *J Mater Chem A* **2013,** *1* (28), 8209-8216. DOI 10.1039/C3TA11226H.

123. De Angelis, F.; Di Valentin, C.; Fantacci, S.; Vittadini, A.; Selloni, A., *Chem. Rev.* **2014,** *114* (19), 9708-9753. DOI 10.1021/cr500055q.

124. Bessekhouad, Y.; Robert, D.; Weber, J., *Journal of Photochemistry and Photobiology A: Chemistry* **2003,** *157*, 47-53. DOI 10.1016/S1010-6030(03)00077-7.

125. Chae, S. Y.; Park, M. K.; Lee, S. K.; Kim, T. Y.; Kim, S. K.; Lee, W. I., *Chem Mater* **2003,** *15* (17), 3326-3331. DOI 10.1021/cm030171d.

126. Fujishima, A.; Rao, T. N.; Tryk, D. A., *Electrochim Acta* **2000,** *45* (28), 4683-4690.

127. Harifi, T.; Montazer, M., *Applied Catalysis A: General* **2014,** *473*, 104–115. DOI 10.1016/j.apcata.2014.01.005.

128. Wang, N.; Li, J.; Zhu, L.; Dong, Y.; Tang, H., *Journal of Photochemistry and Photobiology A: Chemistry* **2008,** *198* (2), 282-287. DOI https://doi.org/10.1016/j.jphotochem.2008.03.021.

129. Ghanem, A.; Badawy, A.; Ismail, N.; Tian, Z.; Abdel Rehim, M.; Rabia, A., *Applied Catalysis A: General* **2014,** *472*, 191–197. DOI 10.1016/j.apcata.2013.12.023.

130. Xiao, X.; Liu, X.; Cao, G.; Zhang, C.; Xia, L.; Xu, W.; Xiao, S., *Polymer Engineering & Science* **2015,** *55* (6), 1296-1302. DOI 10.1002/pen.24068.

131. Arain, R. A.; Khatri, Z.; Memon, M. H.; Kim, I.-S., *Carbohyd Polym* **2013,** *96* (1), 326-331. DOI https://doi.org/10.1016/j.carbpol.2013.04.004.

132. Zhang, X.; Liu, S.; Salim, A.; Seeger, S., *Small* **2019,** *15* (34), 1901822. DOI 10.1002/smll.201901822.

133. Johnson, R. E.; Dettre, R. H., *Journal of Physical Chemistry* **1964,** *68* (7), 1744-&.

134. Gao, X. F.; Jiang, L., *Nature* **2004,** *432* (7013), 36-36.

135. Zhang, G. M.; Zhang, J.; Xie, G. Y.; Liu, Z. F.; Shao, H. B., *Small* **2006,** *2* (12), 1440-1443.

136. Ganesh, V. A.; Raut, H. K.; Nair, A. S.; Ramakrishna, S., *Journal of Materials Chemistry* **2011,** *21* (41), 16304-16322.

137. Parkin, I. P.; Palgrave, R. G., *Journal of Materials Chemistry* **2005,** *15* (17), 1689-1695.

138. Ragesh, P.; Ganesh, V. A.; Naira, S. V.; Nair, A. S., *Journal of Materials Chemistry A* **2014,** *2* (36), 14773-14797.

139. Jin, M. H.; Feng, X. J.; Xi, J. M.; Zhai, J.; Cho, K. W.; Feng, L.; Jiang, L., *Macromolecular Rapid Communications* **2005,** *26* (22), 1805-1809.

140. Onda, T.; Shibuichi, S.; Satoh, N.; Tsujii, K., *Langmuir* **1996,** *12* (9), 2125-2127. DOI 10.1021/la950418o.

141. Barthlott, W.; Neinhuis, C., *Planta* **1997,** *202* (1), 1-8.

142. Chu, Z. L.; Seeger, S., *Chemical Society Reviews* **2014,** *43* (8), 2784-2798.

143. Zhang, X.; Shi, F.; Niu, J.; Jiang, Y.; Wang, Z., *Journal of Materials Chemistry* **2008,** *18* (6), 621-633. DOI 10.1039/B711226B.

144. Nakajima, A., *Npg Asia Materials* **2011,** *3*, 49. DOI 10.1038/asiamat.2011.55.

145. Crick, C. R.; Ismail, S.; Pratten, J.; Parkin, I. P., *Thin Solid Films* **2011,** *519* (11), 3722-3727. DOI https://doi.org/10.1016/j.tsf.2011.01.282.

146. Chen, X.; Mao, S. S., *Chemical Reviews* **2007,** *107* (7), 2891-2959. DOI 10.1021/cr0500535.

147. He, Z.; Ma, M.; Lan, X.; Chen, F.; Wang, K.; Deng, H.; Zhang, Q.; Fu, Q., *Soft Matter* **2011,** *7* (14), 6435-6443. DOI 10.1039/C1SM05574G.

148. Goswami, D.; Medda, S. K.; De, G., *ACS Applied Materials & Interfaces* **2011,** *3* (9), 3440-3447. DOI 10.1021/am200666m.

149. Hwang, G. B.; Page, K.; Patir, A.; Nair, S.; Allan, E.; P. Parkin, I., *The Anti-Biofouling Properties of Superhydrophobic Surfaces are Short-Lived.* **2018**.
150. Kamegawa, T.; Shimizu, Y.; Yamashita, H., *Adv Mater* **2012,** *24* (27), 3697-3700.
151. Wang, Y.; Huang, Z.; Gurney, R. S.; Liu, D., *Colloids and Surfaces A: Physicochemical and Engineering Aspects* **2019,** *561*, 101-108. DOI https://doi.org/10.1016/j.colsurfa.2018.10.054.
152. Kelly, K. L.; Coronado, E.; Zhao, L. L.; Schatz, G. C., *The Journal of Physical Chemistry B* **2003,** *107* (3), 668-677. DOI 10.1021/jp026731y.
153. Nursanto, E.; Jeon, H.; Kim, C.; Jee, M.; Koh, J. H.; Hwang, Y.; Koun Min, B., *Gold catalyst reactivity for CO2 electro-reduction: From nano particle to layer.* **2015**.
154. Koh, J. H.; Jeon, H. S.; Jee, M. S.; Nursanto, E. B.; Lee, H.; Hwang, Y. J.; Min, B. K., *The Journal of Physical Chemistry C* **2015,** *119* (2), 883-889. DOI 10.1021/jp509967m.
155. Kibria, M. A.; Anisur, M. R.; Mahfuz, M. H.; Saidur, R.; Metselaar, I. H. S. C., *Energy Conversion and Management* **2015,** *95*, 69-89. DOI https://doi.org/10.1016/j.enconman.2015.02.028.
156. Zhang, Z.; Lin, P.-C., Chapter 7 - Noble metal nanoparticles: synthesis, and biomedical implementations. In *Emerging Applications of Nanoparticles and Architecture Nanostructures*, Barhoum, A.; Makhlouf, A. S. H., Eds. Elsevier: 2018; pp 177-233.
157. Khan, Z. U. H.; Khan, A.; Chen, Y.; Shah, N. S.; Muhammad, N.; Khan, A. U.; Tahir, K.; Khan, F. U.; Murtaza, B.; Hassan, S. U.; Qaisrani, S. A.; Wan, P., *Journal of Photochemistry and Photobiology B: Biology* **2017,** *173*, 150-164. DOI https://doi.org/10.1016/j.jphotobiol.2017.05.034.
158. Jain, P. K.; Lee, K. S.; El-Sayed, I. H.; El-Sayed, M. A., *The Journal of Physical Chemistry B* **2006,** *110* (14), 7238-7248. DOI 10.1021/jp057170o.
159. Li, J.; Zhao, T.; Chen, T.; Liu, Y.; Ong, C. N.; Xie, J., *Nanoscale* **2015,** *7* (17), 7502-7519. DOI 10.1039/C5NR00857C.
160. Marassi, V.; Di Cristo, L.; Smith, S. G. J.; Ortelli, S.; Blosi, M.; Costa, A. L.; Reschiglian, P.; Volkov, Y.; Prina-Mello, A., *R Soc Open Sci* **2018,** *5* (1), 171113-171113. DOI 10.1098/rsos.171113.
161. Rizvi, S. A. A.; Saleh, A. M., *Saudi Pharm J* **2018,** *26* (1), 64-70. DOI 10.1016/j.jsps.2017.10.012.

162. Wang, L.; Ma, W.; Xu, L.; Chen, W.; Zhu, Y.; Xu, C.; Kotov, N. A., *Materials Science and Engineering: R: Reports* **2010,** *70* (3), 265-274. DOI https://doi.org/10.1016/j.mser.2010.06.012.
163. Fratoddi, I.; Venditti, I.; Cametti, C.; Russo, M. V., *J Mater Chem B* **2014,** *2* (27), 4204-4220. DOI 10.1039/C4TB00383G.
164. Dreaden, E. C.; Alkilany, A. M.; Huang, X.; Murphy, C. J.; El-Sayed, M. A., *Chem Soc Rev* **2012,** *41* (7), 2740-2779. DOI 10.1039/C1CS15237H.
165. Shah, K. W., *Energy and Buildings* **2018,** *175*, 57-68. DOI https://doi.org/10.1016/j.enbuild.2018.06.043.
166. Amendola, V.; Meneghetti, M., *Physical Chemistry Chemical Physics* **2009,** *11* (20), 3805-3821. DOI 10.1039/B900654K.
167. Hainfeld, J. F.; Smilowitz, H. M.; O'Connor, M. J.; Dilmanian, F. A.; Slatkin, D. N., *Nanomedicine* **2012,** *8* (10), 1601-1609. DOI 10.2217/nnm.12.165.
168. Tomar, A.; Garg, G., *Global Journal of Pharmacology* **2013,** *7*, 34-38. DOI 10.5829/idosi.gjp.2013.7.1.66173.
169. Romo-Herrera, J. M.; Alvarez-Puebla, R. A.; Liz-Marzán, L. M., *Nanoscale* **2011,** *3* (4), 1304-1315. DOI 10.1039/C0NR00804D.
170. Thompson, D. T., *Nano Today* **2007,** *2* (4), 40-43. DOI https://doi.org/10.1016/S1748-0132(07)70116-0.
171. Israelsen, N. D.; Hanson, C.; Vargis, E., *The Scientific World Journal* **2015,** *2015*, 12. DOI 10.1155/2015/124582.
172. FRONT MATTER. In *Catalysis by Gold*, PUBLISHED BY IMPERIAL COLLEGE PRESS AND DISTRIBUTED BY WORLD SCIENTIFIC PUBLISHING CO.: 2006; Vol. Volume 6, pp i-xv.
173. Alvarez-Puebla, R. A.; Liz-Marzán, L. M., *Small* **2010,** *6* (5), 604-610. DOI 10.1002/smll.200901820.
174. Xie, W.; Qiu, P.; Mao, C., *J Mater Chem* **2011,** *21* (14), 5190-5202. DOI 10.1039/C0JM03301D.
175. Maitani, M. M.; Ohlberg, D. A. A.; Li, Z.; Allara, D. L.; Stewart, D. R.; Williams, R. S., *J Am Chem Soc* **2009,** *131* (18), 6310-6311. DOI 10.1021/ja809347y.
176. Le Ru, E. C.; Grand, J.; Félidj, N.; Aubard, J.; Lévi, G.; Hohenau, A.; Krenn, J. R.; Blackie, E.; Etchegoin, P. G., *The Journal of Physical Chemistry C* **2008,** *112* (22), 8117-8121. DOI 10.1021/jp802219c.

177. Sunil Sekhar, C. A.; Vinod, P. C., *Molecules* **2016,** *21* (5). DOI 10.3390/molecules21050667.
178. Zhao, P.; Feng, X.; Huang, D.; Yang, G.; Astruc, D., *Coordination Chemistry Reviews* **2015,** *287*, 114-136. DOI https://doi.org/10.1016/j.ccr.2015.01.002.
179. Haruta, M.; Kobayashi, T.; Sano, H.; Yamada, N., *Chemistry Letters* **1987,** *16* (2), 405-408. DOI 10.1246/cl.1987.405.
180. Hutchings, G. J., *Journal of Catalysis* **1985,** *96* (1), 292-295. DOI https://doi.org/10.1016/0021-9517(85)90383-5.
181. Bond, G. C.; Sermon, P. A.; Webb, G.; Buchanan, D. A.; Wells, P. B., *Journal of the Chemical Society, Chemical Communications* **1973,** (13), 444b-445. DOI 10.1039/C3973000444B.
182. Corma, A.; Garcia, H., *Chem Soc Rev* **2008,** *37* (9), 2096-2126. DOI 10.1039/B707314N.
183. Hutchings, G. J.; Brust, M.; Schmidbaur, H., *Chem Soc Rev* **2008,** *37* (9), 1759-1765. DOI 10.1039/B810747P.
184. Valden, M.; Lai, X.; Goodman, D. W., *Science* **1998,** *281* (5383), 1647. DOI 10.1126/science.281.5383.1647.
185. Loedolff, M. J.; Goh, B.-M.; Koutsantonis, G. A.; Fuller, R. O., *New Journal of Chemistry* **2018,** *42* (18), 14894-14900. DOI 10.1039/C8NJ03076F.
186. Sádaba, I.; López Granados, M.; Riisager, A.; Taarning, E., *Green Chemistry* **2015,** *17* (8), 4133-4145. DOI 10.1039/C5GC00804B.
187. Mosier-Boss, P. A., *Nanomaterials (Basel)* **2017,** *7* (6), 142. DOI 10.3390/nano7060142.
188. Fürstner, R.; Barthlott, W.; Neinhuis, C.; Walzel, P., *Langmuir* **2005,** *21* (3), 956-961. DOI 10.1021/la0401011.
189. Lu, Y.; Sathasivam, S.; Song, J.; Chen, F.; Xu, W.; Carmalt, C. J.; Parkin, I. P., *J Mater Chem A* **2014,** *2* (30), 11628-11634. DOI 10.1039/C4TA02181A.
190. Wang, L.; Gong, Q.; Zhan, S.; Jiang, L.; Zheng, Y., *Adv Mater* **2016,** *28* (35), 7729-7735. DOI 10.1002/adma.201602480.
191. Zang, D.; Zhu, R.; Zhang, W.; Yu, X.; Lin, L.; Guo, X.; Liu, M.; Jiang, L., *Adv Funct Mater* **2017,** *27* (8), 1605446. DOI 10.1002/adfm.201605446.
192. Tripathy, A.; Kumar, A.; Sreedharan, S.; Muralidharan, G.; Pramanik, A.; Nandi, D.; Sen, P., *ACS Biomaterials Science & Engineering* **2018,** *4* (6), 2213-2223. DOI 10.1021/acsbiomaterials.8b00209.

193. Yohe, S. T.; Colson, Y. L.; Grinstaff, M. W., *J Am Chem Soc* **2012,** *134* (4), 2016-2019. DOI 10.1021/ja211148a.
194. Feng, L.; Zhang, Z.; Mai, Z.; Ma, Y.; Liu, B.; Jiang, L.; Zhu, D., *Angewandte Chemie* **2004,** *116* (15), 2046-2048. DOI 10.1002/ange.200353381.
195. Cottin-Bizonne, C.; Barrat, J.-L.; Bocquet, L.; Charlaix, E., *Nature Materials* **2003,** *2* (4), 237-240. DOI 10.1038/nmat857.
196. Dong, S.; Li, Y.; Tian, N.; Li, B.; Yang, Y.; Li, L.; Zhang, J., *Acs Appl Mater Inter* **2018,** *10* (49), 41878-41882. DOI 10.1021/acsami.8b17825.
197. Shiu, J.-Y.; Kuo, C.-W.; Chen, P.; Mou, C.-Y., *Chem Mater* **2004,** *16* (4), 561-564. DOI 10.1021/cm034696h.
198. Qian, B.; Shen, Z., *Langmuir* **2005,** *21* (20), 9007-9009. DOI 10.1021/la051308c.
199. Gong, D.; Long, J.; Jiang, D.; Fan, P.; Zhang, H.; Li, L.; Zhong, M., *Acs Appl Mater Inter* **2016,** *8* (27), 17511-17518. DOI 10.1021/acsami.6b03424.
200. Tan, J.; Hao, J.; An, Z.; Liu, C., *Rsc Adv* **2017,** *7* (42), 26145-26152. DOI 10.1039/C7RA03308G.
201. Wang, N.; Xiong, D.; Deng, Y.; Shi, Y.; Wang, K., *Acs Appl Mater Inter* **2015,** *7* (11), 6260-6272. DOI 10.1021/acsami.5b00558.
202. Peng, C.; Chen, Z.; Tiwari, M. K., *Nature Materials* **2018,** *17* (4), 355-360. DOI 10.1038/s41563-018-0044-2.
203. Lu, Y.; Sathasivam, S.; Song, J.; Crick, C. R.; Carmalt, C. J.; Parkin, I. P., *Science* **2015,** *347* (6226), 1132.
204. Yanagisawa, T.; Nakajima, A.; Sakai, M.; Kameshima, Y.; Okada, K., *Materials Science and Engineering: B* **2009,** *161* (1), 36-39. DOI https://doi.org/10.1016/j.mseb.2008.11.016.
205. Jung, Y. C.; Bhushan, B., *ACS Nano* **2009,** *3* (12), 4155-4163. DOI 10.1021/nn901509r.
206. Zhang, J.; Seeger, S., *ChemPhysChem* **2013,** *14* (8), 1646-1651. DOI 10.1002/cphc.201200995.
207. Zhou, H.; Wang, H.; Niu, H.; Gestos, A.; Lin, T., *Advanced Functional Materials* **2012,** *23* (13), 1664-1670. DOI 10.1002/adfm.201202030.
208. Zimmermann, J., **2008**.
209. Zimmermann, J.-H. Silicone nanofilaments as functional coatings : properties, applications and modifications. Zürich, **2008**.

210. Yu, H. G.; Yu, J. G.; Cheng, B., *J. Mol. Catal. A-Chem.* **2006,** *253* (1-2), 99-106. DOI 10.1016/j.molcata.2006.03.012.

211. Zhou, Y.; Vuille, K.; Heel, A.; Patzke, Greta R., *Zeitschrift für anorganische und allgemeine Chemie* **2009,** *635* (12), 1848-1855. DOI 10.1002/zaac.200900187.

212. Turkevich, J.; Stevenson, P. C.; Hillier, J., *Discussions of the Faraday Society* **1951,** *11* (0), 55-75. DOI 10.1039/DF9511100055.

213. Turkevich, J., *Gold Bulletin* **1985,** *18* (3), 86-91. DOI 10.1007/BF03214690.

214. Hoseini, S. J.; Rashidi, M.; Bahrami, M., *J Mater Chem* **2011,** *21* (40), 16170-16176. DOI 10.1039/C1JM11814E.

215. Raman, V.; Venkataraman, K. S., *Proceedings of the Royal Society of London. Series A, Mathematical and Physical Sciences* **1939,** *171* (945), 137-147.

216. Braun, D., *International Journal of Polymer Science* **2009,** *2009*. DOI 10.1155/2009/893234.

217. Hiorns, R., *Polym Int* **2000,** *49* (7), 807-807. DOI 10.1002/1097-0126(200007)49:7<807::AID-PI436>3.0.CO;2-1.

218. Zimmermann, J.; Reifler, F. A.; Schrade, U.; Artus, G. R. J.; Seeger, S., *Colloids and Surfaces a-Physicochemical and Engineering Aspects* **2007,** *302* (1-3), 234-240.

219. Wypych, G., PS polystyrene. In *Handbook of Polymers*, Elsevier: Oxford, 2012; pp 541-547.

220. Wannatong, L.; Sirivat, A.; Supaphol, P., *Polym Int* **2004,** *53* (11), 1851-1859.

221. Yamamoto, T.; Higashitani, K., *KONA Powder and Particle Journal* **2018,** *35*, 66-79. DOI 10.14356/kona.2018012.

222. Ha, S. T.; Park, O. O.; Im, S. H., *Macromol Res* **2010,** *18* (10), 935-943.

223. Lok, K. P.; Ober, C. K., *Canadian Journal of Chemistry* **1985,** *63* (1), 209-216. DOI 10.1139/v85-033.

224. Meng, F.; Engbers, G. H. M.; Feijen, J., *Journal of Biomedical Materials Research Part A* **2004,** *70A* (1), 49-58. DOI 10.1002/jbm.a.30056.

225. Zheng, G.; Stöver, H. D. H., *Macromolecules* **2002,** *35* (18), 6828-6834. DOI 10.1021/ma0121464.

226. Han, S. W.; Park, E. J.; Jeong, M.-G.; Kim, I. H.; Seo, H. O.; Kim, J. H.; Kim, K.-D.; Kim, Y. D., *Appl Surf Sci* **2017,** *400*, 405-412. DOI https://doi.org/10.1016/j.apsusc.2016.12.147.
227. Cao, C.; Ge, M.; Huang, J.; Li, S.; Deng, S.; Zhang, S.; Chen, Z.; Zhang, K.; Al-Deyab, S. S.; Lai, Y., *J Mater Chem A* **2016,** *4* (31), 12179-12187. DOI 10.1039/C6TA04420D.
228. Zhu, D.; Handschuh-Wang, S.; Zhou, X., *J Mater Chem A* **2017,** *5* (32), 16467-16497. DOI 10.1039/C7TA04577H.
229. Liang, W.; Wang, Y.; Sun, H.; Chen, P.; Zhu, Z.; Li, A., *Rsc Adv* **2015,** *5* (127), 105319-105323. DOI 10.1039/C5RA21791A.
230. Artus, G. R. J.; Seeger, S., *Advances in Colloid and Interface Science* **2014,** *209*, 144-162.
231. Wang, G. W.; Yu, B.; Chen, S. G.; Uyama, H., *Sci Rep-Uk* **2017,** *7*.
232. Bell, A. T., *Science* **2003,** *299* (5613), 1688. DOI 10.1126/science.1083671.
233. Schlögl, R., *Angewandte Chemie International Edition* **2015,** *54* (11), 3465-3520. DOI 10.1002/anie.201410738.
234. Che, M.; Bennett, C. O., The Influence of Particle Size on the Catalytic Properties of Supported Metals. In *Advances in Catalysis*, Eley, D. D.; Pines, H.; Weisz, P. B., Eds. Academic Press: 1989; Vol. 36, pp 55-172.
235. Meseck, G. R.; Fabbri, E.; Schmidt, T. J.; Seeger, S., *Adv Mater Interfaces* **2015,** *2* (12).
236. Meseck, G. R.; Kontic, R.; Patzke, G. R.; Seeger, S., *Advanced Functional Materials* **2012,** *22* (21), 4433-4438.
237. Meseck, G. R.; Kach, A.; Seeger, S., *J Phys Chem C* **2014,** *118* (43), 24967-24975.
238. Holmes, A. B.; Gu, F. X., *Environmental Technology* **2018**, 1-10. DOI 10.1080/09593330.2018.1430173.
239. Ragesh, P.; Anand Ganesh, V.; Nair, S. V.; Nair, A. S., *J Mater Chem A* **2014,** *2* (36), 14773-14797. DOI 10.1039/C4TA02542C.
240. Byun, D.; Hong, J.; Saputra; Ko, J. H.; Lee, Y. J.; Park, H. C.; Byun, B.-K.; Lukes, J. R., *Journal of Bionic Engineering* **2009,** *6* (1), 63-70. DOI https://doi.org/10.1016/S1672-6529(08)60092-X.
241. Hashimoto, K.; Irie, H.; Fujishima, A., *Japanese Journal of Applied Physics* **2005,** *44* (12), 8269-8285. DOI 10.1143/jjap.44.8269.
242. Eslamian, M.; Zabihi, F., *Nanoscale Research Letters* **2015,** *10*.

---

243. Liu, S. Q.; Pandey, A.; Duvigneau, J.; Vancso, J.; Snoeijer, J. H., *Macromolecules* **2018,** *51* (7), 2411-2417.
244. Higashimoto, S., *Catalysts* **2019,** *9* (2). DOI 10.3390/catal9020201.
245. Schneider, J.; Matsuoka, M.; Takeuchi, M.; Zhang, J.; Horiuchi, Y.; Anpo, M.; W Bahnemann, D., *Understanding TiO2 Photocatalysis: Mechanisms and Materials*. **2014**; Vol. 114.
246. Linsebigler, A. L.; Lu, G.; Yates, J. T., *Chem. Rev.* **1995,** *95* (3), 735-758. DOI 10.1021/cr00035a013.
247. Prakash, J.; Sun, S.; Swart, H. C.; Gupta, R. K., *Applied Materials Today* **2018,** *11*, 82-135. DOI https://doi.org/10.1016/j.apmt.2018.02.002.
248. A Damodar, R.; You, S.-J.; Chou, H.-H., *Study the self cleaning, antibacterial and photocatalytic properties of TiO2 entrapped PVDF membranes*. **2009**; Vol. 172, p 1321-8.
249. Kubacka, A.; Suarez-Diez, M.; Rojo, D.; Bargiela, R.; Ciordia, S.; Zapico, I.; Albar, J.; Barbas, C.; Martins dos Santos, V.; Fernández-García, M.; Ferrer, M., *Understanding the antimicrobial mechanism of TiO2-based nanocomposite films in a pathogenic bacterium*. **2014**; Vol. 4, p 4134.
250. Vermeulen, N.; Keeler, W. J.; Nandakumar, K.; Leung, K. T., *Biotechnology and Bioengineering* **2008,** *99* (3), 550-556.
251. Bekbolet, M.; Araz, C. V., *Chemosphere* **1996,** *32* (5), 959-965.
252. Fang, Z. K.; Yang, J. N.; Cao, Y.; Zhu, L. F.; Zhang, Q.; Shu, D.; He, C., *2013 International Symposium on Environmental Science and Technology (2013 Isest)* **2013,** *18*, 503-508. DOI 10.1016/j.proenv.2013.04.067.
253. Ouyang, K.; Dai, K.; Walker, S. L.; Huang, Q.; Yin, X.; Cai, P., *Scientific Reports* **2016,** *6*, 25702. DOI 10.1038/srep25702

https://www.nature.com/articles/srep25702#supplementary-information.
254. Carre, G.; Hamon, E.; Ennahar, S.; Estner, M.; Lett, M. C.; Horvatovich, P.; Gies, J. P.; Keller, V.; Keller, N.; Andre, P., *Applied and Environmental Microbiology* **2014,** *80* (8), 2573-2581.
255. Zimmermann, J.; Artus, G. R. J.; Seeger, S., *Journal of Adhesion Science and Technology* **2008,** *22* (3-4), 251-263. DOI 10.1163/156856108X305165.
256. Pensa, E.; Cortés, E.; Corthey, G.; Carro, P.; Vericat, C.; Fonticelli, M. H.; Benítez, G.; Rubert, A. A.; Salvarezza, R. C., *Accounts of Chemical Research* **2012,** *45* (8), 1183-1192. DOI 10.1021/ar200260p.

257. Pearson, R. G., *J Am Chem Soc* **1963,** *85* (22), 3533-3539. DOI 10.1021/ja00905a001.
258. Woehrle, G. H.; Brown, L. O.; Hutchison, J. E., *J Am Chem Soc* **2005,** *127* (7), 2172-2183. DOI 10.1021/ja0457718.
259. Dewi, M. R.; Laufersky, G.; Nann, T., *Rsc Adv* **2014,** *4* (64), 34217-34220. DOI 10.1039/C4RA05035E.
260. Liu, J.; Hlady, V., *Colloids and Surfaces B: Biointerfaces* **1996,** *8* (1), 25-37. DOI https://doi.org/10.1016/S0927-7765(96)01298-2.
261. Nieto, G.; Jongberg, S.; Andersen, M. L.; Skibsted, L. H., *Meat Science* **2013,** *95* (2), 177-184. DOI https://doi.org/10.1016/j.meatsci.2013.05.016.
262. Enustun, B. V.; Turkevich, J., *J Am Chem Soc* **1963,** *85* (21), 3317-3328. DOI 10.1021/ja00904a001.
263. Kimling, J.; Maier, M.; Okenve, B.; Kotaidis, V.; Ballot, H.; Plech, A., *The Journal of Physical Chemistry B* **2006,** *110* (32), 15700-15707. DOI 10.1021/jp061667w.
264. Souza, T. G. F.; Ciminelli, V. S. T.; Mohallem, N. D. S., *Journal of Physics: Conference Series* **2016,** *733*, 012039. DOI 10.1088/1742-6596/733/1/012039.
265. Shafiqa, A. R.; Abdul Aziz, A.; Mehrdel, B., *Journal of Physics: Conference Series* **2018,** *1083*, 012040. DOI 10.1088/1742-6596/1083/1/012040.
266. Mie, G., *Annalen der Physik* **1908,** *330* (3), 377-445. DOI 10.1002/andp.19083300302.
267. Deepracha, S.; Vibulyaseak, K.; Ogawa, M., Chapter 2.1 - Complexation of TiO2 With Clays and Clay Minerals for Hierarchically Designed Functional Hybrids. In *Advanced Supramolecular Nanoarchitectonics*, Ariga, K.; Aono, M., Eds. William Andrew Publishing: 2019; pp 125-150.
268. Hildebrandt, P.; Stockburger, M., *The Journal of Physical Chemistry* **1984,** *88* (24), 5935-5944. DOI 10.1021/j150668a038.
269. Sergiienko, S.; Moor, K.; Gudun, K.; Yelemessova, Z.; Bukasov, R., *Physical Chemistry Chemical Physics* **2017,** *19* (6), 4478-4487. DOI 10.1039/C6CP08254H.
270. Chang, S.; Combs, Z. A.; Gupta, M. K.; Davis, R.; Tsukruk, V. V., *ACS Appl Mater Interfaces* **2010,** *2* (11), 3333-9. DOI 10.1021/am100758k.

271. Velev, O. D.; Kaler, E. W., *Adv Mater* **2000,** *12* (7), 531-534. DOI 10.1002/(SICI)1521-4095(200004)12:7<531::AID-ADMA531>3.0.CO;2-S.

272. Wang, H. H.; Liu, C. Y.; Wu, S. B.; Liu, N. W.; Peng, C. Y.; Chan, T. H.; Hsu, C. F.; Wang, J. K.; Wang, Y. L., *Adv Mater* **2006,** *18* (4), 491-495. DOI 10.1002/adma.200501875.

273. Hong, S.; Li, X., *Journal of Nanomaterials* **2013,** *2013*, 9. DOI 10.1155/2013/790323.

274. Chiang, C.-Y.; Liu, T.-Y.; Su, Y.-A.; Wu, C.-H.; Cheng, Y.-W.; Cheng, H.-W.; Jeng, R.-J., *Polymers* **2017,** *9* (3), 93.

275. Chen, Y.-W.; Liu, T.-Y.; Chen, P.-J.; Chang, P.-H.; Chen, S.-Y., *Small* **2016,** *12* (11), 1458-1468. DOI 10.1002/smll.201502917.

276. Takale, B. S.; Bao, M.; Yamamoto, Y., *Organic & Biomolecular Chemistry* **2014,** *12* (13), 2005-2027. DOI 10.1039/C3OB42207K.

277. Zhang, J.; Yan, Z.; Fu, L.; Zhang, Y.; Yang, H.; Ouyang, J.; Chen, D., *Appl Clay Sci* **2018,** *166*, 166-173. DOI https://doi.org/10.1016/j.clay.2018.09.026.

278. Zhang, X.; Liu, S.; Salim, A.; Seeger, S., *Small* **2019,** *0* (0), 1901822. DOI 10.1002/smll.201901822.

279. Suchomel, P.; Kvitek, L.; Prucek, R.; Panacek, A.; Halder, A.; Vajda, S.; Zboril, R., *Sci Rep-Uk* **2018,** *8* (1), 4589. DOI 10.1038/s41598-018-22976-5.

280. Rahman, Z. u.; Ma, Y.; Hu, J.; Xu, Y.; Wang, W.; Chen, X., *Rsc Adv* **2014,** *4* (10), 5012-5020. DOI 10.1039/C3RA44434A.

281. Bogireddy, N. K. R.; Pal, U.; Gomez, L. M.; Agarwal, V., *Rsc Adv* **2018,** *8* (44), 24819-24826. DOI 10.1039/C8RA04332A.

282. Lin, C.; Tao, K.; Hua, D.; Ma, Z.; Zhou, S., *Molecules* **2013,** *18* (10). DOI 10.3390/molecules181012609.

283. Patakfalvi, R.; Dekany, I., *Colloid Polym Sci* **2002,** *280* (5), 461-470. DOI 10.1007/s00396-001-0629-0.

284. Ware, C. S.; Smith-Palmer, T.; Peppou-Chapman, S.; Scarratt, L. R. J.; Humphries, E. M.; Balzer, D.; Neto, C., *ACS Applied Materials & Interfaces* **2018,** *10* (4), 4173-4182. DOI 10.1021/acsami.7b14736.

285. Scarratt, L. R. J.; Hoatson, B. S.; Wood, E. S.; Hawkett, B. S.; Neto, C., *ACS Applied Materials & Interfaces* **2016,** *8* (10), 6743-6750. DOI 10.1021/acsami.5b12165.

286. Verho, T.; Bower, C.; Andrew, P.; Franssila, S.; Ikkala, O.; Ras, R. H. A., *Advanced Materials* **2011,** *23* (5), 673-678. DOI 10.1002/adma.201003129.

---

287. Saddiqi, N.-u.-H.; Seeger, S., *Advanced Materials Interfaces 0* (0), 1900041. DOI 10.1002/admi.201900041.
288. Das, A.; Deka, J.; Raidongia, K.; Manna, U., *Chemistry of Materials* **2017,** *29* (20), 8720-8728. DOI 10.1021/acs.chemmater.7b02880.
289. Bhushan, B.; Jung, Y. C.; Koch, K., *Langmuir* **2009,** *25* (5), 3240-3248. DOI 10.1021/la803860d.
290. Wong, T.-S.; Kang, S. H.; Tang, S. K. Y.; Smythe, E. J.; Hatton, B. D.; Grinthal, A.; Aizenberg, J., *Nature* **2011,** *477*, 443. DOI 10.1038/nature10447

https://www.nature.com/articles/nature10447#supplementary-information.
291. Lu, Y.; Sathasivam, S.; Song, J.; Crick, C. R.; Carmalt, C. J.; Parkin, I. P., *Science* **2015,** *347* (6226), 1132-1135. DOI 10.1126/science.aaa0946.

Abbreviations

AIBA	2,2'-Azobis(2-methylpropionamidine) dihydrochloride
ATR-FTIR	attenuated total reflectance Fourier transform infrared
AuNPs	gold nanoparticles
CA	contact angle
CFU	colony forming unit
CNC	carbon nanocomponents
CNF	carbon nanofibers
CNT	carbon nanotubes
CVD	chemical vapor deposition
DAGS	droplet-assisted growth and shaping
EDX	energy dispersive X-ray analysis
EMC	equilibrium moisture content
EPS	extracellular polymeric substances
ETCS	ethyltrichlorosilane
EtOH	ethanol
FRP	free radical polymerization
FTO	fluorine doped tin oxide
GBs	glass beads
GO	graphite oxide
ICP-MS	inductively coupled plasma mass spectrometry
LDPE	low density polyethylene
MB	methylene blue
MFCM	multifunctional composite materials
MPTMS	(3-mercaptopropyl)trimethoxysilane
MTCS	methyltrichlorosilane
MTES	methyltriethoxysilane
MTMS	methyltrimethoxysilane
NPs	nanoparticles
OD_{600}	optical density measured at a wavelength of 600 nm
OTES	octyltriethoxysilane
PDMS	polydimethylsiloxane
PE	polyester
PEG	polyethylene glycol
PP	polypropylene
PS	polystyrene
R6G	rhodamine 6G
SA	sliding angle
SAED	selected area electron diffraction
SEM	scanning electron microscope
SERS	surface enhanced Raman scattering

SFLS	supercritical fluid-liquid-solid
SLS	solution-liquid-solid
SNFs	silicone nanofilaments
STEM	scanning transmission electron microscope
TEM	transmission electron microscope
TEOS	tetraethoxysilane
TiO_2 NPs	titanium dioxide nanoparticles
TTIP	titanium isopropoxide
VLS	vapor-liquid-solid
VTCS	vinyltrichlorosilane
WRE	water repellent effectiveness
WUR	relative water uptake
XRD	X-ray diffraction

Curriculum Vitae

Name: Zhang
First Name: Xiaotian
Date of Birth: 06 Sep 1989
Place of origin: Zhejiang, P.R.China

Education:

2015 – 2020 PhD Program
University of Zurich, Switzerland

2012 – 2014 Master of Science in Industrial Chemistry
National University of Singapore, Singapore & Technical University of Munich (Joint Degree)

Thesis title:
Synthesis of Waterborne Polyurethane Dispersion Product on Personal Care Application by Bio-based Materials

2008 – 2012 Bachelor of Science in Chemistry
Lanzhou University, P.R.China

Thesis title:
One-Pot Synthesis of Indolo[2,3-c]quinolin-6-ones by Sequential Photocyclizations of 3-(2-Azidophenyl)-N-PAA

有志者、事竟成，破釜沉舟，百二秦关终属楚；

苦心人、天不负，卧薪尝胆，三千越甲可吞吴。

金生 Sheng Jin (1589—1645)